Phase-coherent electron transport through non- and ferro-magnetic atomic-sized metal contacts

Zur Erlangung des akademischen Grades eines
DOKTORS DER NATURWISSENSCHAFTEN
von der Fakultät für Physik der Universität (TH)
Karlsruhe

genehmigte

DISSERTATION

von

Dipl.-Phys. Michael Friedrich Häfner
aus Ulm

Tag der mündlichen Prüfung	12.06.2009
Referent	Prof. Dr. Gerd Schön
Korreferent	Prof. Dr. Juan Carlos Cuevas

Acknowledgments

With this PhD thesis I finish the education at the Universität Karlsruhe. During the years of formation I appreciated the accompaniment of many people. Here I can only mention a limited number of them so that this list necessarily must remain incomplete.

First of all I would like to thank Prof. Gerd Schön for giving me the possibility to write the thesis in his group at the Institut für Theoretische Festkörperphysik (TFP). I benefited very much from lively and inspiring atmosphere at the TFP. During the time of the thesis he gave me the possibility to experience international cooperation, to attend many conferences, workshops, and summer schools. For his continuous support I am much obliged.

I am deeply indebted to my supervisor, Juan Carlos Cuevas. He taught me the physics behind the work of this thesis and made the stay in Madrid and the collaboration with many people, including experimentalists possible. His trust in my work and his enthusiasm for physics was always encouraging. Beyond all I want to express my deep gratitude for his generosity and his everyday support during my stay in Madrid.

My sincere thanks go to my former office mate Janne Viljas. At any time he was open to discuss any technical issue. His expertise and profound knowledge greatly alleviated to surmount the many challenges. For valuable discussions and the pleasant collaboration I want to deeply thank Fabian Pauly. I appreciated very much his motivation to attack new problems. Sincere thanks owe I to Markus Dreher for the supply with Molecular Dynamics simulations of atomic contacts.

The work presented in this thesis could not have been carried out without the great infrastructure provided by the TFP/TKM. In particular I want to acknowledge Andreas Poenicke and his administrator colleagues Daniel Hermann and Tobias Ulbricht for keeping up this incomparable system. Many thanks for their support and never ending patience.

I acknowledge financial support from the Karlsruhe House of Young Scientist for the stay in Madrid.

Thanks also to all the – present and former – members of TFP in Karlsruhe and C-V in Madrid for making me feel at home in both places. I highly appreciated the many interesting and fruitful discussions. Besides the above mentioned people I am deeply grateful to Ulrich Meier and Wolf-Dieter Heller for proofreading large parts of this thesis. Thanks to my friends, for helping, supporting and encouraging me when needed.

Finally I want to express my profound gratitude to my family, who gave me invaluable support all the time.

Contents

Chapter 1

Introduction

When the size of a nanocontact approaches the atomic scale, its physical properties are significantly altered [1]. As an example, the conductance of any macroscopic metallic contact is described by Ohm's law, which states that the conductance of the contact is proportional to its cross-section and inversely proportional to its length. But when the size of the contact reaches the atomic scale, Ohm's law breaks down. The parallel advance of theory and of micro-fabrication techniques made it possible to obtain a thorough understanding of this regime, both theoretically and experimentally.

On the theory side, the limits of Ohm's law for thin diffusive contacts were already discussed by Maxwell [2]. Later Sharvin derived an expression of the conductance for a ballistic contact, by comparing the electrical current passing the contact with the flow of a dilute ideal gas through an orifice [3]. Although based on semi-classical arguments, Sharvin's expression for the conductance describes thick ballistic nanocontacts well.

However, due to the limitations of the semi-classical approach, the Sharvin conductance does not account for purely quantum effects which dominate when the size of the contact becomes so small that the wave nature of an electron can no longer be ignored. Landauer pointed out [4, 5] that in this case, the conductance G for the sample is described by its quantum mechanical transmission. This description was later expanded by Büttiker [6, 7] to the case of several transmission channels with transmission τ_j and the presence of a magnetic field. The Landauer-Büttiker formula of the conductance marks the basis of the present understanding of the conductance properties of mesoscopic samples and it reads for spin-degenerate systems:

$$G = \frac{2e^2}{h} \sum_j \tau_j \ , \tag{1.1}$$

where e is the electron charge and h Planck's constant. The constant of proportionality $G_0 = 2e^2/h$ is called the quantum of conductance. The Landauer-Büttiker expression for a linear chain of atoms with one orbital per site was first derived by Caroli and coworkers [8]. Later it was generalized to arbitrary contacts by Ferrer *et al.* [9]. In this form, the conduction properties can be derived once the system's electronic Hamiltonian is known.

On the experimental side, the invention of the scanning tunneling microscope (STM) by

Binnig and Rohrer [10, 11] stimulated the development of a variety of related instruments that are able to measure a variety of physical properties of a surface with atomic resolution. Very appealing examples of the possibilities to manipulate atoms on surfaces in a controlled manner were given by Eigler and coworkers [12, 13].

Gimzewski and Möller have been the first to employ an STM to study the conductance of an atomic contact [14]. Later it was used by Agraït and coworkers to characterize the mechanical properties [15] as well as the elastic [16] and inelastic [17] conduction properties of contacts consisting of atomic chains of gold.

In spite of the great versatility of the STM technique, it mainly suffers from mechanical instability due to long, unsupported parts in the construction. As a remedy, in 1992 Muller and coworkers [18] introduced the so-called Mechanically Controllable Break Junction (MCBJ) technique, dedicated to the study of atomic-sized junctions. With minimization of the unsupported parts it is possible to mechanically stabilize the contacts during the breaking process with a precision of some picometers. This technique was intensively used to study the conduction properties of various atomic metal contacts. Using the nonlinear subgap structure of the superconducting I-V-curves of atomic contacts – elaborated independently by Cuevas and Averin (and coworkers) [19, 20] – Scheer *et al.* [21] could measure the conductance channels of atomic contacts of example metals. They find that the number of conductance channels of a one-atom contact is limited by the number of available valence orbitals. For an overview of the experimental results on conduction properties of atomic metal contacts we refer to the PhD thesis of Yanson [22].

Parallel to the experimental progress also the theoretical understanding of the properties of nanoscale wires advanced. Molecular Dynamics (MD) simulations were used to describe the mechanical deformation of an atomic wire during stretching [23]. The conduction properties of metallic atomic contacts were investigated with different approaches to describe the electronic structure of the contacts, such as a semi-empirical potential [24], a tight-binding Hamiltonian [25, 26], and later *ab initio* Density Functional Theory (DFT) calculations [27].

Until recently, the discussion of transport in atomic contacts was limited to metals with partially occupied valence bands only. In the case of atoms of divalent elements like magnesium and zinc the outermost s orbitals are filled. As a consequence, small atomic clusters of these materials show an insulating behavior with an important gap between Highest Occupied Molecular Orbital (HOMO) and Lowest Unoccupied Molecular Orbital (LUMO) [28, 29]. However in the bulk limit the s and p orbitals hybridize and lead to metallic properties. For the intermediate case of atomic contacts however it is *a priori* not obvious whether metallic or insulating behavior is retained. The aim of the first part of this thesis is to extend the analysis of transport properties of atomic contacts to the case of the divalent metals magnesium and zinc.

In non-magnetic atomic metal contacts the electronic spin is degenerate. The second part of the thesis is dedicated to the analysis of ferromagnetic atomic contacts, in which this degeneracy is lifted. The non-zero spin as additional degree of freedom opens a new field of applications beyond the charge-controlled electronics, the "Spintronics" [30].

The most remarkable spin-related effect appears in multilayer systems, where ferromagnetic layers are separated by nonmagnetic spacers. When the magnetization direction in one of the ferromagnetic layers is rotated with respect to the other, the resistance changes drastically (up to 80%). This so-called Giant Magnetoresistance is a purely spin-related effect and it was discovered independently by the groups of Grünberg and Fert in 1988 [31, 32].

In the limit of atomic contacts, also the magnetic properties differ considerably from bulk [33] and therefore may give rise to interesting effects in this regime. Indeed Garcia and coworkers reported a strongly enhanced Magnetoresistance of 200% in nanowires of Ni [34]. Although the origin of these findings is under debate [35] and the high Magnetoresistance is supposed to be rather due to magnetostriction than of electronic nature, these experiments stimulated the research in ferromagnetic atomic contacts in the following years.

A lot of attention has been devoted to the experimental [22, 36–55] and theoretical [56–68] analysis of atomic contacts of the $3d$ ferromagnetic materials. In particular the analysis of conductance histograms of those contacts has produced contradictory results. On one hand, several groups have reported conductance histograms that resemble those of noble metals like Au, with peaks at half-integer multiples of G_0 [42–47]. Similar to the case of Au, these findings were attributed to conductance quantization in those contacts [45]. On the other hand, Untiedt *et al.* [48] reported the absence of conductance quantization in atomic contacts of the $3d$ ferromagnetic materials. Instead they find conductance histograms of those contacts that are typical for transition metals like Pt.

Furthermore it was reported that the Anisotropic Magnetoresistance (AMR) in atomic contacts of the $3d$ ferromagnetic materials shows an increased amplitude and deviates strongly from the bulk behavior (see Fig. refFig:amr-exp(b),(c) and [54, 55]).

The theoretical works dedicated to the study of atomic contacts of the $3d$ ferromagnetic materials are either limited to idealized systems like linear chains [57–59, 61–63, 69, 70] or focus on particular issues of one material only [64–68]. The aim of the second part of this thesis is to study general conduction properties of the atomic contacts of the $3d$ ferromagnetic materials iron, cobalt, and nickel. In particular we will analyze the contribution of the $3d$ orbitals to the conductance and discuss the consequences that arise in the tunneling regime. Furthermore we will study in detail the peculiar change of the AMR properties when going from bulk to the atomic contact limit.

Outline of the thesis:

The main interest of this thesis consists in the analysis of the conduction properties of metallic atomic contacts. In Chapter 2 we will introduce the models used to describe the electronic structure of such systems, with special emphasis on a tight-binding model. Furthermore we will derive the expressions for the equilibrium properties [mainly the local density of states (LDOS)] and the elastic current there.

In Chapter 3 we first discuss a simplified linear chain model. Then we use the tight-binding model to discuss the elastic transport properties for non-magnetic atomic contacts of some example metals.[1] In the case of Al we can directly compare to *ab initio* calculations by means of density functional theory [72]. We will expand the discussion to the bivalent metals Mg and Zn [73–75], which were not analyzed until now. We can compare our theoretical results to experiments that were simultaneously carried out in the groups of Prof. Scheer at Universität Konstanz and Prof. van Ruitenbeek at Leiden University.

In Chapter 4 we extend the model to the study of ferromagnetic atomic contacts of Fe, Co, and Ni [76]. We first focus on ideal contact geometries of the $3d$ ferromagnets and discuss their general conduction properties. In particular we will analyze the current in the tunneling regime. By combining the electronic structure calculation with a separate Molecular Dynamics simulation we can analyze at the same time the evolution of an atomic contact of Ni and derive its conduction properties, including a conductance histogram [77].

Chapter 5 is devoted to the anisotropy properties of the ferromagnetic atomic contacts, induced by the spin-orbit coupling [78]. We first analyze a minimal model of a linear chain similar to Chapter 3 and derive the most striking features. Next we discuss the anisotropy properties of the conduction for ideal contact geometries of those materials and under perturbation of the geometries. Then we analyze the anisotropy properties of the contact geometries obtained from Molecular Dynamics simulations and discuss the small orbital momentum induced by the spin-orbit coupling. Finally we study the influence of impurities in the leads on the anisotropy and conclude on the temperature dependence of the observed anisotropies.

A summary of this thesis is presented in Chapter 6.

---

[1] An extension to inelastic transport due to electron-phonon interaction (not considered here) can be found in Ref. [71].

Chapter 2

Theoretical framework

In this Section we want to discuss the model we use to describe the current through an atomic constriction. We start with the description of the electronic structure mainly in terms of a tight-binding (TB) model and derive the expression for the current from that.

2.1 Electronic structure

We show in this Section how we describe the electronic structure of an atomic contact. As in this work we concentrate on metallic atomic contacts, we will mainly apply the TB approach, which proofs to be an efficient and sufficiently accurate way to describe the electronic structure of those systems. Thus the focus in the following will lie on this approach. However we will compare for some exemplary cases with more advanced and justified *ab initio* density functional theory (DFT) calculations. For this reason we also give a brief introduction to the DFT approach at the end of this Section.

The TB approach originates from applications in solid-state physics and is reviewed in most textbooks (see for example [79, 80]). In the next Sections we follow closely an overview given in [81].

2.1.1 Tight-binding approach

Let us start with defining the meaning of "tight-binding" model: The problem we are interested in is how to determine the electronic structure of a system composed of a collection of atoms that are located in different positions that we denote by $\mathbf{R}_i$. The corresponding Hamiltonian H of this system can always be written in a local basis, i.e. in a basis formed by single-particle wave functions that are localized around the different atomic positions. This is the spirit of the method known as linear combination of atomic orbitals (LCAO), which is widely used in theoretical chemistry. The first approximation in the tight-binding approach is to assume that the Hamiltonian written in second quantization adopts the following form:

$$\hat{\mathbf{H}} = \sum_{ij,\alpha\beta,\sigma} [\mathbf{H}]_{i\alpha,j\beta,\sigma}\, \hat{c}^{\dagger}_{i\alpha,\sigma}\hat{c}_{j\beta,\sigma} \ , \tag{2.1}$$

where $\hat{c}^{\dagger}_{i\alpha,\sigma}$ creates the state $|i\alpha\sigma\rangle$ that corresponds to the localized orbital α with spin σ that is centered around $\mathbf{R}_i$, i.e. $\langle \mathbf{r}|i\alpha\sigma\rangle = \phi_{i\alpha\sigma}(\mathbf{r}) = \phi_{\alpha\sigma}(\mathbf{r} - \mathbf{R}_i)$. This generic form for the Hamiltonian implies that either the many-body interactions – such as the electron-electron interaction – are neglected or that they are taken into account in a mean field manner by an appropriate choice of the matrix elements. In the case of the preceding Hamiltonian, the matrix elements are rigorously defined as

$$[\mathbf{H}]_{i\alpha,j\beta,\sigma} = \int d^3\mathbf{r}\ \phi^{*}_{\alpha\sigma}(\mathbf{r} - \mathbf{R}_i) \left[-\frac{\hbar^2}{2m}\nabla^2 + V(\mathbf{r}) \right] \phi_{\beta\sigma}(\mathbf{r} - \mathbf{R}_j), \tag{2.2}$$

where $V(\mathbf{r})$ is the potential that describes the Coulomb interaction between the electrons and ions. Note that, in the absence of spin-orbit coupling, the Hamiltonian is diagonal in spin space. Finally, in the TB approach, as it is used here, the matrix elements are not determined from first principles, i.e. from a direct evaluation of the integral in Eq. 2.2, but they are used merely as parameters that may be derived approximately or may be fitted to experiment or other theory.[1] So, by TB model we mean here a model, in which the system is described in terms of a single-particle Hamiltonian written in a local basis, the elements of which are determined in a empirical or semi-empirical way. The various TB models differ in the way in which these parameters are obtained. In a later Section 2.1.4 we will describe in detail, how these parameters are determined in practice.

Generally, there are two situations where the wave function associated with a TB model can be easily determined. The first one corresponds to the case of a small finite system such as a cluster of atoms or a molecule and the second one corresponds to the case of an infinite periodic system. In the first case, the Hamiltonian can be diagonalized by writing first the wave function as a combination of localized orbitals:

$$\Phi_{\sigma}(\mathbf{r}) = \sum_{j\beta} a_{j\beta}\phi_{j\beta\sigma}(\mathbf{r}), \tag{2.3}$$

Together with the Schrödinger equation this leads immediately to the following set of equations for the coefficients:

$$\sum_{j\beta} [\mathbf{H} - \varepsilon\mathbf{S}]_{i\alpha,j\beta,\sigma}\, a_{j\beta} = 0\ , \tag{2.4}$$

where ε is the energy and

$$[\mathbf{S}]_{i\alpha,j\beta,\sigma} = \int d^3\mathbf{r}\ \phi^{*}_{\alpha\sigma}(\mathbf{r} - \mathbf{R}_i)\, \phi_{\beta\sigma}(\mathbf{r} - \mathbf{R}_j) \tag{2.5}$$

is the overlap between the states $|i\alpha\sigma\rangle$ and $|j\beta\sigma\rangle$. Here, we have taken into account the possibility that the localized orbitals centered on different atoms usually are non-orthogonal. These equations have non-trivial solutions if

$$\det(\mathbf{H} - \varepsilon\mathbf{S}) = 0\ , \tag{2.6}$$

---

[1] In this sense the orbital index α should rather be considered as a projection of the Hamiltonian elements on the orbital symmetries α than being due to an atomic orbital α.

where the symbol “det” denotes the determinant of the matrix appearing inside the brackets. The roots of this secular equation yield the eigenenergies or energy levels of the finite problem and the eigenfunctions are the corresponding waves functions (or molecular orbitals) of the system. The dimension of the matrices in Eq. (2.6) is simply the total number of localized orbitals in the problem. Therefore, the solution of the generalized eigenvalue problem of Eq. (2.6) typically requires resorting to numerics.

In the case of an infinite periodic system, typical in solid state physics, one can diagonalize the Hamiltonian making use of Bloch's theorem (see for instance Ref. [79]). The idea goes as follows: Consider a periodically replicated unit cell, where the lattice vectors are denoted as $\mathbf{R}_m$, with a set of atoms i located at positions $\mathbf{b}_i$ in each unit cell. Associated with each atom is a set of atomic-like orbitals $\phi_{i\alpha\sigma}$, where α denotes both the orbital and angular quantum number of the atomic state. The Hamiltonian can be easily diagonalized in reciprocal space as follows. We first construct the wave functions (Bloch sums)

$$\Phi_{\mathbf{k}i\alpha\sigma}(\mathbf{r}) = \frac{1}{\sqrt{N}} \sum_n \exp\left(i\mathbf{k}\cdot\mathbf{R}_n\right) \phi_{\alpha\sigma}\left(\mathbf{r} - \mathbf{R}_n - \mathbf{b}_i\right), \tag{2.7}$$

where $\mathbf{k}$ is the Bloch wave vector, which is restricted to the Brillouin zone, and N is the number of unit cells in the sum. The solution of Schrödinger's equation for wave vector $\mathbf{k}$ requires the diagonalization of the Hamiltonian matrix using the basis functions of Eq. (2.7). Since the Hamiltonian has the periodicity of the lattice, this basis will block-diagonalize the Hamiltonian, with each block having a single value of $\mathbf{k}$. Within one of these blocks, the matrix elements can be written in the form

$$[\mathbf{H}]_{i\alpha,j\beta,\sigma}(\mathbf{k}) = \sum_n \exp\left(i\mathbf{k}\cdot\mathbf{R}_n\right) \int d^3\mathbf{r}\ \phi^*_{\alpha\sigma}\left(\mathbf{r} - \mathbf{R}_n - \mathbf{b}_i\right) \left[\frac{-\hbar^2\nabla^2}{2m} + V(\mathbf{r})\right] \phi_{\beta\sigma}\left(\mathbf{r} - \mathbf{b}_j\right), \tag{2.8}$$

where we have used the translation symmetry of the lattice to remove one of the sums over the lattice vector $\mathbf{R}_m$. In the same way, one can also define the overlap matrix in reciprocal space where the different elements adopt the form:

$$[\mathbf{S}]_{i\alpha,j\beta,\sigma}(\mathbf{k}) = \sum_n \exp\left(i\mathbf{k}\cdot\mathbf{R}_n\right) \int d^3\mathbf{r}\ \phi^*_{\alpha\sigma}\left(\mathbf{r} - \mathbf{R}_n - \mathbf{b}_i\right) \phi_{\beta\sigma}\left(\mathbf{r} - \mathbf{b}_j\right). \tag{2.9}$$

This time the corresponding secular equation reads

$$\det\left[\mathbf{H}(\mathbf{k}) - \varepsilon\mathbf{S}(\mathbf{k})\right] = 0\ . \tag{2.10}$$

The solution of this generalized eigenvalue problem yields the different energy bands, $\varepsilon_\mu(\mathbf{k})$ of the solid and the eigenvector matrix $\left[\mathbf{Q}(\mathbf{k})\right]_{\aleph,\mu}$. Here $\aleph$ collects the indices of the atom i of the unit cell, orbital α, and spin σ, and μ counts the energy bands. Notice that the total number of energy bands, i.e. the number of solutions of Eq. (2.10), equals the number of atoms in the unit cell times the number of orbitals per atom and spin.

An important quantity for many purposes is the density of states (DOS) per unit energy ε (and per unit volume in extended matter). The DOS projected onto a given atom, orbital and spin of the unit cell (fixed by the index $\aleph$) is defined in terms of the energy bands $\varepsilon_\mu(\mathbf{k})$ as follows:

$$\rho_\aleph(\varepsilon) = \frac{1}{N}\sum_{\mathbf{k},\mu}\left|[\mathbf{Q}(\mathbf{k})]_{\aleph,\mu}\right|^2 \delta(\varepsilon_\mu(\mathbf{k})-\varepsilon) = \frac{\Omega_{cell}}{(2\pi)^d}\sum_{\mu}\int_{BZ} d^d\mathbf{k}\ \left|[\mathbf{Q}(\mathbf{k})]_{\aleph,\mu}\right|^2 \delta(\varepsilon_\mu(\mathbf{k})-\varepsilon)\,, \tag{2.11}$$

where BZ denotes the Brillouin zone, Ω_{cell} is the volume of the unit cell, and d is the dimensionality of the system.

In the case of infinite, non-periodic systems, like the atomic-scale junctions we are interested in, the determination of the wave function is literally impossible. However, the use of the Green's functions techniques described below allows to extract most of the relevant information about the electronic structure from a tight-binding model.

2.1.2 Matrix elements

In the context of solid state physics most applications are based on the seminal paper of Slater and Koster (SK) [82], in which a modified LCAO method to interpolate the results of first-principles electronic structure calculations was proposed. As Slater and Koster noted, at that time (1954) it was computationally impossible to directly evaluate the large number of integrals occurring in the LCAO method. However, since this approach shows all the correct symmetry properties of the energy bands and provides solutions of the single-particle Schrödinger's equation at arbitrary points in the Brillouin zone, they suggested that these integrals could be considered as adjustable constants determined from the results of other, more detailed, calculations. In order to understand the basis of the simplified LCAO/TB method proposed by SK, we first need to discuss in certain detail the nature of the matrix elements that appear in the tight-binding approach. This will be done in the rest of this Section, whereas the explanation of the SK-method will be postponed to a next Section (2.1.4).

The symmetries of the basis orbitals and the crystal or molecule are considered in the tight-binding approach. The atom-like functions ϕ_{nlm} can be written as radial functions multiplied by spherical harmonics,

$$\phi_{nlm}(\mathbf{r}) = \phi_{nl}(r)\,Y_{lm}(\hat{r})\,, \tag{2.12}$$

where $r = |\mathbf{r}|$, $\hat{r} = \mathbf{r}/r$, and n indicates different functions with the same angular momentum. The imaginary part of the spherical harmonics is controlled by the magnetic quantum number m: $Y^*_{lm} = Y_{l,-m}$. Typically, we use real basis functions that can be defined similarly in terms of real angular functions as $S^+_{lm} = (Y_{lm} + Y_{l,-m})/\sqrt{2}$ and $S^-_{lm} = (Y_{lm} - Y_{l,-m})/i\sqrt{2}$. The examples of real s ($l = 0$), p ($l = 1$), and d ($l = 2$) orbitals are given in Fig. 2.1. Analytical expressions of the angular dependence of these real orbitals can be found in many textbooks, see e.g. Refs. [80, Chapter 1] or [83]. These atomic-like orbitals then serve as basis function on each site of the physical system.

The key problem in a TB model is to determine the matrix elements (or integrals) that appear both in Eq. (2.8) and in Eq. (2.9). Those matrix elements can be divided into one-,

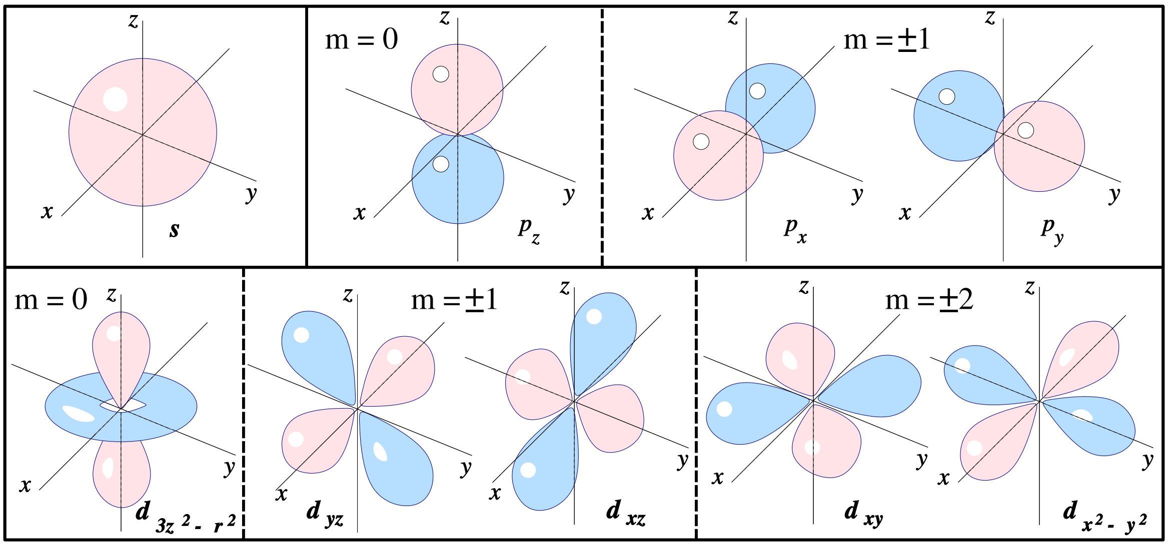

Figure 2.1: A sketch of the contours of the s-orbital and the d-orbitals with different magnetic quantum number m. The p_x- and p_y-orbitals, as well as the d_{yz}- and d_{zx}-orbitals (d_{xy}- and $d_{x^2-y^2}$-orbitals) transform into each other with a rotation by $\pm\pi/2$ ($\pm\pi/4$) around the z-axis.

two-, and three-center integrals. The simplest is the overlap matrix in Eq. (2.9), which involves only one center if the two orbitals are on the same site and two centers otherwise. The Hamiltonian matrix elements appearing in Eq. (2.8) consist of kinetic and potential terms

$$\mathbf{H} = -\frac{\hbar^2}{2m}\nabla^2 + \sum_{nk} V(\mathbf{r} - \mathbf{R}_n - \mathbf{b}_k), \tag{2.13}$$

where the first term is the usual kinetic energy and the second is the potential decomposed into a sum of spherical terms centered on each site k in the unit cell. The kinetic part of the Hamiltonian matrix element always involves one or two centers. However, the potential terms may depend upon the positions of other atoms; they can be divided into:

- One-center, where both orbitals and the potential are centered on the same site. These terms have the same symmetry as an atom in free space.
- Two-center, where the orbitals are centered on different sites and the potential is on one of the two. These terms have the same symmetry as other two-center terms.
- Three-center, where the orbitals and the potential are all centered on different sites. These terms can also be classified into various symmetries based upon the fact that three sites define a triangle.
- A special class of two-center terms with both orbitals on the same site and the potential centered on a different site. These terms add to the one-center terms above,

but depend upon the crystal symmetry.

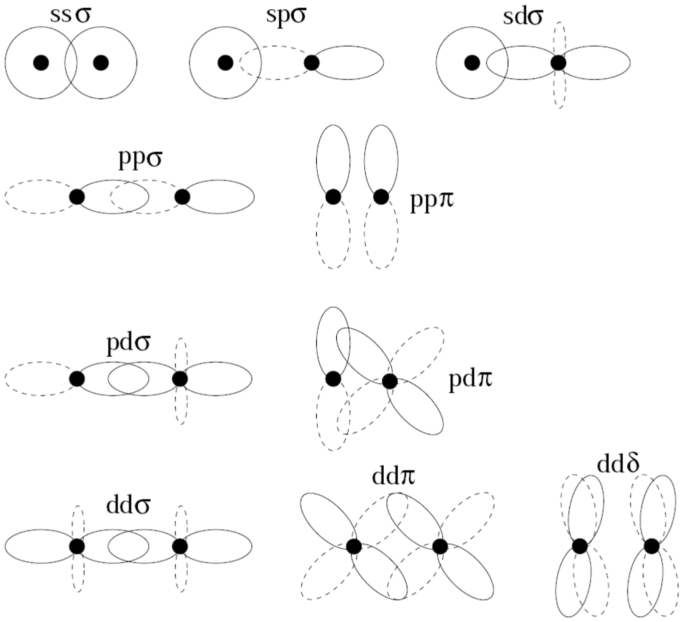

Figure 2.2: The 10 irreducible SK-parameters for the s, p and d orbitals, which are classified by the angular momentum about the axis with the notation σ ($m = 0$), π ($m = 1$), and δ ($m = 2$). The orbitals shown are real combinations of the angular momentum eigenstates. Positive and negative lobes are denoted by solid and dashed lines, respectively.

Two-center matrix elements play a special role in most practical TB approaches and are considered in more detail here. The analysis applies to all overlap terms and to any Hamiltonian matrix element that involves only orbitals and potential on two sites. For these integral the problem is similar to that of a diatomic molecule in free space with cylindrical symmetry. The orbitals can be classified in terms of the azimuthal angular momentum about the line between the centers, i.e. the value of m with the axis chosen along the line. The only non-zero matrix elements are between orbitals with the same m. Let $K_{lm,l'm'}$ denote an overlap or two-center Hamiltonian matrix element for states lm and $l'm'$. In the standard form with orbitals quantized about the axis between the pair of atoms, the matrix elements are then diagonal in $m'm$ and can be written as $K_{lm,l'm'} = K_{ll',m}\delta_{m'm}$. The quantities $K_{ll',m}$ are independent matrix elements that are irreducible, i. e. they cannot be further reduced by symmetry. By convention the states are labeled with l or l' denoted by s, p, d, ..., and $m = 0, \pm1, \pm2, ...$, denoted by σ, π, δ, ..., leading to the notation $K_{ss\sigma}$, $K_{sp\sigma}$, $K_{pp\pi}$, ...

In Fig. 2.2 we show the orbitals of the non-zero σ, π, and δ matrix elements for s, p, and d orbitals. The orbitals shown are actually the real basis functions $S^{\pm}_{lm}$ defined as combinations of the $\pm m$ angular momentum eigenstates. These are oriented along the axes defined by the line between the neighbours and two perpendicular axes. All states except the s state have positive and negative lobes. Note that states with odd l are odd under inversion. Their sign must be fixed by convention (typically one chooses the positive lobe along the positive axis). The direction of the displacement vector is defined to lie between the site denoted by the first index and that denoted by the second index. For example, in Fig. 2.2, the $K_{sp\sigma}$ matrix element in the top center has the negative lobe of the p function oriented toward the s function. Interchange of the indices leads to $K_{ps\sigma} = -K_{sp\sigma}$ or, more generally, to $K_{l'lm} = (-1)^{l'+l} K_{l'lm}$.

An actual set of basis functions is constructed with the quantization axis fixed in space, so that the functions must be transformed to utilize the standard irreducible form of the matrix elements. Examples of two-center matrix elements for s and $p_i = p_x, p_y, p_z$ orbitals for atoms separated by displacement vector $\mathbf{R}$ are shown in Fig. 2.3. Each of the orbitals on the left-hand side can be expressed as a linear combination of orbitals in the standard form, oriented along the rotated axes, as shown on the right. An s orbital is invariant and a p orbital is transformed to a linear combination of p orbitals. The only non-zero matrix elements are the σ and π matrix elements, as shown. The top row of the figure illustrates the transformation of the p_x orbital needed to write the matrix element K_{s,p_x} in terms of $K_{sp\sigma}$. The bottom row illustrates the relation of K_{p_x,p_z} to $K_{pp\sigma}$ and $K_{pp\pi}$. Specific relations for all s, p, and d matrix elements are given in Table A.1 and in Refs. [80, 82].

2.1.3 Slater-Koster two-center approximation

Now we are in the position to describe the Slater and Koster approach [82]. The authors proposed that the Hamiltonian matrix elements can be approximated with the two-center terms. Subsequently these parametrized matrix elements can be fitted to theoretical calculations (or empirical data) as a simplified way of describing and extending calculations of electronic bands. Within this approach, all matrix elements have the same symmetry as two atoms in free space [see Fig. 2.3 and Table 2.1]. This is a great simplification that leads to an extremely useful approach to understand electrons in materials.

Slater and Koster gave the extensive tables for matrix elements, including the s, p, and d matrix elements, which are reproduced in Table A.1 of Appendix A. In addition, they presented analytical formulae for bands in several crystal structures. However, the primary use of the SK approach in electronic structure has become the description of complicated systems, including band structures, total energies, and forces for relaxation of structures and molecular dynamics. The variety of applications have very distinct requirements that often lead to different choices of SK parameters.

For the bands, the parameters are usually designed to fit selected eigenvalues for a particular crystal structure and lattice constant. For example, the extensive tables derived by Papaconstantopoulos [84] are very useful to interpolate of results of more expensive methods. It has been pointed out by Stiles [85], that for a fixed ionic configuration, effects of multi-center integrals can be included in two-center terms that can be generated by an automatic procedure. This makes it possible to describe any band structure accurately with a sufficient number of matrix elements in SK form. However, the two-center matrix

Element	Expression
$K_{s,s}$	$ss\sigma$
K_{s,p_x}	$x\ sp\sigma$
K_{p_x,p_x}	$x^2\ pp\sigma + (1-x^2)\, pp\sigma$
K_{p_x,p_y}	$xy\,(pp\sigma - pp\pi)$

Table 2.1: Table of two-center matrix elements for either the overlap or the Hamiltonian, with real orbitals s and p_x, p_y, p_z. The vector $\mathbf{R}$ between sites, as shown in Fig. 2.3, defines the direction components $\hat{\mathbf{R}} = \mathbf{R}/\left|\mathbf{R}\right| = (x, y, z)$ The matrix elements are then expressed in terms of these components and the four irreducible matrix elements: $ss\sigma, sp\sigma, pp\sigma$, and $ss\sigma$. Other matrix elements can be found by permuting elements. For a full list of two-center matrix elements for the s, p, and d orbitals, see Table A.1 of Appendix A.

elements are not transferable to different structures.

On the other hand, any calculation of total energies, forces, etc., requires knowledge of the parameters as function of the atomic positions. Thus, the choices are usually compromises that attempt to fit a large range of data. Such models are fit to structural data and, in general, are only qualitatively correct for the bands. Since the total energy depends only upon the occupied states, these model usually describe the conduction bands with a poor precision. Of particular note, Harrison [80] has introduced a table that provides parameters for any element or compound. The forms are chosen for simplicity, generality, and ability to describe many properties in a way that it is instructive and useful. The basis is assumed to be orthonormal, i. e. $S_{mm'} = \delta_{mm'}$. For each atom, the diagonal Hamiltonian matrix elements are given in a table. Any Hamiltonian matrix element for orbitals on neighbouring atoms separated by a distance $\mathbf{R}$ is given by a factor times $1/R^{l+l'+1}$ [84, 86, 87]. Many other SK parametrization have been proposed, each tailored to particular elements and compounds.

2.1.4 The NRL tight-binding method

There is a basic difficulty in generating TB models that can describe very different structures. In models that have only two-center matrix elements, the values of the matrix elements must take into account effects of three-center terms. These effects change drastically between structures. There are two primary approaches towards tight-binding models that are transferable between different structures. One is to define environment dependent matrix elements, the values of which depend upon the presence of other neighbours. The other approach involves non-orthogonal TB, and is therefore more transferable than

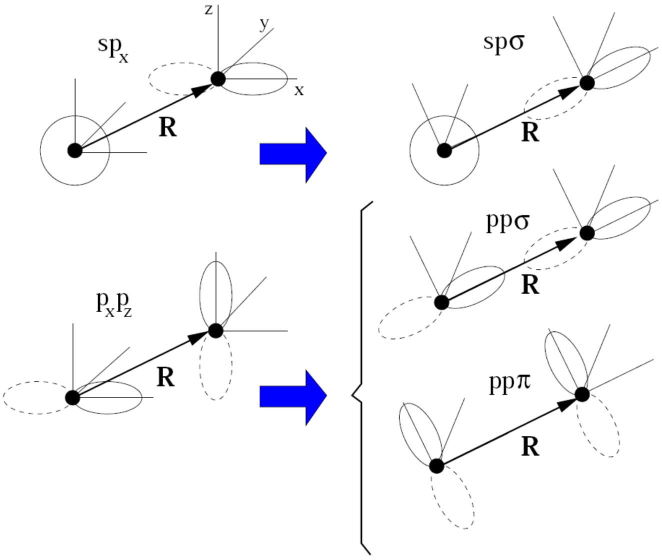

Figure 2.3: Schematic representation of two examples of two-center matrix elements of s and p orbitals for atoms separated by a displacement vector $\mathbf{R}$. Matrix elements are related to σ and π integrals by the transformation to a combination of orbitals that are aligned along $\mathbf{R}$ and perpendicular to $\mathbf{R}$. The upper figure illustrates the transformation to write a real matrix element K_{s,p_x} in terms of $sp\sigma$: the s orbital is unchanged and the p_x orbital is written as a function of the σ orbital, which is shown, and the π orbitals, which are not shown because there is no $sp\pi$ matrix element. The lower figure illustrates the transformation needed to write K_{p_x,p_z} in terms of $pp\sigma$ and $pp\pi$. The coefficients for the transformation of the s and p matrix elements are given in Table 2.1. The corresponding full set for the s, p, and d orbitals can be found in Table A.1 of Appendix A.

orthogonal forms.

The goal of this Section is to describe in certain detail a sophisticated TB parametrization in the spirit of the SK approach that meets the two requirements discussed in the previous paragraph. Moreover, this parametrization, developed by Cohen, Mehl, and Papaconstantopoulos [88, 89], also allows for the computation of total energies and related quantities. This method has been be widely used, in particular to analyze transport properties of metallic atomic-sized contacts, as we will show in later Chapters. This parametrization is referred to as NRL,[2] and it has been extensively described in several review articles by their authors [90, 91].

Up to this point we have mainly discussed tight-binding parametrization of the band structure alone[3]. Typically total-energy information is not given by these calculations,

---

[2] NRL stands for "Naval Research Laboratory". For more practical information about this parametrization, visit the web page: http://cstwww.nrl.navy.mil/bind/.

[3] The only exception was the method put forward by Harrison that was briefly mentioned in the previous

although a band energy can be readily determined from the sum of the eigenvalues over occupied states. However, in single-particle band theory, this sum is only a partial contribution to the total energy. In the Kohn-Sham single particle density functional theory (DFT) ansatz, which will shortly be introduced in the next Section, the total energy ε is given by

$$\varepsilon = \int \frac{d^3\mathbf{k}}{(2\pi)^3} \sum_n \varepsilon_n(\mathbf{k}) + F[n(\mathbf{r})], \tag{2.14}$$

where the integral is over the first Brillouin zone, the sum is over occupied states, and $F[n(\mathbf{r})]$ is a functional of the density which includes the repulsion of the ionic cores, correlation effects, and part of the Coulomb interaction. Note that the value of the integral depends upon the choice of zero for the Kohn-Sham (KS) potential $v_{KS}(\mathbf{r})$ which generates the eigenvalue spectrum:

$$-\nabla^2\psi_n(\mathbf{r}) + v_{KS}(\mathbf{r})\psi_n(\mathbf{r}) = \varepsilon_n\psi_n(\mathbf{r}). \tag{2.15}$$

This choice is arbitrary. In the method developed at NRL [88, 89], the potential v_{KS} in the previous equation is shifted by an amount

$$V_0 = F[n(\mathbf{r})]/N_e, \tag{2.16}$$

where N_e is the number of electrons in the unit cell. The total energy of the system is

$$\begin{aligned} \varepsilon &= \int \frac{d^3\mathbf{k}}{(2\pi)^3} \sum_n \varepsilon_n(\mathbf{k}) + F[n(\mathbf{r})] =, \int \frac{d^3\mathbf{k}}{(2\pi)^3} \sum_n \varepsilon_n(\mathbf{k}) + N_e V_0 = \\ &= \frac{d^3\mathbf{k}}{(2\pi)^3} \sum_n [\varepsilon_n(\mathbf{k}) + V_0] \end{aligned} \tag{2.17}$$

Note that V_0 depends upon the structure of the crystal, as well as the original method for determining the energy zero. Notice also that the $\varepsilon'(k)$ are in some sense "universal". That is, if any two band structure methods are sufficiently well converged, they will give the same total energy, and the eigenvalues derived from the two methods will only differ by a constant. The definition of V_0 for each method will be such that the shifted eigenvalues $\varepsilon'(k)$ are identical.

In the NRL method, the authors proceed as follows: First, they construct a first-principles[4] database of eigenvalues $\varepsilon_i(k)$ and total energies ε for several crystal structures at several volumes. Next they find V_0 for each system, and shift the eigenvalues. Finally, they attempt to find a set of parameters which will generate non-orthogonal, two-center SK Hamiltonians which will reproduce the energies and eigenvalues in the database.

Let us now describe how the TB parameters for elemental systems are constructed. One assumes that the on-site terms are diagonal and sensitive to the environment. For

---

Section.

[4] The first-principle methods used by the authors are typically the augmented plane wave method (APW) or the linearized augmented plane wave method (LAPW).

single-element systems one assigns atom i in the crystal and for each spin σ an embedded-atom-like "density"

$$\rho_{i\sigma} = \sum_j \exp\left(-\lambda_\sigma^2 R_{ij}\right)\ F\left(R_{ij}\right), \tag{2.18}$$

where the sum is over all the atoms j within a range R_C of atom i; λ_σ is the first fitting parameter, squared to ensure that the contributions are greater from the nearest neighbours; and $F(R)$ is a cut-off function, $F(R) = \theta(R_C - R)/\{1 + \exp[(R - R_C)/l + 5]\}$, where $\theta(z)$ is the step function. Typically one takes R_C between 10.5 and 16.5 Bohr and l between 0.25 and 0.5 Bohr. One then defines the angular-momentum-dependent on-site terms by

$$H_{il\sigma} = a_{l\sigma} + b_{l\sigma}\rho_{i\sigma}^{2/3} + c_{l\sigma}\rho_{i\sigma}^{4/3} + d_{l\sigma}\rho_{i\sigma}^2, \tag{2.19}$$

where $l = s, p$, or d. These $(a, b, c, d)_{l\sigma}$ form the next 12 fitting parameters per spin.

In the spirit of the two-center approximation, one assumes that the hopping integrals depend only upon the angular momentum of the orbitals and the distance between the atoms. As we showed before, all the two-center (spd) hopping integrals can then be constructed from ten independent parameters per spin, the SK parameters, $H_{ll'm}^\sigma$, where

$$(ll'm) = ss\sigma, sp\sigma, pp\sigma, pp\pi, sd\sigma, pd\sigma, pd\pi, dd\sigma, dd\pi, dd\delta \tag{2.20}$$

Then the following polynomial × exponential form for these parameters is assumed :

$$H_{ll'm}^\sigma(R) = (e_{ll'm\sigma} + f_{ll'm\sigma}R + g_{ll'm\sigma}R^2)\exp(-h_{ll'm\sigma}^2 R)F(R), \tag{2.21}$$

where R is the separation between these atoms and $F(R)$ is the cut-off function defined above. The parameters $(e, f, g, h)_{ll'm\sigma}$ constitute the next 40 fitting parameters per spin. Since this is a non-orthogonal calculation, one must also define a set of SK overlap functions. They represent the overlap between two orbitals separated by a distance R, and have the same angular momentum behavior as the hopping parameters[5]:

$$S_{ll'm}^\sigma(R) = (p_{ll'm\sigma} + q_{ll'm\sigma}R + r_{ll'm\sigma}R^2)\exp(-s_{ll'm\sigma}^2 R)F(R). \tag{2.22}$$

The parameters $(p, q, r, s)_{ll'm\sigma}$ make up the final 40 fitting parameters per spin for a monatomic system, yielding a total of 93 fitting parameters that are chosen to reproduce the contents of the first-principles database, as noted above.

So in summary, this parametrization uses an analytical set of two-center integrals, non-orthogonal parameters, and on-site parameters that depend on the local environment. The method not only reproduces the band structure, but also the total energy of the system. It has been demonstrated that this method also yields to a good precision structural energy differences, elastic constants, phonon frequencies, vacancy formation energies, and surface energies for both transition metal and noble metals.

---

[5] Note that in the case of Nb [92] additionally a slight variation of the form of the parametrization of the overlap parameters is applied: $S_{ll'm}^\sigma(R) = (\delta_{ll'} + p_{ll'm\sigma}R + q_{ll'm\sigma}R^2 + r_{ll'm\sigma}R^3)\exp(-s_{ll'm\sigma}^2 R)F(R)$.

As an application of this parametrization, we have computed the bulk density of states of four different metals that play an important role in molecular electronics. The results can be seen in Fig. 3.3. Notice that in the case of Ag and Au, like in any other noble metal, the Fermi energy lies in the region where the DOS is dominated by the s band. In the case of Al and Pb, the s and p bands dominate the DOS around the Fermi energy. The main difference between these two metals is that Pb has 4 valence electrons and therefore, the Fermi energy lies well inside the p band. Finally, Nb and Pt are examples of transition metals, where the d band dominates the DOS at the Fermi energy and for this reason, the d orbitals play a fundamental in the transport properties of these metals.

2.1.5 Density Functional Theory

In this Section we give a brief overview on the *ab initio* density functional theory (DFT) approach to the electronic structure. We restrict ourselves to describing the general ideas. For a thorough introduction to calculations based on DFT we refer to [93].

Let us start with the Schrödinger equation for a stationary system consisting of M atoms with N electrons:

$$\hat{H}\Psi_\mu(\mathbf{x}_1, ..., \mathbf{x}_N, \mathbf{R}_1, ..., \mathbf{R}_M) = \varepsilon_\mu \Psi_\mu(\mathbf{x}_1, ..., \mathbf{x}_N, \mathbf{R}_1, ..., \mathbf{R}_M) \ . \tag{2.23}$$

Here $\mathbf{R}_i$ refers to the spatial coordinates of the i-th nucleus and $\mathbf{x}_j = \{\mathbf{r}_j, \sigma_j\}$ is the combined variable of the j-th electron's position and spin. In atomic units, the Hamiltonian $\hat{H}$ reads:

$$\hat{H} = -\frac{1}{2}\sum_{i=1}^{N} \nabla_i^2 - \sum_{A=1}^{M} \frac{1}{2M_A}\nabla_A^2 - \sum_{i=1}^{N}\sum_{A=1}^{M} \frac{Z_A}{r_{iA}} + \sum_{i=1}^{N}\sum_{j>i}^{N} \frac{1}{r_{ij}} + \sum_{A=1}^{M}\sum_{B>A}^{M} \frac{Z_A Z_B}{R_{AB}} \ , \tag{2.24}$$

where Z_A and M_A are the A-th nucleus' charge and its mass relative to the electron's mass, $r_{ij} = |\mathbf{r}_i - \mathbf{r}_j|$ ($R_{AB} = |\mathbf{R}_A - \mathbf{R}_B|$) is the distance between electrons i and j (nuclei A and B), and $r_{iA} = |\mathbf{r}_i - \mathbf{R}_A|$ the distance between electron i and nucleus A. The first two terms in this expression describe the kinetic energy of electrons and nuclei. The remaining three terms define the potential part of the Hamiltonian. They represent the attractive electrostatic interaction between nuclei and electrons and the repulsive potential due to electron-electron and nucleus-nucleus interaction, respectively. ε_μ is the energy of the states, described by the wave function Ψ_μ

Due to the relatively high mass of the nuclei compared to the electrons they move much slower. Thus, in the Born-Oppenheimer approximation applied in the following, their movement is completely neglected. As a consequence, the nuclear kinetic energy is zero and their potential energy a constant. The electrons can be considered as moving in the field created by the fixed nuclei. The reduced electronic Hamiltonian then reads:

$$\hat{H}_{elec} = -\frac{1}{2}\sum_{i=1}^{N} \nabla_i^2 - \sum_{i=1}^{N}\sum_{A=1}^{M} \frac{Z_A}{r_{iA}} + \sum_{i=1}^{N}\sum_{j>i}^{N} \frac{1}{r_{ij}} = \hat{T} + \hat{V}_{Ne} + \hat{V}_{ee} \ , \tag{2.25}$$

and the corresponding Schrödinger equation:

$$\hat{H}_{elec}\Psi_{\mu,elec}(\mathbf{x}_1,...,\mathbf{x}_N;\mathbf{R}_1,...,\mathbf{R}_M) = E_{\mu,elec}\Psi_{\mu,elec}(\mathbf{x}_1,...,\mathbf{x}_N;\mathbf{R}_1,...,\mathbf{R}_M) \ . \tag{2.26}$$

The total energy of the system then consists of the electronic term and the constant nuclear repulsion term $\varepsilon_{tot} = \varepsilon_{elec} + \sum_{A=1}^{N}\sum_{B>A}^{N} Z_A Z_B / R_{AB}$.

The variational principle states that the energy ε_{trial} for a normalized trial wave function Ψ_{trial} is an upper bound to the true ground-state energy ε_0 with the true ground state wave function Ψ_0:

$$\left\langle \Psi_{trial} \middle| \hat{H} \middle| \Psi_{trial} \right\rangle = \varepsilon\left[\Psi_{trial}\right] \geq \varepsilon\left[\Psi_0\right] = \left\langle \Psi_0 \middle| \hat{H} \middle| \Psi_0 \right\rangle \ , \tag{2.27}$$

where equality holds if and only if $\Psi_{trial} = \Psi_0$. The problem of finding the true ground state wave function can thus be traced back to minimization of $\varepsilon\left[\Psi_{trial}\right]$ with respect to all allowed N-electrons wave functions Ψ_{trial}:

$$\varepsilon_0 = \min_{\Psi_{trial}\to N} \varepsilon\left[\Psi_{trial}\right] = \min_{\Psi_{trial}\to N} \left\langle \Psi_{trial} \middle| \hat{T} + \hat{V}_{Ne} + \hat{V}_{ee} \middle| \Psi_{trial} \right\rangle \ . \tag{2.28}$$

Thus, for a given electron number N and nuclear potential $\hat{V}_{Ne}$ (depending on Z_A and R_A), the variational principle provides a procedure to determine the ground state Ψ_0 and the ground state energy, which is a functional of N and $\hat{V}_{Ne}$: $\varepsilon_0\left[N, \hat{V}_{Ne}\right]$. Symbolically we can write this in the following way:

$$\left\{N, \hat{V}_{Ne}\right\} \ \rightarrow \ \hat{H} \ \rightarrow \ \Psi_0 \ \rightarrow \ \varepsilon_0 = \varepsilon[N, \hat{V}_{ext}] \ . \tag{2.29}$$

This means that the ground state energy ε_0 is uniquely defined by N and $\hat{V}_{ext}$.

Up to here it is still necessary to perform a costly minimization over the wave function for N electrons (i. e. a function of $4N$ variables: 3 spatial coordinates plus one spin per electron). A remedy is put forward by considering the electron density $\rho(\mathbf{r})$ instead. It is defined as the integral of the wave function over the spin coordinates of all electrons and over all but one of the spatial coordinates:

$$\rho(\mathbf{r}_1) = N \int\int \cdots \int ds_1 d\mathbf{x}_2 \cdots d\mathbf{x}_N \ \left|\Psi\left(\{\mathbf{x}_i\}\right)\right|^2 \ . \tag{2.30}$$

It describes the probability to find any of the N electrons with arbitrary spin within the volume element $d\mathbf{r}_1$, while the other $N-1$ electrons have arbitrary positions and spins. So the basic idea of DFT is to express the ground state as a function of the electron density, which depends on three spatial coordinates only. This simplifies considerably the minimization process. The Hohenberg-Kohn theorems [94] then assure that this approach is equivalent to the minimization with respect to the full wave functions.

The first Hohenberg-Kohn theorem proofs that the Hamilton operator is indeed a unique functional of the electron density ρ. Then the second theorem shows that the energy functional of the lowest energy $\varepsilon_0\left[\rho\right]$ is minimal exactly for the true ground state density ρ_0.

Up to here we know that the ground state energy and wave function are uniquely defined by minimizing a functional of the electron density. We moved the problem towards finding a functional that correctly describes the total energy in terms of this density. In fact, if this functional was known we would have solved the Schrödinger equation (2.26) exactly. Thus the main task is to construct a functional that yields a reasonable approximation to the total energy.

Historically the Thomas-Fermi model [95, 96] was probably the first example of a DFT. Both, Thomas and Fermi, approximated the kinetic energy $T[\rho]$ with that of a free electron gas:

$$T_{TF}[\rho] = \frac{3}{10}(3\pi)^{2/3} \int \left[\rho\left(\mathbf{r}\right)\right]^{5/3} d^3\mathbf{r} \ . \tag{2.31}$$

The electron-electron and nuclear-electron interactions were taken into account with the classical terms

$$V_{TF,ee}[\rho] + V_{TF,Ne}[\rho] = \frac{1}{2} \iint \frac{\rho\left(\mathbf{r}_1\right)\rho\left(\mathbf{r}_2\right)}{r_{12}} d^3\mathbf{r}_1 d^3\mathbf{r}_2 - \sum_{A=1}^{M} Z_A \int \frac{\rho\left(\mathbf{r}_1\right)}{r_{1A}} d^3\mathbf{r}_{1A} \ . \tag{2.32}$$

The ground state is then found by minimizing the total energy under the constraint $\int \rho(\mathbf{r})\ d^3\mathbf{r} = N$. The accuracy of the Thomas-Fermi description is rather poor, mainly due to the manner the kinetic energy is determined. The Hartree-Fock method usually performs much better as it takes into account orbital-based wave functions via Slater determinants. This led Kohn and Sham [97] to introduce the following approach.

First they collect as much terms as possible that can be computed exactly. These are – besides the electron-nuclei interaction $V_{Ne}\left[\rho\right]$ – the classical Coulomb interaction $J\left[\rho\right]$:

$$J\left[\rho\right] = \frac{1}{2} \iint \frac{\rho\left(\mathbf{r}_1\right)\rho\left(\mathbf{r}_2\right)}{r_{12}} d^3\mathbf{r}_1 d^3\mathbf{r}_2 \ . \tag{2.33}$$

Next they introduce as reference a non-interacting system with an effective local potential $V_S(\mathbf{r})$:

$$\hat{H}_S = -\frac{1}{2}\sum_{i=1}^{N} \nabla_i^2 + \sum_{i=1}^{N} \hat{V}_S(\mathbf{r}_i) \ . \tag{2.34}$$

In analogy to the Hartree-Fock method they construct the wave functions of the reference system as Slater-determinants from Kohn-Sham orbitals φ_i, which fulfill:

$$\hat{f}^{KS}\varphi_i = \left[-\frac{1}{2}\nabla^2 + \hat{V}_S(\mathbf{r})\right]\varphi_i = \varepsilon_i\varphi_i \ . \tag{2.35}$$

The reference system is related to the full system by choosing $\hat{V}_S$ such that the density of the non-interacting reference system exactly equals the ground state density of the target system of interacting electrons:

$$\rho_S(\mathbf{r}) = \sum_{i=1}^{N}\sum_{\sigma} \left|\varphi_i(\mathbf{r},\sigma)\right|^2 = \rho_0(\mathbf{r}) \ . \tag{2.36}$$

In this way the functional $F[\rho]$ is brought into the form

$$F[\rho] = T_S[\rho] + J[\rho] + \varepsilon_{XC}[\rho] \ , \tag{2.37}$$

where

$$T_S = -\frac{1}{2} \sum_{i=1}^{N} \sum_{\sigma} \langle \varphi_i | \nabla^2 | \varphi_i \rangle \ . \tag{2.38}$$

In this form ε_{XC}, the so called exchange-correlation energy, collects all the deviation from the easily accessible information. It is defined as

$$\varepsilon_{XC}[\rho] = (T[\rho] - T_S[\rho]) + (\varepsilon_{ee}[\rho] - J[\rho]) = T_C[\rho] + \varepsilon_{ncl}[\rho] \ . \tag{2.39}$$

The residual part T_C of the true kinetic energy, which is not recovered by T_S, is just added to the non-classical electrostatic contributions. In this way the exchange correlation energy ε_{XC} is the functional, which contains everything that is unknown so far.

Collecting all contributions including the electron-nuclei interaction, the total energy of the interacting system reads:

$$\varepsilon[\rho] = T_S[\rho] + J[\rho] + \varepsilon_{XC}[\rho] + \varepsilon_{Ne}[\rho] \ . \tag{2.40}$$

Now we can come back to the somehow artificially introduced effective local potential V_S of the non-interacting system of Eq. (2.34). It can be expressed as:

$$V_S(\mathbf{r}_1) = \int \frac{\rho(\mathbf{r}_2)}{r_{12}} d^3\mathbf{r}_2 + V_{XC}(\mathbf{r}_1) - \sum_{A=1}^{M} \frac{Z_A}{r_{1A}} \ , \tag{2.41}$$

where the exchange-correlation potential $V_{XC} = \delta\varepsilon_{XC}/\delta\rho$ is the functional derivative of ε_{XC}. Up to this point the KS approach is exact. Unfortunately the explicit form of ε_{XC} and thus V_{XC} is unknown and the approximations enter, when we decide on an explicit form for them. The central goal of research in DFT is to find better and better approximations to ε_{XC} and V_{XC}.

With a choice for the basis of the KS orbitals φ_i and an expression for ε_{XC} the minimization of the total energy is a rather technical issue. In practice, powerful program packages like TURBOMOLE© perform this task. For a detailed insight into the technical subtleties of the DFT approach and its application to molecular electronic devices we recommend the PhD thesis of Fabian Pauly [93]. At the end of the day one receives an matrix expression of the Hamiltonian and the overlaps in the chosen basis, which can be treated similar to the ones obtained in the TB model of the preceding Section.

2.2 Local density of states and elastic current

In this Section we focus on the calculation of equilibrium- and transport properties of atomic contact geometries. We start with the Hamiltonian **H** and overlap matrices **S**

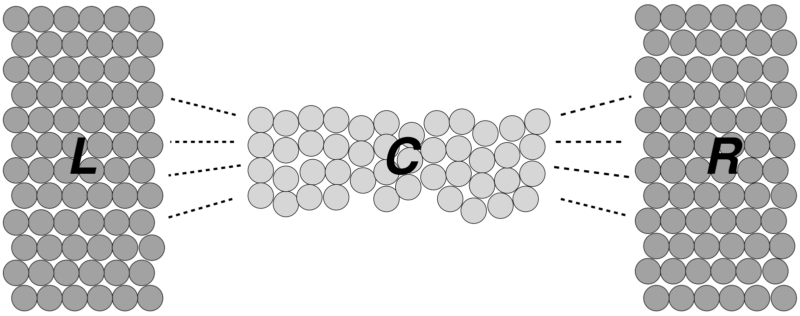

Figure 2.4: Sketch of a central region connected to left and right leads.

which are obtained from TB or DFT calculations as described in the previous Sections. From these we derive the expressions for the contact's local density of states (LDOS) and the stationary elastic current through the contact.

We express the Hamiltonian in a non-orthogonal orbital basis $|i\alpha\sigma\rangle$, where i refers to the site, α to the orbital, and σ to the spin index. The real-space wave functions $\phi_{i\alpha\sigma}(\mathbf{r}) = \langle \mathbf{r}|i\alpha\sigma\rangle$ are taken to be real. The elements $\langle i\alpha\sigma|j\beta\sigma'\rangle$ of the overlap matrix $\mathbf{S}$ are real, symmetric, and diagonal in spin space:

$$[\mathbf{S}]_{i\alpha,j\beta;\sigma} = [\mathbf{S}]_{j\beta,i\alpha;\sigma}\,. \tag{2.42}$$

In this basis, the creation and annihilation operators satisfy:

$$\{\hat{c}_{i\alpha\sigma}, \hat{c}^{\dagger}_{j\beta\sigma'}\} = \delta_{\sigma\sigma'}[\mathbf{S}^{-1}]_{i\alpha,j\beta;\sigma}\,. \tag{2.43}$$

The matrix representation of a Hamiltonian like (2.25) is then also real, symmetric and diagonal in spin space. However, here we want to keep the expressions general and allow for complex intra-atomic entries, because they are needed to describe finite orbital angular momenta or intra-atomic spin-orbit coupling (SOC) contributions. So the Hamiltonian matrix elements are chosen to obey:

$$[\mathbf{H}]_{i\alpha\sigma,j\beta\sigma'} = \begin{cases} [\mathbf{H}]^{*}_{i\beta\sigma',i\alpha\sigma} & \text{if } i = j \\ [\mathbf{H}]_{j\beta\sigma,i\alpha\sigma}\,\delta_{\sigma'\sigma} & \text{if } i \neq j. \end{cases} \tag{2.44}$$

The system we have in mind is depicted in Fig. 2.4 and consists of a finite central region attached to ideal leads. The Hamiltonian- and overlap matrices of such a system are block tridiagonal and have the following form:

$$\mathbf{H} = \begin{pmatrix} \mathbf{H}_{LL} & \mathbf{H}_{LC} & 0 \\ \mathbf{H}_{CL} & \mathbf{H}_{CC} & \mathbf{H}_{CR} \\ 0 & \mathbf{H}_{RC} & \mathbf{H}_{RR} \end{pmatrix}, \quad \mathbf{S} = \begin{pmatrix} \mathbf{S}_{LL} & \mathbf{S}_{LC} & 0 \\ \mathbf{S}_{CL} & \mathbf{S}_{CC} & \mathbf{S}_{CR} \\ 0 & \mathbf{S}_{RC} & \mathbf{S}_{RR} \end{pmatrix}. \tag{2.45}$$

There is no direct coupling between left and right leads and $\mathbf{S}^{T}_{\Omega C} = \mathbf{S}_{C\Omega}$, $\mathbf{H}^{T}_{\Omega C} = \mathbf{H}_{C\Omega}$,[6] with $\Omega \in \{L, R\}$.

---

[6] Note that the hoppings to the leads are off diagonal and we restricted the possible complex contributions to intra-atomic terms only.

2.2.1 Equilibrium properties: Bulk and local density of states

In this Section we want to consider equilibrium properties only.

By definition of the advanced/retarded equilibrium Green's function $\mathbf{G}^{\overset{r}{a}}$ [98]:

$$\left(\varepsilon^{\pm}\mathbf{S} - \mathbf{H}\right) \mathbf{G}^{\overset{r}{a}}\left(\varepsilon\right) = \mathbb{1}, \tag{2.46}$$

with $\varepsilon^{\pm} = \varepsilon \pm i0^{+}$. From the definition and the hermicity of $\mathbf{H}$ (symmetry of $\mathbf{S}$ respectively) it follows $\mathbf{G}^{r} = \left(\mathbf{G}^{a}\right)^{\dagger}$.

For a periodic system like a bulk lattice, we can similar to Eq. (2.11) write the Green's functions $\mathbf{G}(\mathbf{k}, \varepsilon) = \left[\varepsilon\mathbf{S}(\mathbf{k}) - \mathbf{H}(\mathbf{k})\right]^{-1}$ in $\mathbf{k}-$space. Then we can express the bulk density of states (DOS) projected on an orbital α and spin σ of the atom j of the unit cell with the Mulliken population analysis:

$$\rho_{j\alpha\sigma}(\varepsilon) = \mp\frac{1}{\pi}\sum_{\mathbf{k}} \operatorname{Im}\left[\mathbf{G}^{\overset{r}{a}}(\mathbf{k}, \varepsilon)\mathbf{S}(\mathbf{k})\right]_{j\alpha\sigma} \ . \tag{2.47}$$

With the following notation for elements of the inverse total Green's function:

$$\mathbf{t}_{XY}\left(\varepsilon\right) = \varepsilon\mathbf{S}_{XY} - \mathbf{H}_{XY} \ \ , \ \ X, Y \in \{L, C, R\} \ , \tag{2.48}$$

the unperturbed Green's functions read:

$$\mathbf{g}^{\overset{r}{a}}\left(\varepsilon\right) = \begin{pmatrix} \mathbf{g}^{\overset{r}{a}}_{LL}\left(\varepsilon\right) & 0 & 0 \\ 0 & \mathbf{g}^{\overset{r}{a}}_{CC}\left(\varepsilon\right) & 0 \\ 0 & 0 & \mathbf{g}^{\overset{r}{a}}_{RR}\left(\varepsilon\right) \end{pmatrix} = \begin{pmatrix} \mathbf{t}_{LL}\left(\varepsilon^{\pm}\right) & 0 & 0 \\ 0 & \mathbf{t}_{CC}\left(\varepsilon^{\pm}\right) & 0 \\ 0 & 0 & \mathbf{t}_{RR}\left(\varepsilon^{\pm}\right) \end{pmatrix}^{-1} . \tag{2.49}$$

Furthermore we introduce the couplings to the leads as perturbation:

$$\mathbf{V}\left(\varepsilon\right) = \begin{pmatrix} 0 & \mathbf{t}_{LC}\left(\varepsilon\right) & 0 \\ \mathbf{t}_{CL}\left(\varepsilon\right) & 0 & \mathbf{t}_{CR}\left(\varepsilon\right) \\ 0 & \mathbf{t}_{RC}\left(\varepsilon\right) & 0 \end{pmatrix} . \tag{2.50}$$

Then the total equilibrium Green's function fulfills the Dyson equation:

$$\mathbf{G}^{\overset{r}{a}}\left(\varepsilon\right) = \mathbf{g}^{\overset{r}{a}}\left(\varepsilon\right) + \mathbf{g}^{\overset{r}{a}}\left(\varepsilon\right)\mathbf{V}\left(\varepsilon\right)\mathbf{G}^{\overset{r}{a}}\left(\varepsilon\right) \tag{2.51}$$

The block structure of the Hamiltonian leads to the expression for the the central part of the full Green's function:

$$\mathbf{G}^{\overset{r}{a}}_{CC}\left(\varepsilon\right) = \left[\varepsilon^{\pm}\mathbf{S}_{CC} - \mathbf{H}_{CC} - \mathbf{\Sigma}^{\overset{r}{a}}_{L}\left(\varepsilon\right) - \mathbf{\Sigma}^{\overset{r}{a}}_{R}\left(\varepsilon\right)\right]^{-1} , \tag{2.52}$$

with the lead self energies $\mathbf{\Sigma}^{\overset{r}{a}}_{X}\left(\varepsilon\right) = \mathbf{t}_{CX}\left(\varepsilon\right)\mathbf{g}^{\overset{r}{a}}_{XX}\left(\varepsilon\right)\mathbf{t}_{XC}\left(\varepsilon\right)$, and again $X \in \{L, R\}$.

The Mulliken population analysis [99] yields the expression for the LDOS of the ith atom projected on orbital α and spin σ:

$$\rho_{i\alpha\sigma}\left(\varepsilon\right) = \mp\frac{1}{\pi}\operatorname{Im}\left\{\mathbf{S}\mathbf{G}^{\overset{r}{a}}\left(\varepsilon\right)\right\}_{i\alpha\sigma, i\alpha\sigma} \ . \tag{2.53}$$

In particular for an atom i in the center:

$$\begin{aligned}\rho_{i\alpha\sigma}\left(\varepsilon\right) &= \mp\tfrac{1}{\pi}\operatorname{Im}\left\{\left[\mathbf{SG}^{\overset{r}{a}}\left(\varepsilon\right)\right]_{CC}\right\}_{i\alpha\sigma,i\alpha\sigma} \\ &= \mp\tfrac{1}{\pi}\operatorname{Im}\left\{\left[\mathbf{S}_{CC}+\textstyle\sum_{\Omega=L,R}\mathbf{S}_{C\Omega}\mathbf{g}^{\overset{r}{a}}_{\Omega\Omega}\left(\varepsilon\right)\mathbf{t}_{\Omega C}\left(\varepsilon\right)\right]\left[\mathbf{G}^{\overset{r}{a}}\left(\varepsilon\right)\right]_{CC}\right\}_{i\alpha\sigma,i\alpha\sigma}\end{aligned} \quad , \tag{2.54}$$

where we applied the Dyson equation to the second part in order to determine the non-diagonal element of the total Green's function $\mathbf{G}^{\overset{r}{a}}_{\Omega C} = \mathbf{g}^{\overset{r}{a}}_{\Omega\Omega}\mathbf{t}_{\Omega C}\mathbf{G}^{\overset{r}{a}}_{CC}$. Note that the so-defined ρ fulfills the properties of a density of states:

$$\rho_{i\alpha\sigma}\left(\varepsilon\right) \geq 0 \quad \text{and} \quad \int_{-\infty}^{\infty} d\varepsilon\ \rho_{i\alpha\sigma}\left(\varepsilon\right) = 1. \tag{2.55}$$

We can then define the occupation of the atom i in the central part as:

$$N_i = \int_{-\infty}^{\infty} d\varepsilon\ f\left(\varepsilon\right)\sum_{\alpha\sigma}\rho_{i\alpha\sigma}\left(\varepsilon\right) \ , \tag{2.56}$$

where $f\left(\varepsilon, T\right) = \left\{\exp\left[\left(\varepsilon-\mu\right)/k_BT\right]+1\right\}^{-1}$ is the Fermi function at temperature T and chemical potential μ with the Boltzmann factor k_B.

Deep in the leads, N_i is constant and equals the occupation N_0 of the neutral bulk atom. In the finite central part, many atoms lie at the surface or close to it and therefore have dangling bonds or reduced coordination. By construction, the NRL TB parametrization applied to such geometries only rudimentarily takes this effect into account via the embedded-atom-like "density" (2.18). As a consequence, the occupation (2.56) of those atoms in the finite contact geometries differs from the occupation N_0 of the neutral bulk atom and creates a local charge imbalance. On the other hand, in metals local charges are efficiently screened within ≈ 1Å [79]. In the metallic atomic contacts we are interested in, we therefore assume local charge neutrality (CN) in each atom.

Following [100], we accomplish that by introducing for each atom i in the contact a local shift ϕ_i to the onsite elements:

$$\left[\mathbf{H}\right]_{i\alpha\sigma,j\beta\sigma} \rightarrow \left[\mathbf{H}\right]_{i\alpha\sigma,j\beta\sigma} + \frac{\phi_i+\phi_j}{2}\left[\mathbf{S}\right]_{i\alpha,j\beta;\sigma} \ . \tag{2.57}$$

Subsequently, we vary the ϕ_i's self-consistently until local charge neutrality is reached in all atoms of the center: $N_i \equiv N_0\ \forall i \in C$. In this way we correct for the intrinsic imperfection of the TB model applied on atomic contacts, which is not present in *ab initio* methods.

From the LDOS we have access to several other equilibrium properties, like the total energy for each atom (via the integration of LDOS up to ε_F), the local magnetic moment (as difference between the partial occupation of the two spin directions), elastic constants, etc.

2.2.2 Out of equilibrium: Elastic current

So far we considered an equilibrium situation. In order to drive a current through the central part, we need to apply a potential difference $\pm eV/2$. We assume the leads to be sufficiently big, so that they remain in equilibrium upon application of the small voltage. The potential is then completely absorbed by a shift of the chemical potential $\mu \to \mu \pm eV/2$ in the leads, where $e = -|e|$ is the electron charge. Thus the potential completely drops over the central region and creates an electric field $\mathbf{E}$ there, which drives the system out of equilibrium.

In general, we therefore need to apply the full apparatus of Keldysh's non-equilibrium Green's functions (NEGF) to determine the current at finite voltages.[7] In the limit of low bias and at low temperatures finally, the conductance should reduce to the Landauer-Büttiker form for a two terminal device. Thus, it should be proportional to the sum of transmission channels, with transmissions between zero and one. In this limit the conductance should be entirely expressible in terms of the equilibrium properties discussed above.

In the following, we will evaluate the current through the left interface of the system depicted in Fig. 2.4. We divide the system into two parts: The index L denotes the left lead as in Fig. 2.4. The central part and the right lead we condense in the index $W = C + R$. The Hamilton- and number operators then read [in the basis of (2.42)]:

$$\hat{H} = \begin{pmatrix} \hat{c}_L^\dagger \hat{c}_W^\dagger \end{pmatrix} \begin{pmatrix} \mathbf{H}_{LL} & \mathbf{H}_{LW} \\ \mathbf{H}_{WL} & \mathbf{H}_{WW} \end{pmatrix} \begin{pmatrix} \hat{c}_L \\ \hat{c}_W \end{pmatrix}, \hat{N} = \begin{pmatrix} \hat{c}_L^\dagger \hat{c}_W^\dagger \end{pmatrix} \begin{pmatrix} \mathbf{S}_{LL} & \mathbf{S}_{LW} \\ \mathbf{S}_{WL} & \mathbf{S}_{WW} \end{pmatrix} \begin{pmatrix} \hat{c}_L \\ \hat{c}_W \end{pmatrix}, \tag{2.58}$$

again with $\mathbf{H}_{LW}^T = \mathbf{H}_{WL}$ and $\mathbf{S}_{LW}^T = \mathbf{S}_{WL}$. Furthermore we may define the partial number operators of the subsystems L, W as

$$\hat{N}_L = \hat{c}_L^\dagger \mathbf{S}_{LL} \hat{c}_L \;, \hat{N}_W = \hat{c}_W^\dagger \mathbf{S}_{WW} \hat{c}_W \;. \tag{2.59}$$

For the $\hat{c}_j$'s, the equation of motion[8] (EOM) $i\hbar \dot{\hat{c}}_j = [\hat{c}_j, \hat{H}]$ leads to:

$$i\hbar \begin{pmatrix} \mathbf{S}_{LL} & \mathbf{S}_{LW} \\ \mathbf{S}_{WL} & \mathbf{S}_{WW} \end{pmatrix} \begin{pmatrix} \dot{\hat{c}}_L \\ \dot{\hat{c}}_W \end{pmatrix} = \begin{pmatrix} \mathbf{H}_{LL} & \mathbf{H}_{LW} \\ \mathbf{H}_{WL} & \mathbf{H}_{WW} \end{pmatrix} \begin{pmatrix} \hat{c}_L \\ \hat{c}_W \end{pmatrix}, \tag{2.60}$$

and a similar expression exists for the Hermitian conjugate $\hat{c}^\dagger$.

The total number of electrons is conserved, $\dot{\hat{N}} = 0$, which leads to:

$$\begin{aligned} 0 = \dot{\hat{N}} &= \underline{\dot{\hat{c}}_L^\dagger \mathbf{S}_{LL} \hat{c}_L} + \left[\dot{\hat{c}}_L^\dagger \mathbf{S}_{LW} + \dot{\hat{c}}_W^\dagger \mathbf{S}_{WW} \right] \hat{c}_W + \dot{\hat{c}}_W^\dagger \mathbf{S}_{WL} \hat{c}_L + \\ & \quad \underline{\hat{c}_L^\dagger \mathbf{S}_{LL} \dot{\hat{c}}_L} + \hat{c}_W^\dagger \left[\mathbf{S}_{WL} \dot{\hat{c}}_L + \mathbf{S}_{WW} \dot{\hat{c}}_W \right] + \hat{c}_L^\dagger \mathbf{S}_{LW} \dot{\hat{c}}_W \\ &= \dot{\hat{N}}_L - \frac{1}{i\hbar} \left\{ \hat{c}_L^\dagger \left[\mathbf{H}_{LW} - i\hbar \mathbf{S}_{LW} \frac{\partial}{\partial t} \right] \hat{c}_W - \hat{c}_W^\dagger \left[\mathbf{H}_{WL} + i\hbar \mathbf{S}_{WL} \frac{\overleftarrow{\partial}}{\partial t} \right] \hat{c}_L \right\} . \end{aligned} \tag{2.61}$$

---

[7] At finite voltage, a nonuniform voltage profile may be present in the contact region. It can in general be calculated self-consistently, but we will neglect it here. Instead we will assume that the voltage drops at the interfaces.

[8] Here, $[\cdot, \cdot]$ indicates the commutator, and a superimposed dot signifies differentiation with respect to time.

In the last line we used the EOMs to replace the expressions in brackets (whereupon the terms in WW cancel), and identified the underlined terms with $\dot{\hat{N}}_L$. From its definition we can now identify the non-equilibrium Green's function:

$$\left[\mathbf{G}^{+-}\right]_{jk}(t,t') = i\left\langle \hat{c}_k^\dagger(t')\hat{c}_j(t)\right\rangle \ , \tag{2.62}$$

where $\langle\cdot\rangle$ signifies statistical average. We arrive at the following expression for the average of the electron current from left through the interface:

$$\begin{aligned} I_L \quad (t) &= e\left\langle \dot{\hat{N}}_L(t)\right\rangle = \\ - \quad &\frac{e}{\hbar}\mathrm{Tr}_W\left\{\mathbf{G}^{+-}_{WL}(t',t)\left[\mathbf{H}_{LW} - i\hbar\mathbf{S}_{LW}\frac{\overleftarrow{\partial}}{\partial t}\right] - \left[\mathbf{H}_{WL} + i\hbar\mathbf{S}_{WL}\frac{\partial}{\partial t}\right]\mathbf{G}^{+-}_{LW}(t,t')\right\}\Bigg|_{t'\to t} \ . \end{aligned} \tag{2.63}$$

Again, $e = -|e|$ is the electron charge.

We are only interested in the stationary case. Then the Green's function depends solely on the time difference $t-t'$ and a Fourier transformation is possible:

$$\left[\mathbf{G}^{+-}\right]_{jk}(t,t') = \left[\mathbf{G}^{+-}\right]_{jk}(t-t') = \int_{-\infty}^{\infty}\frac{d\varepsilon}{2\pi}e^{-i\varepsilon(t-t')/\hbar}\ \left[\mathbf{G}^{+-}\right]_{jk}(\varepsilon) \ . \tag{2.64}$$

Finally we arrive at

$$I_L(t) = -\frac{e}{h}\int_{-\infty}^{\infty} d\varepsilon\ \mathrm{Tr}_W\left[\mathbf{G}^{+-}_{WL}(\varepsilon)\mathbf{t}_{LW}(\varepsilon) - \mathbf{t}_{WL}(\varepsilon)\mathbf{G}^{+-}_{LW}(\varepsilon)\right] \ , \tag{2.65}$$

where we performed the time derivative and identified the hopping matrices $\mathbf{t}_{XY}$ from Eq. (2.48). Note that a similar expression holds for the current from the right $I_W(t) = e\left\langle \dot{\hat{N}}_W(t)\right\rangle$ with L and W interchanged in Eq. (2.65), and in the stationary case $I_L(t) = -I_W(t)$, as it should be.

In this form, the current expression would be suitable to study systems that are conveniently separable into two parts, like in the case of tunneling current between a STM tip and a surface. However, in systems like the one depicted in Fig. 2.4, the focus lies on the central part that is then connected to the leads. Due to the absence of direct coupling between left and right leads [$\mathbf{H}_{LR} \equiv 0$ etc. in Eq. (2.45)], the generalization to systems with a central part is straightforward. For the current from the left evaluated at the left interface, the indices W in (2.65) are to be replaced by C.[9]

In expression (2.65) for the current, we shifted the problem to the calculation of the non-equilibrium Green's functions $\mathbf{G}^{+-}(\varepsilon)$. As we indicated at the beginning of this Section, in the zero bias limit, the conductance should be fully expressible in terms of equilibrium

---

[9] For the current from the right evaluated at the right interface, I_R, one only needs to replace the indices (L,W) by (R,C) in Eq. (2.65). However, the demonstration for current conservation, i.e. $I_L(t) = -I_R(t)$, is i.g. not straightforward.

properties. Therefore, we aim to write the current in a form, that in equilibrium reduces to an expression containing the equilibrium $\mathbf{G}^{r/a}$ of the preceding Section only.

First the "Langreth rules" [101] for $\mathbf{G}^{+-}_{LC}(\varepsilon)$ yield:

$$\begin{aligned} \mathbf{G}^{+-}_{LC}(\varepsilon) &= \mathbf{g}^{+-}_{LL}(\varepsilon)\,\mathbf{t}_{LC}(\varepsilon)\,\mathbf{G}^{a}_{CC}(\varepsilon) + \mathbf{g}^{r}_{LL}(\varepsilon)\,\mathbf{t}_{LC}(\varepsilon)\,\mathbf{G}^{+-}_{CC}(\varepsilon) \\ \mathbf{G}^{+-}_{CL}(\varepsilon) &= \mathbf{G}^{+-}_{CC}(\varepsilon)\,\mathbf{t}_{CL}(\varepsilon)\,\mathbf{g}^{a}_{LL}(\varepsilon) + \mathbf{G}^{r}_{CC}(\varepsilon)\,\mathbf{t}_{CL}(\varepsilon)\,\mathbf{g}^{+-}_{LL}(\varepsilon)\ . \end{aligned}$$

We define the selfenergies

$$\mathbf{\Sigma}^{x}_{\Omega}(\varepsilon) = \mathbf{t}_{C\Omega}(\varepsilon)\,\mathbf{g}^{x}_{\Omega\Omega}(\varepsilon)\,\mathbf{t}_{\Omega C}(\varepsilon) \quad , \ x \in \{+-, -+, r, a\} \quad , \ \Omega \in \{L, R\}\ . \tag{2.66}$$

Then, with the relations

$$\mathbf{\Sigma}^{+-} - \mathbf{\Sigma}^{-+} = \mathbf{\Sigma}^{a} - \mathbf{\Sigma}^{r}\ ,\ \mathbf{G}^{+-} - \mathbf{G}^{-+} = \mathbf{G}^{a} - \mathbf{G}^{r} \tag{2.67}$$

for the selfenergies and Green's functions, we can rewrite the current from Eq. 2.65:

$$I_L(t) = \frac{e}{h}\int_{-\infty}^{\infty} d\varepsilon\ \mathrm{Tr}_C\left[\mathbf{G}^{+-}_{CC}(\varepsilon)\mathbf{\Sigma}^{-+}_{L}(\varepsilon) - \mathbf{\Sigma}^{+-}_{L}(\varepsilon)\mathbf{G}^{-+}_{CC}(\varepsilon)\right]\ . \tag{2.68}$$

For the central part Green's functions the following relation holds:

$$\mathbf{G}^{\pm\mp}_{CC}(\varepsilon) = \mathbf{G}^{r}_{CC}(\varepsilon)\left(\mathbf{\Sigma}^{\pm\mp}_{L}(\varepsilon) + \mathbf{\Sigma}^{\pm\mp}_{R}(\varepsilon)\right)\mathbf{G}^{a}_{CC}(\varepsilon)\ . \tag{2.69}$$

With the definition of the positive definite transition rate matrices $\mathbf{\Gamma}$:

$$\mathbf{\Gamma}_{\Omega} = i\left(\mathbf{\Sigma}^{r}_{\Omega} - \mathbf{\Sigma}^{a}_{\Omega}\right) \quad , \ \Omega \in \{L, R\}\ . \tag{2.70}$$

the selfenergies can be written:

$$\mathbf{\Sigma}^{+-}_{\Omega}(\varepsilon) = i\mathbf{\Gamma}_{\Omega}(\varepsilon) f_{\Omega}(\varepsilon, T) \tag{2.71}$$

$$\mathbf{\Sigma}^{-+}_{\Omega}(\varepsilon) = i\mathbf{\Gamma}_{\Omega}(\varepsilon)\left[f_{\Omega}(\varepsilon, T) - 1\right]\ , \tag{2.72}$$

where in the left and right Fermi functions f_{Ω} the potential shift $\pm eV/2$ was incorporated in the chemical potential.

Plugged in the current expression, we arrive at:

$$I_L = \frac{e}{h}\int_{-\infty}^{\infty} d\varepsilon\ \mathrm{Tr}_C\left\{\mathbf{G}^{r}_{CC}(\varepsilon)\mathbf{\Gamma}_{L}(\varepsilon)\mathbf{G}^{a}_{CC}(\varepsilon)\mathbf{\Gamma}_{R}(\varepsilon)\right\}\left[f_L(\varepsilon, T) - f_R(\varepsilon, T)\right]. \tag{2.73}$$

Making use of the positive definiteness of the scattering matrix we can symmetrize the expression under the trace and introduce the transmission matrix

$$\mathbb{t}(\varepsilon, V) = \mathbf{\Gamma}^{1/2}_{R}(\varepsilon)\mathbf{G}^{r}_{CC}(\varepsilon, V)\mathbf{\Gamma}^{1/2}_{L}(\varepsilon)\ . \tag{2.74}$$

Finally we arrive at the expression for the elastic current:

$$I(T, V) = \frac{e}{h}\int d\varepsilon\ \tau(\varepsilon, V)\left[f_L(\varepsilon, T) - f_R(\varepsilon, T)\right], \tag{2.75}$$

where $\tau(\varepsilon, V) = \mathrm{Tr}_C \ \left[\mathbb{t}^\dagger(\varepsilon, V)\mathbb{t}(\varepsilon, V)\right]$ is the transmission function.

At zero temperature, Eq. (2.75) reduces to an integration of $\tau(\varepsilon, V)$ over a finite energy interval of $\pm eV/2$ around the Fermi energy. Then the linear conductance is given by the Landauer formula:

$$G = \frac{e^2}{h}\tau(\varepsilon_F, 0) = \frac{e^2}{h}\mathrm{Tr}_C \ \left[\mathbb{t}^\dagger(\varepsilon_F, 0)\mathbb{t}(\varepsilon_F, 0)\right] = \frac{e^2}{h}\sum_i \tau_i(\varepsilon_F) \ . \tag{2.76}$$

Here the $\tau_i(\varepsilon_F)$ are the eigenvalues of $\mathbb{t}^\dagger\mathbb{t}$, the eigenchannel transmission probabilities. In the case of spin degeneracy, the trace over spin yields a factor two and it is convenient to define $G_0 = 2e^2/h = 1/(12.9\ \mathrm{k}\Omega)$ as the quantum of conductance.

Let us summarize at this stage: From the Hamiltonian of the system (2.45) we can derive the central part's Green's function and subsequently the LDOS of the atomic contact and the current through it. In the following we will use this formalism to determine the conduction properties of metallic atomic contacts.

Chapter 3

Conduction properties of non-magnetic metallic atomic contacts

In this Chapter we concentrate on the transport properties of non-magnetic metallic atomic contacts. We first discuss in some detail how we calculate the transmission following the concepts of Chapter 2. This is accomplished in Section 3.1 using a minimal model system consisting of linear chains of atoms. Then we apply the full description to atomic contacts of metals with partially filled shells, namely atomic contacts made of noble, p-valent, and transition metals. We end the Section 3.2 with comparing the results of the tight-binding model calculations with reliable *ab initio* results.

The following Sections 3.3 and 3.4 then focus on the limiting case of the bivalent metals Zn and Mg, where the outermost shell of s-orbitals is full. We can directly compare our theoretical results presented there with jointly done experiments and find good agreement. We finish this part with a conclusion.

3.1 Linear chain model

In the preceding Chapter we showed how we determine the electronic structure of atomic contacts and calculate the current through it. Before applying the full machinery to atomic contacts of different metals, we want to start in this Section with a minimal model. We consider a contact formed by two linear, semi-infinite, z-directional chains of identical atoms, joined in a central region consisting of the two tip atoms (see scheme in Fig. 3.1). We will take into account coupling between nearest neighbour (NN) atoms only and the hopping integrals are assumed to be equal between all lead atoms but may differ between the two central atoms. This linear chain model is similar to what was studied in the 1960s by P. W. Anderson and D. M. Newns [102, 103].

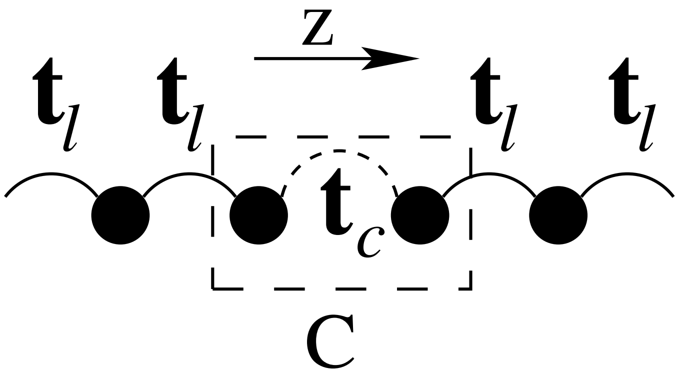

Figure 3.1: Sketch of two semi-infinite linear monatomic chains in $\vec{e}_z$-direction with nearest neighbour coupling and joined in the tip atoms.

The Hamiltonian **H** corresponding to the linear chain shown in Fig. 3.1 has the form:

$$\mathbf{H} = \begin{pmatrix} \ddots & \ddots & 0 & 0 & 0 & 0 \\ \ddots & \mathbf{H}_0 & \mathbf{t}_l & 0 & 0 & 0 \\ 0 & \mathbf{t}_l^\dagger & \mathbf{H}_0 & \mathbf{t}_c & 0 & 0 \\ 0 & 0 & \mathbf{t}_c^\dagger & \mathbf{H}_0 & \mathbf{t}_l & 0 \\ 0 & 0 & 0 & \mathbf{t}_l^\dagger & \mathbf{H}_0 & \ddots \\ 0 & 0 & 0 & 0 & \ddots & \ddots \end{pmatrix}. \tag{3.1}$$

The diagonal blocks $\mathbf{H}_0$ (with dimension number of orbitals times spin) are the onsite elements of the orbitals of the atoms under consideration and $\mathbf{t}_l, \mathbf{t}_c$ contain the hopping integrals from Table A.1. We assume an orthogonal basis and thus the overlap matrix is unity: $\mathbf{S} = \mathbb{1}$.

With the expression of Eq. (2.52) we can directly evaluate the central part's Green's function:[1]

$$\mathbf{G}_{CC}(\varepsilon) = \left[\varepsilon^+ \mathbb{1} - \mathbf{H}_{CC} - \begin{pmatrix} \mathbf{\Sigma}_L(\varepsilon) & 0 \\ 0 & \mathbf{\Sigma}_R(\varepsilon) \end{pmatrix}\right]^{-1}. \tag{3.2}$$

Here $\mathbf{\Sigma}_{L,R}(\varepsilon)$ are the self-energy matrices arising from the coupling of the left/right C atom to the semi-infinite, homogeneous chains. They are of the form

$$\mathbf{\Sigma}_L(\varepsilon) = \mathbf{t}_l^\dagger \mathbf{g}_{LL}(\varepsilon)\mathbf{t}_l \; ; \; \mathbf{\Sigma}_R(\varepsilon) = \mathbf{t}_l \mathbf{g}_{RR}(\varepsilon)\mathbf{t}_l^\dagger \;, \tag{3.3}$$

where the Green's functions of the left and right "surfaces" satisfy:

$$\mathbf{g}_{LL}(\varepsilon) = [\varepsilon - \mathbf{H}_0 - \mathbf{t}_l \mathbf{g}_{LL}(\varepsilon)\mathbf{t}_l^\dagger]^{-1} \; ; \; \mathbf{g}_{RR}(\varepsilon) = [\varepsilon - \mathbf{H}_0 - \mathbf{t}_l^\dagger \mathbf{g}_{RR}(\varepsilon)\mathbf{t}_l]^{-1}. \tag{3.4}$$

---

[1] Here and in the rest of the Chapter we will consider retarded Green's functions only.

From $\mathbf{G}_{CC}$ we obtain directly the LDOS projected onto orbital $\alpha\sigma$ of the atom i in the center:

$$\rho_{i\alpha\sigma}(\varepsilon) = -\frac{1}{\pi}\,\mathrm{Im}\,[\mathbf{G}_{CC}]_{i\alpha\sigma,i\alpha\sigma}\,. \tag{3.5}$$

The Hamiltonian of the system under consideration is real and symmetric and therefore the Green's functions are symmetric. Then the scattering matrices have the form

$$\mathbf{\Gamma}_{L/R} = 2\,\mathrm{Im}\left[\mathbf{\Sigma}_{L/R}\right]\ . \tag{3.6}$$

The zero-bias conductance then follows directly with Eq. 2.76. In the following we will consider two exemplary cases: Noble or alkali metals and *s*-*p*-metals.

We first aim to model alkali- or noble metals, with valent *s*-orbitals. In this case the orbital basis consists of one (spin-degenerate) *s*-orbital with onsite energy ε_s and hopping integral $t_{l,c} = ss\sigma_{l,c}$ between lead (l) and the center atoms (c) according to Table A.1. The matrices reduce thus to scalars and the resulting "surface" Green's function can easily be calculated analytically. Then the self-energies are of the form $\Sigma_{L,R}(\varepsilon) = t_l e^{i\Phi}$, with $\cos\Phi = (\varepsilon - \varepsilon_s)/2t_l$.

In this case the LDOS of one tip atom has the simple analytical form:

$$\rho(\varepsilon) = -\frac{1}{\pi}\,\mathrm{Im}\left\{\frac{\varepsilon - \varepsilon_s - \Sigma_L(\varepsilon) - \Sigma_R(\varepsilon)}{t_c^2 - \left[\varepsilon - \varepsilon_s - \Sigma_L(\varepsilon) - \Sigma_R(\varepsilon)\right]^2}\right\}\ . \tag{3.7}$$

Analogously the transmission $\tau(\varepsilon)$ reads:

$$\tau(\varepsilon) = \frac{t_c^2\Gamma_L(\varepsilon)\Gamma_R(\varepsilon)}{\left|t_c^2 - \left[\varepsilon - \varepsilon_s - \Sigma_L(\varepsilon) - \Sigma_R(\varepsilon)\right]^2\right|^2}. \tag{3.8}$$

In figure Fig. 3.2(a) we plot the transmission and LDOS as function of the energy ε of such a system with a single orbital per atom.[2] In order to get a reasonable figure, we take the hopping integral $ss\sigma_l$ as the first NN term of the orthogonal two-center parametrization of Na from Ref. [84].

The center hopping t_c term was reduced to model a constriction with a NN distance d increased by 10%. Following [84], the corresponding hopping scales like $(d_0/d)^{l+l'+1}$ with d_0 being the equilibrium NN distance and l, l' the orbital quantum number of the orbitals involved (see discussion in Section 2.1.3).

As a consequence of the reduced hopping in the center, the transmission over energy is not quantized but given by Eq. (3.8). Depending on the value of the central hopping, the LDOS of Eq. (3.7) somehow interpolates between the two extreme cases of a perfect infinite chain with van Hove singularities $\propto 1/\sqrt{\varepsilon}$ at the band edges and the semi-infinite chain with a elliptical LDOS in the tip atoms, as stated above. The value of the hopping integral $ss\sigma \approx -0.64$eV gives rise to a bandwidth of the linear chain of 2.56eV, as shown in Fig. 3.2(a).

---

[2] We assume that one s orbital is a reasonable approximation to describe the properties of alkali metals.

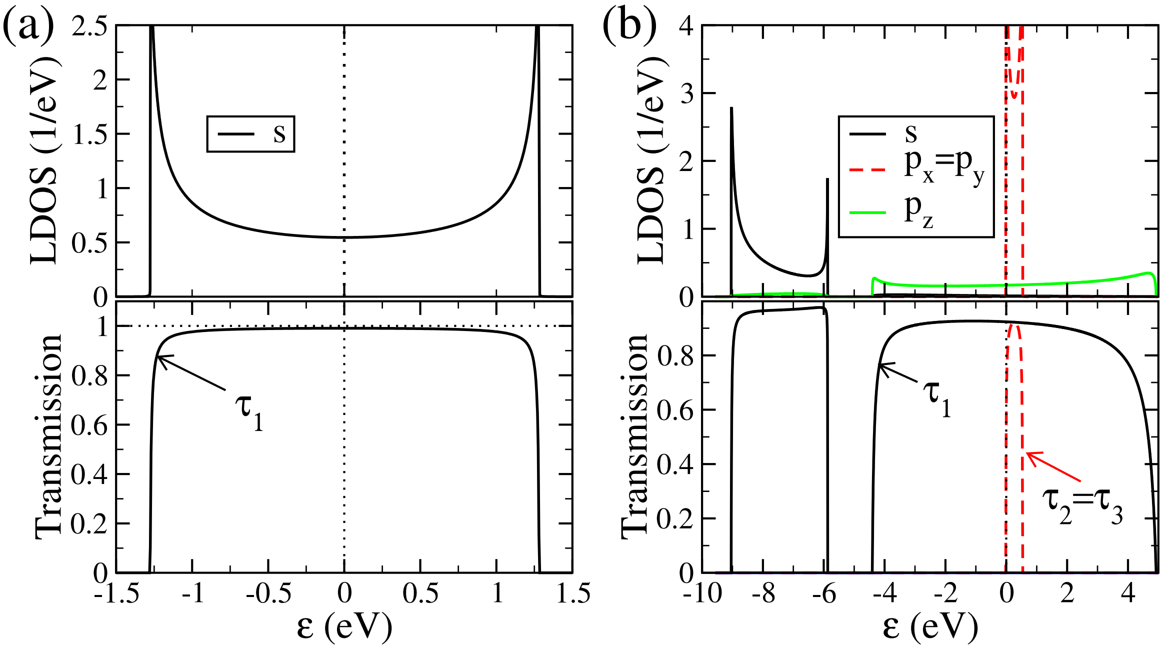

Figure 3.2: LDOS and transmission for monatomic chains of Fig. 3.1 with (a) one s orbital per site modelling alkali metals like Na and (b) four orbitals per site (one s- and three p-orbital) modelling s-p metals like Al.

The prototype of the case of more than one orbital per atom is Al with one s and three p orbitals present around the Fermi energy. For the linear chain along $\vec{e}_z$, the orbitals oriented perpendicular to the chain axis, p_x and p_y, only couple to their own species. The corresponding hopping integral is $pp\pi_l$ (see Fig. 2.1, and Tables 2.1 or A.1). On the other hand, the remaining two s and p_z orbitals have couplings amongst themselves (hopping integrals $ss\sigma_l$ and $pp\sigma_l$) as well as amongst each other ($sp\sigma$). In the (s, p_x, p_y, p_z)-basis, the resulting Hamiltonian has the form[3]:

$$\mathbf{H}_0 = \begin{pmatrix} \varepsilon_s & 0 & 0 & 0 \\ 0 & \varepsilon_p & 0 & 0 \\ 0 & 0 & \varepsilon_p & 0 \\ 0 & 0 & 0 & \varepsilon_p \end{pmatrix}, \quad \mathbf{t}_l = \begin{pmatrix} ss\sigma_l & 0 & 0 & -sp\sigma_l \\ 0 & pp\pi_l & 0 & 0 \\ 0 & 0 & pp\pi_l & 0 \\ sp\sigma_l & 0 & 0 & pp\sigma_l \end{pmatrix}. \tag{3.9}$$

Note that now the hoppings in the leads contain non-diagonal elements and thus there is no simple analytical solution for the Green's functions of the uncoupled leads anymore. However, with a recursion method introduced by Guinea and coworkers [104], it is possible to evaluate the "surface" Green's function numerically. This technical issue is discussed in detail in Appendix D of F. Pauly's PhD thesis [93].

Again we take as a qualitative orientation the hopping integrals for Al from the orthogonal two-center parametrization [84] and reduce the central hopping according to the

---

[3] Note the sign convention of positive lobe in positive z-direction.

scaling law. The result is shown in Fig. 3.2(b). First, as the p_x- and p_y-orbitals are orthogonal to the rest, they separate and show a LDOS and transmission properties like chains of single orbitals [Eqs. (3.7) and (3.8)]. According to [84] their hopping integrals are small ($pp\pi \approx -0.14$eV) and as a consequence their LDOS very narrow and peaked. As we need to distribute 3 electrons, the Fermi energy lies at the lower edge of the peak of the p_x and p_y orbitals. On the other hand the s and p_z with large hopping integrals ($ss\sigma \approx -0.8$eV and $pp\sigma \approx 2.3$eV) are extended and the orbitals hybridize due to the strong inter-orbital hopping element $sp\sigma \approx -1.3$eV. The onsite elements $\varepsilon_s, \varepsilon_p$ of s and p orbitals are separated by $\varepsilon_p - \varepsilon_s \approx 7.72$eV.

Over the whole energy range, the transmission is mainly carried by one channel arising from a symmetric combination of s-p_z orbitals. Only around the Fermi energy, where the p_x, p_y orbitals are present, a degenerate 2nd and 3rd channel from the p_x, p_y orbitals contribute. Again the transmission properties basically follow the LDOS. Note that a possible second channel (fourth channel around ε_F) is completely closed. This can be traced back to the fact, that to a good approximation the hopping integrals $ss\sigma$, $pp\sigma$, and $sp\sigma$ fulfill:

$$ss\sigma \cdot pp\sigma \approx -sp\sigma^2 \ . \tag{3.10}$$

Under this condition, in the two-dimensional subspace of the s and p_z orbital, the determinant of the transition rate matrix vanishes [105]. Then at least one eigenvalue of $\mathbb{t}^\dagger\mathbb{t}$ (i.e. one transmission channel) must be zero. In the simple case of an Al-like single atom chain, Eq. (3.10) holds to a good approximation and in consequence the fourth channel is absent in the transmission of Fig. 3.2(b). But more generally most metals fulfill Eq. (3.10) and in most single atom contacts of metals, a possible fourth channel is absent in regions where s and p orbitals dominate.

In conclusion, the linear chain model yields a basic understanding of the relevant ingredients needed to calculate transport properties of metallic atomic contacts. It may serve to elucidate the findings from more sophisticated calculations.

However it is by construction much too simple to capture the essential differences between materials and geometries and suffers from pathologies intrinsic to one-dimensional systems like the van Hove singularities at the band edges. In the following Chapter we will therefore consider more advanced models to describe the atomic contacts.

3.2 Atomic contacts of noble, p-valent, and transition metals

The aim of this Section is to summarize general features of atomic contacts for archetypical non-magnetic metals: noble-, s-p-, and transition metals. We consider as examples two metals in each case, namely Ag and Au as representative for the noble metals, Al and Pb for the s-p metals, and Nb and Pt for the transition metals.

Here we consider more realistic description of the materials' electronic structure and the crystal structure. First we discuss the bulk DOS then we concentrate on transport

Element	Bulk lattice, Lattice constant	Reference parametrization http://cst-www.nrl.navy.mil/bind/	Parameter files
Ag	fcc, 4.09 Å	[89], ag.html	ag_par
Al	fcc, 4.05 Å	[106], al.html	al_par
Au	fcc, 4.08 Å	[89], au.html	au_par au_par_99
Co	hcp, 2.51 Å	[107], co.html	co_ferro_par
Fe	bcc, 2.86 Å	[107, 108], fe.html	fe_ferro_par
Mg	hcp, 3.21 Å	[109], mg.html	mg_par
Nb	bcc, 3.25 Å	[89, 92], nb.html	nb_par nb_par_125
Ni	fcc, 3.52 Å	[107, 110], ni.html	ni_ferro_par
Pb	fcc, 4.95 Å	[111], pb.html	pb_par
Pt	fcc, 3.92 Å	[89], pt.html	pt_par
Zn	hcp, 2.66 Å	[84], p. 123: orthogonal parameters.	

Table 3.1: Parametrization of the tight-binding Hamiltonian used in this work.

through atomic contacts of the corresponding material. In particular we will show how to get the formalism of Chapter 2 to work.

3.2.1 Bulk density of states

In the previous Section we discussed how some simple estimates of the hopping integrals involved in the Hamiltonian of a minimal model allow for gaining insight in the mechanisms that for instance control the transport properties of an atomic contact.

We will apply the non-orthogonal NRL parametrization[4] introduced in Section 2.1.4 to various materials in the following. Table 3.1 resumes the different parameters used in this work.

The NRL parametrization is described to fit bulk band structure. In particular, it is designed to correctly reproduce the bulk DOS. Here we apply the NRL parametrization to describe the bulk DOS for six exemplary metals. Five out of those metals possess a fcc equilibrium lattice structure but Nb crystallizes in bcc. For these different materials and crystal structures we calculate the bulk DOS.

In Fig. 3.3 are shown the bulk DOS projected on the orbitals that are relevant around the Fermi energy,[5] which is indicated with a vertical dotted line.

First consider the noble metals Ag and Au. In this case the Fermi energy lies some

---

[4] Only in the case of Zn (discussed in Section 3.3) we will - in lack of NRL parameters - resort to the orthogonal two-center parametrization of [84].

[5] Note that when we project onto “orbital α” in fact what we do - as discussed in the previous Chapter - is to project on the fit basis that has the same symmetry as orbital α.

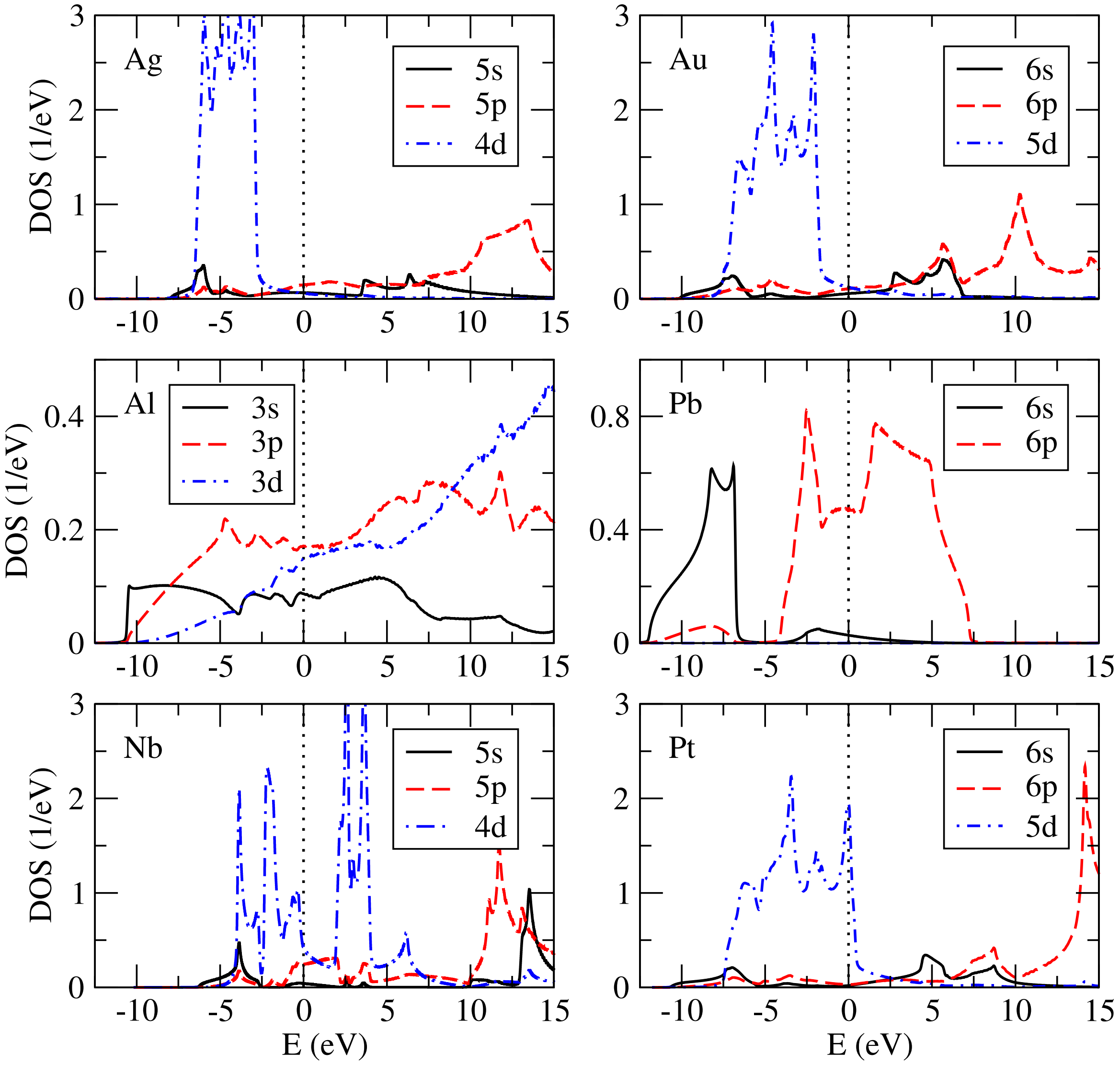

Figure 3.3: Bulk DOS as a function of energy for the noble metals Ag and Au, the p-valent metals Al and Pb, and the transition metals Nb and Pt, computed with the NRL TB parametrization. The DOS is projected on the s, p, and d bands that are relevant around the Fermi energy, which is set to zero and indicated with a dotted line.

2.5eV / 1.5eV above the d-bands, which are nearly filled. At ε_F the s- ($5s/6s$) and p-bands ($5p/6p$) dominate. It results a close to free-electron behaviour with high Fermi velocities.

Next s-p-metals: In the case of Al the coupling to second next NNs and the higher coordination in bulk as compared with the linear chain close the gap between s and $p$bands. At the Fermi energy s and p-bands dominate. For Pb, the s-band is located some 8eV below ε_F and is nearly full. With a total occupation of 4 electrons, the Fermi energy lies in the p-band and fills it partially.

Transition metals Nb and Pt show strong hybridization between the d bands and the s, p bands. The d bands are present around the Fermi energy, which for Pt (with electronic configuration [Xe]$5d^8 6s^2$) lies in the vicinity of the upper edge of the d band. For Nb, with five valence electrons less, the Fermi energy lies much deeper in the d bands.

The information obtained from the bulk DOS, which is most interesting here, consists of the value of the Fermi energy and the orbitals that are relevant around it. This information then also determines the transport properties atomic contacts discussed in the next Section.

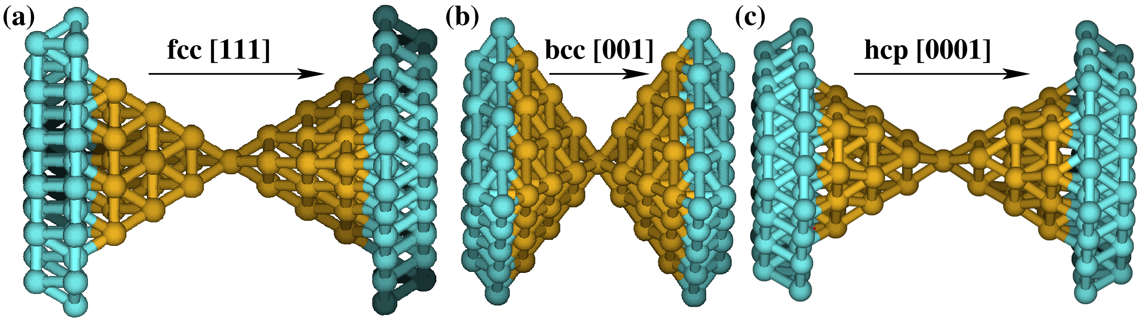

Figure 3.4: Set of ideal single atom contact geometries most commonly used in this work. (a) Contact of a fcc lattice grown in [111]-direction. (b) Contact of a bcc lattice grown in [001]-direction. (c) Contact of a hcp lattice grown in [0001]-direction.

3.2.2 Transmission properties of ideal single-atom contacts

We want to determine conduction properties of metallic atomic contacts. First we construct ideal contact geometries. The materials we are interested in crystallize in different lattices. We take the equilibrium lattice at room temperature and construct ideal atomic geometries out of it. We start with the central atom of the later contact and collect the NN atoms in the next layer along desired direction. For fcc in [111] direction and hcp in [0001] direction there are three NN atoms in the first layer next to the central atom (and four NN atoms for bcc in [001] direction). Next we continue to add NN atoms of the neighbouring layers along the transport direction, until the desired contact size is reached. Finally we connect the contact geometry to the ideal surfaces.

Examples of such contact geometries are depicted in Fig. 3.4. Atoms belonging to the contact region are marked in yellow and those of the coupled surface in blue. Transport direction is $\vec{e}_z$, which corresponds to a threefold rotation axis for the fcc contact geometry (in [111] direction) and a fourfold for the bcc contact geometry in [001] direction. Those two geometries additionally have an inversion center, in contrast to the hcp contact geometry in [0001] direction, which only possesses a mirror in the xz-plane.

Note that for the contact geometries in fcc [111]-direction and hcp [0001]-direction the apex angles are the same for the first layer next to the central atom. This is because both geometries are in close-packed structures and in the two cases the contacts are grown in directions of close-packed planes. In contrast, the bcc contact geometry in [001]-direction shows a much larger apex angle. As a consequence, in the bcc contact the planes next to the central atom are much closer to each other. Then the coupling between those planes left and right of the central atom is enhanced.

Once the contact geometries are constructed, we obtain the electronic Hamiltonian and overlap matrix for the system from the NRL parametrization described in Section 2.1.4.[6] The Hamiltonian consists of onsite and hopping elements for the atoms of the central part of the geometry (marked in yellow in Fig. 3.4) and of hopping elements between atoms of the centre and those of the leads. Hamiltonian and overlap matrices then have the block tridiagonal form of Eq. (2.45).

The finite contact geometry is coupled to the atoms of ideal lead surfaces painted blue in Fig. 3.4. We calculate the Hamiltonian of the uncoupled lead's surface by applying a decimation technique [104] subsequent to lateral Fourier transformation. The surface Green's function then follow by inversion of the Hamiltonian. The technical aspects related to the determination of the surface Green's functions are discussed to some in detail in Appendix D of [93]. From the lead Green's function, together with the hoppings to the leads, we obtain the lead selfenergies.

At this stage we know the full center Green's function $\mathbf{G}^r_{CC}(\varepsilon)$. Next we correct for charge neutrality in the central part: From Eq. (2.55) we obtain $\rho_{i\alpha\sigma}$ and by integrating up to ε_F the occupation N_i of each central atom i. Then we add an onsite shift ϕ_i on each atom according to Eq. (2.57) and recalculate N_i until convergence to N_0 is reached in each central atom.

With the corrected Hamiltonian and the selfenergies, we can calculate the LDOS in the central atom and the transmission of the contact following Eq. (2.76). As examples we calculated the transmission of the ideal contact geometries of Fig. 3.4 for the six exemplary non-magnetic materials.

Let us first consider in Fig. 3.5 the case of the noble metal Ag. Its equilibrium crystal lattice is fcc and we consider the ideal contact geometry of Fig. 3.4(a). The LDOS as function of the energy, projected on the orbitals of the central atom of this geometry is shown in the uppermost panel. We can identify the region where the d orbitals dominate, some 5eV below ε_F (which is set to zero and indicated with a dotted vertical line). The s orbitals are relevant around the Fermi energy and the p orbitals gain weight above ε_F. The LDOS of the orbitals is narrower than the bulk bands due to the reduced coupling of the central atom in the contact geometry as compared to bulk. The p_x, p_y (the d_{xy}, $d_{x^2-y^2}$ and the d_{yz}, d_{zx}) orbitals are degenerate as it is expected from the orbital structure in Fig. 2.1 and the contact geometry. It is interesting to examine how this translates to transmission.

Below the LDOS in Fig. 3.5 we show the spin-degenerate transmission channels $\tau_i(\varepsilon)$ for Ag and the same contact geometry. According to Eq. (2.76), the zero-bias conductance corresponds to $G_0 = 2e^2/h$ times the transmission at the Fermi energy (again set to zero and indicated with a dotted vertical line). We can identify three distinct energy regions: A first region, some 4eV below ε_F, where up to five partially open transmission channels

---

[6] We fix the NN distance in the ideal contact geometry to its bulk value.

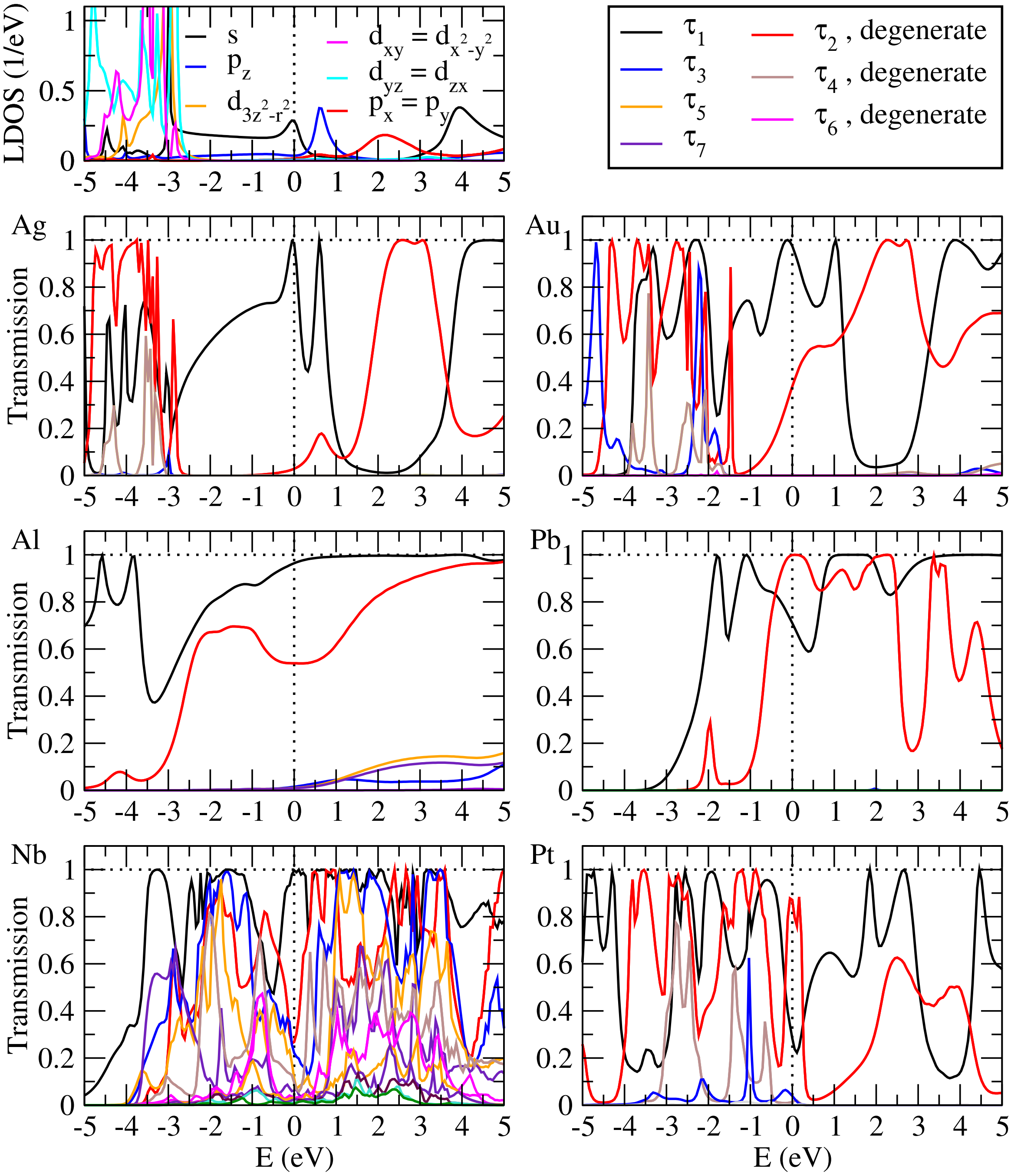

Figure 3.5: Top panel: LDOS projected on the orbitals of the central atom for the single atom contact of Ag. Lower panels: Transmission channels as a function of energy for single atom contacts of Ag, Au, Al, Pb, Nb, and Pt computed with the NRL TB parametrization. All geometries are ideal pyramids grown in fcc [111]-direction, with exception of Nb, which is grown bcc [001]-direction. The Fermi energy is set to zero and indicated with a dotted line.

contribute. In the second interval around and below one channel dominates and finally above ε_F a degenerate second and third channel gains weight. These regions are correlated with the LDOS, where the d, s, and $s-p$ orbitals dominate.[7]

A similar analysis holds for the other exemplary metals. Depending on the position of the Fermi energy with respect to the orbitals, the zero bias conductance of the single atom contacts typically consists of one, three or up to five channels. It is thus mainly determined by the valence of the material under consideration [21]. As a consequence, the zero bias conductance of Au single atom contacts is also dominated by one channel (and a degenerate second/third channels arises due to the geometry). Furthermore, Al and Pb show three channels: one single channel arising from a symmetric combination of the s, p_z orbitals and a degenerate channel arising from the p_x, p_y orbitals. In Pt as a transition metal, the zero bias conductance consist of up to five partially open channels. Note the particularity of the other transition metal Nb: It is the only metal out of the six considered here that crystallizes in the bcc crystal structure. As described before, the corresponding ideal single atom contact has a large apex angle and therefore the coupling between second next layers around the central atom gives rise to additional channels. Again, many partially open channels and strong variation of the transmission with energy around ε_F mark the contribution of the d orbitals to the zero bias conductance in Nb.

So far we considered only ideal single atom contacts with one central atom. Molecular dynamics (MD) simulations of the breaking of an atomic contact [23, 77, 112] show a dimer configuration in the last steps before breaking. In order to simulate this behaviour, we replace the central atom in the contact geometries of Fig. 3.4 with a dimer, where we fix the distance between the dimer atoms to bulk NN distance. As a consequence, the two pyramids forming the contact geometry are separated and the coupling between second next layers around the central atoms is reduced.

In Fig. 3.6 are shown the resulting transmissions for the same materials as in Fig. 3.5. Note that the channels that arise from the s orbitals (symmetric combination of s, p_z orbitals, respectively) are hardly changed as compared to Fig. 3.5. On the other hand channels arising from the p_x, p_y, and d orbitals are strongly altered. This can be understood with the anisotropy of the p and d orbitals and in consequence a strong dependence of the orbital decomposition of the transport eigenchannels on the contact geometry. On the other hand, the s orbital is isotropic (and in combination with the p_z orbital oriented along the transport direction). Therefore the corresponding transport eigenchannels are much more robust against small changes in the geometry. As a consequence, in conductance histograms, where the conductance is recorded during the last stages of breaking of an atomic contact, alkali and noble metals (as Na, Ag, Au) show a strong peak at $1G_0$ carried by one channel [22, 112]. The $s-p$ and p metals (Al, Pb) give rise to a more broadened peak at $1G_0$ (Al) and $1.7G_0$ (Pb), typically carried by three channels, and transition metals (Nb, Pt) show ample peaks well above $1G_0$ (around $2.3G_0$ for Nb and around $1.7G_0$ for Pt) consisting of up to five channels [22, 77].

---

[7] Note that in the region of s-p orbitals, a possible fourth channel is absent as discussed in the previous Section 3.1.

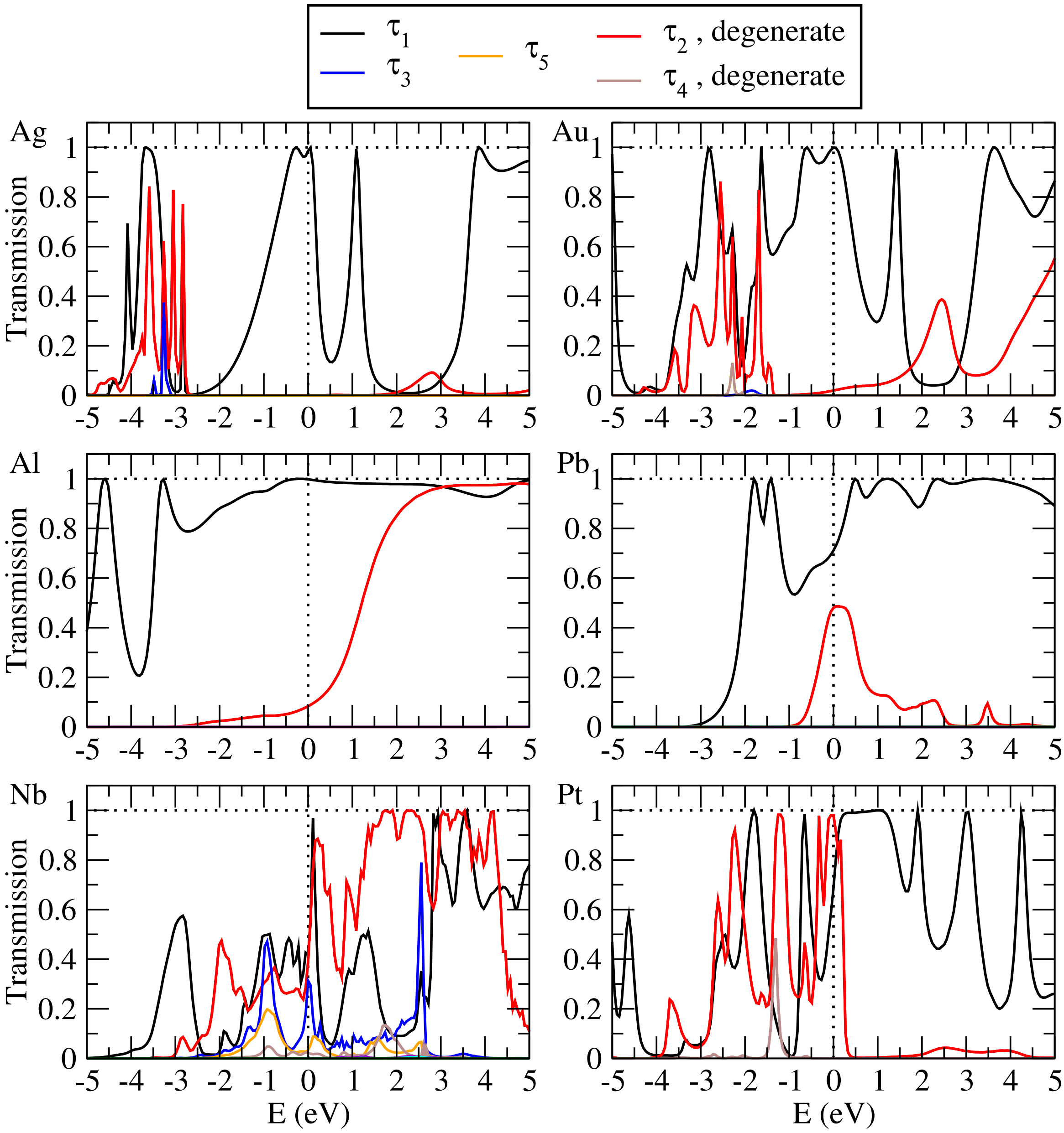

Figure 3.6: Transmission channels as a function of energy for dimer contacts of Ag, Au, Al, Pb, Nb, and Pt computed with the NRL TB parametrization. All geometries are ideal pyramids grown in fcc [111] direction, with exception of Nb, which is grown bcc [001] direction. The Fermi energy is set to zero and indicated with a dotted line.

In conclusion we can observe overall features for different elements and geometrical structures of the contact geometries. Common to all is the fact that around the Fermi energy, the transmission of the atomic contacts is simply determined by the valence orbitals of the element [21].

3.2.3 Comparison tight-binding results vs. *ab initio* results

So far we only described the atomic contact within the NRL TB parametrization. This method contains the most important information (orbital symmetry of the electronic Hamiltonian, relevant bands around ε_F etc.) of the atomic constriction. However, strictly speaking, the parametrization is valid for bulk structures only. In this Section we will briefly discuss the transmission of an exemplary system using an *ab initio* DFT method and compare the result to that obtained with the TB NRL approach.

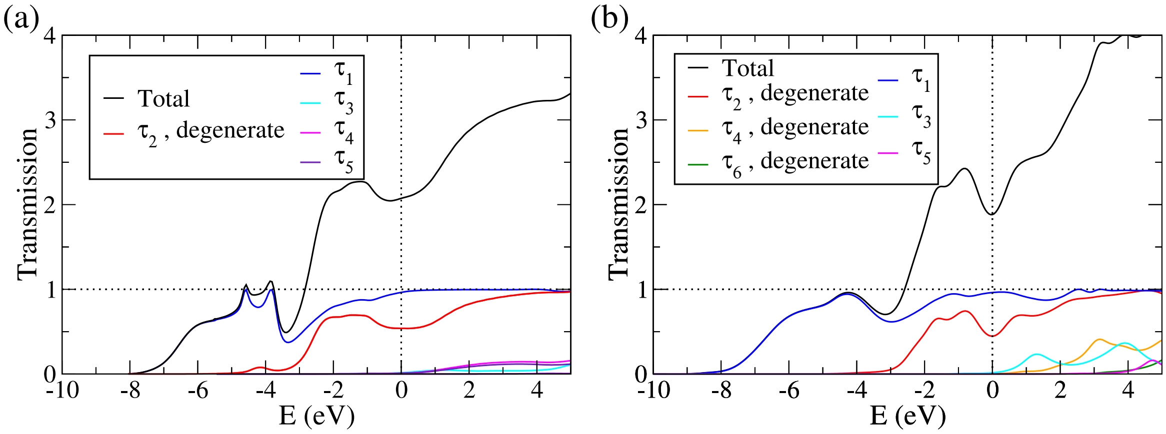

Figure 3.7: Total transmission and transmission channels as a function of energy for an ideal single atom contact of Al in [111]-direction, as depicted in Fig. 3.4. (a) NRL TB calculation (corresponds to Fig. 3.5). (b) Full DFT calculation from [72]. The Fermi energy is indicated with a vertical dotted line.

As an example system we consider a single atom contact of Al like in Fig. 3.4(a). The transmission calculation with the NRL approach for this Al contact was already discussed in Fig. 3.5, and we reproduce that result in Fig. 3.7(a). On the other hand, within the DFT approach, we follow [72, 93], and reproduce the result in Fig. 3.7(b).

In both cases, a tail of the transmission reaches around 8eV below the Fermi energy and is composed of a single transmission channel which grows to unity and dominates the transmission at ε_F. Around 3eV below ε_F a second, degenerate channel emerges and continuously raises but does not cross the first channel within the energy window under consideration. Further channel appear above ε_F. We conclude that there is no obvious discrepancy between the two approaches for this system under consideration.

For thick atomic contacts - when approaching bulk limit - the NRL method is expected to become even more accurate. In this limiting case, *ab initio* methods rapidly face size problems. It is therefore interesting to explore the NRL approach for such contacts. We will briefly discuss this in Section 3.4.5 for Mg contacts and in the context of bulk ARM.

In the opposite limit, for systems low coordination (like atomic contacts with a central dimer, chains of atoms, etc.), the NRL approach has to be treated with care.[8] However, in the tunneling limit, the conductance should not depend on contact details but decay exponentially with the tip distance, where the exponent is related to the work function of the metal under consideration.

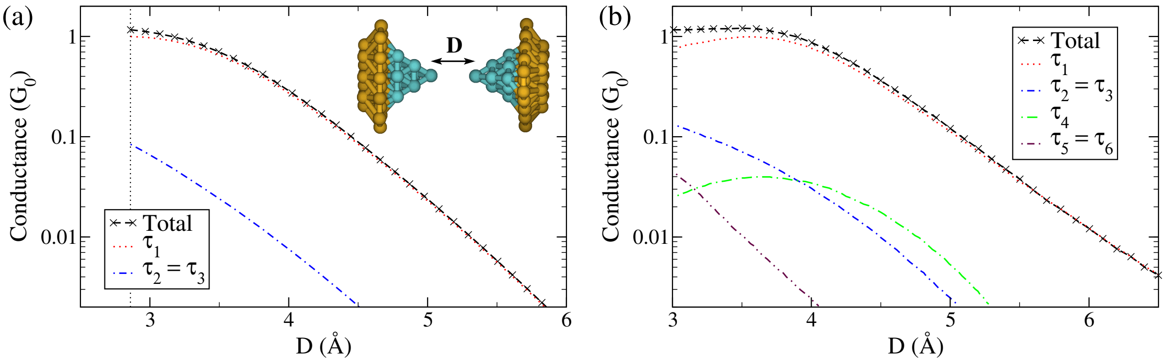

Figure 3.8: (a) TB-conductance of a dimer contact in fcc [111]-direction of Al as a function of the separation D between the tip atoms. The positions of the atoms are fixed to lattice sites. Three-point bending mechanism. (b) DFT-conductance of a similar geometry as in (a) (taken from [113]). Note that in (b) the positions of the four tip atoms are relaxed resulting in a apparently larger tip separation and an increased contribution of the next layers to the conductance.

In order to evaluate the performance of the NRL approach, we compared the conductance of an Al dimer contact like in Fig. 3.6 during separation of the tip atoms. We start with the dimer in NN distance (2.86 Å for Al) and calculate the conductance as a function of the tip distance, while we keep the geometry of the two pyramids. This can again be compared to a similar calculation using the DFT approach [113]. Note that in the DFT calculation the four tip atoms in each pyramid of the contact was relaxed. As a consequence, the tip Al atom relaxed towards the frustum of the pyramid and the distance between the tip atoms appears larger than the distance between atoms of the frustum would be. Furthermore, in the relaxed position, the closer by atoms of the next to tip layers give a contribution to the conductance resulting in additional channels. This explains the main differences between the Fig.3.8(a) and (b). But more importantly, the uniform exponential decay $\propto \exp(-\beta D)$ is roughly the same in both approaches with $\beta \approx 2\ \text{Å}^{-1}$. This leads to an estimate for the work function of 4.5 eV in reasonable agreement with experimental value of 4.26 eV for the (111) surface of Al [114].

In conclusion we showed here the overall agreement of the NRL TB method with results

---

[8] Even in this case, the NRL method can be used to analyze conductance during the last steps of breaking of an atomic contact [77, 112]. It reproduces the most important features of the conductance histogram of atomic contacts of the different metals, like structure of the peaks at low conductances, transmission channels,...

from an *ab initio* DFT approach in the case of a metallic ideal single atom contact. We continue now to apply this method to limiting material that have not been analyzed so far, namely the bivalent metals Zn and Mg on one hand, and – in the next Chapter – the 3*d* ferromagnetic materials Fe, Co, and Ni.

3.3 Bivalent metals: zinc

In this Section we want to study the conduction properties of atomic contacts of the bivalent metal Zn. In particular we shall investigate the conductance channels for single atom contacts of Zn and shed some light on how the geometry of thicker contacts is reflected in their conduction properties. In this section we will compare the theoretical observations directly compared with experiments. The experimental results were obtained by the group of Prof. Elke Scheer at the Universität Konstanz.

As we showed above for some example metal contacts with partially filled valence orbitals (noble, *p*-valent, and transition metals), the number of conductance channels in such contacts is mainly determined by the chemical valence and the local atomic environment [21, 25, 26]. Thus, for instance, a one-contact of a monovalent metal such as Au sustains a single channel. For *p*-valent metals such as Al or Pb one finds three channels due to the contribution of the *p* orbitals. Finally, in a transition metal such as Nb the contribution of the *d* orbitals leads to five channels. Using the non-linearity of superconducting current-voltage (I-V) characteristics, it is possible to determine the transmission coefficients of those contacts [115]. Up to now, these attractive ideas have only been tested in four materials (Au, Al, Pb, and Nb) due to the need of superconductivity for the channel analysis.

In this sense, it would be highly desirable to investigate other groups of metals. An interesting possibility is the analysis of the bivalent metals of the IIB group of the periodic table such as Zn. The electronic structure of a Zn atom is [Ar]$3d^{10}4s^2$, i.e. the outermost *s* orbital is full with two electrons. In its solid state, due to the overlap between the 4*s* and the 4*p* bands,a Zn is a conductor. Therefore, for one-atom contacts one expects Zn to be an intermediate case between the noble metals and Al. The goal of this Section is to elucidate what determines the conductance channels of one-atom Zn contacts.

This section is organized as follows: First we consider the case of one-atom contacts of Zn. We can directly compare our theoretical analysis of the conduction properties of those contacts with experimental results for the analysis of the conductance channels. In a second part in 3.3.2 we will extend the analysis to thicker contacts. By comparing experimental conductance traces to theoretical predictions for different contact orientations we can conclude on a correlation between conductance traces and atomic configuration of Zn atomic contacts. We end this section with a summary of the results for atomic contacts of Zn.

3.3.1 Conductance channels of one-atom zinc contacts

Let us first limit ourselves to the case of single atom contacts. Here we will briefly describe how the conductance channels of single-atom contacts of Zn could be derived experimentally. Then we compare the experimental results to calculations of the conduction properties in such contacts.

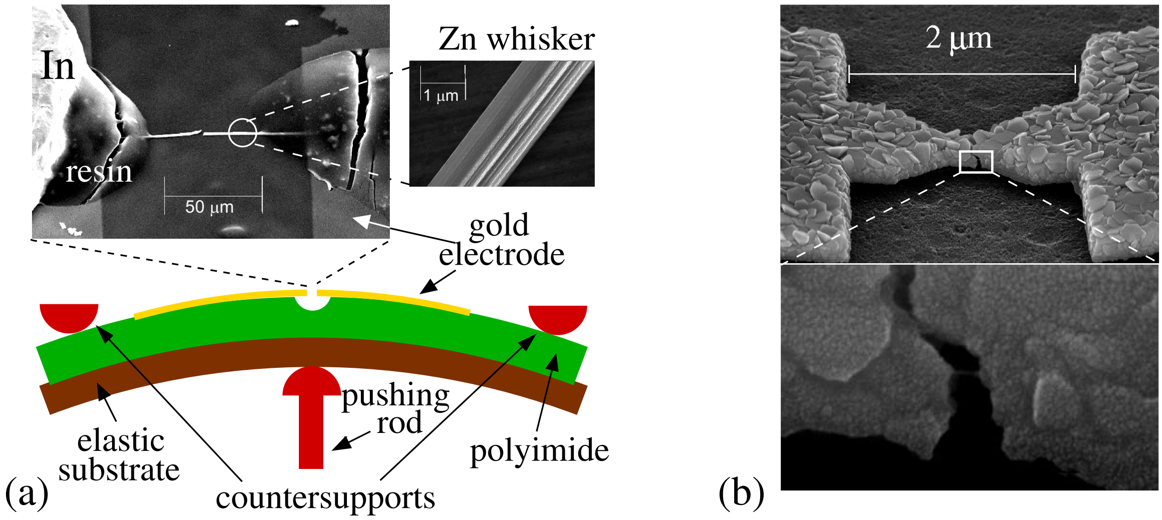

Figure 3.9: (a) Three-point bending mechanism. The pushing rod bends the elastic substrate. The optical micrograph shows a whisker MCBJ after measurement. Right inset: blow up of a typical Zn whisker with a diameter of 1.7 μm. (b) Electron micrograph of a lithographically fabricated Zn sample after measurement; the poly-crystalline structure of the Zn is clearly visible. Lower inset: Magnification of the central part of the sample. A remaining spacing of the bridge arms of several nm and a nanowire between them is observed.

3.3.1.1 Conductance channels of Zn whiskers

Experimentally the atomic contacts were obtained using the mechanically controllable break junction (MCBJ) technique [18, 116], which is shown schematically in Fig. 3.9(a). For this technique, a pre-fabricated wire is fixed on a flexible substrate which is then bent in a three point configuration by pushing the central piston against the fixed endpoints. Due to the advantageous ratio between the advancement of the pushing rod and the movement at the level of the contact, the nanocontact can be broken with a precision down to the pm range.

In the experimental work described below, such a MCBJ technique was used in different variations: On one hand a notched wire or a whisker was glued on the substrate and contacted with electrodes as shown in the inset of Fig. 3.9(a). On the other hand lithographically fabricated break junctions were used as shown in Fig. 3.9(b). However, due to the characteristics of Zn at surfaces, the lithographically fabricated break junctions exhibited strong granularity in the mesoscopic scale. Together with the gap anisotropy [117] this prevented from obtaining neat *I*-*V*s in the superconducting regime for such contacts. In order to circumvent these problems it was necessary to develop a variation of the MCBJ technique which comprises a Zn whisker as central part. This new technique allows for fabrication of reproducible one-atom Zn contacts with well-characterized lattice properties of the electrodes. In the following we will concentrate on those whisker MCBJs and come back to the case of the lithographically fabricated MCBJs in the next Section.

Using the superconducting *I*-*V* characteristics [115] the transmission coefficients have been reliably extracted for the whisker MCBJs. We find that in the last plateau, where the conductance is around 0.8 G_0 (Refs. [22, 118]), the transport is largely dominated by a single channel. In order to understand these findings we have performed tight-binding calculations of the conductance of one-atom Zn contacts. Our theoretical results show that the transport takes place through the 4s and 4p bands of Zn. In agreement with the experiment, we obtain for the one-atom case a conductance between 0.8 and 1.0 G_0, and it is dominated by a single channel which is a combination of the s orbital and the p orbital along the transport direction of the central atom.

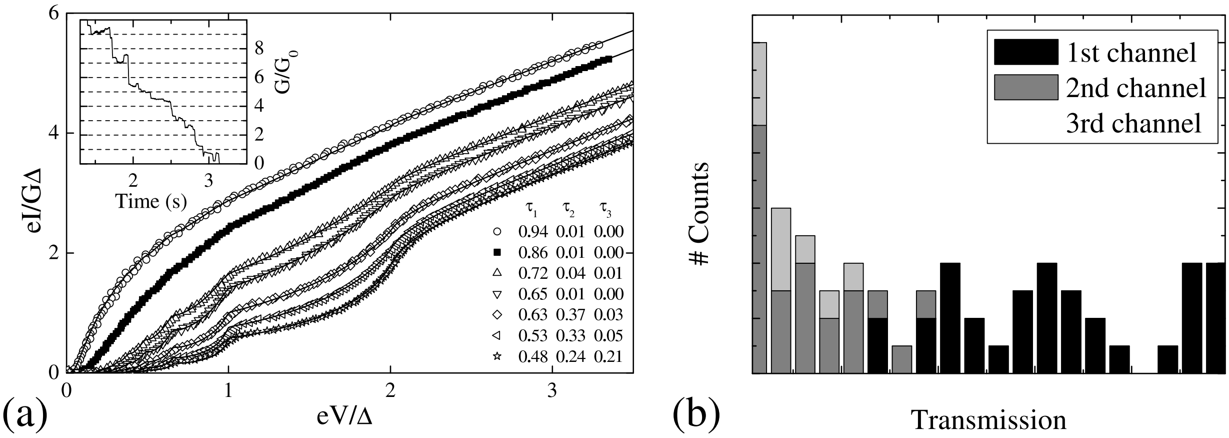

Figure 3.10: (a) Current-voltage characteristics of several one-atom contacts of Zn arranged with a whisker MCBJ at $T = 0.27$ K (symbols) and best fits to MAR theory [19, 20]. The value of $\Delta = 160$ μeV was used to fit all the curves. The transmission coefficients obtained from the fit are indicated in the figure. Inset: typical opening curve recorded at $T = 1.5$ K. (b) Experimental histogram of the channel transmissions τ_i obtained in the last conductance plateau of a Zn-whisker MCBJ. We count all those contacts as belonging to the last plateau that have been recorded when the conductance once dropped to or below G_0. The channels are labeled as 1st, 2nd, ... according to their $\tau_i' s$.

The first attempts to investigate Zn contacts were carried out with both "notched-wire" break junctions [18] and thin-film break junctions [116]. However, the granular structure of the evaporated films and the intrinsic gap anisotropy of Zn hampered the observation of neat superconducting I-Vs, which are necessary to obtain the channel transmissions. To solve these problems MCBJs consisting of Zn whiskers glued on top of a pre-patterned flexible substrate were prepared [see Fig. 3.9(a)]. Whiskers are thin single-crystalline needles, which in the case of Zn are grown by the so-called pressure method [119]. Following Ref. [119] whiskers of diameter ranging from 0.5 to 2 μm and length of the order of 0.5 to 1 mm were grown [see inset of Fig. 3.9(a)], which takes approximately 3 to 6 months. They are preferably oriented along the a-axis ([11$\bar{2}$0] direction) with a probability of 67%. To contact the whiskers bronze substrates of size 3×18 mm^2 were prepared, covered with an insulating layer of polyimide and 70 nm thick gold electrodes separated by 100 μm. Then, individual whiskers are deposited onto the substrate and mechanically contacted by two small dots of epoxy resin. The electrical contact between the whiskers and the electrodes is obtained by gluing two small pieces of In onto the whiskers and the gold pads. With this method whisker break junctions with resistances of 10 to 100 Ω at room temperature were obtained. Finally, they are mounted onto a three point bending mechanism [18] [see Fig. 3.9(a)] thermally anchored to the base temperature pot ($\approx$ 260 mK) of a ^{3}He cryostat.

Breaking the contact, the conductance evolves as usual in a step-like manner. An example of an opening curve is shown in the inset of Fig. 3.10(a), where one sees the typical behavior for Zn atomic-sized contacts with a conductance in the last plateau of the order of 0.8 G_0. The stability of the setup allows for halting at any point along the breaking to record the I-Vs. In particular, to determine the superconducting gap the whisker of Fig. 3.9(a) was broken to form a tunnel contact. In this limit a well-pronounced gap is visible in the I-Vs, and a value of $\Delta = 160$ μeV was deduced. This value is slightly larger than the expected value for the x-direction in real space, corresponding to the crystallographic [11$\bar{2}$0] direction, the direction with the largest gap.[9] In Fig. 3.10(a) are shown the superconducting I-Vs obtained at 0.27 K for seven different contacts. Together with the data points the best fit is shown, which was obtained with the multiple Andreev reflection (MAR) theory [19, 20] at zero temperature. The details of the fit procedure are explained in detail in Refs. [105, 115]. The excellent agreement with the MAR theory allows for the determination of the whole set of transmission coefficients $\{\tau_i\}$ with a precision of a few percent (depending on the value of τ_i) for up to 4 channels. To investigate the conductance channels of the smallest contacts (presumably one-atom contacts), the transmission coefficients obtained in the last plateau of 33 contact realizations were collected. The results are shown in the histogram of Fig. 3.10(b). From this plot we draw two important conclusions: (i) the conductance in the last plateau is largely dominated by a single channel with a high transparency, and (ii) depending on the contact geometry a second and third channels with low transmissions can also contribute to the transport.

---

[9] In Ref. [117] gap values of $\Delta = 108$ μeV for the c axis and of $\Delta = 137$ μeV for the x direction were reported. These values should be taken with care, since they depend on the purity and dimensionality of the sample. The estimated critical temperature of the whiskers used here is 0.80 K, while the typical bulk values are between 0.84 K and 0.88 K.

3.3.1.2 Transmission properties of Zn single-atom contacts

In order to understand the experimental findings we have performed conductance calculations following the method described in Refs. [25, 26] and Chapter 2. In contrast to the NRL method we used before in Chapter 3.2 to describe transport, we will use here for Zn the orthogonal two center SK parametrization of Ref. [84], which is fitted to band structure of bulk materials. Here the on-site energies and hopping parameters do not explicitly depend on the local environment and are fixed to first, second, and third nearest neighbour positions in bulk. Our basis is formed by 9 atomic orbitals: $3d, 4s, 4p$, which give rise to the main bands around the Fermi energy. We have imposed local charge neutrality in all the atoms of the constriction by means of a self-consistent variation of the on-site energies to partially compensate for surface effects. The leads are described with bulk atoms. The transmission of the contacts is calculated as described above using the NEGF, which allow us to express the set of transmission coefficients $\{\tau_i\}$ in terms of the microscopic parameters of the atomic contacts.

It is instructive to first discuss the bulk density of states (DOS) of Zn in its hcp structure, which is shown in Fig. 3.11(a). Notice that the d band is rather narrow, it lies ≈ 9 eV below the Fermi energy and it is practically full. It is then obvious that the s and p bands will play the main role in the conduction. Since there is an uncertainty in the growth direction of the whiskers, we have studied the conductance of geometries with different crystallographic orientations. In the inset of Fig. 3.11(b) we show an example of an one-atom contact along the [0001] direction (c-axis). The geometry is constructed starting with a single atom and choosing the nearest-neighbours in the next layers. For this geometry, in Fig. 3.11(b-c) the local DOS at the central atom and the transmission of the individual channels τ_i as a function of energy are shown. In the local DOS we see that the p_z level (z is the transport direction) is shifted to lower energies. This is due to its better coupling to the leads as compared with p_x and p_y, which remain degenerate in this ideal geometry. This fact implies that the orbital p_z plays a more important role in the transport. In the relevant energy range the d band has a very tiny local DOS and it has therefore not been depicted. In Fig. 3.11(c) we see that at the Fermi energy the total transmission is 0.86 and it is dominated by a single channel with $\tau_1 = 0.81$. The second and third channel are degenerate and their transmission at the Fermi energy is $\tau_2 = \tau_3 = 0.025$, while the fourth gives a negligible contribution $\tau_4 = 0.001$. To understand the origin of these conductance channels we have analyzed the character of the eigenfunctions of the transmission matrix by looking at their weights in the different orbitals of the central atom. This analysis reveals that the dominant channel is basically a symmetric combination of the s and p_z orbitals of the central atom. The second nd third channels are mainly due to the contribution of the p_x and p_y orbitals. The degeneracy of these two channels is a consequence of the symmetry of this ideal geometry and reflects the degeneracy of the local DOS, see Fig. 3.11(b). Their transmission is rather low because the transport takes place through the tails of the p_x and p_y bands. The antisymmetric combination of s and p_z forms a channel of negligible transmission due to the fact that this combination is orthogonal to the states of the leads. So in short, the nature of the channels in this one-atom Zn contact is similar to the Al case [25]. The main difference is that Zn has one valence electron less than Al. Thus, the Fermi energy is lower and consequently lies further away from the center of the p bands, resulting in a lower transmission of the p_x-p_y channels.

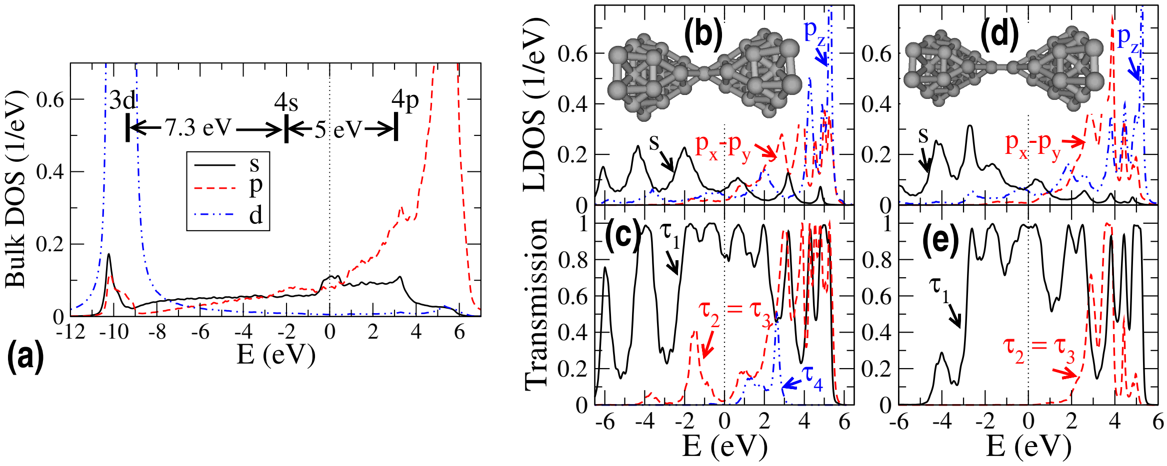

Figure 3.11: (a) Bulk density of states of Zn hcp projected onto the s, p and d orbitals as a function of energy. The labels indicate the value of the on-site energies. Inset of panel (b): contact along the [0001] direction, with a single central atom and containing 45 atoms. The distance between the different atoms is the bulk distance. (b-c) Local DOS at the central atom projected onto the s and p orbitals and channel transmissions as a function of energy for the contact of the inset of panel (b). Notice that the channel p_x-p_y is two-fold degenerate. Inset of panel (d): the same contact as in panel (b), but with a dimer in the narrowest part. The distance between the central atoms is the bulk nearest-neighbour distance. (d-e) The same as in panels (b-c) for the dimer geometry. The Fermi energy is set to zero and indicated with vertical lines.

As explained above, the second and third channels have a low transmission due to the fact that the transport takes place through the tails of the p_x and p_y bands. This suggests that a reduction of the coupling to these orbitals could result in a negligible contribution of these channels. To test this idea we have analyzed one-atom contacts with a dimer in the narrowest part of the contact, see inset of Fig. 3.11(d). This type of geometry has been frequently observed in molecular dynamics simulations of atomic contacts of Al (Ref. [120]) and Au (Ref. [112]). In Fig. 3.11(d-e) the local DOS in one of the central atoms and the transmission through this dimer contact are shown. The total transmission at the Fermi energy is 0.97, and as suspected, it is completely dominated by a single channel ($\tau_2 = 4 \times 10^{-4}$), while the character of the channels is the same as in the case analyzed above. Thus, by changing the contact geometry from a short contact with a single atom in the constriction to a long contact in a dimer configuration the conductance may increase by about 0.1 G_0. Opening traces that support this prediction are reported in the literature [22, 118] and have also been found in the present experiment [see inset of Fig.3.10(a)].

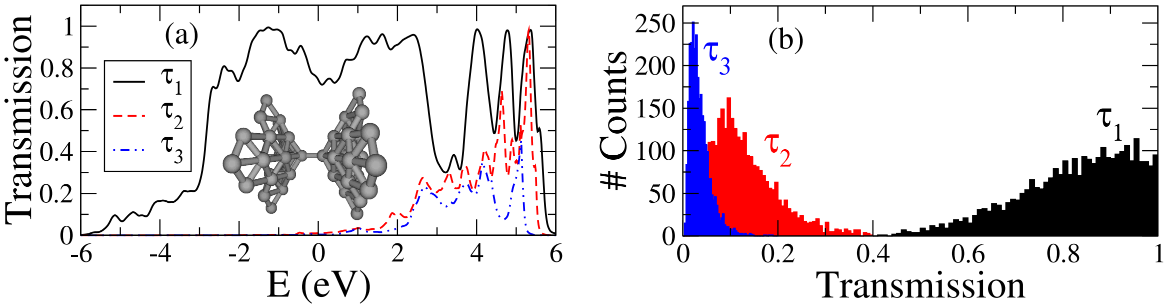

Figure 3.12: (a) Channel transmissions as a function of energy for the contact of the inset, which is grown along the $[11\bar{2}0]$ direction, has a dimer in the middle and contains 60 atoms. The Fermi energy is set to zero. (b) Histograms of the transmission coefficients for 3000 disorder realizations (see text) of the one-atom contact of the inset of Fig. 3.11(b).

Let us now discuss the results for contacts along the $[11\bar{2}0]$ direction (a-axis). An example of a contact geometry with a dimer configuration and its corresponding transmission is shown in Fig. 3.12. As in the case of the [0001] direction, the total transmission ($\tau_{tot} = 0.77$) is clearly dominated by a single channel ($\tau_1 = 0.75$), which is formed by a symmetric combination of the s and p_x orbitals of the central atoms (x is now the transport direction). The second channel is on the border of what is measurable ($\tau_2 = 0.01$), while the transmission of the third one is $\tau_3 = 0.004$. Notice that in this case these two channels are not degenerate. We find that the transmission for contacts along the $[11\bar{2}0]$ direction is slightly lower than for the [0001] one, which we attribute to the larger apex angle in the first direction, which produces less adiabatic contacts. These findings are in agreement with the observation of Ref. [118] where a splitting of the first peak of the histogram into two sub-peaks with 0.7 and 0.9 G_0 was reported.

For all the geometries analyzed in this work we have checked that the results do not change qualitatively with the number of atoms in the constriction region. We have also studied the influence of disorder, which we simulate by changing randomly the positions of the atoms in the contact region with a very large maximum amplitude of 20% of the nearest-neighbour distance. The hoppings - initially fixed to bulk values - are then computed using the scaling laws proposed in Ref. [84, 86, 87] and explained above. In Fig. 3.12(b) we show a histogram of the individual transmissions for 3000 realizations of contacts along the [0001] direction with a single central atom. As it can be seen, the transmission is still dominated by a single channel, and depending on the local environment of the central atom a second and even a third channel can have a measurable contribution, in agreement with the experimental results [see Fig. 3.10(b)]. Similar histograms for the dimer geometries show that τ_2 and τ_3 typically lie below the measurement threshold.

In summary, we have analyzed experimentally and theoretically the conductance channels in Zn single-atom junctions. We have shown that, although Zn is a bivalent metal, the conductance of one-atom contacts is dominated by a single well-transmitting channel, which we have traced back to the symmetry of the valence orbitals (s and p) of the central atom. Our results illustrate that the number of channels in an one-atom contact is not simply determined by the chemical valence, but by the number of valence orbitals together with their symmetry.

So far we only considered experimental results for whisker break junctions as we needed superconducting I-V curves to determine the transmission values of the conductance channels. The price we had to pay was the poor statistics due to the complex and time-consuming fabrication method of Zn whiskers. In what follows we will consider different, cheaper fabrication methods which allows us to study a full conduction histogram of Zn contacts and conclude on some correlations between the contact geometries and the conductance.

3.3.2 Correlation between conductance and atomic configuration of atomic contacts of zinc

Experiments on a large ensemble of metallic contacts have demonstrated the *statistical* tendency of atomic-size contacts to adopt element-specific preferred values of conductance. The actual preferred values depend not only on the metal under investigation but also on the experimental conditions. However, for many metals, and in particular 'simple' ones (like Na, Au...) which represent good 'free-electron' systems in the bulk, the smallest contacts have a conductance G close to G_0 (Ref. [1]). Statistical examinations of Al point contacts at low temperatures yield preferred values of conductance at $G = 0.8\,G_0, 1.9\,G_0, 3.2\,G_0$ and $4.5\,G_0$ (Ref. [121]), indicating that single-atom contacts of Al have a typical conductance slightly below the conductance quantum. However, it has been shown by the analysis of current-voltage characteristics in the superconducting state that Al single-atom contacts accommodate in general three transport channels, the transmissions of which add up to a value $0.8 \lesssim \tau \lesssim 1$ (Ref. [115]). These findings are in agreement with measurements of shot noise [122, 123], conductance fluctuations [124], thermopower [125] and supercurrent [126] in such contacts. In particular, the experiments on Al have shown the following behaviour: for a given contact geometry the transmission coefficients of the individual channels almost continuously change upon further deformation of the contact and no preferred transmission values can be found [115]. A quantum-chemical model [21], which links the τ_{i} to the chemical valence and the atomic arrangement of the region around the central atom of the constriction, gives a prediction about the number of transport channels, but the $\{\tau_{\mathrm{i}}\}$ depend on the precise atomic arrangement of the contacts.

So far Al appears to be the only metal to show peaks in the histogram close to multiples of G_0, although this does not correspond to quantized transmission values. However, since no information about the atomic arrangement of the contacts can be deduced from the experiments, a direct correlation between transport channels and configuration is still lacking. Therefore it is worth studying a class of elements that are likely to possess similar transport behavior as Al, but which simultaneously offer the possibility to correlate the transport properties to the crystal structure. So far, only for the monovalent metal

Au signatures of different growing directions of nanowires could be found in the conductance traces. In this case a combination of those measurements with transmission electron microscopy [127, 128] was needed. However, in those experiments, no direct information about the conductance channels was available.

As pointed out above bivalent elements such as the alkaline-earth elements or the IIB subgroup elements Cd, Zn and Hg should be insulating, since they have a completely filled outer s-shell. This apparent discrepancy to the experimental findings indicates that additional orbitals besides the s-orbitals contribute to the electronic conductance. Detailed calculations reveal that in the case of Zn the 4p orbitals are the most relevant ones for a correct description of the bulk band structure [84]. With these considerations, single-atom contacts of Zn are expected to have very similar transport properties as Al single-atom contacts. However, the distribution of the transmission coefficients may deviate, since it depends on the exact atomic configuration as we showed in the previous Section 3.3.1. Since Zn crystallizes in a hexagonal, slightly distorted hcp structure while Al is a fcc crystal, the actual atomic arrangement of the point contacts might be different. Moreover the closed s-shell in the limit of isolated Zn atoms may lead to new features in the conductance histogram of Zn atomic contacts.

We will show that the conductance histogram of Zn shows several peaks, a fact that is unusual for multivalent metals. The first peak, which corresponds to the single-atom contact - is located slightly below one conductance quantum and is split-up into two subpeaks. This evidences the existence of two or more preferred configurations of the single-atom contact. We will demonstrate that indications for preferred atomic arrangements can be found in individual opening and closing traces of the junctions both measured in the normal as well as in the superconducting state. With the help of a tight-binding model for the transport channels we establish a correlation between the preferred conductance values deduced from the histograms and preferred channel transmissions which we use for linking the peaks in the histogram to preferred atomic configurations.

3.3.2.1 Lithographic break junctions of Zn

Let us first discuss briefly the fabrication and low-temperature electronic transport properties of lithographic MCBJs of Zn which are used for measuring the conductance histogram. The samples are fabricated using electron beam lithography along the lines of Ref. [116]. These samples are 2 μm long, 200 nm thick suspended Zn nanobridges, with a 200×100 nm^2 constriction in the center [cf. Fig. 3.9(b)]. The metal structure is deposited onto a polyimide layer which is partially etched away for suspending the nanobridge. If Zn is evaporated at room temperature, it grows in islands of micron-size with the hexagonal axis preferably perpendicular to the substrate plane. Since this structure is not suitable for the formation of atomic-size contacts, special care is taken to reduce the grain size. The parameters could be chosen empirically such that the grain size of the Zn layer does not exceed $\approx$ 200 nm. Finally, the bridge is underetched so that at the narrow constriction the nanobridge is now unsupported. The resistance of the nanobridge does not increase during the etching process, indicating that reaction between the oxygen ions and Zn is weak.

The bridge is then mounted on a three-point bending mechanism and cooled down to 1.5 K. A μm screw moves the pushing rod that bends the substrate such that the relative motion of the anchor points of the bridge can be controlled with a precision of around 1 pm. This was verified using the exponential dependence of the conductance on the inter-electrode distance in the tunnel regime. The resistance of the sample is recorded by a 4-point resistance bridge with a measuring current of 1 nA. Due to the texture of the evaporated film shown in the micrograph of Fig. 3.9(b) and its consequences to the mechanical deformation of the bridge during the breaking process, only few of the bridges can be closed again (5 out of 20 samples). In these cases the formation of a nanowire was often observed in the electron micrograph [see lower panel of Fig. 3.9(b)]. During the systematic measurements the opening speeds of the bridge-anchor points were typically around 35 pm/s, much slower than typical opening speeds of nanocontacts fabricated with the help of a STM or the "notched-wire" break junction technique [1]. This limitation in opening speed also limits the number of opening traces that can be recorded within a reasonable time. The output of the resistance bridge is recorded by an oscilloscope and then transferred to a computer for calculating the histogram.

When elongating the bridge, its conductance G decreases in steps of the order of one G_0, their exact sequence changing from opening to opening (see right panels of Fig. 3.13). Since the mechanical deformation is different for opening and closing, we construct separate histograms for both experiments. Fig. 3.13a displays the conductance histograms calculated from $\approx$ 600 subsequent opening and closing sequences recorded during two weeks on the sample shown in Fig. 3.9(b), which has been kept at low temperatures. Similar histograms were achieved with a lower motion speed of the bridge arms of 17 pm/s.

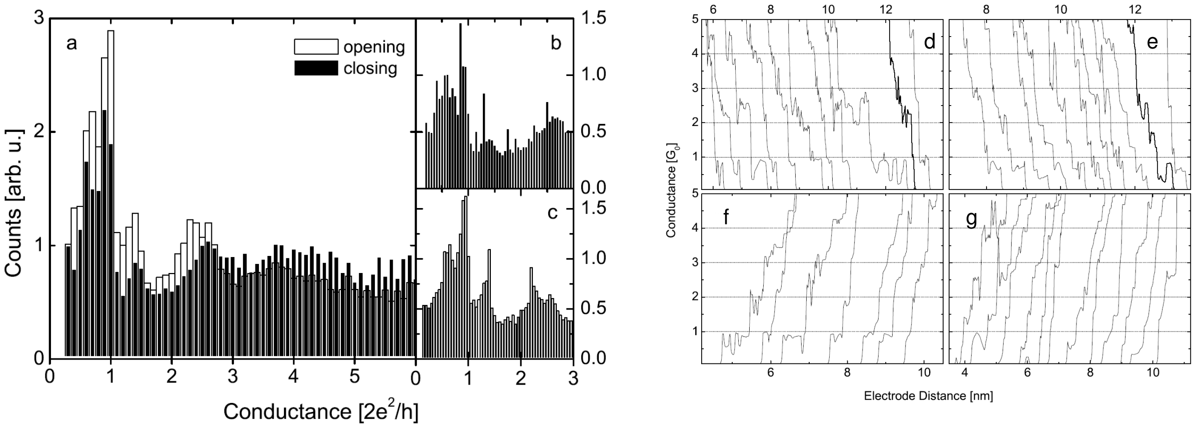

Figure 3.13: (a-c) Conductance histograms for opening (a,c) and closing (a,c) the contacts, recorded on two samples like the one shown in Fig. 3.9(b) at T = 1.5 K. The histograms have been calculated from $\approx$ 600 individual opening and closing curves, respectively. (d-g) Opening (panels d,e) and closing (f,g) traces of the sample in Fig. 3.9(b) recorded at 1.4 K. Panels d and f (e and g) show examples without (with) the plateau at 1.4 G_0.

Several peaks appear for both motion directions at similar positions of 0.8 G_0, 1.4 G_0 and ≈2.5 G_0. The first peak is split into two substructures at ≈0.7 G_0 and 0.9 G_0, a feature which has not been observed for other materials. This splitting has been observed in several independent measurements carried out with four different samples. Although the splitting is observed in all the measurements, the absolute values of the peak positions and the relative peak heights vary slightly from experiment to experiment (see Fig. 3.13b and c). A possible explanation of the splitting could be two different configurations of the last contact. This will be discussed in detail below.

The second peak appears already at 1.4 G_0 for both closing and opening traces. This spacing of neighbouring peaks is unusually small for metals. The third peak appears to be shifted to slightly lower values (2.2 G_0) in the opening traces as compared to the closing traces (2.5 G_0). In similar experiments by Yanson et al. [22] on ”classical” break junctions made of notched Zn wires, no splitting of the first peak is found, but a shoulder that is compatible with our findings. The peaks at higher conductance values are in reasonable agreement with our findings as well. It is well known that details of the histograms do depend on the experimental conditions (see for example the different experimental results for the most extensively studied metal gold). In the experiment with Zn described in Ref. [22] higher voltages have been applied, a slightly higher temperature and faster opening speeds have been used, and only opening traces were recorded. In the experiment presented here, the main difference between opening and closing consists in the peak heights; the low-conductance peaks are less pronounced when closing.

When analyzing the individual opening and closing traces further, we observe the following correlation: When opening the contact, we either observe jumps from a conductance of around 2.2 G_0 via 0.9 G_0 to almost 0 G_0 or a plateau series 2.5 G_0, 1.4 G_0, 0.7 G_0 (see Fig. 3.13 d and e). Only very rarely plateaus at 2 G_0 and 1.4 G_0 exist in the same trace; jumps from 1.4 G_0 to 0.9 G_0 do not occur at all. We also observe direct jumps from values around 2.2 G_0 or slightly above to tunnel regime, but we never observe conductance changes from 1.4 G_0 directly to zero. The plateaus at 2.2 G_0 are usually rather short, while those at 1.4 G_0, 0.9 G_0 or 0.7 G_0 are well pronounced. In particular on the 0.9 G_0 plateau we often observe oscillations to much smaller values $\leq$ 0.4 G_0. About 38% of all opening curves show the series 2.5 G_0, 0.9 G_0 and about the same ratio belongs to the group 1.4 G_0, 0.7 G_0. In the closing traces (see Fig. 3.13 f and g) we often observe the series 0, 0.9 G_0, 2.5 G_0 or the series 0 G_0, 0.7 G_0, 1.4 G_0, 2.5 G_0, but jumps directly to the 1.4 G_0 or 2.5 G_0 - plateaus are possible. We attribute the latter observation to the formation of contacts larger than a single-atom contact since the apex atoms from the previous opening sequence might have relaxed back to positions deeper in the tip. Also in the closing curves, an oscillating behavior is more pronounced for the 0.9 G_0-plateau than for the 0.7 G_0-plateau. Among all recorded closing traces, 48% show the 0.9 - 2.5 G_0-plateau series and 28 % the 0.7 - 1.4 G_0-series. We note that the difference between the opening and the closing histogram is rather small compared to other metals (see e.g. Ref. [129] for Au).

In summary, two different opening or closing paths seem to be preferred. One includes geometries giving rise to conductances of 0.9 and 2.2 G_0, while the other gives conductances of 0.7, 1.4 and 2.5 G_0, respectively. This interpretation is further supported by the following analysis of the step heights: The data of the individual conductance traces during elongation is collected, the conductance difference between neigboured elongation steps is calculated (at constant elongation speed) and displayed in a histogram over step height (not shown). If there was no preferred step height, the histogram should decrease monotonously with increasing step height. However, the histogram of the collected data shows a clear peak at 0.7 to 1.0 G_0 but no structure at smaller values. This indicates that during rearrangement jumps with a minimum step height of 0.7 to 1.0 G_0 are preferred. In particular this statistical analysis suggests that the neighboured peaks in the conductance histogram at 1.4 G_0 and 0.9 G_0 and at 0.9 G_0 and 0.7 G_0 respectively do not arise from the same conductance traces with plateaus at the corresponding conductance values. This was already inferred by the individual conductance traces of Fig. 3.13(d-g). In total, this analysis demonstrates that the conductance histogram is a superposition of two or more histograms with different sets of preferred values.

3.3.2.2 Whisker break junctions of Zn

In this Section, the question about the origin of these two distinct sub-histograms is treated. In order to clarify this issue we use the conductance channel analysis in Zn whisker MCBJs as described in the previous Section. We can then compare the channel-resolved conductance traces with those obtained with lithographic MCBJs of Fig. 3.13(d-g). At least two sub-groups leading to the two subpeaks are distinguishable. Finally by comparing those results to the conduction properties of the simplest atomic geometries, a link of the sub-groups to different crystallographic directions is suggested.

Conductance histograms of multivalent metals in general do not show well pronounced multiple peaks [22, 37, 130]. As already discussed above in Section 3.3.2, the only exception of this general observation was so far Al. The histogram of Zn shows similarities to that of Al: Several peaks occur with an average spacing between the peaks of about 0.7 G_0. Now we want to verify whether this similarity is mirrored in the quantum transport properties, i.e. the conductance channels. Therefore it is again necessary to switch to whisker break junctions, as in the case of lithographic break junctions beyond single atom contacts (more than two open channels), where the superconducting DOS deviates markedly from the BCS shape [131]. The sample preparation of the whisker MCBJs is as described above. It should be pointed out that in the lithographic break junctions the [0001] direction is preferably oriented perpendicularly to the film plane whereas Zn whiskers mainly grow in [$11\bar{2}0$] direction. However during the breaking process the emerging nanowire may be oriented along any of those directions.

The I-Vs with a dominating single channel are routinely observed at the end of a last plateau after an abrupt change of the I-V. This often includes an *increase* of the conductance, and thus a re-arrangement of the atomic-size contact. Once such a contact has been established, it remains stable for an elongation of the bridge of 2-3 Å. This length compares with the equilibrium nearest neighbour distance of 2.6 Å of Zn atoms in the bulk. For Al samples, contacts with a dominating channel and one or two smaller channels

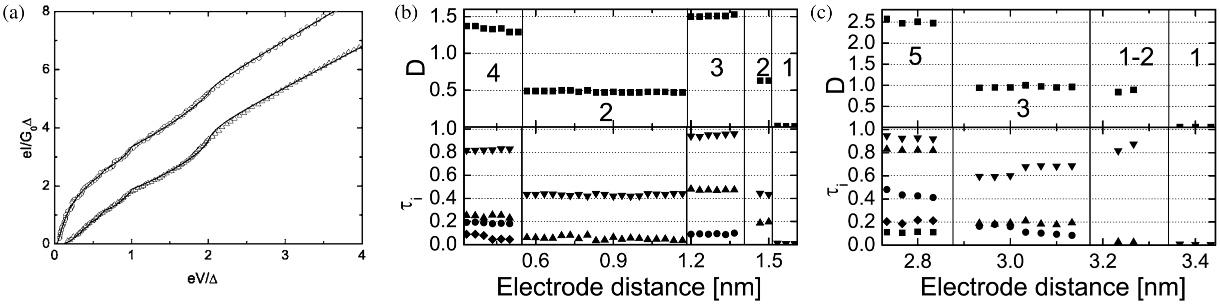

Figure 3.14: (a) Current-voltage characteristics of two atomic-size contacts of Zn arranged with a whisker MCBJ at $T = 0.27$ K (symbols) and best fits according to the theory of MAR [19, 20] (lines) with a superconducting gap value $\Delta = 165$ μeV. The transmission coefficients are for the lower curve (triangles): $\tau_1 = 0.82$, $\tau_2 = 0.25$, $\tau_3 = 0.19$, $\tau_4 = 0.09$; and for the upper curve (circles) $\tau_1 = 0.96$, $\tau_2 = 0.47$, $\tau_3 = 0.08$. The lower (upper) curve has been measured at position 0.35 nm (1.37 nm) of panel (b). (b) Opening traces with decomposition into individual channels for a whisker break junction showing plateaus at 1.4 G_0, 0.5 G_0, 1.5 G_0, and 0.6 G_0. Transport direction presumably close to [0001]. (c) Opening traces with decomposition into individual channels for a whisker break junction showing plateaus at 2.5 and 1 G_0. Transport direction presumably close to [11$\bar{2}$0]. The origins of the electrode distance axes are at arbitrary values.

could be observed as well [115, 126]. However, for Al these contacts evolved continuously from a situation with three channels, occurred only very rarely [129], and were immediately destroyed when further pulling the electrodes apart.

In order to go beyond the case of single atom contacts studied in the previous Section, we combine the lithographic and the whisker MCBJ techniques and aim to establish a correlation between the atomic configuration and the transport properties. This procedure is justified by the following facts. First, the comparison of individual opening traces shows the same preferred plateau sequences for both types of samples. Second, the transmission coefficients inferred from the lithographic break junctions with up to two channels (not shown) are in accordance with those found for the whisker break junctions. Now, we have extended our investigation to larger contacts and the analysis of opening traces.

In Fig. 3.14(a) we show two examples of I-Vs measured on a whisker break junction at $T = 0.27$ K and their fits according to the theory of MAR [19, 20] with three and four channels, respectively. The details of the fitting procedure are described in Ref. [115]. The I-Vs are examples recorded on the opening trace shown in Fig. 3.14(b) at the positions indicated in the caption. Although the total conductance of the two contacts is similar (1.37 G_0 and 1.51 G_0, respectively), the I-Vs differ markedly due to the different distribution of transmission coefficients. This example visualizes the possibility to deduce the set of transmission coefficients from the I-Vs. In the following we will use this knowledge for correlating the structure to the transport behavior.

Figures 3.14(b,c) show examples of opening traces recorded on two different whisker MCBJs. In the upper panels the total transmission deduced from the conductance is shown, while in the lower panels the decomposition into individual channels is plotted. The example in Fig. 3.14(b) shows an opening trace with the typical plateaus at 1.4 G_0 (with 4 channels) and 0.5 G_0 (with 2 channels), a re-closure of the contact to 1.5 G_0 (with 3 channels) and a last plateau at 0.6 G_0 (again with 2 channels). Although the overall conductance of the starting configuration and the part with three channels is very similar, the channel analysis clearly shows that another atomic configuration is adopted.

Figure 3.14(c) depicts an example for the other preferred opening sequence with the plateaus at 2.5 G_0 (5 channels) and 1 G_0 (3 channels), with an abrupt rearrangement of channels and reduction from three to one (or two) channels within the last plateau. The opening curve displayed in Fig. 3.14(c) starts with a conductance of 2.5 G_0 distributed among five channels. The conductance drops then to about 1 G_0 accommodated by three channels. The change of the channel configuration to one dominating channel is hardly seen in the total conductance which remains close to 1 G_0 upon further stretching. However, the I-Vs changes markedly, signalling a distinct atomic rearrangement of the narrowest region. Around the electrode distances 2.9 nm and 3.15 nm no stable I-Vs could be recorded because of frequent rearrangements of the contact. For an example of those rearrangements see Ref. [131].

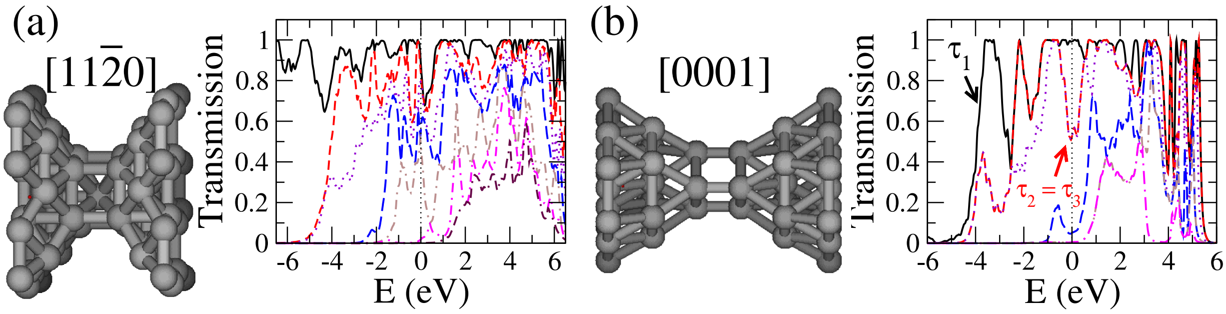

Figure 3.15: (a) A contact grown along the [11$\bar{2}$0] direction with a single central atom and channel transmissions $\{\tau_i\}$ as a function of the energy for this contact. The Fermi energy is set to zero and is indicated with a vertical line. The total conductance is 3.6 G_0 and it is dominated by 5 conductance channels. (b) The same as for (a) for a contact grown in the [0001] direction with a minimum cross section of 3 atoms. The total conductance is 2.1 G_0 with the contribution of 4 channels. Notice that the second and third channels are degenerate at the Fermi energy.

3.3.2.3 Transmission properties of thicker Zn atomic contacts

In order to provide further insight into the origin of the sequence of plateaus described above, we have extended the conductance calculations presented in the previous Section to contacts of a larger cross section. The calculations are performed exactly as described above. The problem that one encounters in the analysis of contacts larger than the single-atom contact is that the number of possible configurations increases rapidly. We therefore restrict ourselves to only two growing directions and perfectly ordered geometries. For a contact grown in $[11\bar{2}0]$ direction the dimer configuration discussed in Fig. 3.12(a) is the only possibility to have a single-channel contact. This is due to the fact that already for the single-atom contact shown in Fig. 3.15(a) next-nearest neighbour-contributions of 4 atoms give rise to 5 transport channels with non-negligible transmission and a total conductance of 3.6 G_0 (see Fig. 3.15(a)). The transmissions of those channels vary between 0.5 and 1. The next larger highly symmetrical contact (not shown here) has 4 atoms in the smallest cross-section with 8 channels. Due to the rather large apex angle the number of relevant atoms and channels increases very fast. A change of the separation of the electrodes (for the perfectly ordered geometries used for the calculations) of 0.2 nm changes the conductance by as much as 2 G_0. Thus, the prediction for this growing direction would be conductance traces with both a rapidly increasing number of channels and rapidly increasing total conductance.

In contrast, for the [0001] direction, starting again with the dimer configuration with a single channel and transmission $\tau = 0.94$, the last but one contact has again one atom in the center of the constriction with one channel and transmission 0.85, as described in Fig. 3.11(b,c). Upon increasing the disorder the contributions of a second and third channel increase. The smallest highly symmetrical contact in this direction with more than one atom in the smallest cross-section is shown in Fig. 3.15(b). It consists of three atoms with 4 to 5 channels and total conductance of 2.1 G_0. From the dimer configuration to this configuration a distance change of more than 0.5 nm changes the conductance by approximately 1 G_0. Since the absolute values of the transmission coefficients depend crucially on the exact atomic configuration, it is again hard to draw conclusions from the analysis of individual opening traces. Nevertheless, when comparing the results of 8 opening traces recorded on 2 whisker MCBJs we find the following trends: The 1.4 G_0 - 0.7 G_0 series gives rise to larger average *transmission* values than the 2.5 G_0 - 0.9 G_0 series. This sounds contradictory at first sight, but reflects the fact that the larger average *conductance* in the 2.5 G_0 - 0.9 G_0 series are achieved by more conductance channels. As can be seen in the lower panel of Fig. 3.14, most of the plateau close to 0.9 G_0 is carried by three channels. In particular contacts with a dominating single channel are more often observed in the 1.4 G_0 - 0.7 G_0 series, in agreement with the calculations for the [0001] direction of Fig. 3.11(b,c). From these considerations we assume the plateau series 2.5 G_0 - 0.9 G_0 to correspond to the $[11\bar{2}0]$ direction while for the 1.4 G_0 - 0.7 G_0 the [0001] direction seems to be applicable. The exact values of the transmission coefficients however differ from the calculated one, presumably because of disorder in the experimental contacts.

3.3.3 Summary

In conclusion, a single-atom or dimer contact of Zn is likely to have a conductance of ≈ 0.7 to 0.9 G_0, depending on its geometry. The histograms for both closing and opening the contacts indicate the importance of different contact geometries. By analyzing individual opening and closing traces we identify two preferred plateau sequences. The analysis of the current-voltage characteristics in the superconducting state suggests different preferred transmissions for those typical plateau sequences. By comparing the experimental findings to our tight-binding calculations for idealized atomic configurations we propose a correlation between the structure and the transport properties of individual contacts.

At the level of atomic contacts, Zn presents conductance properties in-between Al and Au, with one highly transmissive channel and eventually a second and third additional channel. However, unlike Au – which is extremely ductile – Zn shows a high degree of mechanical stability, which is amongst others reflected by a similar opening- and closing traces and histograms. Furthermore, Zn is a superconductor and in general allows for channel analysis of atomic contacts. These feature make Zn an interesting option for an electrode material.

3.4 Bivalent metals: magnesium

In this Section we will present an theoretical and experimental study of the conductance of atomic-sized contacts of magnesium. The experiments we consider here were performed by the group of Prof. Jan van Ruitenbeek at Leiden University.

Using Mechanically Controllable Break Junctions (MCBJ), it was observed that at room temperature the conductance histogram exhibits a series of peaks, which suggests the existence of shell effects. Its periodicity, however, cannot be simply explained in terms of either an atomic or electronic shell effect. It was also found that at room temperature, contacts of the diameter of a single atom are absent. A possible explanation could be the occurrence of a metal-to-insulator transition (MIT) as the contact radius is reduced, in analogy with what it is known in the context of Mg clusters. However, our first principle calculations show that while an infinite linear chain can be insulating, Mg wires with larger atomic coordinations, as in realistic atomic contacts, are always metallic. Finally, at liquid helium temperature our measurements show that the conductance histogram is dominated by a pronounced peak at $1G_0$. This is in good agreement with our calculations based on a tight-binding model that indicate that the conductance of a Mg one-atom contact is dominated by a single fully open conductance channel.

3.4.1 From bulk to atomic clusters

The situation for Mg is at first sight comparable to that of Zn studied in the previous Section: It is a divalent metal with a closed outermost s shell and the electronic configuration [Kr]$3s^2$. Small N-atom clusters of Mg are insulators (just as Zn), with an important gap between HOMO and LUMO and van der Waals type binding for $N \leq 3$ [28]. With increasing cluster size the gap rapidly vanishes for clusters containing more than 18 atoms [29], and bulk Mg shows a strong hybridization of the $3s$ and $3p$ orbitals, again comparable to Zn discussed in Section 3.3.

This is shown in Fig. 3.16, where the DOS of bulk Mg projected on the relevant orbitals

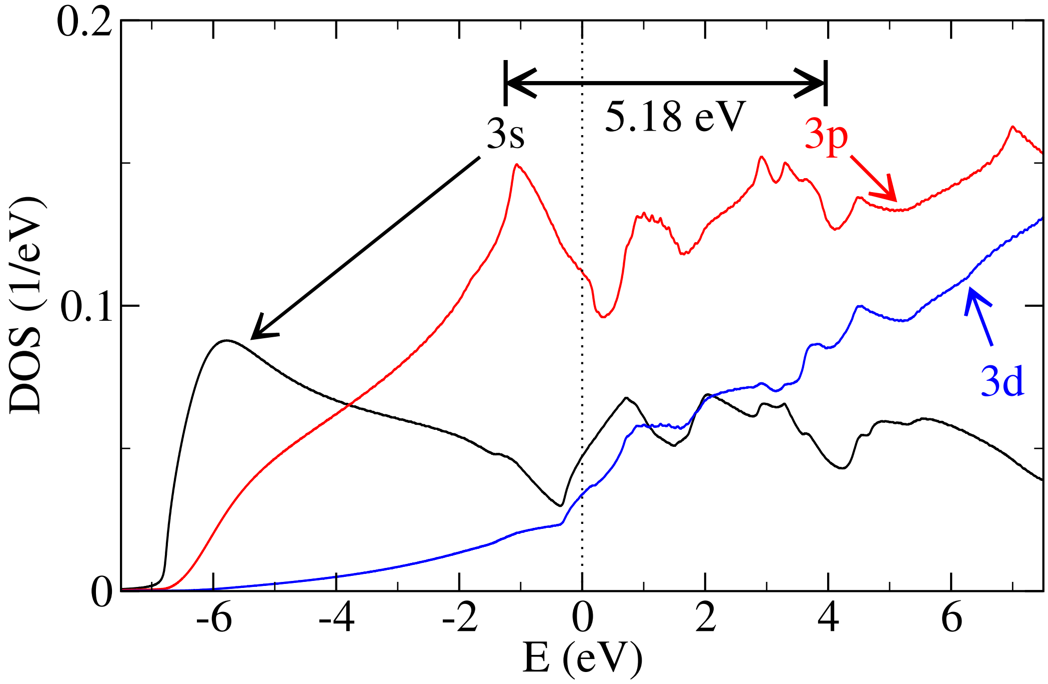

Figure 3.16: Bulk density of states of hcp Mg projected on the s, p, and d orbitals as a function of energy where the Fermi energy indicated with a vertical dotted line is set to zero. The labels indicate the value of the onsite energies of the s and p orbitals. calculated. The Fermi energy is set to 0.

around the Fermi energy is presented. Note that the total DOS shows a $\sqrt{E}$-dependence as expected for free electrons in 3 dimensions. As a consequence of the strong hybridization, bulk Mg is a metal at room temperature with a conductivity of $9\mu\Omega$cm [114].

In point contacts however, there is – similar to clusters – a reduction of the coordination of the atoms and, with it, the hybridization. The first question we want to address here, is whether this reduction is strong enough to induce a MIT for small Mg contacts.

Besides the cross-over from insulating to metallic behavior, cluster experiments also demonstrated a shell structure [132]. One speaks of a shell structure if the mass spectrum shows a periodicity as a function of the radius [133]. The first observation of a shell structure in magnesium clusters was found to be due to the closing of facets and the crystalline arrangement [134]. The hexagonally close pack lattice leads to the periodic occurrence of highly stable icosahedrons. Later experiments performed with magnesium in super-cold helium droplets showed shell structure due to the delocalized electrons showing electronic level bunching [135].

Analogies to cluster shell structures were already found in quantum point contacts of alkali metals [136] and subsequent work showed that these are not limited to this chemical group [137, 138]. For metallic contacts to demonstrate shell structures the atoms require sufficient thermal energy in order to find the local minima in energy. For sodium the necessary temperature for observing the shell effects was found to be around 80 K [139]. Since magnesium has a much higher melting temperature (922 K versus 371 K for Na), one expects the necessary temperature in this case to be of order 200 K. The second question we want to address, therefore, is whether magnesium point contacts demonstrate shell structures at room temperature. The fact that small clusters are insulating, while small contacts have their electronic structure influenced by the leads, makes the comparison between the two manifestations of the shell structures all the more interesting.

In order to investigate Mg contacts experimentally, notched wire MCBJs as introduced in Section 3.3.1.1 were used at both room and liquid helium temperature. Starting with a magnesium wire (purity better than 99.9 %) of 125 μm diameter and about 15 mm length, a small incision is introduced in the middle. Great care is taken to reduce the possible contamination, which is important due to the strong chemical affinity of magnesium to hydrogen [140]. This is achieved by maintaining ultra high vacuum (UHV) of $< 10^{-5}$ mbar and 5×10^{-10} mbar at low and room temperatures respectively. Using a mechanical axis for the coarse movement, the wire is broken at the incision. In this way the two electrodes are formed by freshly exposed surfaces, which is critical for the study of reactive materials such as magnesium.

3.4.2 Experimental results at room temperature

The evolution of conductance when breaking the wire at room temperature has a characteristic that can be seen in the example of figure 3.17 (left panel). An intermittently sudden lowering of the conductance towards zero with stretching of the wire can be observed. Relatively stable intervals or plateaus occur when the mechanical tension on the contact gradually builds up. When this tension is released by a mechanical reconfiguration of the contact, its diameter and conductance are reduced stepwise [16]. The plateaus in conductance appear flat and the jumps during the mechanical reconfigurations are large. This is an indication that some values of conductance are stabilized when they are related to structures with a local minimum in the energy.

In order to verify that these plateaus occur at reproducible values a statistic description by means of a conductance histogram [141] is used. This histogram is constructed by dividing the conductance interval of interest in equal sub-intervals or bins. For each measured data point the corresponding bin is determined, resulting in a probability distribution for the conductance during breaking. An example of such a distribution or histogram for Mg is given in figure 3.17 (right panel).

The result in figure 3.17 indeed shows a series of peaks at higher conductance values. These could indicate the presence of a shell structure, but in order to investigate whether the peaks in figure 3.17 are indeed periodic in the radius one needs to plot the histogram as a function of radius, R. Since the range of conductances in this graph corresponds to the ballistic conduction regime the radius R can be obtained from G via the corrected Sharvin formula

$$G \approx \mathrm{G}_0 \left[\left(\frac{k_F R}{2} \right)^2 - \frac{k_F R}{2} + \frac{1}{6} + \dots \right] \tag{3.11}$$

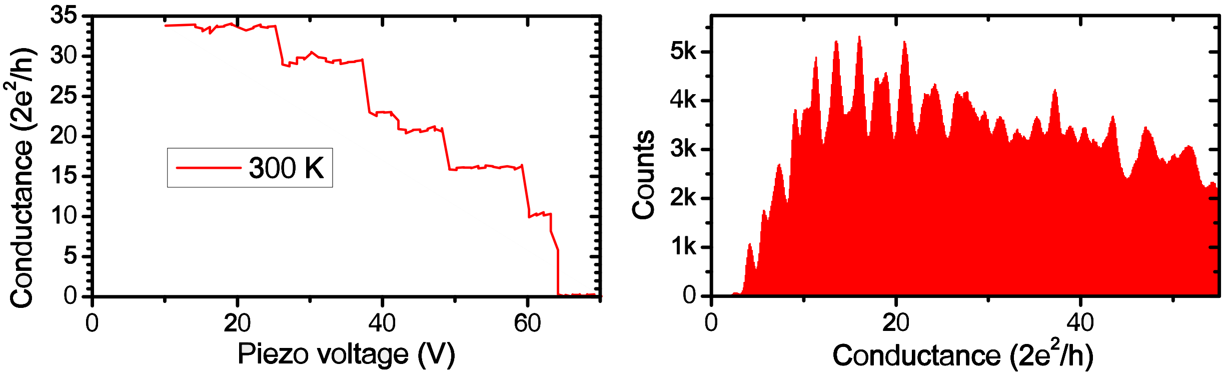

Figure 3.17: The left panel shows the conductance evolution during the stretching of a magnesium contact at room temperature in UHV. The conductance was measured at a bias voltage of 20 mV, but had no significant effect on the shape of the trace. The right panel shows a conductance histogram resulting from 1.2×10^4 of these traces. The resolution of this histogram was set to 10 bins per G_0.

where k_F represents the Fermi wave vector [142, 143].

More than 90% of the measured histograms for all six samples at room temperature show a periodicity in $k_F R$, but the period varies between recordings. This makes it likely that its appearance is related to multiple properties of the metal. The most common and pronounced frequency is 1.7 $(k_F R)^{-1}$. To compare this value to the periodicity expected for shell structure due to atomic packing, one starts from a simple packing model for a close packed hexagonal lattice and increases the contact diameter facet by facet. One then obtains a periodicity of 2.3 $(k_F R)^{-1}$, which is only slightly influenced when considering other crystal structures such as face (body) centered cubic.

Possible electronic shell structures have been studied for metallic point contacts as well. Both, calculations using jellium models [144] and nanoscale free-electron models [145] applied to aluminum point contacts [138] give frequencies up to 1 $(k_F R)^{-1}$. As the frequencies for magnesium are suggested to be the same [145], the shell effect seen in the present experiments is still without satisfactory explanation. A remaining possibility is that the contact is simultaneously governed by competing effects of the atomic packing and the electronic free energy. Similar mixed structures were also found for Mg clusters [146].

Another feature of the histogram in figure 3.17, that is even more remarkable, is the absence of plateaus below 5 G_0. This minimal value is much higher than for all other metals studies with this technique [137, 138, 147]. Below this threshold value only a smooth exponential decrease in conductance was found, typical for tunneling behavior. This is a clear indication that smaller contacts are not stable, leading the contact to break. This behavior can be indicative of a MIT. While reducing the contact radius, the hybridization of the electron states will decrease. The overlap between s and p will therefore decrease, driving the contact towards a metal-insulator transition. When this transition is reached, the metallic bonds are reduced to van der Waals bonds, weakening the contact considerably [146], and producing an early loss of contact.

3.4.3 Theory: infinite wires and one-atom contacts

The numerous results on Mg clusters cannot be simply extrapolated to our problem. Instead we have studied the stability and electronic structure of a series of Mg infinite wires with small coordination numbers, in order to investigate whether low-dimensional Mg structures could be insulating. To this purpose, we have carried out density functional theory (DFT) calculations of wires ranging from the smallest possible coordination, two in the case of a chain, up to 6. In the insets of Fig. 3.18 we show two examples of the configurations of the studied wires. In the upper panel one can see a linear chain, while the lower one shows an infinite wire with a cross section of 3 atoms (coordination number equal 6) grown along the *c*-axis of a hcp bulk structure ([0001] direction) and keeping the bulk relative positions.

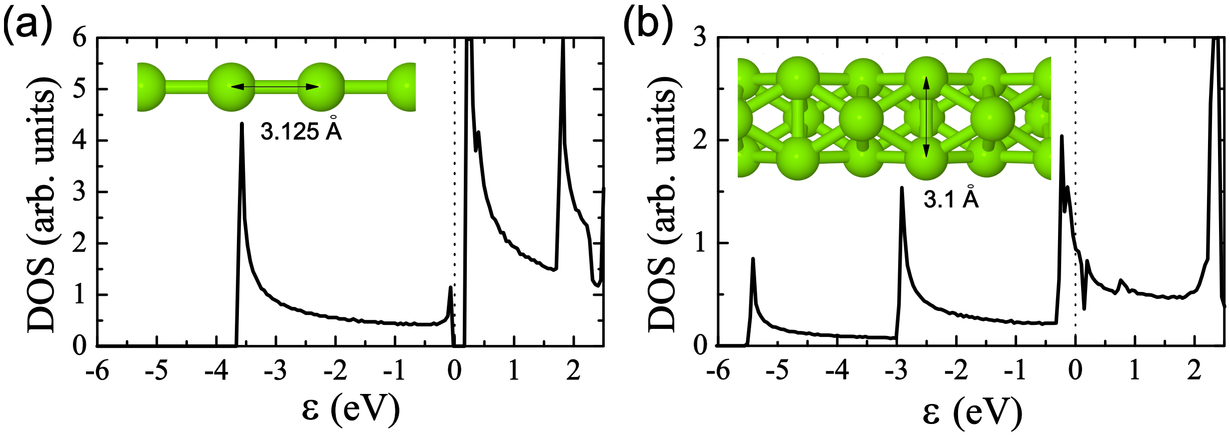

Figure 3.18: Density of states (DOS) of Mg wires calculated with CASTEP [148] for: (a) a linear chain with an optimal inter-atomic distance of 3.125Å; and (b) an infinite wire with a 3 atoms section. The wire is built up along the *c*-axis keeping the bulk symmetry as shown in the inset. The inter-atomic distance that minimizes the total energy is 3.1Å.

For these *ab initio* calculations we have used a standard implementation of DFT [94, 97] with a plane waves basis set and ultrasoft pseudopotentials [149]. The Perdew-Burke-Ernzerhof approach (PBE) [150] has been chosen for the exchange-correlation contribution. The calculations were performed with the CASTEP v4.2 code [148]. The plane wave cutoff used (375 eV) in all our calculations assures well-converged structural and electronic properties. Convergence criteria for the atomic relaxations involved in the different calculations are: 0.01 eV/Å for the mean value of the forces, 0.001Å for the atomic positions and 10^{-6} eV for the total energy. Minimizing the system energy, we have optimized the inter-atomic distances of the wires keeping the original symmetry with a Monkhorst-Pack (MP) $\vec{k}$-sampling mesh of $1 \times 1 \times 64$ [151]. The density of states (DOS) has been calculated with a mesh of 1 × 1 × 1024.

Turning to the results, in the two systems shown in Fig. 3.18, we have found inter-atomic distances of 3.1Å, slightly smaller than the bulk value of 3.2Å. This is in accordance with calculations of Mg clusters [146]. In Fig. 3.18a we show the DOS of the linear chain for the optimized inter-atomic distance.[10] A small gap of 0.3 eV is observed; consequently the linear chain does not show metallic behavior. However, even for this wire with the lowest coordination number, the broadening due to the 3*s*-3*p* hybridization has nearly closed the gap. Indeed, we have found that all the wires with larger coordination than the linear chain are metallic. The DOS of a wire with a cross-section of 3 atoms is shown in Fig. 3.18(b) and does not exhibit any gap. In fact, up to 5 different bands cross the Fermi level. We have investigated whether the application of some additional stress could modify these results, but we have found that even increasing the inter-atomic distances by 10%, the wires remain metallic. So, in short, from this analysis we do not expect the formation of insulating Mg wires in the last stages of the breaking of Mg contacts.

The results above show that low-coordinated Mg structures are energetically stable, which suggests that the formation of few-atom contacts might be possible – at least at low temperatures. Since these structures are moreover metallic, the following question arises naturally: What is the expectation for the linear conductance of the smallest imaginable Mg contacts? In order to answer this question we have computed the conductance of Mg one-atom contacts within the Landauer formalism. For this purpose, we have combined the tight-binding parametrization of Ref. [109] with non-equilibrium Green's functions techniques as described in Chapter 2 and applied in the preceding Sections.

We now turn to the analysis of the results for the linear conductance of some ideal, and yet plausible, one-atom geometries. They have been chosen to simulate the behaviour at the last conductance plateau before the rupture of the nanowires. In the inset of Fig. 3.19(a) we show an example of an one-atom contact grown along the [0001] direction (*c*-axis) which contains a dimer in its central part. Different molecular dynamics simulations of atomic contacts of various metals have suggested that this type of geometry is realized very frequently at the last plateau [77, 112, 120]. This particular geometry is constructed starting with the dimer and choosing the nearest-neighbours in the next layers. Finally, the leads are modeled as infinite surfaces grown along the same direction [yellow atoms in the inset of Fig. 3.19(a)]. In this ideal case, all inter-atomic distances are fixed to their bulk values, which is justified by the ab initio calculation of Mg clusters [146] and our results for infinite wires presented above. The total transmission and the individual transmission coefficients, τ_i, for this contact are shown in Fig. 3.19(a) as a function of energy. First it can be noted that the system is metallic, in accordance with our expectations based on the DFT results described above. Furthermore, the conductance, i.e. the transmission at ε_F, is very close to $1G_0$ and completely dominated by a single fully open channel. The second and third

---

[10] We have studied the stability of the linear chain allowing the 4 atoms of the supercell to relax starting form a zig-zag configuration. For cell lengths larger than 10.5Å the final configuration is a lineal chain slightly distorted, with a energy minimum corresponding to an inter-atomic distance of 3.125Å and a zig-zag angle of 177^o. The stable solution for smaller supercell lengths is a compressed zig-zag chain where the atoms have 4 nearest-neighbours with an inter-atomic distance of 3.1Å.

channels, which are degenerate due to the symmetry of the contact, have transmissions below 10^{-3}. One can get a deeper insight into these results and, in particular, into the nature of the conductance channels, by analyzing the local density of states projected onto the different orbitals of the two central atoms (not shown here). Such analysis indicates that the dominant channel is formed by a symmetric (bonding) combination of the s and p_z orbitals of the central atoms (z is the transport direction), while the p_x and p_y orbitals are responsible for the second and third channels. A fourth channel, which in this case has a transmission below 10^{-5}, is formed by the antisymmetric combination of the s and p_z orbitals. Such anti-bonding combination is basically orthogonal to incoming states (from the leads) and therefore does not contribute significantly to the transport. In short, these results resemble very much the behaviour of Zn one-atom contacts discussed in Section 3.3.1, and also the case of the final stages of the last plateau of Al contacts [25, 115]. This is, after all, quite reasonable since in all these cases the electronic structure at the Fermi energy is governed by s and p orbitals.

Since the growth direction of the Mg atomic contacts is not exactly known, we have studied the conductance of geometries with different crystallographic orientations. In Fig. 3.19(c) we show another example of a dimer contact, but this time grown along the $[11\bar{2}0]$ direction (a-axis). Notice that the total conductance and the transmission coefficients are similar to those of the [0001] case, the main difference being the larger values for the second and third channels and the lifting of their degeneracy. While the lack of degeneracy reflects the lower symmetry of the contacts in $[11\bar{2}0]$ direction, the larger transmission values can be attributed to the larger apex angle of those contact geometries and in consequence a stronger coupling of the dimer atoms and next layers.

In principle, the contact geometries should be determined from molecular dynamic simulations, but computationally this is very demanding. Instead, and in order to test the robustness of our results, we have studied the role of disorder in the atomic positions. For this purpose, starting from the ideal geometries of Fig. 3.19(a) and (c), we have changed randomly the positions of the atoms in the constriction region (those highlighted in brown in Fig. 3.19(b) and (d)) with a maximum amplitude of ±5% of the nearest-neighbour distance. Then, we have computed the total transmission and the transmission coefficients of the disorder geometries. The results are shown in form of histograms in Fig. 3.19(b) and (d). As one can see, in both cases the conductance is still dominated by a single channel that is almost fully open. Therefore, these results confirm our basic conclusion, namely the fact that a Mg one-atom contact is expected to have a conductance close to $1G_0$ dominated by a single channel.

3.4.4 Experimental results at low temperature

In order to verify the theoretical prediction for the conductance of atomic contacts experimentally, we repeated the experiments of Section 3.4.2 at low temperatures. Here we broke the contact by ramping the piezo element continuously with a speed of 1.8×10^3 V/s (corresponding to 1.0×10^2 nm/s electrode separation, a factor 3 faster then for the experiments on Zn in Chapter 3.3.2). This resulted in traces as the one shown in figure 3.20 (left panel).

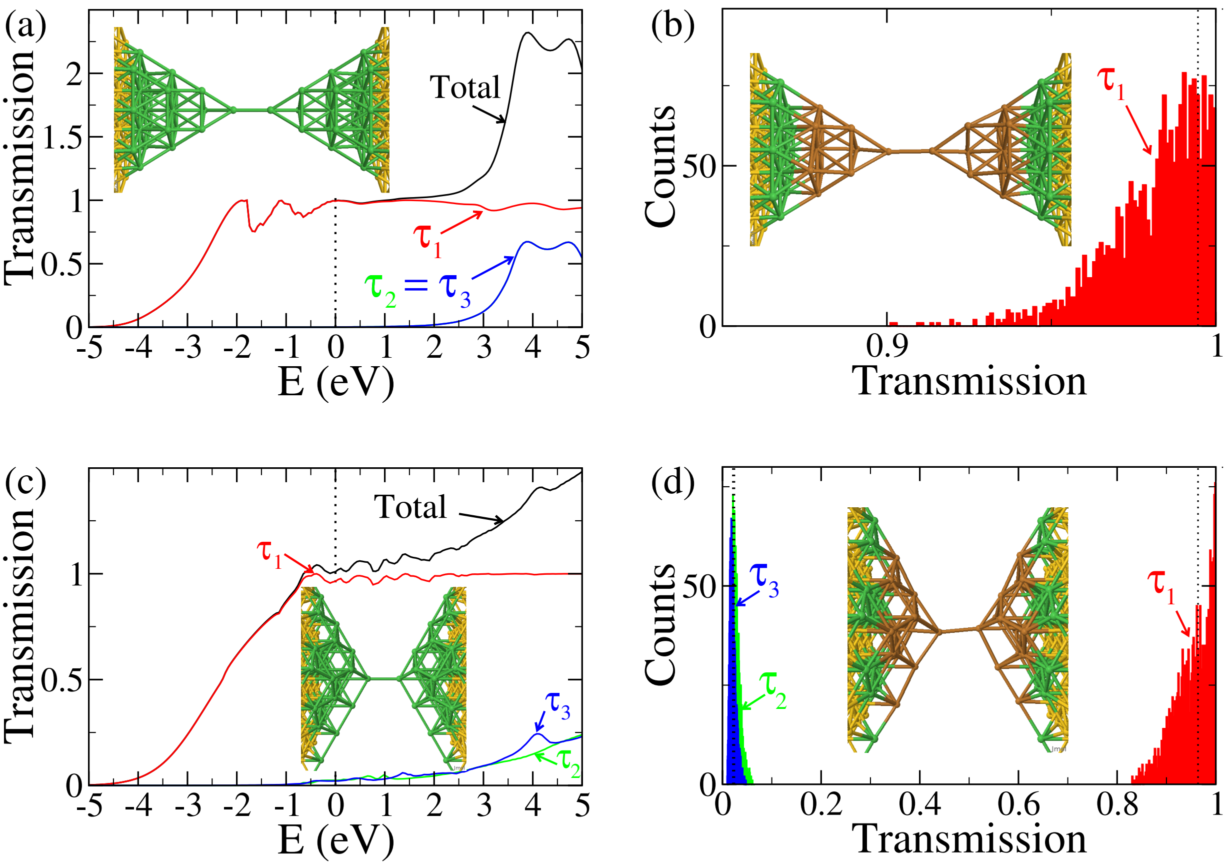

Figure 3.19: (a) Total transmission and transmission coefficients as a function of energy for the contact shown in the inset. This geometry is grown along the [0001] direction (c axis), it contains a dimer in its central part and the inter-atomic distances are fixed to the bulk values. The yellow atoms correspond to atoms in the semi-infinite surfaces that are used to model the leads. The transmission coefficients at the Fermi energy (set to zero and indicated with a dotted vertical line) are $\tau_1 = 0.993$, $\tau_2 = \tau_3 = 0.76 \times 10^{-3}$ and the total conductance is $\sim 0.995 G_0$. (b) Histograms of the transmission coefficients for 2000 disorder realizations (see text) of the one-atom contact shown in the inset of panel (a). The brown atoms are those which have been randomly displaced. The vertical dotted lines indicate the values of the transmission coefficients for the ideal geometry. The transmission values of the second and third channels remain below 2×10^{-3}. (c) The same as in panel (a), but for the contact grown along the $[11\bar{2}0]$ direction (a-axis) shown in the inset. The total conductance is $\sim 1.01 G_0$ with $\tau_1 = 0.9640$, $\tau_2 = 0.024$, $\tau_3 = 0.021$ and $\tau_4 = 0.3 \times 10^{-3}$. (d) The same as in panel (b) for the contact in the inset of panel (c).

The plateaus in conductance appear more structured and the jumps during the mechanical reconfigurations are smaller than those measured at room temperature. In the histogram, presented in figure 3.20, this results in a flat distribution at higher conductance values.

The shell structures found at room temperature are thus absent at low temperatures, as expected.

When focusing on the trace at low conductance values, the staircase of plateaus indeed continues down to values below 5 G_0. The histogram, the shape of which was reproduced over a set of ten different samples, shows its lowest conductance peak close to 1 G_0. For a minority of the histograms a shoulder down to values as low as 0.8 G_0 is seen. In rare cases this shoulder even grows to form the primary peak. Although the conductance does not reveal information on the individual values τ_i of transmission of the electron states, the strong asymmetry and the closeness of the peak to 1 G_0 do suggest that its conductance is given by only one, almost fully opened, channel. For multiple channels the value of 1 G_0 would not form a fundamental limit.

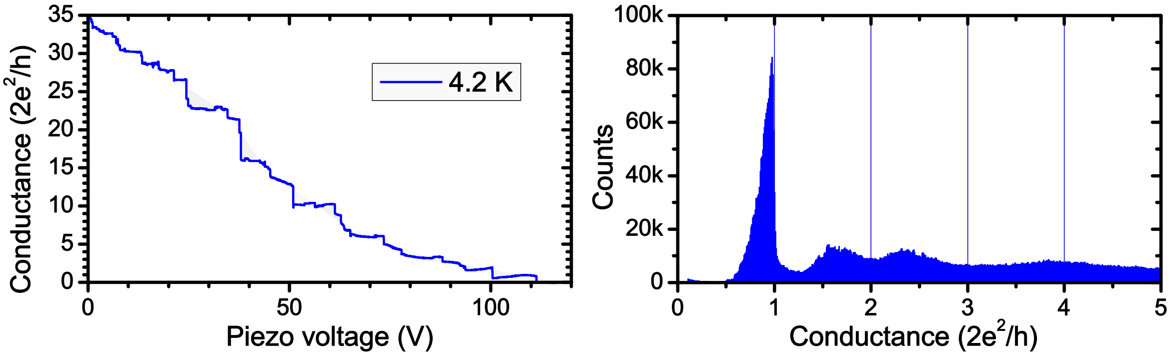

Figure 3.20: Figure comparable to figure 3.17, but for a measurement performed at liquid helium temperature. The left panel shows the conductance evolution measured at a bias voltage of 100 mV. The right panel shows a conductance histogram resulting from 3×10^3 of these traces. The resolution of this histogram was set to 115 bins per G_0.

This result agrees with our calculations, where single-atom contacts of Mg are connected to bulk-like electrodes. Therefore the properties of Mg at low temperatures are very close to the results for Zn discussed in Section 3.3.1. The most noticeable differences are the absence of data points between 0.5 G_0 and tunneling and the higher relative intensity of the peak close to 1 G_0 in the case of Mg. The presence of this peak indicates that the instability of small point contacts at room temperature is not related to a metal to insulator transition.

In conclusion, magnesium contacts at room temperature demonstrate shell effects at multiple frequencies. The most frequent and intense frequency of 1.7 $(k_F R)^{-1}$ did not match with either the expected frequency for atomic packing or the previously calculated frequencies for electronic shell structures. This value therefore remains without satisfactory explanation. A possibility is that both effects play an important role at the same time.

The histograms at low temperatures exhibit a first peak close to 1 G_0. The strong asymmetric shape of the peak, with a minimum weight above 1 G_0 suggests this conductance to be dominated by a single channel. Our calculations confirm this and identify this channel to be a symmetric combination of the s and p_z orbital of the central Mg atom. This behavior is similar to the results obtained for Zn in Section 3.3.1, although the tendency for the channel to be fully open is stronger.

At room temperature contacts with a diameter corresponding to a single atom are absent. The instability of these smaller contacts is not caused by a metal to insulator transition at lower coordination. From the appearance of the peak at 1 G_0 at low temperatures, we can conclude that the metal-insulator transition is absent even in the smallest of contacts. Although our calculations indicate that a one-dimensional infinite chain for Mg should be an insulator, the coordination of the atoms in a realistic contact at low temperatures are too high for observation of a MIT.

3.4.5 Limit of thick contacts

So far we only considered thin infinite wires or atomic contacts of Mg. However, the total DOS of Mg shown in Fig. 3.16 indicates a free electron behaviour with an energy dependence of the DOS like $\sqrt{E}$. On the other hand the semi-classical Sharvin formula 3.11 is based on free electrons passing a circular orifice. Here we are interested in how the conductance behaves for contacts with increasing radius R and whether we can approach the regime where Sharvin formula is valid.

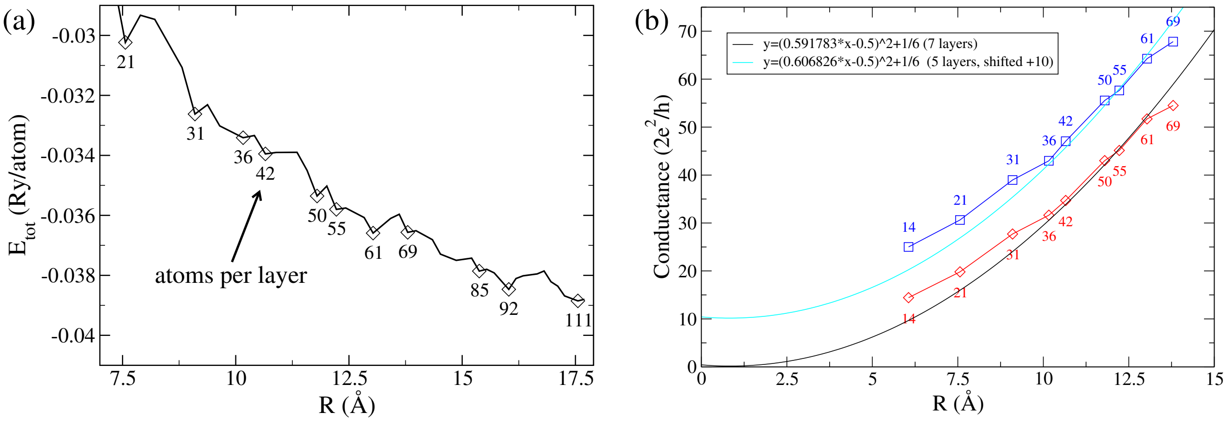

Figure 3.21: (a) Total energy calculated within the NRL approach for regular wires with atoms on lattice sites and increasing number of atoms per layer as a function of the wire radius. (b) Conductance of pieces of the wires considered in (a) containing 5 and 7 layers between ideal surface. Fit: Sharvin formula for ideal wires of free electrons as a function of wire radius (assuming Fermi momentum k_F fixed).

The electronic structure of atomic contacts and wires depends crucially on details of the geometry. In order to obtain – out of the innumerable possible configurations – a series of comparable wires and contacts, we fix the allowed atom positions to the hcp lattice sites that bulk Mg exhibit. Then we construct a series of wires along the [0001] direction with increasing radius R, with all the atoms of the wire lying within R around the [0001] axis through the origin. In this way we can classify the different wires according to their radius. The second simplest geometry (after a zig-zag wire) corresponds to the one discussed in Fig. 3.18(b) with three atoms per layer.

For this set of infinite wires – with the nearest neighbour distance fixed to the bulk value – we calculate the total energy per atom of the layer using the TB parametrization of [109] as above. According to the construction of the TB parametrization, the total energy is related to the coordination of the atoms in the layer. Thus, for instance, a wire geometry in which many atoms of the layer have dangling bonds will show a higher total energy per atom than a geometry where all atoms are highly coordinated. In this sense we can identify the highly coordinated geometries as the one with a relative minimum in the total energy per atom.

This curve is shown in Fig. 3.21(a) for the full set of infinite wires. We marked with a diamond the geometries that we identified to show a local energy minimum. In a second step we determine the conductance of thick contacts constructed out of that set of selected wires. For each of the wires from the selection we take a finite number of layers, place them between ideal surfaces, and calculate the linear conductance of the so-constructed with Eq. (2.76). In Fig. 3.21(b) is plotted the conductance as a function of the contact radius for the series of thick contacts containing five or seven layers of the selected wire geometries.[11] In a naïve picture we would expect the Sharvin formula Eq. (3.11) to hold in the limit of thick contacts. Therefore we fitted in Fig. 3.21(b) the conductance with it and observe an approximate R^2 dependence of the conductance. Generally the thicker contacts fit better. From the fit assuming a fixed Fermi momentum k_F for all the contacts, we extract the value $k_F \approx 0.6\text{Å}^{-1}$.

For ballistic but thick atomic contacts ($G \approx 40G_0$) we find that the Sharvin formula yields a good approximation for the conductance and derive a Fermi wavelength of $k_F \approx 0.6\text{Å}^{-1}$.

3.5 Conclusion

In this Chapter we discussed the conduction properties of non-magnetic atomic metal contacts. We applied the NRL TB parametrization consistently for all studied materials. For atomic contacts of example metals we can reproduce the established close connection between chemical valency and the conduction properties of the corresponding single atom contacts. Furthermore we compared the example case of Al atomic contacts with an *ab initio* DFT calculation and find good overall agreement.

Applied to the limiting case of the bivalent elements Mg and Zn, we find metallic conduction properties at the limit of atomic contacts, in agreement with experimental findings at low temperature.

---

[11] The conductance of the contacts with five layers was shifted upwards by 10G_0 for clarity.

In particular, for Zn we can compare directly to experiments that determine the conductance channels. In agreement with them we find that at the level of single atom contacts, the s and p bands already hybridize and give rise to one dominating channel at ε_F, with a second and third contributing eventually. These conduction properties lie in-between what is typically observed in single atom contacts of Au and Al. For thicker atomic contacts we can predict conductance sequences for evolution of contacts along preferred crystallographic directions and thus associate typical steps in the experimental conductance traces with crystallographic directions. Finally, due to the mechanical stiffness at the atomic scale and the superconducting properties at low temperatures, Zn may be an interesting electrode material.

For Mg, insulating behaviour with a small gap at ε_F is only found for the ideal single-atom chain. Therefore it seems improbable that a MIT accounts for the abrupt truncation of room temperature conductance traces at high conductance values. For single-atom contacts at low temperature however we predicted metallic behaviour with one nearly open conductance channel for both investigated contact directions. This is confirmed by conductance traces recorded at 4.2 K, which typically show a conductance plateau at $1G_0$ before breaking and yield a pronounced peak at $1G_0$ in the conductance histogram.

We conclude that for nonmagnetic atomic metal contacts the NRL TB description is a reasonable approximation. In the following we will expand this description to ferromagnetic metals, where the spin degeneracy is lifted by the exchange field.

Chapter 4

Conduction properties of ferromagnetic metallic atomic contacts

In this Chapter we analyze the conduction properties of atomic contacts of the ferromagnetic $3d$ materials Fe, Co, and Ni. We employ the spin-polarized version of the TB model discussed in Sec. 2.1.4 and we first focus in the analysis of ideal contact geometries. In agreement with the previous theoretical results for transition metals, the $3d$ bands of these metals play the key role in the electrical conduction of atomic contacts. As a consequence, in the contact regime there are partially open conductance channels and the conductance of the last plateau is typically above the quantum of conductance $G_0 = 2e^2/h$. Furthermore, in this regime there is no complete spin polarization of the current (i.e. both spin bands contribute to transport) and the amplitude of the conductance as well as its spin polarization are very sensitive to disorder in the contact geometry. Finally, we find that in the tunneling regime a high spin polarization of the current can be achieved.

In the second part of this Chapter we will analyze the conduction properties of Ni atomic contacts more statistically. For this purpose we combine the TB model for the electronic structure with a molecular dynamics (MD) simulation of the evolution of the contact geometry during elongation. In this way we have at the same time access to the electrical and mechanical properties of the contact during the evolution. From this information we derive histograms of the conductance [and also the minimal cross Section (MCS)], which can directly be compared to experimental findings.

This Chapter is organized as follows: In the first part, Sec. 4.1, we consider ideal contact geometries (and perturbations on them). In Sec. 4.1.1 we first analyze the results of the conductance of representative one-atom thick contacts of Fe, Co, and Ni. Then, in Sec. 4.1.2 we focus on the conductance in the tunneling regime. Finally, in Sec. 4.1.3 we discuss the influence of atomic disorder on the conductance of single-atom contacts. In the second part, Sec. 4.2 we combine the NRL TB calculation of the electronic structure with a molecular dynamics (MD) simulation of the evolution of an atomic contact of Ni during elongation. In particular we discuss the conduction properties during the evolution of an example contact in Sec. 4.2.2 and in Sec. 4.2.3 we derive a conductance histogram from a collection of different contact evolutions. We end this Chapter with a short conclusion.

4.1 Conduction properties of ideal atomic contacts of ferromagnetic metals

In the last years a lot of attention has been devoted to the experimental [22, 34, 36–55, 152–154] and theoretical [56–68, 155–159] analysis of contacts of the 3*d* ferromagnetic materials. In particular, several experimental groups have analyzed conductance histograms of these materials. Basically, two contradictory results have been reported. On the one hand, several groups have observed peaks in the conductance histogram at half-integer multiples of G_0 [42–47]. This has been interpreted as a manifestation of half-integer conductance quantization [45], implying that only fully open channels contribute to the conductance. In this sense, a peak at $0.5G_0$ would then additionally mean the existence of a full spin polarization of the current. Furthermore, some authors have reported conductance histograms that are very sensitive to an external magnetic field [40].

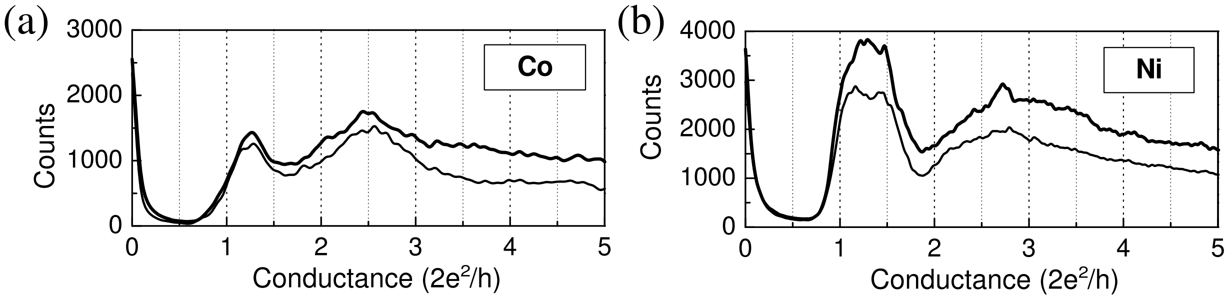

Figure 4.1: (a,b) Experimental conductance histograms for Co and Ni measured under cryogenic vacuum conditions. The histograms with thick lines were obtained when an external magnetic field of 5 T was applied, the thin lines refer to the case with no external field. The graphs are taken from [48].

On the other hand, Untiedt *et al.* [48] have measured the conductance for atomic contacts of the 3*d* ferromagnetic metals (Fe, Co, and Ni) using break junctions under cryogenic vacuum conditions (see Fig. 4.1). Contrary to the experiments mentioned above, they have reported the absence of fractional conductance quantization, even when a high external magnetic field was applied. Instead, they observe conductance histograms that show broad peaks above $1G_0$, with only little weight below it, which is generally expected for transition metals [22, 160].

In order to resolve the contradiction of the experimental results about the existence of half-integer conductance quantization, several authors have already investigated theoretically the electronic structure and conductance of nanocontacts of the 3*d* ferromagnetic metals. Most of the work has been focused on the accurate *ab initio* description of the electronic structure of ideal systems [57, 58, 61, 62, 64–66, 68, 157, 159]. In the case of monatomic wires, different aspects such as the influence of a domain wall on the electronic structure [57], the effect of electronic correlations [61] or the magnetic properties [63] have been discussed. The conduction properties of ideal atomic-contact geometries have also been investigated both with *ab initio* methods [62, 64–66, 68, 157, 159] and TB models for the case of Fe atomic contacts and wires [67, 161]. Based on these studies, one would not expect either conductance quantization or full spin polarization in ferromagnetic atomic contacts.

Here we focus on the conduction properties of ideal atomic contacts of the $3d$ ferromagnetic materials (Fe, Co, and Ni). Our goal is to provide further insight into basic issues such as the orbitals relevant for the electron transport, the role of atomic disorder, the dependence of the spin polarization of the current on the contact geometry, and the main differences between these three materials. For this purpose, we have analyzed ideal geometries of few-atom contacts, assuming them to form a single magnetic domain. To describe the electronic structure, we use the spin-polarized TB model discussed in Sec. 2.1.4. The conductance can then be calculated as described in Sec. 2.2.2.

In contrast to the non-magnetic materials discussed in the previous Chapters we now need to take into account spin σ explicitly (where $\sigma =\uparrow / \downarrow$ refers to the majority/minority spin). We consider a ferromagnetic contact within a single domain, where all spins are aligned. In this case the spin degeneracy is lifted, but the Hamiltonian remains diagonal in spin space [cf. Eq. (2.1)]:

$$\hat{\mathbf{H}} = \sum_{ij,\alpha\beta,\sigma} [\mathbf{H}]_{i\alpha,j\beta,\sigma} \, \hat{c}^{\dagger}_{i\alpha,\sigma} \hat{c}_{j\beta,\sigma} \ . \tag{4.1}$$

Then the zero-bias conductance is given by:

$$G = G_{\uparrow} + G_{\downarrow} = \frac{e^2}{h} \left[\tau_{\uparrow}(\varepsilon_F, 0) + \tau_{\downarrow}(\varepsilon_F, 0) \right] \ , \tag{4.2}$$

where G_σ for the electrons with spin $\sigma =\uparrow, \downarrow$ are the partial conductances. The total transmission per spin τ_σ is the sum of the transmission channels as in the non-magnetic case: $\tau_\sigma = \sum_n \tau_{n,\sigma}$. We can measure the polarization of the current with:

$$P = \frac{G_{\uparrow} - G_{\downarrow}}{G_{\uparrow} + G_{\downarrow}} \times 100\% \ , \tag{4.3}$$

which generally differs from zero for ferromagnets.

By combining the TB model with independent structural simulations, we can address important issues presently out of the scope of *ab initio* approaches, such as the interplay between mechanical and electronic properties in conductance histograms. This will be discussed in the second part of this Chapter. Here we focus on general conduction properties of the ferromagnetic atomic contacts and we will mainly consider ideal contact geometries. However we test the robustness of our conclusions by studying the influence of variations in the atomic positions on the conductance. These are modeled with random disorder in the ideal geometries.

The results of our calculations for the three materials can be summarized as follows: Due to the partially open conductance channels of the minority spin electrons there is in general no conductance quantization and the conductance of the last plateau has a value typically above $G_0 = 2e^2/h$. In the contact regime both spin species contribute to the transport and the current is never fully spin polarized. Furthermore, the value of the conductance and the current polarization are very sensitive to the contact geometry and disorder. The origin of all these findings can be traced back to the fact that the d bands of these transition metals play an important role in the electrical conduction. Finally, we find that in the tunneling regime, which is reached when the contacts are broken, the nature of the conduction changes qualitatively. In this case almost fully spin-polarized currents are indeed possible.

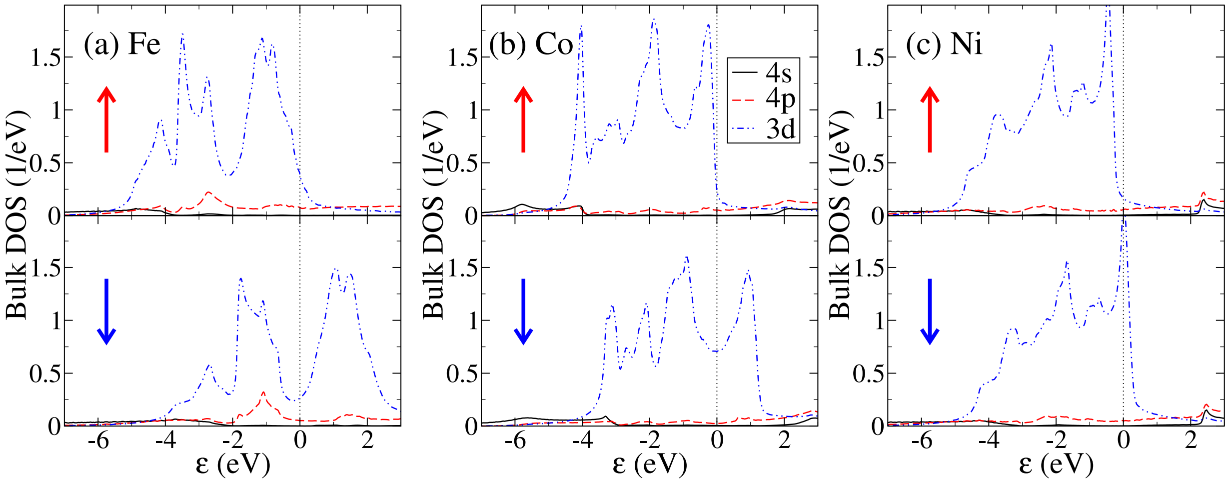

Figure 4.2: Bulk density of states (DOS) of Fe, Co, and Ni, resolved with respect to the individual contributions of $3d$, $4s$, and $4p$ orbitals, as indicated in the legend. Furthermore, the upper panels show the DOS for the majority spins and the lower ones the DOS for minority spins. The Fermi energy is set to zero and it is indicated by the vertical dashed line.

4.1.1 Conductance of ideal single-atom contacts of Fe, Co, and Ni

The goal of this Section is the analysis of the conductance of ideal, yet plausible one-atom contact geometries for the three ferromagnetic metals (Fe, Co, and Ni) considered in this work. In order to understand the results described below, it is instructive to first discuss the bulk density of states (DOS). The spin- and orbital-resolved bulk DOS of these materials around ε_F, as calculated from our TB model, is shown in Fig. 4.2. The common feature

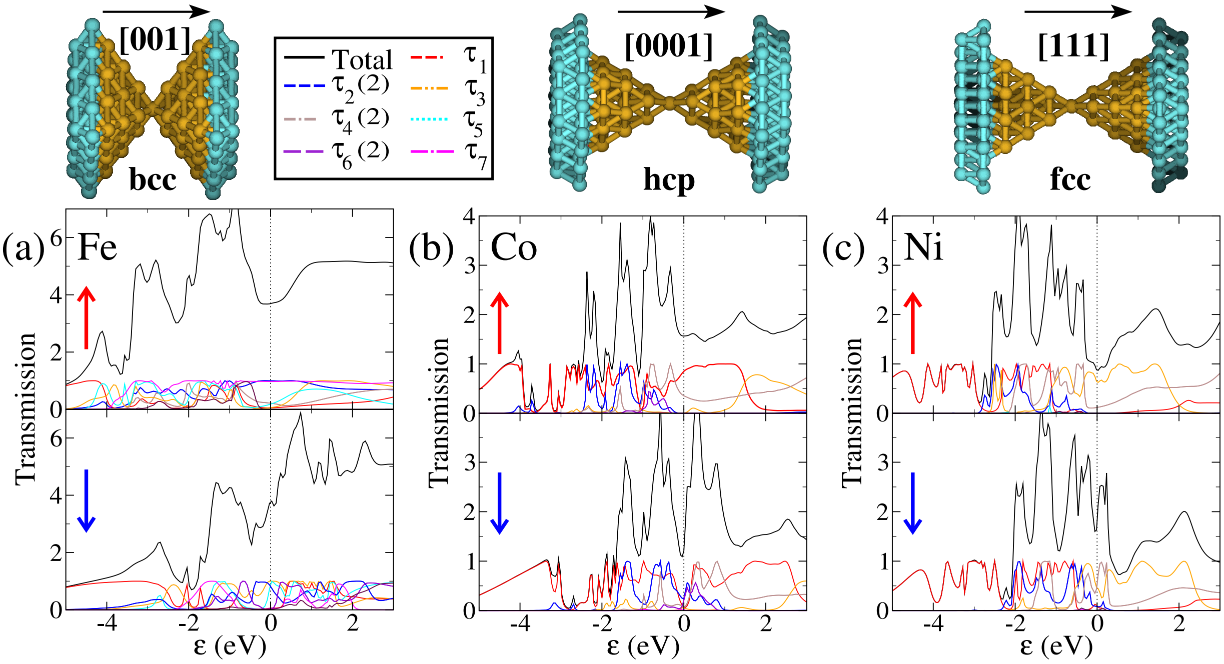

Figure 4.3: Transmission as a function of energy for the three single-atom contacts of (a) Fe, (b) Co, and (c) Ni, which are shown in the upper panels. We present the total transmission (black solid line) for both majority spins and minority spins as well as the transmission of individual conductance channels that give the most important contribution at Fermi energy, which is indicated by a vertical dotted line. The blue, brown, and violet dash-dotted lines of τ_2, τ_4, and τ_6 (even channels) refer to twofold degenerate conductance channels. The legends in the upper graphs indicate, in which direction the contacts are grown. These contacts contain in the central region 59 atoms for Fe, 45 for Co, and 39 for Ni. The blue atoms represent a part of the atoms of the leads (semi-infinite surfaces) that are coupled to the central atoms in our model.

for the three ferromagnets is that the Fermi energy for the minority spins lies inside the d bands. This fact immediately suggests [21, 25] that the d orbitals may play an important role in the transport. Occupation of the s and p orbitals for both spins is around 0.25 and 0.4 electrons, respectively. For the majority spins the Fermi energy lies close to the edge of the d band. The main difference between the materials is that for Fe there is still an important contribution of the d orbitals, while for Ni the Fermi level is in a region where the s and p bands become more important. The calculated values of the magnetic moment per atom (in units of the Bohr magneton) of 2.15 for Fe, 1.3 for Co, and 0.45 for Ni are reasonably close to literature values [114].

We now proceed to analyze in detail the conductance of some ideal one-atom geometries, which are chosen to simulate what happens in the last conductance plateau before the breaking of the nanowires. First, we consider the one-atom contacts shown in the upper panels of Fig. 4.3. These geometries are constructed starting with a single atom and choosing the nearest neighbours (NN) in the next layers of the ideal lattice along the direction indicated with an arrow, similar to the geometries used for the discussion of ideal non-magnetic contacts in Fig. 3.4. In the case of Fig. 4.3, for Fe (bcc lattice with a lattice constant of 2.86 Å) the contact is grown along the [001] direction, for Co (hcp lattice, lattice constant 2.51 Å) along the [0001] direction (parallel to "c axis") and for Ni (fcc lattice and lattice constant 3.52 Å) along the [111] direction. The number of atoms in the central region has been chosen large enough, such that the transmission does not depend anymore on the number of layers included. Moreover, as explained in the previous Section, the central region is coupled seamlessly to ideal surfaces grown along the same direction.

Let us start describing the results for the Fe one-atom contact of Fig. 4.3(a). There we present the total transmission for majority spins and minority spins as a function of energy as well as the individual transmissions. We find for this particular geometry the spin-resolved conductances $G_\uparrow = 3.70e^2/h$ ($\uparrow$ for majority spins) and $G_\downarrow = 3.75e^2/h$ ($\downarrow$ for minority spins), which results in a total conductance of $3.7G_0$. The conductance $G_\uparrow$ for the majority spins is the result of up to 8 open channels (with a transmission higher than 0.01), while for the minority spins there are 11 channels giving a significant contribution to $G_\downarrow$. The large number of channels and consequently the high conductance, are partially due to the large apex angle of 71° of the pyramids. As a consequence of this, the layers next to the central atom couple to each other and give rise to a significant tunneling current that proceeds directly without traversing the central atom. On the other hand, the larger number of channels for the minority spins is due to the key contribution of the d orbitals that dominate the transport through this spin species, while for the majority spins the s and p orbitals are the more relevant ones. This fact, which is supported by the analysis of the local density of states (not shown here), is a simple consequence of the position of the Fermi energy and the magnitude of the spin splitting (see discussion of the bulk DOS above).

With the definition 4.3 of the spin polarization P of the current we find a value of $P = -0.7\%$ for the Fe one-atom contact of Fig. 4.3(a). In order to compare to the polarization of bulk we have calculated the transmission at the Fermi energy for a series of contact geometries where a bar of constant diameter bridges the two lead surfaces. When the diameter of the bar (or central region of the contact) is increased, the polarization grows continuously and saturates at a value of $P = +40\%$ for a contact containing 219 atoms in 7 layers. This is in good agreement with a simple estimate from the ratio of the bulk DOS for $\sigma = \uparrow, \downarrow$ at ε_F and the experimental value for P obtained using normal-metal-superconductor point contacts [162]. Notice that P can be quite different in an atomic contact as compared to bulk. This is because the conductance is not simply controlled by the DOS at the Fermi energy, but the precise coupling between the orbitals in the constriction plays a crucial role.

For the Co contact depicted in Fig. 4.3(b) the transmission is lower than for Fe, partly due to the smaller apex angle of the hcp pyramids. In this case we find $G_\uparrow = 1.57e^2/h$ for majority spins and $G_\downarrow = 1.21e^2/h$ for minority spins, summing up to a total conductance of $1.4G_0$. There are 3 channels contributing to $G_\uparrow$ and 8 channels to $G_\downarrow$. As in the case of Fe, the larger number of channels for the minority spins is due to the position of the Fermi level and the resulting contribution of the d orbitals for this spin. We also find that there is a small but non-negligible contribution of channels that proceed directly without crossing the central atom. This explains, in particular, why one has 8 channels for the minority spins, although at most 6 bands (s and d) have a significant DOS at this energy. Turning to the current polarization, we find a value of $P = +13\%$ for the Co one-atom contact. We also calculate the polarization for a series of Co bars with increasing diameter in hcp [0001] direction. As the diameter increases, the polarization decreases to a value of $P = -41\%$ for a contact containing five layers of 37 atoms each, again in good agreement with the experiment [162] and the estimate from the bulk DOS. Notice again that not only the magnitude of P for a one-atom contact can be quite different from bulk, but also its sign can be the opposite.

Finally, the Ni contact shown in Fig. 4.3(c) exhibits conductances of $G_{\uparrow} = 0.85e^2/h$ for majority and $G_{\downarrow} = 1.80e^2/h$ for minority spins, adding up to a total conductance of $1.3G_0$. The $G_{\uparrow}$ consists of 3 channels, due to the contribution of the s and p orbitals, and $G_{\downarrow}$ contains 6 channels, which originate from the contribution of the d orbitals. In this case we find a value for the polarization of $P = -34\%$. Once more we have investigated the polarization of bulk Ni in a series of large Ni bars in fcc [111] direction. Interestingly, the polarization decreases from $P = +3\%$ for a contact of 28 atoms in four layers to $P = -41\%$ for a contact consisting of 244 atoms in four layers.

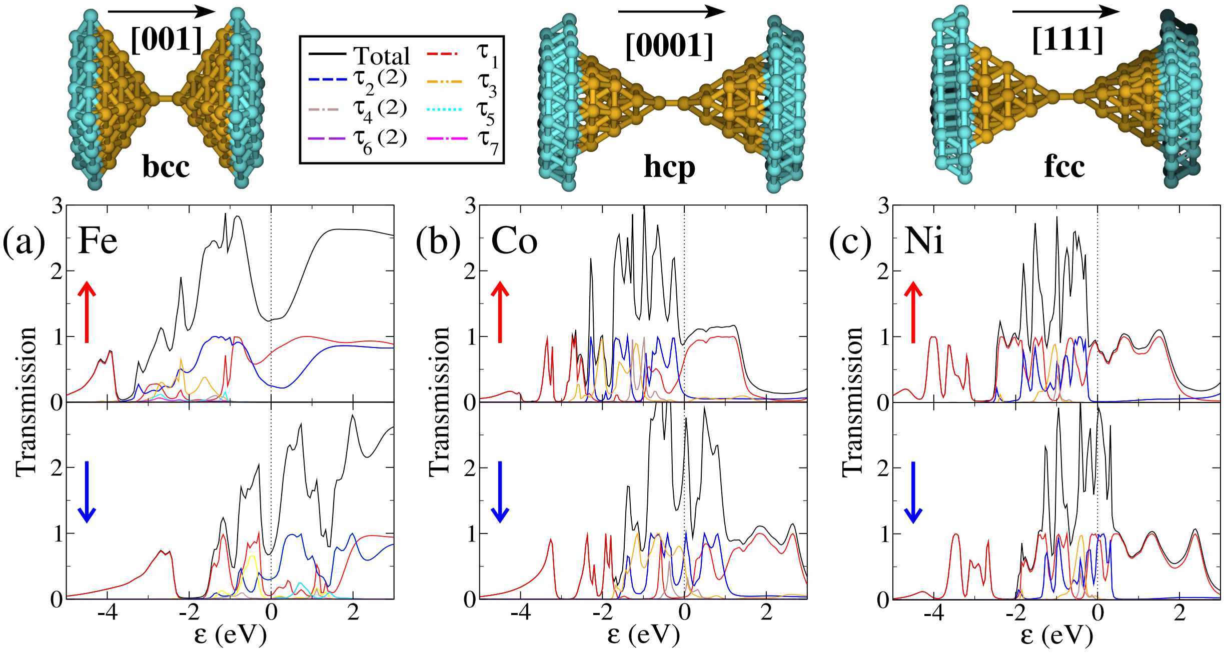

Figure 4.4: The same as in Fig. 4.3 but for the geometries shown in the upper graphs, which contain a dimer in the central part of the contact. The two dimer atoms are at the bulk nearest neighbour distance from each other.

Now we turn to the analysis of the geometries shown in the upper panels of Fig. 4.4. The difference with respect to the geometries of Fig. 4.3 is the presence of a dimer in the central part of the contacts. This type of geometry has frequently been observed in molecular dynamics simulations of atomic contacts of Al (Ref. [120]) and Au (Ref. [112]) and we also find them in our simulations of Ni contacts in the last stages of the breaking process (see [77] and Section 4.2).

Inserting a dimer with an atom separation equal to the bulk NN distance in the geometries of Fig. 4.3 results in a larger separation of the pyramids to the left and right of the central atom and therefore in a weaker coupling between the layers next to the dimer. This is particularly important in the case of Fe. The resulting transmission for the Fe contact with a central dimer is shown in Fig. 4.4(a), where one can see that only 3 channels remain for the majority spins, yielding $G_\uparrow = 1.24e^2/h$, while for the minority spins 3 channels contribute to $G_\downarrow = 0.70e^2/h$. The total conductance is $1.0G_0$ and the polarization $P = +28\%$. For Co the contact of Fig. 4.4(b) with a central dimer exhibits $G_\uparrow = 0.90e^2/h$ and $G_\downarrow = 2.23e^2/h$, summing up to a total conductance of $1.6G_0$. The transmission is formed by 3 channels for the majority spins (with one clearly dominant) and 6 channels for minority spins and polarization is $P = -42\%$. Finally, for the Ni contact in Fig. 4.4(c) with a central dimer, a single channel contributes to $G_\uparrow = 0.86e^2/h$ and 4 channels add up to $G_\downarrow = 2.66e^2/h$. This means that one has a total conductance of $1.8G_0$, while the current polarization adopts a value of $P = -51\%$.

Beyond the precise numerical values detailed in the previous paragraph, we would like to stress the following conclusions from the analysis of Fig. 4.4. First, the transport contribution of the minority spins is dominated by the d orbitals, which give rise to several channels (from 3 to 5 depending on the material). Second, for the majority spins there is a smaller number of channels ranging from 3 for Fe to 1 for Ni. This contribution is dominated by the d and s orbitals for Fe and only by the s orbitals for Co and Ni. The relative contribution and number of channels of the two spin species is a simple consequence of the position of the Fermi level and the magnitude of the spin splitting. In particular, notice that as we move from Fe to Ni, the Fermi energy lies more and more outside of the d band for the majority spins, which implies that the number of channels is reduced for this spin species. In particular, for Ni a single majority spin channel dominates. On the other hand, notice that the conductance values for the different contacts lie typically above G_0, which is precisely what is observed experimentally [48].

4.1.2 Tunneling conductance of Fe, Co, and Ni contacts

So far, we have analyzed geometries for the so-called contact regime where the nanowires are formed. As shown above, in this case the contribution of the d bands makes it difficult to obtain large values of the current polarization. In this sense, one may wonder what happens in the tunneling regime when the contact is broken. In order to address this issue, we have simulated the breaking of the contacts by progressively separating the electrodes of the dimer geometries of Fig. 4.4. In this way, we have computed the conductance and the current polarization as a function of the tip separation D (measured between the centers

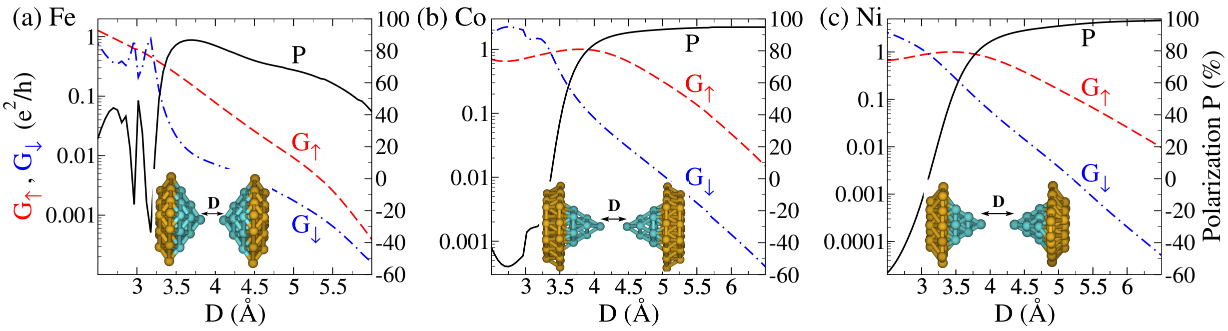

Figure 4.5: Conductance over tip separation D of similar geometries as in Fig. 4.4. The conductance of majority spin ($G_\uparrow$, dashed lines and left scales) and minority spin ($G_\downarrow$, dash-dotted lines and left scales) is shown, together with the resulting current polarization (solid lines and right scales).

of the tip atoms) and the results for the three materials are summarized in Fig. 4.5. With increasing D one enters the tunneling regime, which is characterized by an exponential decay of the conductance. In the regime shown in the graphs, Fe does not yet exhibit an exponential decay. In contrast, the conductances for Co and Ni are well fitted by an exponential $\exp(-\beta D)$ with $\beta = 2.3$ Å^{-1} and $\beta = 1.9$ Å^{-1}, respectively. These values are in reasonable agreement with the WKB approximation [163], which yields $\beta = 2.2$ Å^{-1} using a work function of 5 eV [114]. Notice that deep in the tunneling regime for the three materials, the conductance for the majority spins largely exceeds the value of the minority spin conductance. This results in positive values of the current polarization P and, in particular, for Co and Ni it reaches values very close to 100%.

The origin of these huge values of current polarization in the tunneling regime is the following. In this regime the current is, roughly speaking, a convolution of the local densities of states on the tips weighted with the squared hoppings of the relevant orbitals of both electrodes. From Fe over Co to Ni the s orbitals gain weight at the Fermi energy (with respect to the d orbitals) for the majority spins, while for the minority spins the d orbitals dominate at ε_F for all three materials. But the hoppings between $3d$ orbitals decay faster with the separation of the tips than the corresponding hoppings of the $4s$ orbitals. As a consequence, from Fe over Co to Ni, with increasing tip separation the conductance is more and more dominated by the majority spins. This property only depends on the relative weight of the s and d orbitals at ε_F for the two spin species and their decay with tip separation. It follows that the spin polarization of the current is positive and tends to 100% for Ni atomic contacts in the tunneling regime. This striking general feature will be analyzed in more detail below for realistic contact geometries of Ni.

4.1.3 Role of atomic disorder

---

[2] The transmission properties of Au are given in Figs. 3.5 and 3.6. Note that there we use the

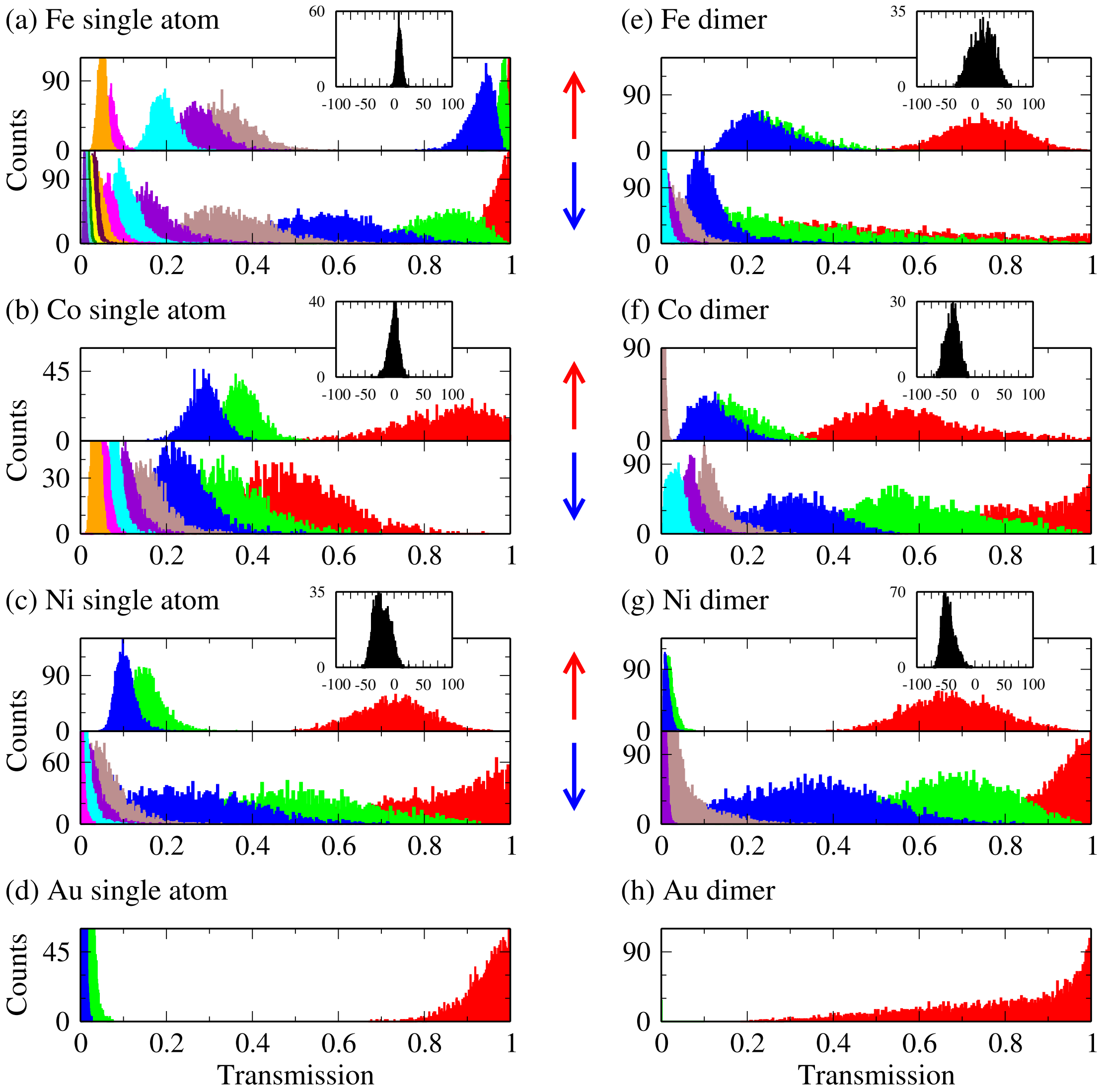

Figure 4.6: Histograms of transmission channels at Fermi energy, $\tau_{n,\sigma}(\varepsilon_F)$, for 3000 perturbed realizations of ideal contact geometries of Fe, Co, and Ni. Panels (a)-(d) show histograms for contacts with a single central atom as in Fig. 4.3 and panels (e)-(h) for contacts with a central dimer as in Fig. 4.4. In panels (a)-(c) and (e)-(g) results for ferromagnetic contacts are presented: the upper parts of the panels refer to majority spin channels and the lower parts to minority spin channels. Only channels that contribute more than 0.01 to transmission are displayed, and the histograms for smaller transmission values are in the front. The insets for the ferromagnetic materials show corresponding histograms for the current polarization P, where on the x axis P is given in %. Finally, panels (d) and (h) show comparison histograms for fcc-Au calculated with a similar set of geometries as for Ni.[2]

In the previous Sections we have seen that the $3d$ orbitals play an important role in transport. These orbitals are rather localized on the atoms and the energy bands that they give rise to have relatively flat dispersion relations. Therefore, one would expect the contribution of these orbitals to the transport to be very sensitive to the contact geometry. Indeed, in the previous Section we have seen examples in which, by changing the structure of the central part of the contacts, one can even change the sign of the current polarization. Motivated by these results, we study in this Section in a more systematic manner how disorder in the atomic positions influences the conductance of one-atom contacts.

In order to simulate the role of disorder we have studied the conductance of contacts in which the atomic positions in the central cluster have been changed randomly using the geometries of Figs. 4.3 and 4.4 as starting points. In Fig. 4.6 we present an example of such a study, where we show histograms of the channel-resolved transmissions at the Fermi energy $\tau_{n,\sigma}(\varepsilon_F)$ for both spins σ constructed from around 3000 realizations of disorder for each contact. The amplitude of the random displacement in each direction was in this case 0.05 times the lattice constant. Similar results for contacts of the noble metal Au are also shown for comparison. Moreover, for the ferromagnetic materials the insets show corresponding histograms of the spin polarization P of the current.

Let us now discuss the main features of the transmission histograms. First, they show that the number of channels obtained for the ideal geometries in the previous Section is robust with respect to disorder, although the transmission coefficients depend crucially on the precise atomic positions. Second, for the minority spins one has a non-negligible contribution of at least 5 channels, which originate mainly from the d bands. For the majority spins the number of channels is clearly smaller and is progressively reduced as we go from Fe to Ni. This is particularly obvious in the panels of the dimer structures, where one can see that for Fe there are three sizable channels and the contribution of the smallest two decreases for Co and Ni. As explained in the previous Section, this is a consequence of the relative position of the Fermi energy in these three metals. For the latter case of Ni, one channel clearly dominates the majority spin conductance, but second and third channels are still present. Thus, unlike in the case of noble metals such as Au, which only have a single channel (see Fig. 4.6), for ferromagnetic materials conductance quantization is not expected. Third, the peaks in the histograms for the ferromagnetic metals are much broader (especially for the minority spins) than for Au. This is due to the higher sensitivity of the d bands to the atomic positions, as compared to the s orbitals that dominate the transport in the case of Au. This higher sensitivity is a result of the anisotropic spatial dependence of the d orbitals.

In addition, we have calculated the values of the current polarization P for each realization of disorder in the contacts. The resulting histograms can be found as insets in the panels of Fig. 4.6. The peaks in each histogram are centered around the polarization values of the corresponding ideal geometries of Sec. 4.1.1.

To end this Section we would like to make the following comment. In this work we have analyzed the conductance of some ideal one-atom geometries and the influence of

---

parametrization with a larger cutoff ("au_par“ from Table 3.1) than here ("au_par_99“ from Table 3.1).

disorder. These types of calculations are very valuable to elucidate the nature of the electrical conduction in atomic wires. However, one has to be cautious in establishing a direct comparison between such theoretical results and the experiments because of the lack of knowledge of the exact geometries realized experimentally. Ideally, the theory should aim at describing the conductance histograms, which contain the full experimental information without any selection of the data. This is precisely what we will analyze for Ni contacts in the next Section.

4.2 Conductance of contacts obtained from molecular dynamics simulation

Here we combine the electronic structure calculations by means of the NRL TB method with a classical molecular dynamics (MD) simulation for the determination of the evolution of the structure (and the mechanical properties) of the nanowires during elongation. In this way we have simultaneously access to the electrical and mechanical properties of the nanowire.

4.2.1 Geometric structure calculations with molecular dynamics simulation

The breaking of metallic nanocontacts is simulated with a classical MD simulation. The forces and energies are calculated using semi-empirical potentials derived from effective-medium theory (EMT) [164, 165]. The evolution of the contacts is then obtained from the integration of the classical Newtonian equations of motion. The temperature is kept fix (usually at 4.2 K here) by means of a Nosé-Hoover thermostat [166]. This model has successfully been used to simulate the breaking of nanowires [15, 23, 24, 167, 168].

The starting configuration consists of 112 atoms (14 layers with 8 atoms each) on fcc lattice sites in [001] direction. Attached to the central contact are two slabs, each containing 288 atoms on fcc lattice sites, at both ends of the central contact. After equilibration, the stretching process is simulated by separating both slabs symmetrically by a fixed distance in every time step. Randomized starting velocities of the 112 wire atoms guarantee different time evolutions of the nanocontacts for each simulation. During the evolution, the minimum cross section (MCS) perpendicular to the stretching direction is computed following [169]. For technical details on the calculation of the geometric structure we refer to [77, 112] and the references therein. The MD simulations were performed by Markus Dreher in the group of Peter Nielaba at the Universität Konstanz.

With the MD simulation we have access to the mechanical properties of the contact during the elongation and can calculate at the same time the conductance of the contact using the NRL method as described previously.

4.2.2 Evolution of individual nickel contacts

In Fig. 4.7 we apply this method to determine the evolution of a Ni contact. In the last stage of the breaking process a dimer structure is formed, which is the most common structure in this stage.

In the panels of Fig. 4.7 we show the evolution of the conductance projected on the $\uparrow$, $\downarrow$ spins and its channel decomposition.[3] The number of contributing channels is given for each regime of the evolution. Some representative geometries during the evolution are depicted. In addition we have plotted the MCS radius, strain force, spin polarization of the current, and contact configurations. The spin polarization of the current P, shown in the inset of the lower panel, is defined as above [see Eq. (4.3)], where G_σ is the conductance of the spin component σ. Notice that in the last stages of the stretching the conductance is dominated by a single channel for the majority spin, while for the minority spin there are still up to four open channels. In the final stages (see regions with three or one open channel(s) for $G_\uparrow$) the conductance for the majority spin lies below $1.2e^2/h$, while for the minority spin it is close to $2e^2/h$, adding up to a conductance of around 1.2–1.6 G_0.

With respect to the evolution of the spin polarization of the current, in the beginning of the stretching process it takes a value of around -40%, i.e., the conductance of the minority-spin component outweighs that of the majority-spin component. This is expected from the bulk DOS of Ni (see Fig. 4.2). For this transition metal the Fermi level lies right in the d band for the minority spin, while for the majority spin one is at the edge of the d band and the s and p bands contribute comparatively more strongly to the DOS. For this reason, there is a larger number of conductance channels for minority-spin component. The value of P is indeed quite close to the value of the spin polarization of the bulk DOS at the Fermi energy, which in our model is equal to -40.5%. As the contact geometry starts changing, the spin polarization of the current begins to fluctuate. It increases even to values above 0%, but keeps a tendency towards negative values, until it starts increasing to over $+80\%$ in the tunneling regime, when the contact is broken.

Let us now try to gain further insight into these findings. We show in Fig. 4.8 the transmission as a function of the energy together with the LDOS for an atom in the narrowest part of the constriction portrayed in the upper part of the figure.

It can be observed that the Fermi energy, as in bulk, is located just at the edge of the d states for the majority-spin component, while it is inside the d states for the minority-spin component.[4] The majority-spin component therefore exhibits a single transmission channel, behaving similar to a noble metal (see the results for Au and Ag in Sec. 3.2 or the discussions in [77, 112]), while there are several open channels for the minority-spin component as in the case of a transition metal (see the results for Pt in Sec. 3.2 or the discussion in [77]).

Concerning the spin polarization of the current, the large DOS at ε_F for the minority-spin component usually gives rise to a higher number of open channels for the minority-spin component than for the majority-spin component, which in turn leads to a negative spin

---

[3] Here again, spin up ($\sigma =\uparrow$) means majority spins and spin down ($\sigma =\downarrow$) minority spins.

[4] Similar to the case of ideal.dimer contacts in [111] direction in Fig.4.4(c).

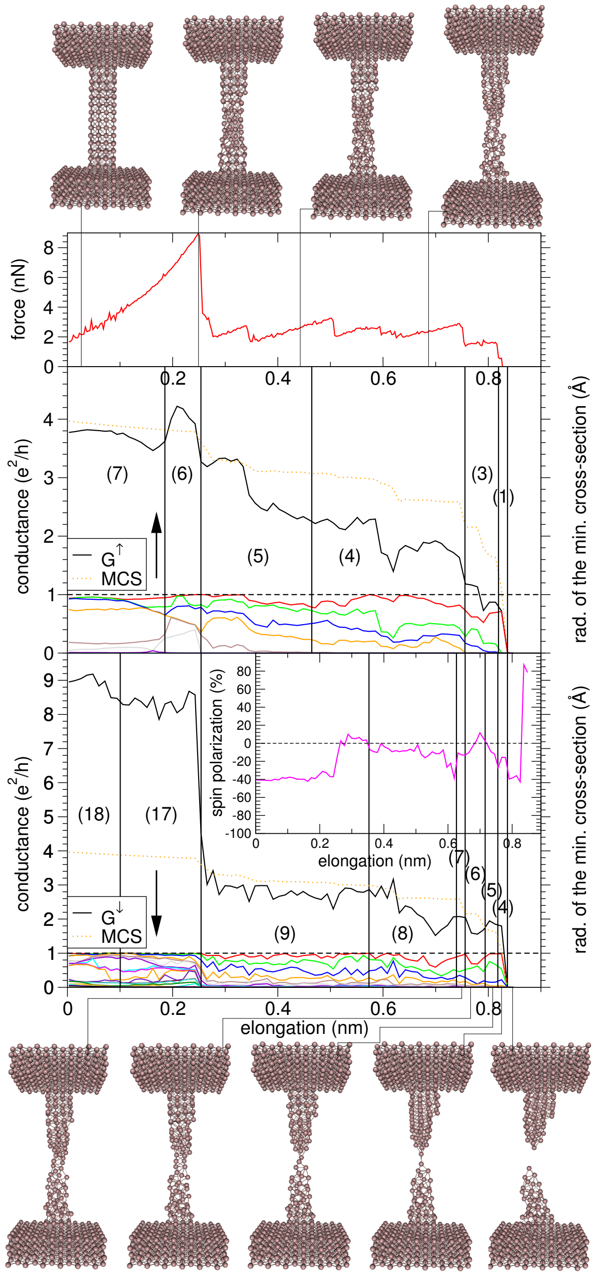

Figure 4.7: Formation of a dimer configuration for Ni (4.2 K, [001] direction). The upper panel shows the strain force as a function of the elongation of the contact. In the lower two panels the conductance G_σ, the MCS radius, and the channel transmissions are displayed for the respective spin component σ. Vertical lines separate regions with different numbers of open channels ranging from 7 to 1 and 18 to 4, respectively. An inset shows the evolution of the spin polarization. Above and below these graphs snapshots of the stretching process are shown.

polarization of the current. However, this argument is just qualitative, because the actual transmission of the channels cannot simply be predicted from the LDOS. The conductance depends also on the overlap of the relevant orbitals and on non-local properties like the disorder in the contact region. As a counter example, Fig. 4.7 shows that also intervals of positive P can be found, although the DOS of the minority-spin component is usually higher than for the majority-spin component. This is particularly dramatic in the tunneling regime at the end of the breaking process, where, for instance, in Fig. 4.7 we see that a

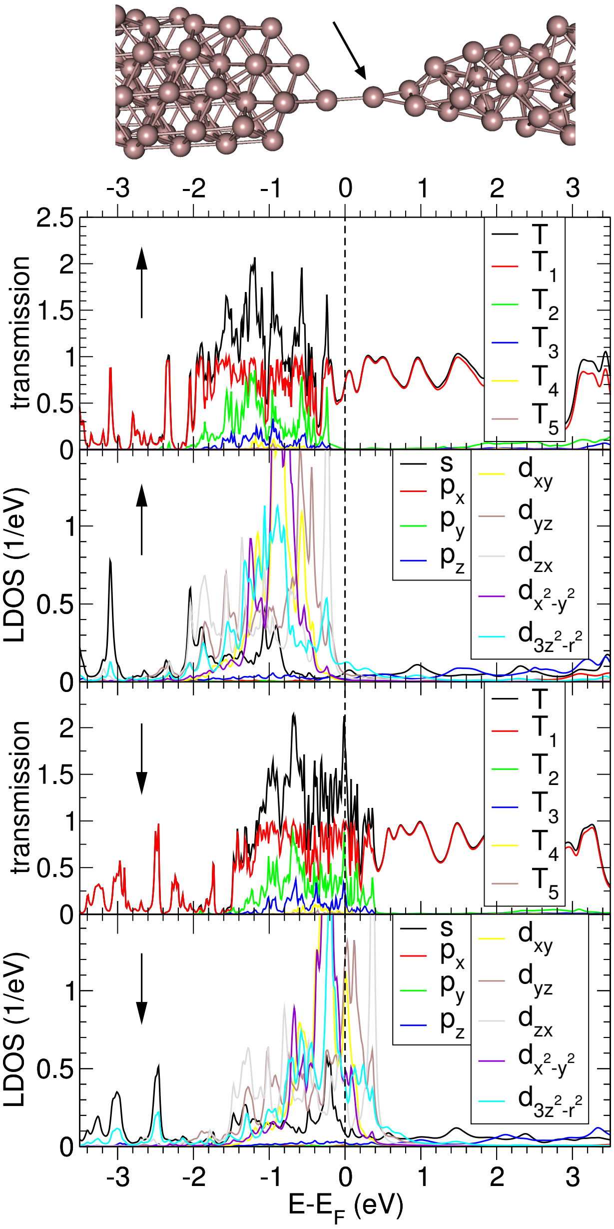

Figure 4.8: Ni contact of Fig. 4.7 at an elongation of 0.83 nm. The transmission is plotted as a function of the energy together with the contributions from the different transmission channels $T_{n,\sigma}$ for the respective spin component σ. Additionally the LDOS is given for each spin component for an atom in the narrowest part of the contact, where the different orbital contributions have been itemized. Above the figure the narrowest part of the Ni contact is displayed in a magnified fashion and the atom is indicated, for which the LDOS is shown.

value of $P = +80\%$ is reached. Such a reversal of the spin polarization is due to the fact that the couplings between the d orbitals of the two Ni tips decrease faster with distance than the corresponding s orbitals. As will be discuss further below, the result is typically a reduction of the minority-spin conductance and therefore a positive value of P.

We would like to point out that the contribution of the minority-spin component to the conductance is very sensitive to changes in the configuration. As is evident from Fig. 4.7, the minority spin shows stronger fluctuations than the majority spin as a function of the elongation. Again, this is a consequence of the fact that the minority-spin contribution is dominated by the d orbitals, which are anisotropic and therefore more susceptible to

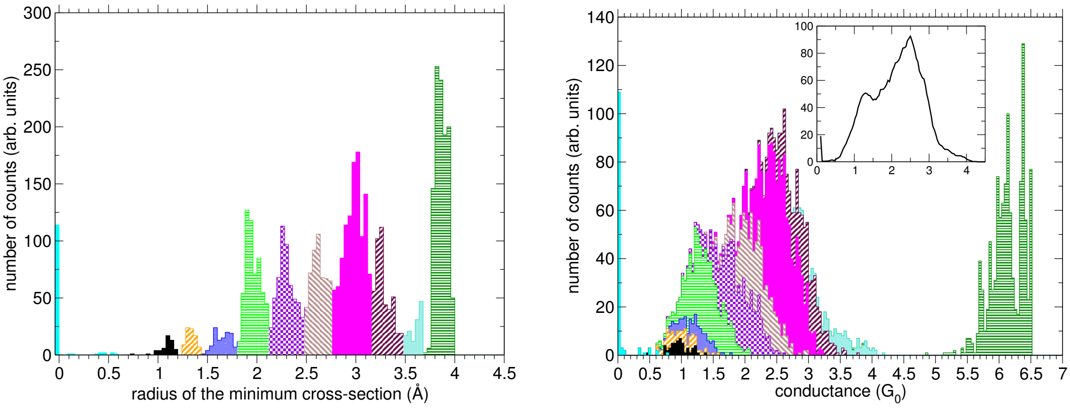

Figure 4.9: MCS histogram (left panel) and conductance histogram (right panel) for Ni (4.2 K, [001] direction, 50 contacts). In the MCS histogram different regions of frequently occurring radii have been marked with different pattern styles. The patterns in the conductance histogram indicate the number of counts for conductances belonging to the corresponding region of the MCS histogram. In the inset of the lower panel the conductance histogram is displayed in the relevant region in a smoothed version by averaging over six NN points.

disorder than the *s* states responsible for the conductance of the majority spins. The sensitivity to atomic configurations is in agreement with the findings for Ag and Pt as discussed above, where stronger fluctuations of the conductance are seen for the transition metal Pt, as compared with the noble metal Ag (see also [77]).

4.2.3 Statistical analysis of nickel contacts

For the Ni contacts we did not observe the formation of any chain in the 50 simulated stretching processes. As a consequence, only a small first peak is visible in the MCS histogram (see Fig. 4.9).

This peak originates from the dimer configurations, which usually form before the contacts break. In the conductance histogram there is a shoulder at around $1.3G_0$. Part of this first peak is buried under the adjacent conductance peak with its maximum at $2.5G_0$. This second very broad peak is mainly influenced by the starting configuration, which means that the small size of our contacts might hide part of the peak structure in the conductance histogram. According to the MCS regions contributing to the shoulder in the Ni conductance histogram, the first peak is mainly composed of thick contacts (with MCS radii of around 2 Å). This also explains the large broadening of the histogram peak, since for thick contacts, there is more configurational variability.

Concerning the comparison with measurements, the shoulder at $1.3G_0$ in our results is in agreement with the experimental conductance histogram, where a particularly broad peak between $1.1G_0$ and $1.6G_0$ is observed (see Fig. 4.1(b) and [48]). Our calculations indicate that this peak contains contributions from high MCS regions. The remarkable width of the first peak in the experimental conductance histogram is then explained by the configurational variability of thick contacts in conjunction with the contribution of configurationally sensitive d states to the conductance of the minority-spin component. However, this interpretation requires further discussion. Usually the first peak in the experimental conductance histograms is believed to arise from single-atom contacts and dimers [21]. With respect to the problems encountered for Al (see [77]), it may be that the employed EMT potential for Ni underestimates the stability of single-atom and dimer configurations in a similar manner. In contrast to our MCS histogram, García-Mochales *et al.* [170] obtain a decreasing peak height for higher MCS radii.[5] Although their results are obtained with a slightly different approach and for thicker contacts, their findings support the conjecture of a possible underestimation of the stability of single-atom contacts and dimers in our calculations. As a consequence the contribution of such configurations to the first peak in the conductance histogram may be too low. In addition, as mentioned above, this first peak in the conductance histogram is not well separated from contributions with a high MCS, which are influenced by our starting configuration. Simulations of thicker contacts and more sophisticated calculations of the contact geometry may be needed to clarify the robustness of our findings.

With regard to the mean channel transmission of the spin-components as a function of the conductance, the minority-spin component exhibits more transmission channels than the majority-spin component (see Fig. 4.10). This further illustrates our previous argument, where we explained that the majority-spin component possesses an Ag-like character, while the minority-spin component behaves more Pt-like. Note also that the first channel for the majority-spin component opens up remarkably slowly compared with Ag or Au in [77].

Now we want to address the question of how the spin polarization of the current is influenced by configurational changes. For this purpose, we show in Fig. 4.11 the spin polarization P as a function of the conductance for all the 50 simulated breaking events.[6]

As already observed in the simulation of a single breaking event (see Fig. 4.7), the spin polarization of all the contacts starts at a value of -40%, when the contact is close to its starting configuration. As explained above, this value for the spin polarization of the current coincides rather well with the polarization of the bulk DOS at the Fermi energy (see Fig. 4.2). As the contact is stretched, also the diversity of geometrical configurations increases and the spin polarization values are widely spread, ranging from around -60 to 20%. There is a tendency towards negative spin polarizations, as can be observed in the inset of Fig. 4.11. The average spin polarization varies between -30 and -10% for conductances above $0.6G_0$. As described in the previous subsection, these variations arise from the high sensitivity of the minority-spin conductance to atomic positions, as compared to the less sensitive majority-spin conductance. The trend towards negative P

---

[5] Note that in Fig. 4 of Ref. [170] the MCS histograms are plotted with counts vs. area and not counts vs. MCS radius as in our case. For a circular area $A = \pi r^2$ this means that according to $dA = 2\pi r dr$ for a constant dA the MCS radius sampling dr needs to decrease for growing r. However, in our calculations dr is fixed, to that the MCS histogram of Ref. [170] is not directly comparable to ours in Fig. 4.9.

[6] Note that bins (where a bin-width of $0.04G_0$ has been used) containing only a single data point are discarded in the inset of Fig. 4.11. The reason is that the calculation of the standard deviation $\tilde{\sigma}$ requires at least two data points.

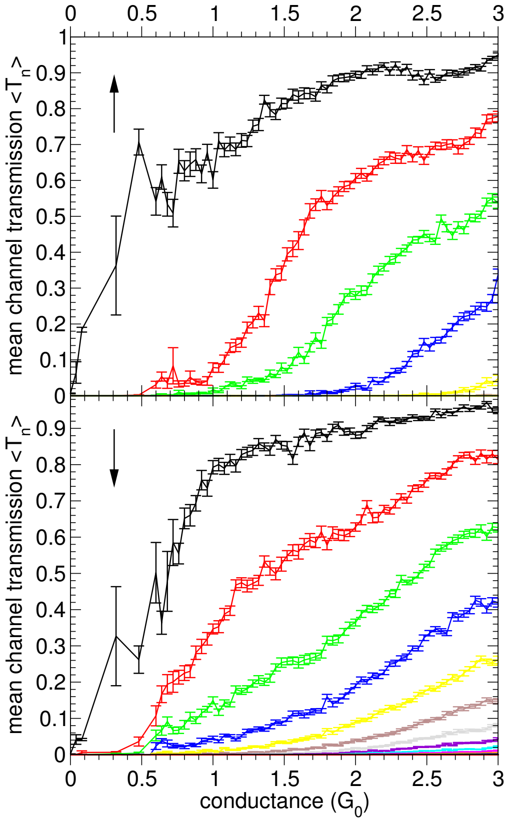

Figure 4.10: Mean value of the transmission coefficient $\langle \tau_{n,\sigma} \rangle$ for the respective spin component σ as a function of the conductance for Ni (4.2 K, [001] direction, 50 contacts). The error bars indicate the standard deviation $\tilde{\sigma}$.

values can be explained by the higher number of states present at the Fermi energy for the minority-spin component as opposed to the majority-spin component.

In the region of conductances below $0.6G_0$ the number of points is comparatively lower, which explains the partly bigger error bars. Nevertheless, the number of realizations is still enough to see the spreading of P values over an even wider interval than in the contact regime, together with an average tendency towards positive values. We attribute this trend of reversed spin polarizations to the faster radial decay of the hoppings between the d orbitals that dominate the minority-spin contribution to the conductance, as compared with the s orbitals that dominate the majority-spin contribution. The faster decay with distance overcomes in the tunneling regime the effect of the higher DOS of the d states versus the s states as explained above in Sec. 4.1.2.

4.3 Conclusion

In this Chapter we have presented a theoretical analysis of the conductance of one-atom thick contacts of the ferromagnetic $3d$ metals Fe, Co, and Ni. Our calculations are based

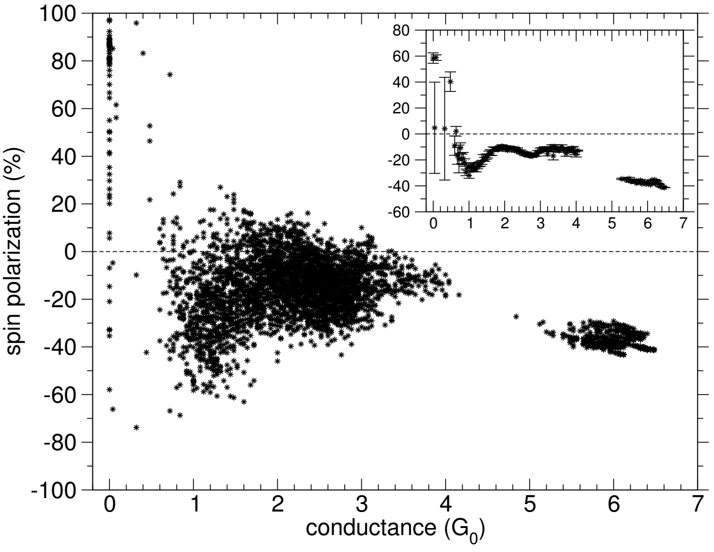

Figure 4.11: Spin polarization of the current P as a function of the conductance. All the data points for the spin polarization are plotted in the graph, while in the inset their arithmetic mean and the corresponding standard deviation $\tilde{\sigma}$ are displayed.

on a self-consistent tight-binding model that has previously been successful in describing the electrical conduction in non-magnetic atomic-sized contacts. Our results indicate that the d orbitals of these transition metals play a fundamental role in the transport, especially for the minority-spin species. In the case of one-atom contacts, these orbitals combine to provide several partially open conductance channels, which has the following important consequences. First, there is no conductance quantization, neither integer nor half-integer. Second, the current in these junctions is, in general, not fully spin-polarized. Third, the conductance of the last plateau is typically above G_0. Finally, both the conductance and the spin polarization of the current are very sensitive to the contact geometry. The ensemble of these theoretical findings supports the recent observations of Untiedt *et al.* [48], while it is in clear contradiction with the observations of half-integer conductance quantization [42–47]. Of course, the appearance of the quantization in those experiments still remains to be understood. A possible explanation has been put forward by Untiedt *et al.* [48], who suggested that it could be explained by the presence of contaminants like foreign molecules at the surfaces of the studied samples.

It is interesting to mention that in the tunneling regime, when the contacts are actually broken, the nature of the conduction changes radically. We have shown that in this case the transport is mainly dominated by the s orbitals and the spin polarization of the current can reach values close to +100%.

We want to stress that in all our calculations we have assumed that the atomic contacts were formed by single magnetic domains. In this sense, it would be interesting to see how the conductance in these calculations is modified by the presence of domain walls in the contact region. The first theoretical studies [57, 59, 64, 66] along these lines show that the presence of a domain wall cannot conclusively explain the appearance of huge magnetoresistance values reported in the literature [34].

In a statistical analysis of Ni contacts obtained by means of MD simulations, we confirmed the basic conclusions drawn from the analysis of ideal contact geometries. In particular, we have shown that the conduction properties of the contacts behave, roughly speaking, like a mixture of a noble metal (such as Au, Ag, for the majority spins) and a transition metal (such as Pt, for the minority spins). In the conductance histogram we obtain a shoulder at $1.3G_0$, whose large width can again be attributed to the extreme sensitivity of the d orbitals (from the minority spins) to atomic configurations. On the other hand, we find that the spin polarization of the current in the Ni contacts is generally negative, increasing and fluctuating as the contacts narrow down and become disordered. In particular, large positive values are possible in the tunneling regime, right after the rupture of the wires. Once more, this behavior can be traced back to the fact that the d orbitals play a key role in the conductance of the minority-spin component.

Chapter 5

Anisotropic Magnetoresistance in ferromagnetic atomic contacts

So far we focussed on general conductance properties of ferromagnetic atomic contacts and assumed the Hamiltonian to be diagonal in spin space. We found that the minority spin d orbitals dominate the transport properties. Here, we will additionally include in our model the spin-orbit coupling (SOC) present in those orbitals. As a consequence, the anisotropic magnetoresistance (AMR) arises when the magnetization throughout the ferromagnetic device is rotated uniformly by a certain angle θ with respect to the current direction. In polycrystalline bulk samples such rotation induces a relative change in the conductance $\Delta G/G$ that varies as $\cos 2\theta$ with an amplitude on the order of 1% [171]. Recently Bolotin *et al.* [54] found that the AMR of Permalloy atomic-sized contacts can be considerably enhanced as compared with bulk samples and that it exhibits an angular dependence clearly deviating from the $\cos 2\theta$ law [see Fig. 5.1(b,c)]. Additionally, they found a significant voltage dependence on the scale of millivolts, which led them to interpret the effect as a consequence of conductance fluctuations due to quantum interference [172]. Independently, Viret and coworkers [55] reported similar results in Ni contacts, but also the occurrence of conductance jumps upon rotation of the magnetization. Similar stepwise variations of the conductance have been found in Co nanocontacts [173].

The jumps have been interpreted as a manifestation of the so-called ballistic AMR (BAMR) [174]. According to this theoretical concept the rotation of the magnetization in a ballistic contact could result in an additional band crossing the Fermi energy, leading to an abrupt change in the conductance on the order of e^2/h. This has been theoretically shown to occur in ideal infinite chains of Ni and Fe [174] as a result of the 1D periodic structure. However, realistic ferromagnetic contacts made of transition metals are not expected to be ballistic [48] and so the interpretation of the conductance jumps in terms of BAMR is at least questionable. Indeed, Shi and Ralph [175] have suggested that these jumps might originate from two-level fluctuations due to changes in atomic configurations [176]. Thus, there remain important open questions about AMR in atomic contacts, concerning the origin of the enhanced amplitude, the anomalous angular dependence, the occurrence of conductance jumps, and the voltage dependence.

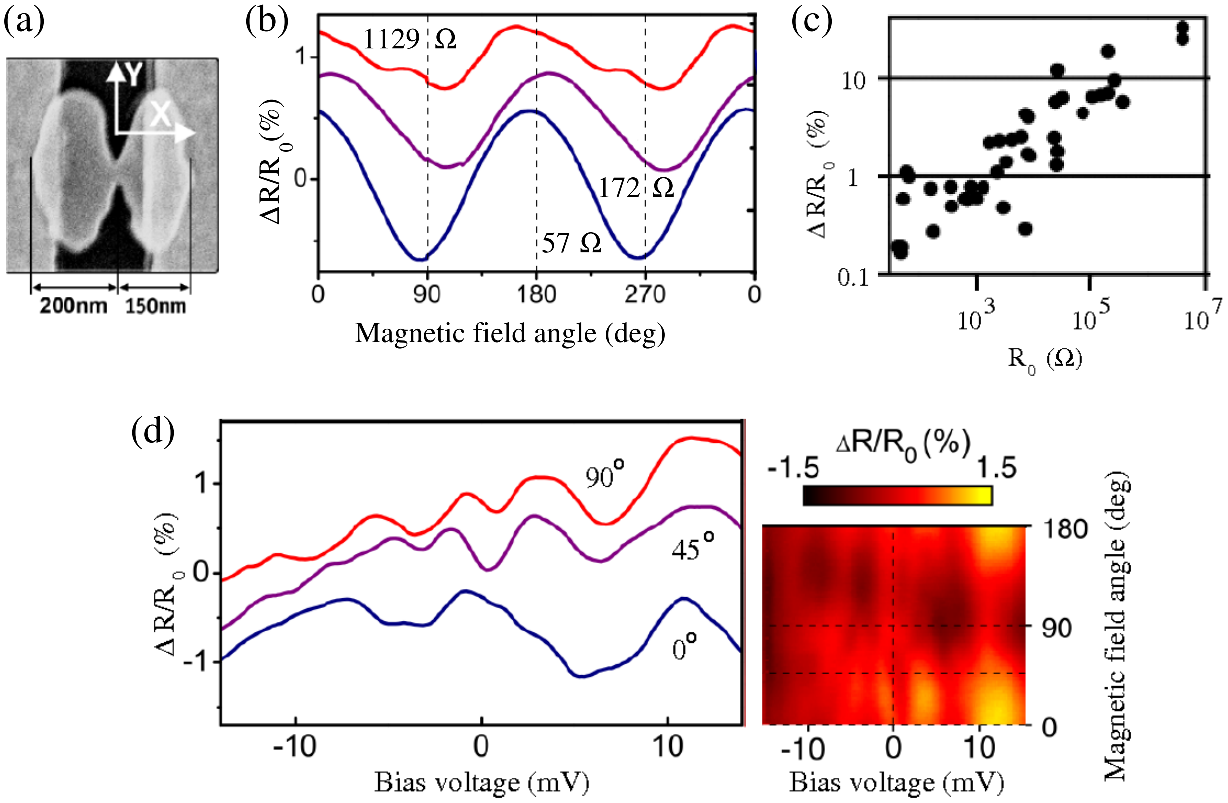

Figure 5.1: (a) Scanning electron micrograph of an electromigrated junction of Permalloy. (b) Zero-bias differential resistance vs. angle of applied magnetic field for such junctions. Evolution of the AMR from bulk behaviour (for junction with large cross-section, i.e. small resistance $R_0 = 57\ \Omega$) to atomic contact regime (higher resistance $R_0 = 1129\ \Omega \approx 1/11G_0$). (c) AMR magnitude as a function of R_0 for 12 different devices. (d) Differential resistance dV/dI at finite bias for a junction with $R_0 = 2.6\ k\Omega$ and for several directions of the magnetic field. The resistance curves in the left plot correspond to the horizontal dotted lines in the color coded map. All graphs are taken from [54].

Here we address these questions using a combination of a tight-binding (TB) model, molecular dynamics (MD) simulations, and a simple toy model. Our calculations suggest that the enhancement of the AMR amplitude and the deviations from the $\cos 2\theta$ law in atomic contacts stem from spin-orbit coupling (SOC) together with a reduced symmetry of the contact geometry. We do not find signs of BAMR in realistic contact geometries. Finally, we find that the conductance of pure atomic contacts has no voltage dependence on the the scale of millivolts, but that the addition of impurities can lead to a significant voltage dependence of the AMR signal.

This Chapter is organized as follows: First we describe in Section 5.1 how we introduce the SOC in the Hamiltonian. Next, in Section 5.2 we apply this Hamiltonian to the minimal model of a linear chain and discuss its anisotropy properties. In Section 5.3 we then focus on the conductance anisotropy of ideal contacts of the $3d$ ferromagnets. Then in Section 5.4 the development of the conductance anisotropy during the evolution of a Ni wire from bulk to the atomic contact regime is studied in a more statistical manner. We also examine the properties of SOC induced orbital momentum there. Finally, we discuss the interplay between distant impurities and the AMR properties in Section 5.5 and end this Chapter with a brief conclusion.

5.1 Tight-binding Hamiltonian with spin-orbit coupling

In order to describe the AMR in ferromagnetic atomic contacts of the $3d$ metals (Ni, Co, and Fe), we add a SOC term to the ferromagnetic Hamiltonian:

$$\hat{H} = \sum_{ij\alpha\beta\sigma\sigma'} \left([\mathbf{H}]^{(0)}_{i\alpha,j\beta;\sigma} \delta_{\sigma\sigma'} + [\mathbf{H}]^{(SO)}_{i;\alpha\sigma,\beta\sigma'} \delta_{ij} \right) \hat{c}^{\dagger}_{i\alpha\sigma} \hat{c}_{j\beta\sigma'} . \tag{5.1}$$

Here the first term $\mathbf{H}^{(0)}$ refers to the Hamiltonian of Eq. (4.1) without SOC. Again the spin-polarized parameters $[\mathbf{H}]^{(0)}_{i\alpha,j\beta;\sigma}$ and the spin-independent overlaps $[\mathbf{S}]_{i\alpha,j\beta}$ are taken from the parametrization of Refs. [89, 107] and are modified according to Eq. (2.57) to satisfy charge neutrality. In absence of SOC the results of the preceding Chapter 4 are reproduced.

The additional intra-atomic spin-orbit term $\mathbf{H}^{(SO)}$ couples the direction of the spin to the geometry. These matrix elements depend on the spin quantization axis (with polar angle θ and azimuthal angle ϕ), which we rotate uniformly to simulate the AMR experiments with saturated magnetization:

$$[\mathbf{H}]^{(SO)}_{i;\alpha\sigma,\beta\sigma'}(\theta,\phi) = \xi_i \langle i\alpha\sigma | \vec{\mathbf{l}} \cdot \vec{\mathbf{s}} | i\beta\sigma' \rangle = \frac{\xi_i}{2} \sum_{\mu,\nu} R_{\mu\nu}(\theta,\phi) l^{(\mu)}_{\alpha\beta} \tau^{(\nu)}_{\sigma\sigma'} \ . \tag{5.2}$$

Here ξ_i is the SOC constant on site i, $\mathbf{l}^{(\mu)}$ are the orbital momentum matrices, and the Pauli matrices $\boldsymbol{\tau}^{(\nu)}$ are given by

$$\boldsymbol{\tau}^{(1)} = \begin{pmatrix} 0 & 1 \\ 1 & 0 \end{pmatrix}, \quad \boldsymbol{\tau}^{(2)} = \begin{pmatrix} 0 & -i \\ i & 0 \end{pmatrix}, \quad \boldsymbol{\tau}^{(3)} = \begin{pmatrix} 1 & 0 \\ 0 & -1 \end{pmatrix} \ . \tag{5.3}$$

Furthermore $\mathbf{R}(\theta,\phi) = \mathbf{R}_z(\phi)\ \mathbf{R}_y(\theta)$ is a relative rotation between the spin and orbital quantization axes, where θ and ϕ are the polar and azimuthal angle. In this way the Hamiltonian has the form of Eq. (2.44) and we can use the expressions derived in Secs. 2.2.1 and 2.2.2 to calculate the conductance.

The $\mathbf{H}^{(SO)}$ matrix has time reversal symmetry: $\left(\mathbf{H}^{(SO)}\right)^T(\theta,\phi) = \mathbf{H}^{(SO)}(\pi-\theta,\pi+\phi) = \boldsymbol{\tau}^{(2)}\mathbf{H}^{(SO)}(\theta,\phi)\boldsymbol{\tau}^{(2)}$. We only consider SOC on d orbitals, for which the matrix elements of Eq. (5.2) can be found in Ref. [177].

We use the SOC constant $\xi_i = 70$ meV, which is the experimental value for Ni. Although this type of model is not expected to be as accurate as *ab initio* counterparts, it captures the essential (orbital) symmetries and has the advantage that it allows us to analyze phenomena like BAMR in realistic contact geometries, which is difficult with *ab initio* methods [178].

Note that in the ferromagnetic Hamiltonian $\mathbf{H}^{(0)}$ we neglected electron-electron correlation effects which in an isolated atom lead to a finite orbital momentum according to Hund's rules. For finite isolated clusters of Ni these were studied by Guirado-López *et al.* [179], and for infinite systems with low coordination (like ideal single-atom chains) of Fe by Desjonquères *et al.* [180]. They show that for bigger cluster sizes ($N \geq 10$) correlation effects become less important due to strong coupling of the atoms and the orbital momentum is reduced. In the bulk limit ($N \geq 150$), the orbital momentum is quenched to a good approximation, as we assume here.

Additionally the SOC introduces a small but finite orbital momentum. For the case of isolated monolayers of the $3d$ ferromagnets this was studied by Bruno [181, 182]. In a perturbative approach he found, that the SOC-induced orbital moment follows the spin direction and its length varies like the anisotropy energy. We will discuss the SOC-induced orbital momentum in more detail in Section 5.4.4.

But let us start with a simple minimal model similar to the Anderson-Newns model, as it was discussed in Sec. 3.1.

5.2 A minimal chain model

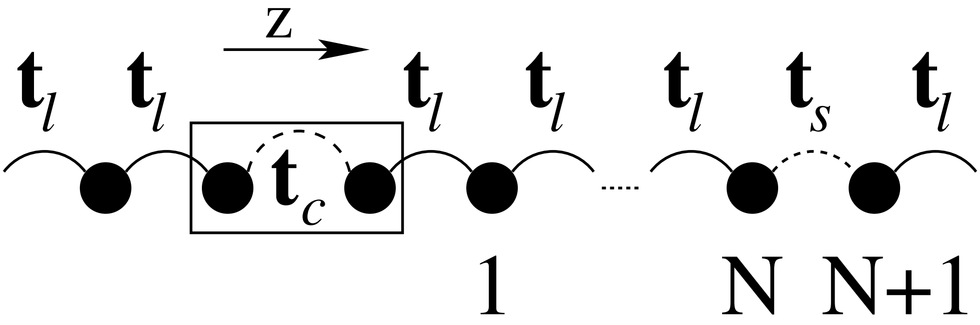

Figure 5.2: Model system: linear chain of d orbitals (chain axis in z direction) eventually coupled to a distant impurity N sites away from the constriction.

In this Section we consider the minimal model of a linear chain. We first introduce the model and then review the case without SOC similar to what we discussed in the preceding Chapter. Finally we discuss the AMR using the example of a chain with SOC. We also prepare for an additional impurity in the lead.

5.2.1 Definition of the model

Here we study the effect of SOC in ferromagnetic atomic contacts of the $3d$ ferromagnets for an idealized model that captures the most essential aspects of the problem. We consider a contact formed by two linear, semi-infinite, z-directional chains of identical atoms joined in a central region consisting of the two tip atoms (see scheme in Fig. 5.2). We first consider the leads as ideal semi-infinite chains. The case of a possible distant impurity as depicted in Fig. 5.2 will be discussed below in Section 5.5.

To describe the electronic structure we consider a tight-binding model taking into account the E_2 subset of the d orbitals with $m_z = \pm 2$ containing the d_{xy} and $d_{x^2-y^2}$ orbitals. The onsite elements for the two spin orientations are assumed to be spin-split by Δ due to ferromagnetic order. The inter-atomic hopping integrals are restricted to nearest neighbours. In terms of Table A.1, the only contributing hopping integral is of the $dd\pi$ type.

Quantity	Symbol	Value
Onsite energy (no splitting)	ε_0	0.0 eV
Spin-splitting	Δ	0.5 eV
Lead hopping $dd\pi$	π_l	1 eV
Center hopping $dd\pi$	π_c	0.4 eV
Impurity hopping $dd\pi$	π_s	0.8 eV
Spin-orbit coupling	ξ	0.2 eV

Table 5.1: Parameters for the d_{E_2} orbitals chain with SOC in the central atoms.

The hoppings are assumed to be equal on all lead atoms but may differ between the two central atoms. Furthermore SOC with a finite coupling constant ξ is taken into account for the central atoms. The used parameters are listed in Tab. 5.1. We want to stress that the conclusions driven here do not depend on the particular choice of parameters.

In the absence of impurities, the term $\mathbf{H}^{(0)}$ in the Hamiltonian has the form

$$\mathbf{H}^{(0)} = \begin{pmatrix} \ddots & \ddots & 0 & 0 & 0 & 0 \\ \ddots & \mathbf{H}_0 & \mathbf{t}_l & 0 & 0 & 0 \\ 0 & \mathbf{t}_l & \mathbf{H}_0 & \mathbf{t}_c & 0 & 0 \\ 0 & 0 & \mathbf{t}_c & \mathbf{H}_0 & \mathbf{t}_l & 0 \\ 0 & 0 & 0 & \mathbf{t}_l & \mathbf{H}_0 & \ddots \\ 0 & 0 & 0 & 0 & \ddots & \ddots \end{pmatrix} . \tag{5.4}$$

The E_2 basis functions $\alpha = 1, 2$ are taken in the order d_{xy}, $d_{x^2-y^2}$. Then the diagonal blocks $\mathbf{H}_0 = \mathrm{diag}(\{\varepsilon_{\alpha\sigma}\})$ are of the form

$$\mathbf{H}_0 = \begin{pmatrix} \varepsilon_0 + \Delta/2 & 0 & 0 & 0 \\ 0 & \varepsilon_0 - \Delta/2 & 0 & 0 \\ 0 & 0 & \varepsilon_0 + \Delta/2 & 0 \\ 0 & 0 & 0 & \varepsilon_0 - \Delta/2 \end{pmatrix} \tag{5.5}$$

and the off-diagonal blocks are $\mathbf{t}_c = \pi_c \mathbb{1}$ and $\mathbf{t}_l = \pi_l \mathbb{1}$. Note that as the atoms lie on a straight line, there are no hopping elements coupling different types of orbitals. In the absence of SOC, this model thus represents four uncoupled linear chains.

Including SOC couples the chains. Equation (5.2) yields the SOC blocks $\mathbf{H}_{i,i}^{(SO)} = (\xi_i/2)\sum_{\mu\nu} R_{\mu\nu}(\theta,\phi)\mathbf{l}^{(\mu)} \otimes \boldsymbol{\tau}^{(\nu)}$, where the Pauli matrices $\boldsymbol{\tau}^{\nu}$ are given in Eq. (5.3) and the orbital angular momentum matrices $\mathbf{l}^{(\mu)}$ reduced to the minimal set of d_{E_2} orbitals are zero except for $\mathbf{l}^{(3)} = 2\boldsymbol{\tau}^{(2)}$. Here ξ_i is taken to be finite only on the atoms i belonging to C.

In order to calculate the current I and the nonlinear conductance $G(V) = dI/dV$ at finite bias voltages, we modify the onsite energies of the C part of $\mathbf{H}^{(0)}$. Thus the current is obtained from Eq. (2.75) where

$$\mathbf{G}_{CC}(\varepsilon, V) = \left[\mathbb{1}\varepsilon^{+} - \tau^{(3)}\frac{eV}{2} - \begin{pmatrix} \mathbf{\Sigma}(\varepsilon - \frac{eV}{2}) & 0 \\ 0 & \tilde{\mathbf{\Sigma}}(\varepsilon + \frac{eV}{2}) \end{pmatrix} - \mathbf{H}_{CC}^{(0)}(V=0) - \mathbf{H}_{CC}^{(SO)} \right]^{-1}.$$

Here $\mathbf{\Sigma}(\varepsilon) = \mathrm{diag}(\{\Sigma_{\alpha\sigma}(\varepsilon)\})$ is a diagonal self-energy matrix arising from the coupling to the left C atom to the four independent, semi-infinite, homogeneous chains [102, 103]. It is of the form

$$\mathbf{\Sigma}(\varepsilon) = \mathbf{t}_l \mathbf{g}_0(\varepsilon) \mathbf{t}_l \tag{5.6}$$

where the Green's function of the "surface" satisfies $\mathbf{g}_0(\varepsilon) = [\varepsilon - \mathbf{H}_0 - \mathbf{t}_l \mathbf{g}_0(\varepsilon)\mathbf{t}_l]^{-1}$. Due to the decoupling the resulting self-energy components are all of the form $\Sigma_{\alpha\sigma}(\varepsilon) = \pi_l e^{i\Phi_{\alpha\sigma}}$, with $\cos\Phi_{\alpha\sigma} = (\varepsilon - \varepsilon_{\alpha\sigma})/2\pi_l$, where π_l is the hopping integral. In the absence of the impurity, the self energy $\tilde{\mathbf{\Sigma}}(\varepsilon)$ for the right-hand C atom is equal to $\mathbf{\Sigma}(\varepsilon)$. The modifications due to the introduction of the impurity are discussed in more detail in Section 5.5.

5.2.2 Transmission in absence of spin-orbit coupling

Let us first discuss the results in the absence of SOC, in which case there are four independent linear chains. The local density of states (LDOS) $\rho_{\alpha\sigma}(\varepsilon)$ projected onto the orbital $\alpha\sigma$ of one of the tip atoms is the same as for two half-infinite chains linked by a weaker hopping [see Section 3.1, Eq. (3.5)]:

$$\rho_{\alpha\sigma}(\varepsilon) = -\frac{1}{\pi}\,\mathrm{Im}\left\{ \frac{\varepsilon - \varepsilon_{\alpha\sigma} - \Sigma_{\alpha\sigma}(\varepsilon)}{\pi_c^2 - [\varepsilon - \varepsilon_{\alpha\sigma} - \Sigma_{\alpha\sigma}(\varepsilon)]^2} \right\}, \tag{5.7}$$

Here, the spin-dependent onsite energies are $\varepsilon_{\alpha\sigma} = \varepsilon_0 \pm \Delta/2$ for majority/minority spin, and the center hopping elements π_c are the corresponding two center integrals. The resulting LDOS projected on one of the tip atoms for the different orbitals is shown in Fig. 5.3.

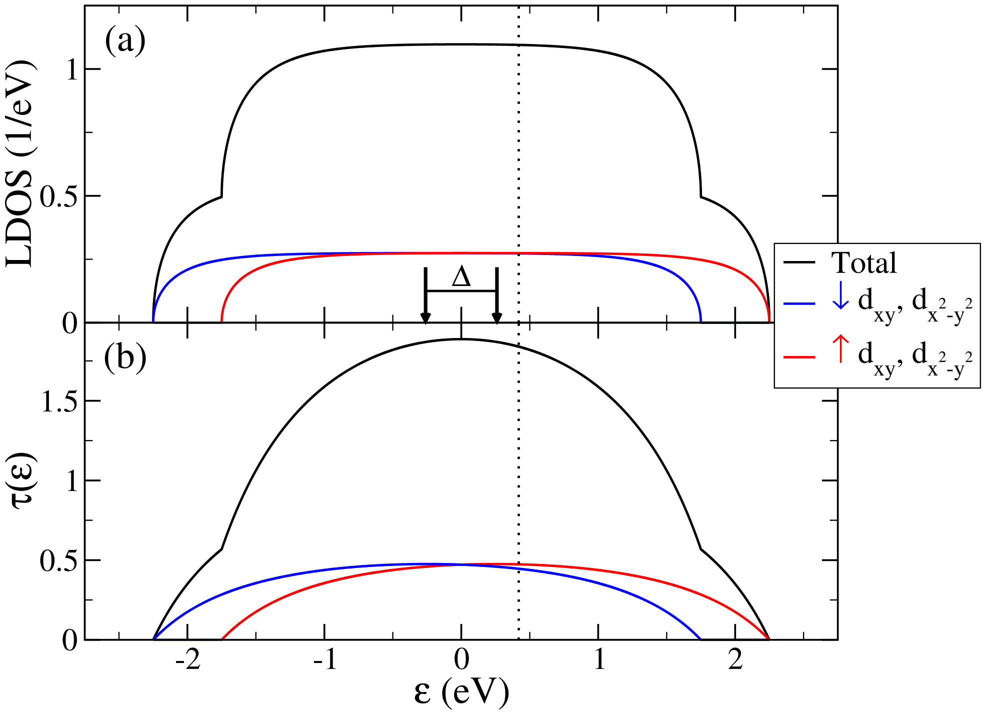

Figure 5.3: Linear chain of d_{E_2} orbitals in absence of SOC: (a) LDOS of the tip atoms projected on the orbitals and (b) total transmission and its channel decomposition. The position of ε_F is indicated with a dotted line.

In the real $3d$ materials ε_F lies close to the edge of the d bands. In this one-dimensional model we choose $\varepsilon_F = 0.42$ eV to be well within the bands to avoid the singularities at the band edges, which are particular to one-dimensional ideal chains (see Fig. 5.3).

Next, let us have a look at the transmission function for the system of four independent chains. The transmission $\tau_{\alpha\sigma}$ for the chain of orbital $\alpha\sigma$ reads (within the band):

$$\tau_{\alpha\sigma}(\varepsilon) = \frac{\left[\Gamma_{\alpha\sigma}(\varepsilon)\right]^2 \pi_c^2}{\left|\pi_c^2 - \left[\varepsilon - \varepsilon_{\alpha\sigma} - \Sigma_{\alpha\sigma}(\varepsilon)\right]^2\right|^2}, \tag{5.8}$$

where we introduced $\Gamma_{\alpha\sigma}(\varepsilon) = -2\,\mathrm{Im}\left[\Sigma_{\alpha\sigma}(\varepsilon)\right]$. These transmission functions are plotted in Fig. 5.3. In absence of impurities in the leads, the transmission curves as a function of energy are structureless. At the Fermi energy the transmission of the two-fold degenerate channels is 0.474 (0.446) for majority (minority) spins.

5.2.3 Conductance anisotropy in presence of spin-orbit coupling

Now we want to explore the anisotropy properties in presence of SOC. In order to keep things simple, we restrict the SOC to the two central atoms in the Hamiltonian Eq. (5.4).

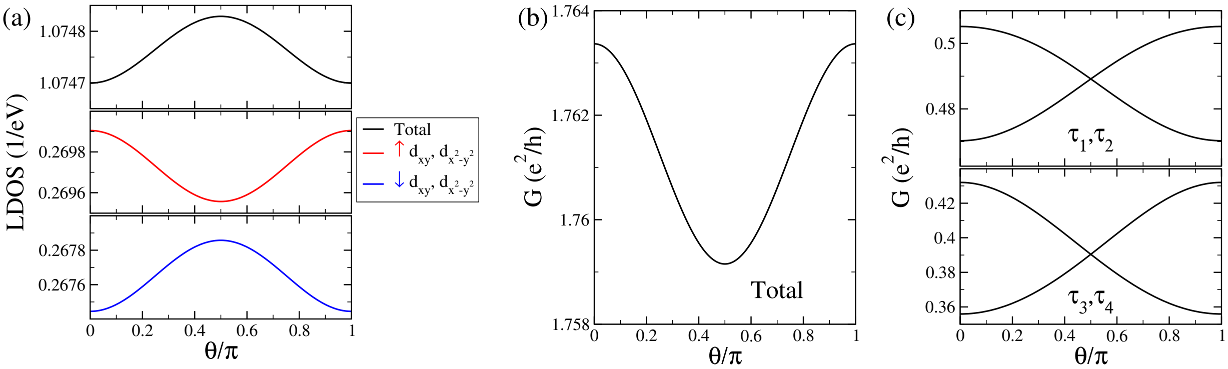

Figure 5.4: Linear chains of d_{E_2} orbitals with SOC in the tip atoms: (a) LDOS at the Fermi energy projected on the orbitals of one of the tip atoms, (b) total conductance and (c) channel decomposition.

Written in the same basis as in Eq. (5.5), the SOC Hamiltonian of Eq. (5.2) reads for each of the two tip atoms:

$$\left[\mathbf{H}^{(SO)}\right]_j = i2\xi \begin{pmatrix} 0 & 0 & -\cos\theta & \sin\theta \\ 0 & 0 & \sin\theta & \cos\theta \\ \cos\theta & -\sin\theta & 0 & 0 \\ -\sin\theta & -\cos\theta & 0 & 0 \end{pmatrix} . \tag{5.9}$$

Now the different orbitals are coupled depending on the direction of the spin quantization axis, which is fixed by the polar angle θ and the azimuthal angle ϕ.

Due to the rotational symmetry of the linear chain around $\vec{e}_z$ and the choice of the subset of the d_{E_2} orbitals, the SOC Hamiltonian (5.9) and thus the anisotropy properties do not depend on the azimuthal ϕ and the LDOS projected on the d_{xy}, $d_{x^2-y^2}$ orbitals are degenerate for each spin. In Fig. 5.4(a) we show the the LDOS at ε_F projected on the d_{xy}, $d_{x^2-y^2}$ orbitals of one of the tip atoms as a function of θ. The anisotropy of the orbitals with different spin have opposite sign but do not cancel, which leads to a finite anisotropy of the total LDOS.

The resulting anisotropy of the total conductance is shown in Fig. 5.4(b). Due to the time reversal symmetry and the invariance with respect to ϕ the total conductance fulfills $G(\theta) = G(\pi - \theta)$. This means that only even harmonics $\cos 2m\theta$ contribute to the total conductance anisotropy. With the parameters from Table 5.1 the conductance varies like $a_0 + a_1 \cos 2\theta$ with a small relative amplitude $a_1/a_0 \approx 0.3\%$.

On the other hand, the conductance channels in Fig. 5.4(c) show a much bigger absolute amplitude of variation and a behavior like $\cos(2m+1)\theta$. In the sum they cancel to a high degree. In particular at $\theta = \pi/2$, the conductance channels are twofold degenerate. This can be understood from the SOC Hamiltonian of Eq. (5.9), where at $\theta = \pi/2$ is only the orbitals of equal spin are coupled and lead to a degenerate conductance. If the full set of d orbitals is considered, the degeneracy at $\theta = \pi/2$ is then lifted by the non-zero orbital momentum matrices $\mathbf{l}^{(1)}$, $\mathbf{l}^{(2)}$ in the SOC Hamiltonian. This behavior is similar to the properties of ideal contacts geometries of Fe and Co in Fig. 5.6 and of Ni in Fig. 5.5.

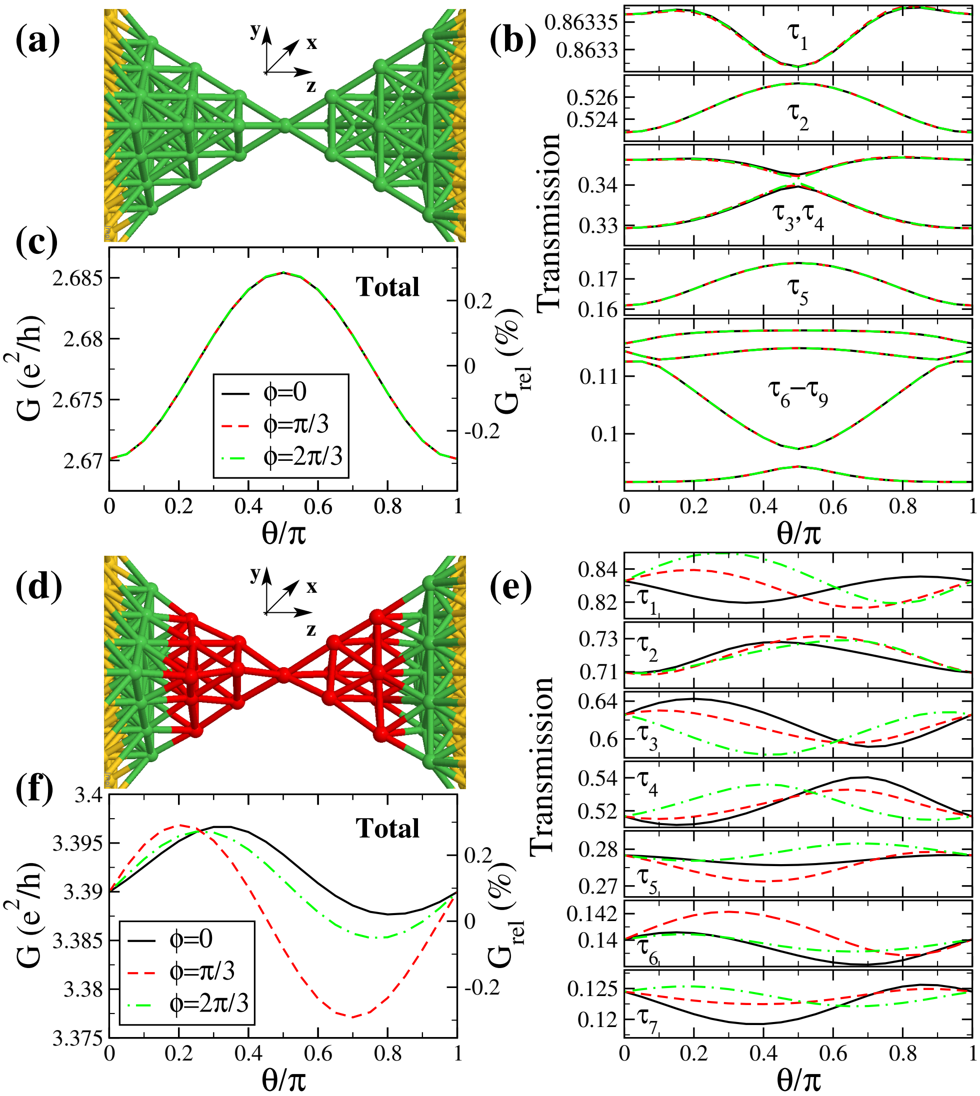

Figure 5.5: (a) Ideal Ni one-atom contact in fcc [111] direction with atoms on lattice positions. Green atoms are those in the atomic constriction, yellow ones are part of the surfaces used to model the leads. (b,c) Channel decomposition and the total linear conductance as a function of θ for different angles ϕ. The relative conductance is defined as $G_{rel} = \left[G(\theta,\phi) - \langle G(\theta,\phi)\rangle_\theta\right] / \langle G(\theta,\phi)\rangle_\theta$, where the conductance average over θ is defined as $\langle G(\theta,\phi)\rangle_\theta = \int_0^\pi \frac{d\theta}{\pi}\, G(\theta,\phi)$. (c) Channel decomposition of (b). (d)-(f) Same as (a)-(c), but with the contact distorted by randomly shifting the red atoms by up to 5% of the nearest-neighbour distance.

5.3 Ideal Contacts

Until now we discussed a minimal model for the AMR in ferromagnetic contacts, which still can be solved analytically. In the following Sections we add the SOC to the NRL approach and apply it to the ideal contact geometries of Fe, Co, and Ni to discuss the AMR there.

5.3.1 Ideal contact of Ni

Here we focus on the AMR in atomic contacts of Ni. In order to limit the calculation effort, we assume the SOC constant to be finite in the central region only and zero in the leads. We state here that this simplification does not alter the general result. In Section 5.4.2 we will explicitly compare the results for the conductance with and without SOC in the leads.

Due to the small SOC constant, the addition of SOC to the ferromagnetic Hamiltonian only changes slightly the overall conductance. However the petiteness of the SOC constant introduces some technical difficulties. As an example, in absence of SOC, the typical energy scales are of the order of the orbital energies, i.e. several electronvolts (see results discussed in Chapter 4), and the numerical calculation needs to be converged with respect to this scale. In presence of SOC however, the relevant energy scale is given by the SOC constant, fixed to 70 meV in this work, which demands correspondingly higher accuracy of the calculation. We typically obtain converged results for a lead broadening $\eta = 1$ mRy = 13.6 meV and 100^2 k-points for the lateral Fourier transformation.[1]

We now calculate the conduction properties of Ni atomic contacts in presence of SOC. First we consider an ideal geometry as in Fig. 4.3 with the atoms kept fixed on fcc lattice positions with a single central atom. The geometry is again depicted in Fig. 5.5(a). In Figs. 5.5(b,c) the conductance and its channel decomposition as function of θ for several values of ϕ are shown. Surprisingly, the conductance of this one-atom contact exhibits the bulk-like AMR with a $\cos 2\theta$ dependence (minimum at $\theta = 0$), an amplitude of 0.5% and practically no dependence on ϕ. In fact, as for the minimal model, the individual channels show a more complicated dependence on θ, and the amplitude of variation for one channel can be bigger than that of the total conductance, but in the latter these features cancel and the $\cos 2\theta$ dependence is recovered.

In the minimal model and for the ideal atomic contact geometry the contributions of the individual conductance channels cancel to a high degree. This suggests that the cancellation is related to the high symmetry of the ideal geometry.

To test this idea we have distorted the contact by shifting randomly the atomic positions by up to 5% of the nearest-neighbour distance [Fig. 5.5(d)]. As seen in Fig. 5.5(e), the individual channels now show roughly the same amplitude of variation with θ as in the ideal contact, but due to the disorder they exhibit a more complex θ dependence, and a strong dependence on ϕ. As a consequence, the contributions of the channels no longer cancel out and the AMR can have a different amplitude, with the conductance extrema shifted in θ and with a strong dependence on ϕ [Fig. 5.5(f)].

---

[1] In absence of SOC calculations are usually converged for $\eta = 500$ meV and 32^2 k-points.

This example illustrates that the origin of the anomalous angular dependence and amplitude of the AMR in atomic contacts can be simply the reduced symmetry of these junctions together with the fact that the conductance is mainly determined by a few atoms in the narrowest part of the constrictions.

5.3.2 Ideal contacts of Fe and Co

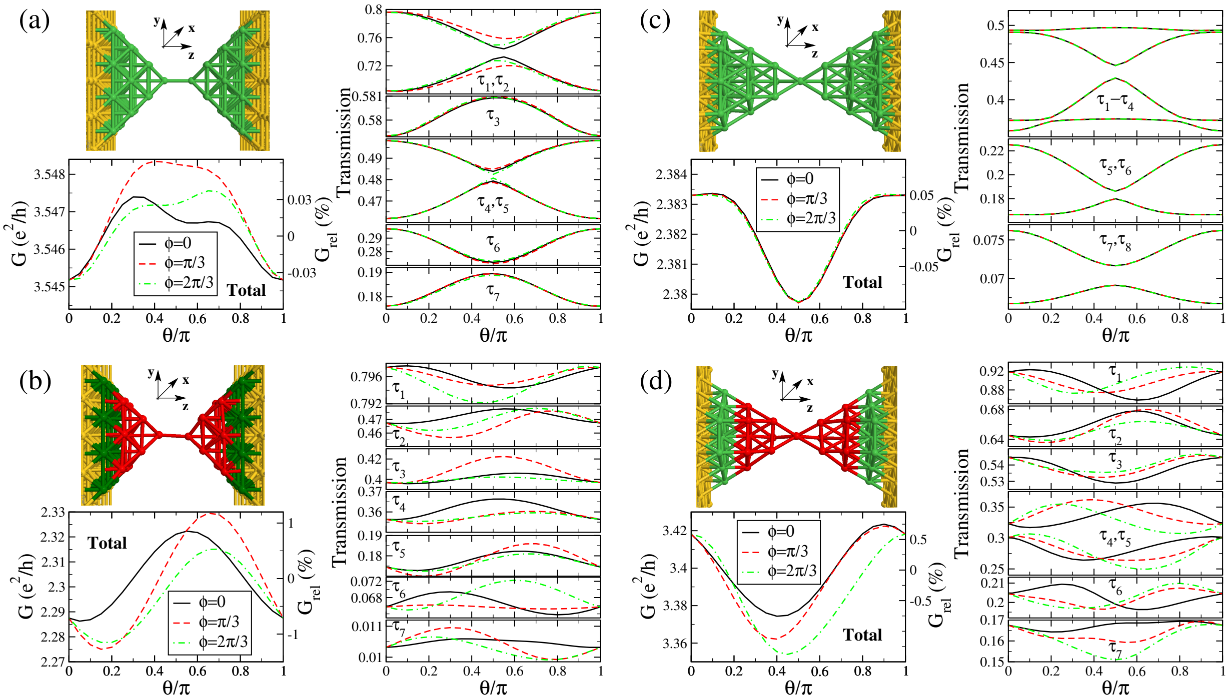

Figure 5.6: (a) The upper left panel shows a Fe dimer contact grown along the bcc [001] direction and with the atoms sitting on lattice positions. The green atoms are those in the atomic constriction, while the yellow ones are part of the surfaces used to model the leads. The lower left panel shows the total and relative conductance of this contact as a function of θ and for different azimuthal angles ϕ, while the right panel shows the corresponding channel decomposition. (b) The same as in (a), but for the geometry shown in the upper left panel, where the ideal contact of (a) has been distorted by changing randomly the atoms marked in the red by a maximum amplitude of 5% of the nearest-neighbour distance. (c,d) The same as in (a,b), but for a Co one-atom contact grown along the hcp [0001] direction.

Similar to the results in Fig. 5.5 for Ni, we also analyzed ideal contacts of Fe and Co. We use the SOC constant $\xi_i = 70$ meV also for these materials.

In the case of Fe, the ideal contact is formed in the bcc [001] direction with atoms on bcc lattice sites [Fig. 5.6(a)]. Due to the large apex angle of the two pyramids forming the contact, the atom layers behind the central atoms give an important contribution to the conductance. This is why in this case we chose a dimer configuration as ideal geometry, in order to reduce this contribution. Note that again, although the absolute anisotropy amplitude of an individual channel exceeds $0.05e^2/h$, the anisotropy amplitude of the total conductance remains more than one order of magnitude smaller, below $0.004e^2/h$ (i.e. $\leq 0.08\%$ in relative conductance variation). Under a perturbation of the contact geometry [Fig. 5.6(b)], the conductance changes remarkably, due to the sensitivity of the d orbitals to the geometry. More strikingly, the absolute anisotropy amplitude of the conductance increases by roughly one order of magnitude to $0.05e^2/h$, a relative conductance variation of more than 2%. Again this follows from the notable robustness of the amplitude of the channel anisotropy against disorder and the fact that the individual channel contributions do not cancel entirely anymore.

Likewise we analyzed atomic contacts of Co. An example for a contact formed by two pyramids with one central atom grown in the hcp [0001] direction is shown in Fig. 5.6(c). Here the total conductance shows a relative anisotropy amplitude of around 0.1%, this time with a maximum at $\theta = 0$ and quasi isotropic in ϕ. Again, the anisotropy amplitude of individual channels exceeds that of the total conductance by more than an order of magnitude. Under perturbation [Fig. 5.6(d)], the individual channel anisotropy amplitudes once again remain on the same order of magnitude but the different channel contributions do not cancel out anymore, leading to a relative anisotropy amplitude of 1% in the conductance. These findings support the general conclusions drawn based on the Ni contacts.

Note that recently Autès and coworkers [183] reported calculations for AMR in chains of Fe atoms between ideal surfaces. The main features of their results are in agreement with ours.

5.4 Anisotropy in contacts obtained from molecular dynamics simulation

So far we only considered ideal and somehow artificially disturbed contacts. Since the geometry plays such a prominent role in the AMR, it is important to analyze it for geometries that can be realized in an actual experiment. For this purpose, we have studied the AMR in the geometries obtained by classical MD simulations of the formation of Ni atomic contacts, as in Section 4.2. Again, the MD simulations were carried out by Markus Dreher of the group of Prof. Peter Nielaba at the Universität Konstanz.

5.4.1 Average conductance during contact evolution

An example of a contact evolution similar to the one discussed in the previous Chapter is shown in Fig. 5.7(a) Again, we start with an ideal Ni bar containing 112 atoms on lattice sites in fcc [001] direction and separate the attached rigid surfaces in a stepwise manner. In Fig. 5.7(b) we show the evolution of the spin-projected and total conductance during elongation in the absence of SOC. Adding SOC introduces only a small change in the averaged total conductance. As usual, the sudden atomic rearrangements are reflected

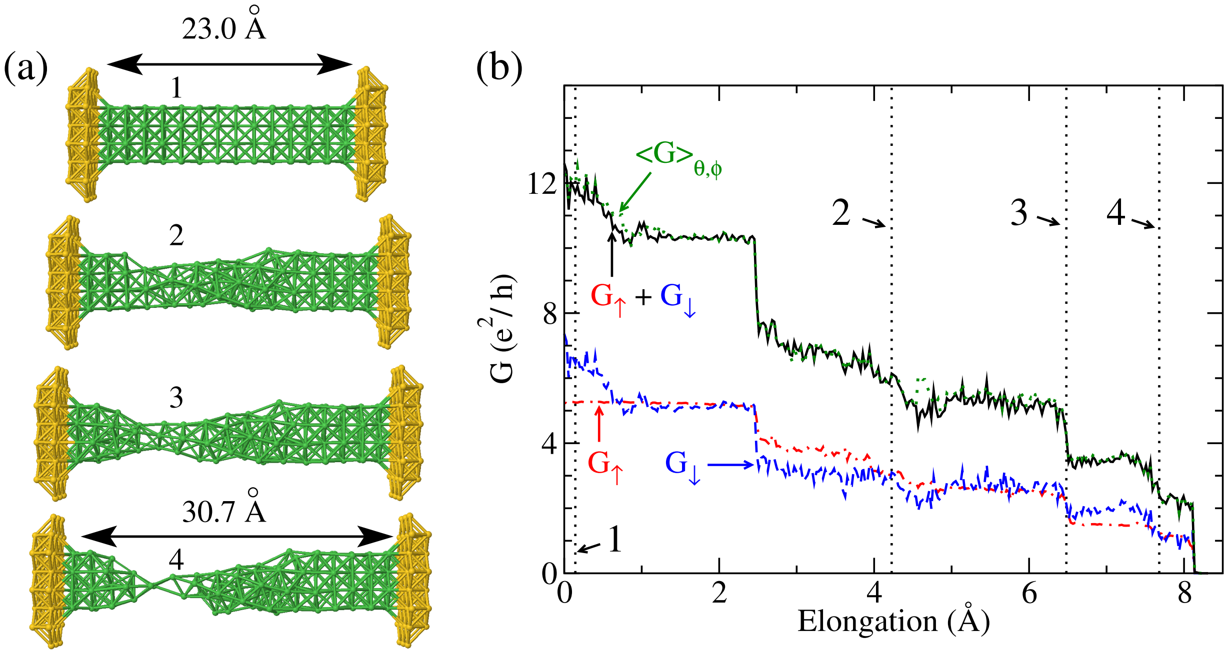

Figure 5.7: (a) Contact evolution of a Ni junction grown in the fcc [001] direction as obtained from the simulations of discussed in Section 4.2. (b) Spin-projected, $G_{\uparrow,\downarrow}$, and total conductance in the absence of SOC and $\langle G(\theta,\phi)\rangle_{\theta,\phi} = \int \frac{d\Omega}{4\pi}\, G(\theta,\phi)$, the total conductance averaged over θ, ϕ in the presence of SOC. Vertical lines correspond to the contact geometries in (a).

as steps in the conductance [1]. The vertical lines refer to the geometries of Fig. 5.7(a) obtained during the elongation.

5.4.2 Conductance anisotropy of representative geometries

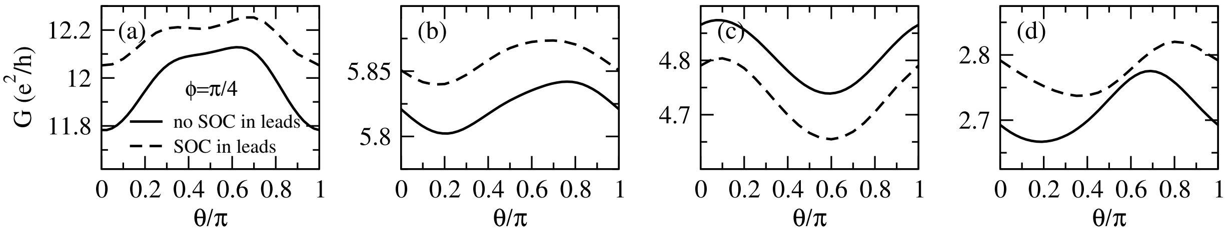

Figure 5.8: (a)-(d) Comparison of the total conductance anisotropy for geometries 1-4 of Fig. 5.7 for $\phi = \pi/4$ with and without SOC in the leads.

In the preceding Section we set the SOC constant $\xi = 0$ in the leads. We shall first ensure that neglecting SOC in the leads does not alter the general results. In order to analyze the influence of a finite SOC constant in the leads we analyzed the change in the conduction properties for the four geometries presented in Fig. 5.7(a). The result is shown in Fig. 5.8 for the total conductance as a function of θ and for $\phi = \pi/4$, with and without SOC in the leads. Neglecting the SOC in the leads introduces an additional potential barrier at the interface, which changes the contact resistance by a few percent However the anisotropy properties which we are interested in here remain basically unchanged.

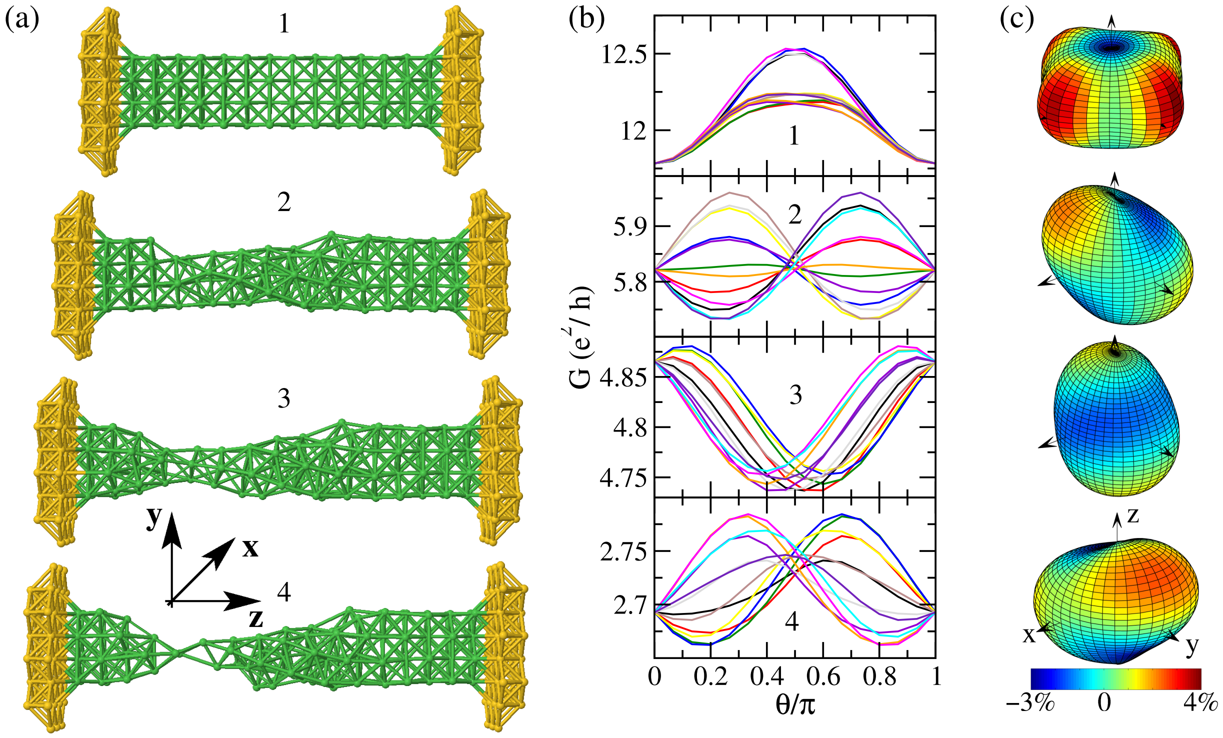

Figure 5.9: (a) Contact geometries as in Fig. 5.7(a) during evolution of the Ni junction. (b) Conductance vs. θ for the geometries in (a) and with ϕ in steps of $\pi/6$. (c) Relative AMR $[G(\theta,\phi) - \langle G(\theta,\phi)\rangle_{\theta,\phi}] / \langle G(\theta,\phi)\rangle_{\theta,\phi}$ in % projected on a "Bloch sphere", where $\langle G(\theta,\phi)\rangle_{\theta,\phi} = \int \frac{d\Omega}{4\pi}\, G(\theta,\phi)$ is the conductance averaged over all angles θ, ϕ.

For the indicated contact geometries we have computed the dependence of the conductance on θ and ϕ, and the results are shown in Fig. 5.9(b). For contact 1, which is just an elastic deformation of the ideal contact, the conductance has two types of behavior depending on ϕ: one is $\cos 2\theta$-like, while the other is clearly more complex. In order to visualize the overall angular dependence, we show the relative AMR on a "Bloch sphere" [Fig. 5.9(c)]. The contact 1 and hence its AMR have an approximate four-fold symmetry. When deformations emerge in the contact, the angular dependence becomes irregular and strongly dependent on ϕ. For example, for contact 2 there is a strong variation of AMR with ϕ, and depending on its value, the AMR amplitude can be almost one order of magnitude larger than in the bulk limit or cancel almost entirely. As the contact evolution proceeds, the AMR has an amplitude of around 2%. In almost all cases, the conductance is not only shifted in θ, but it also has a more complicated behavior than just $\cos 2\theta$.

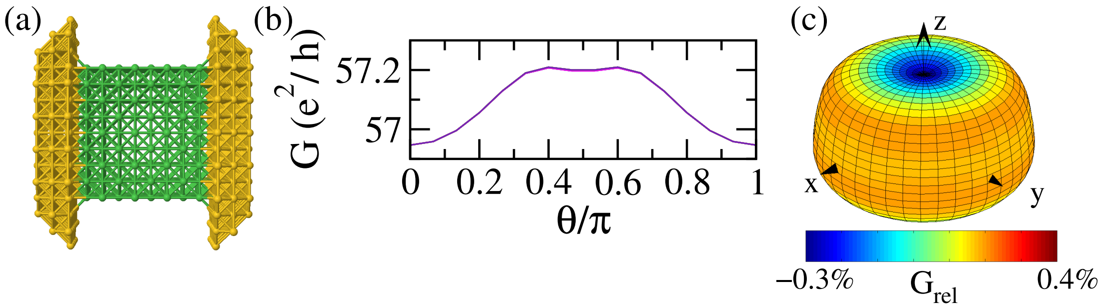

Figure 5.10: (a) Thick ideal contact geometry with 324 atoms in the center to model the bulk limit. (b,c) Conductance vs. θ (for several ϕ) for the geometry in (a) and relative AMR projected on a “Bloch sphere” as in Fig. 5.9(c). Note the scale change by a factor 10.

We can exploit the flexibility of the NRL approach to explore the conduction properties also in the opposite limit of thick contacts, which approach the bulk limit, similar to what we discussed in Section 3.4.5. We construct regular thick contact geometries with atoms on lattice positions coupled to ideal surfaces. An example of such a contact in is shown in Fig. 5.10(a). It contains 324 atoms in eight layers and has a fourfold symmetry around the transport axis $\vec{e}_z$.

The resulting conductance anisotropy as a function of θ is presented in Fig. 5.10(b) for different values of ϕ. It is basically isotropic in ϕ and approaches the bulk comportment with a variation like $\cos 2\theta$ and an amplitude of 0.5%. However there are still important deviations from the pure $\cos 2\theta$ angular dependency. In fact, when we fit the conductance anisotropy with a $\cos(2m\theta + \alpha_m)$ series, terms up to $m = 4$ give a significant contribution, which corresponds to λ^8 in the perturbation series of Section B. Again, the relative conductance anisotropy is projected on a Bloch sphere in Fig. 5.10(c).

5.4.3 Statistical analysis of the conductance anisotropy amplitude

In the preceding Sections we described the AMR from bulk to the atomic contact regime just before breaking of the contact. We can collect the data and conclude on some general tendencies that mark the difference between bulk and atomic contacts.

In Fig. 5.11 we present such a statistical analysis. Each contact geometry of the evolution of the Ni junction considered above is identified with its average conductance. Then for each geometry, the conductance anisotropy amplitudes are calculated as a function of the azimuthal ϕ. The statistical analysis of all contact geometries shows an increase of

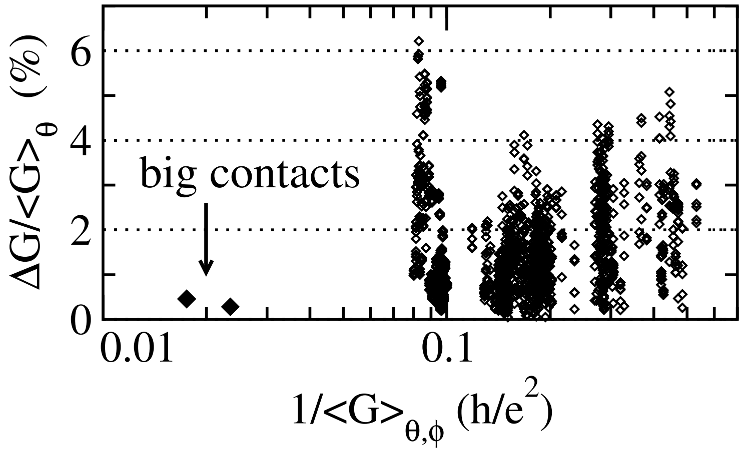

Figure 5.11: Statistical analysis of the conductance anisotropy amplitude as a function of the average resistance. For each contact geometry, characterized by an average conductance amplitude $\langle G(\theta,\phi)\rangle_{\theta,\phi} = \int \frac{d\Omega}{4\pi}\, G(\theta,\phi)$, the anisotropy amplitude is calculated for twelve values of ϕ (in steps of $\pi/12$). Here the anisotropy amplitude is defined as $\Delta G/\langle G\rangle_\theta$, where $\Delta G(\phi) = \max_\theta [G(\theta,\phi)] - \min_\theta [G(\theta,\phi)]$ and $\langle G(\theta,\phi)\rangle_\theta = \int_0^\pi \frac{d\theta}{\pi}\, G(\theta,\phi)$. In the graph the values of the anisotropy amplitude for the twelve ϕ values are represented with diamonds and are plotted as a function of the average resistance. If the ϕ dependency is weak, the diamonds for different ϕ lie close to each other (as in the case of the big contacts).

AMR to 2% on average in the last steps before breaking. This confirms that the lack of symmetry in atomic contacts gives rise to the enhancement of the AMR signal.

Approaching the tunneling regime ($G < 0.1e^2/h$, not shown in Fig. 5.11), we do not observe a further increase of the AMR amplitude, contrary to experiments (Fig. 5.1(c) and [54]). One reason may be that the isolated tip atoms in tunneling regime exhibit a finite orbital moment [180] (not considered here), which may lead to a local deviation of the spin-quantization axis from the field direction and an additional increase in resistance.

5.4.4 Spin-orbit coupling induced orbital momentum

In an isolated atom the Coulomb interaction leads to a finite orbital angular momentum according to Hund's third rule. For the case of Ni with electronic configuration [Ar]$3d^8 4s^2$, the ground state of an isolated atom is $^3\mathrm{F}_4$ with total orbital magnetic moment $\mu_L = 3\mu_B$ and total spin magnetic moment $\mu_S = g_e/2\mu_B$. Here $\mu_B = \frac{e\hbar}{2m_e}$ is the Bohr magneton and $g_e \approx 2.002$ the electron gyromagnetic ratio. In a bulk metal, due to the strong coupling with neighbouring atoms, the intra-atomic Coulomb interaction can be neglected, and the orbital momentum is practically quenched (experimentally, one finds $\mu_L \approx 0.05\mu_B$ per atom for bulk Ni [184]). The experimental spin magnetic moment per atom is [114] in Ni and can be compared to the value derived from the bulk DOS in Section 4.1.1.

For the intermediate case of a surface or a nanowire, neglecting the SOC, Desjonquères

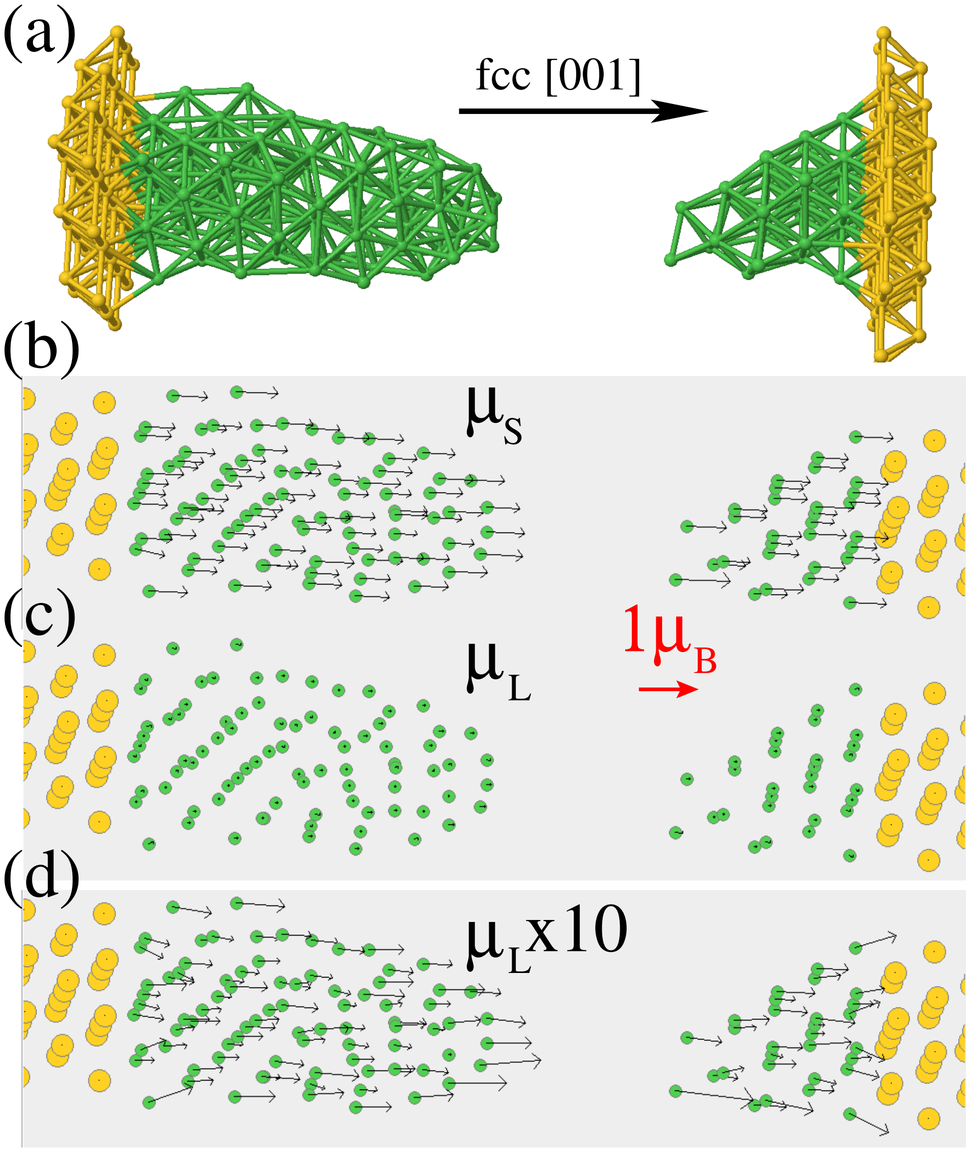

Figure 5.12: SOC induced orbital (and spin) magnetic momentum. (a) Geometry of the MD simulation series in the tunneling regime just after breaking of the contact. (b) Spin magnetic moment in the presence of SOC. The direction of the external field is indicated by the red arrow, whose length correspond to one Bohr magneton $\mu_B = \frac{e\hbar}{2m_e}$. The spin magnetic moments do not differ much from the quantization axis and are roughly $0.5 - 1.1\mu_B$ in magnitude, larger than the spin magnetic moment of bulk atoms of Ni [114]. SOC induced orbital magnetic moments (c) in the same scale as and (d) magnified by a factor of 10 compared to the spin magnetic moments from (b). They measure roughly $0.07\mu_B$ and tend to be bigger in atoms of the surface than for the higher coordinated atoms. The orbital magnetic moments of the surface atoms cease to be parallel to the spin quantization axis and tend to follow the surface of the geometry.

et al. [180] treated the intra-atomic electronic interaction in a Hartree-Fock scheme. They find for Fe, that when the coordination is reduced the orbital magnetic momentum per atom increases from $\mu_L \approx 0.05\mu_B$ in bulk Fe to $\mu_L \approx 0.2\mu_B$ on surfaces and finally $\mu_L \approx 1\mu_B$ for a monatomic wire.

In the case of the atomic contact in the tunneling limit, due to the reduced coordination of the tip atoms, such a finite orbital momentum may appear in those atoms and in consequence an additional increase in the AMR as discussed in the preceding Section 5.4.3.

However including Coulomb interaction is beyond the scope of this work and instead we will focus on changes in spin and magnetic orbital momenta when SOC is taken into account in an atomic contact. Such a SOC induced orbital momentum and its relation to the energy anisotropy was investigated by Bruno for monolayers of Co [181, 182].

Similar to what was discussed in Chapter 2, we can express the quantum-mechanical expectation value of an operator $\left\langle \hat{A} \right\rangle$ written in second quantization in terms of the non-equilibrium Green's function. In the basis of the creation operator $\hat{c}_{j\alpha\sigma}$ of orbital α and spin σ at site j, an intra-atomic operator $\hat{A}$ reads $\hat{A} = \sum_{j;\alpha\sigma,\beta\sigma'} [\mathbf{A}]_{j\alpha\sigma,j\beta\sigma'} \hat{c}^{\dagger}_{j\alpha\sigma} \hat{c}_{j\beta\sigma'}$ and at temperature zero its expectation value projected on the site j takes the form

$$\begin{aligned} \left\langle \hat{A}(t) \right\rangle_j &= \sum_{\alpha\sigma,\beta\sigma'} [\mathbf{A}]_{j\alpha\sigma,j\beta\sigma'} \left\langle \hat{c}^{\dagger}_{j\alpha\sigma}(t) \hat{c}_{j\beta\sigma'}(t') \right\rangle \Big|_{t' \to t} \qquad (5.10) \\ &= \frac{1}{i} \mathrm{Tr}_{\alpha\sigma} \left\{ \mathbf{A} \mathbf{G}^{+-}(t,t') \right\}_j \Big|_{t' \to t} = \int_{-\infty}^{\varepsilon_F} \frac{d\varepsilon}{2\pi} \mathrm{Tr}_{\alpha\sigma} \left\{ \mathbf{A} \left[\mathbf{G}^r(\varepsilon) - \mathbf{G}^a(\varepsilon) \right] \right\}_j \ . \end{aligned}$$

Applied to the spin magnetic momentum:

$$\vec{\mu}_{S,j} = \frac{e}{2m_e} g_e \frac{\hbar}{2} \vec{s}_j = \mu_B \frac{g_e}{2} \left(\langle \hat{\tau}_x \rangle_j, \langle \hat{\tau}_y \rangle_j, \langle \hat{\tau}_z \rangle_j \right)^t \ , \qquad (5.11)$$

where $g_e \approx 2.002$ is the electron gyromagnetic ratio. Similarly the Orbital magnetic moment reads:

$$\vec{\mu}_{L,j} = \frac{e}{2m_e} \frac{\hbar}{2} \vec{l}_j = \mu_B \left(\langle \hat{l}_x \rangle_j, \langle \hat{l}_y \rangle_j, \langle \hat{l}_z \rangle_j \right)^t \ , \qquad (5.12)$$

where the $\hat{l}_\mu$ (and before $\hat{\tau}_\mu$) can be expressed in terms of the orbital angular momentum matrices $\mathbf{l}^{(\mu)}$ (Pauli matrices $\tau^{(\mu)}$) as in Eq. (5.2).

We can now calculate the spin- and orbital magnetic moment of an arbitrary structure. As an example we take the geometry of the MD simulation just after breaking of the contact. This geometry is shown in Fig. 5.12(a) and in simplified form of unconnected atoms in Fig. 5.12(b-d). The two tips are sufficiently separated such that the tip atoms have only low coordination.

We orient the spin quantization along the transport direction as indicated with the red arrow, which has a length of one μ_B. The resulting spin magnetic moments in each atom as calculated from Eq. (5.11) are shown in Fig. 5.12(b). The arrows indicate the the direction and magnitude of the spin magnetic moment on each atom (as compared to the red arrow pointing in the direction of the spin quantization axis with a length of one μ_B). They show only small deviation from the spin quantization axis and measure $0.5 - 1.1\mu_B$. Notice that for higher coordinated atoms the spin magnetic moment tends to be smaller.

On the other hand, we can evaluate the orbital magnetic moment with Eq. 5.12. Note that in the orbital basis the orbital momentum matrices are imaginary and therefore antisymmetric. On the other hand, in absence of SOC, the Hamiltonian (5.1) is real and symmetric and thus the Green's functions then are symmetric, too. So, without SOC, the expression of the orbital magnetic moment consists of the trace over the product of a symmetric and an antisymmetric matrix, which is zero. Thus the orbital momentum vanishes.

In presence of SOC, the Green's functions are no longer symmetric, which causes a finite orbital momentum. This orbital magnetic moment is depicted for each atom in Fig.5.12(c,d): in (c) the length of the arrows is plotted in the same scale as for the spin magnetic moments in (b), and in (d) they are magnified by a factor 10 for visibility. The size of the orbital magnetic moments varies from $\approx 0.02\mu_B$ and $\approx 0.15\mu_B$, roughly one order of magnitude smaller than the spin magnetic moments. The small orbital magnetic moments exclusively appear in highly coordinated atoms and the highest value is found for the tip atom with lowest coordination. The direction of the orbital magnetic moments is roughly oriented along the spin quantization axis and follows more the When we rotate the direction spin quantization axis $\vec{e}_{z'}$, spin and orbital momenta follow roughly $\vec{e}_{z'}$ with stronger deviations for the orbital momenta (not shown here).

The fact that the SOC introduces a finite orbital momentum suggest to apply a perturbative treatment of the orbital magnetic moment in terms of the SOC Hamiltonian, as it was done by Bruno in the case of monolayers of Co [181]. This treatment is beyond the scope of this Section and can be found in Appendix B. Let us mention here that the momenta in second order perturbation theory are already reasonably close to the full results discussed in this Section.

We can conclude that the SOC induced orbital magnetic moments in Ni atomic contacts typically are smaller than the spin magnetic moments by a factor of 10 and are roughly parallel to the spin quantization axis. Thus if a orbital magnetic moment is at the origin of the strong increase of the AMR in the tunneling regime (as proposed by Autès *et al.* [183]), it must stem from another mechanism than SOC, like the intra-atomic Coulomb interactions discussed at the beginning of this Section.

5.5 Role of impurities in the leads

In none of the calculations have we found indications of tip resonances, which are present in ideal one-dimensional geometries [69, 70] and which were suggested as the origin of the experimental findings [69]. For example, the transmission for the contact of Fig. 5.5(a) has almost no structure around ε_F on the scale of millielectronvolts, as shown in Fig. 5.13(a). We thus believe that the voltage and temperature dependences reported in Refs. [54, 176] and shown in Fig. 5.1(d) are indeed associated with impurities close to the constriction, as reported earlier for non-magnetic junctions [124, 185].

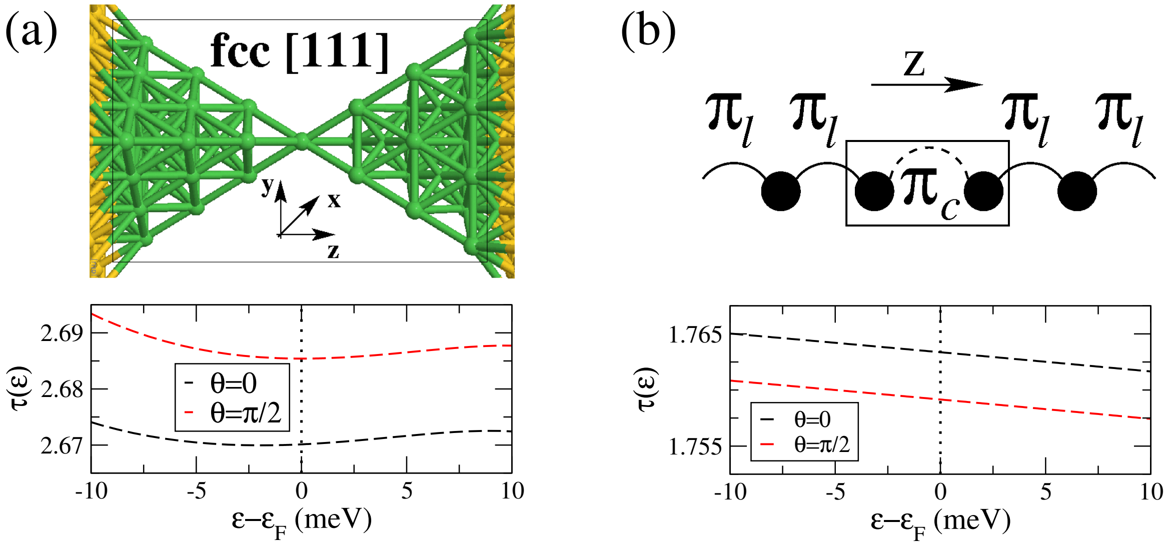

Figure 5.13: (a) Transmission $\tau(\varepsilon, V = 0)$ for the contact depicted in the upper panel [similar to Fig. 5.5(a)] with $\theta = 0,\pi/2$. (b) Total transmission for $\theta = 0,\pi/2$ of the chain model shown in the upper panel.

Following Ref. [185], one may estimate that the reported (Fig. 5.1(d) and [54]) voltage period of a few millivolts can stem from impurities located hundreds of nanometers away from the contact. Such length scales cannot be modeled realistically. However the minimal model that we discussed in Section 5.2 proofed to reproduce the main anisotropy features of ideal contacts. As an example, in Fig. 5.13(b) we show the transmission around ε_F for the minimal model, which does not show any structure on the scale of meVs in resemblance which the result for the ideal contact. In the minimal model it is then straightforward to introduce distant impurities in the leads.

In order to describe the conductance oscillations due to quantum interference, we may place an impurity in one of the leads, far away from the center. We choose to place it in the right lead, and model it by a modified hopping $\mathbf{t}_s$ between the N th and the $(N+1)$ th atom in this lead as indicated in the sketch of Fig. 5.14(a).

The lead self energy modified by the impurity is of the form $\tilde{\boldsymbol{\Sigma}}(\varepsilon)$ reads

$$\tilde{\boldsymbol{\Sigma}}(\varepsilon) = \mathbf{t}_l \tilde{\mathbf{g}}_0(\varepsilon) \mathbf{t}_l \tag{5.13}$$

where $\tilde{\mathbf{g}}_0(\varepsilon) = \tilde{\mathbf{g}}_{1,1}(\varepsilon)$ is the "surface" component of the impurity-modified lead Green's function $\tilde{\mathbf{g}}(\varepsilon)$. Placing now the impurity N sites away from the tip atom as indicated in Fig. 5.14(a), we find

$$\tilde{\mathbf{g}}_{1,1}(\varepsilon) = \mathbf{g}_{1,1}(\varepsilon) + \mathbf{g}_{1,N}(\varepsilon)\mathbf{t}_s \left(\mathbf{g}_0^{-1}(\varepsilon) - \mathbf{t}_s \mathbf{g}_{N,N}(\varepsilon)\mathbf{t}_s\right)^{-1} \mathbf{t}_s \mathbf{g}_{N,1}(\varepsilon). \tag{5.14}$$

Here $\mathbf{t}_s = \pi_s \mathbf{1}$ is the modified hopping modelling the impurity (with a reduced hopping integral π_s), $\mathbf{g}_0(\varepsilon)$ is as in Eq. 5.6, and the Green's functions $\mathbf{g}_{1,N}(\varepsilon)$, $\mathbf{g}_{N,1}(\varepsilon)$, $\mathbf{g}_{1,1}(\varepsilon)$,

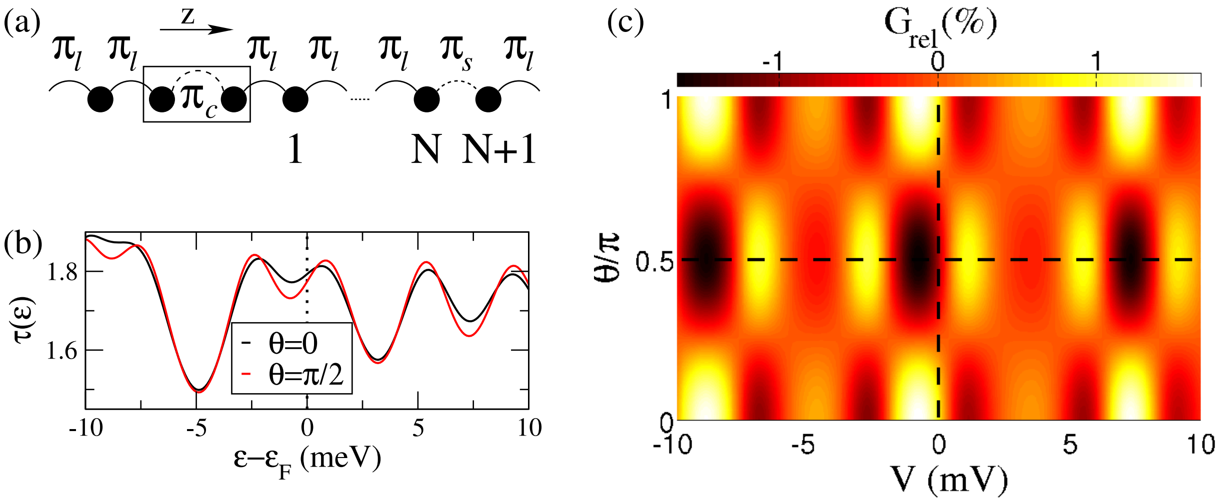

Figure 5.14: (a) Sketch of the chain model with an impurity in the right lead. (b) Corresponding transmission $\tau(\varepsilon, V = 0)$ for $\theta = 0,\pi/2$ with an impurity $N = 751$ sites from the scattering region. (c) Relative nonlinear conductance $G_{rel}(\theta, V) = [G(\theta, V) - \langle G(\theta, V)\rangle_\theta] / \langle G(\theta, V)\rangle_\theta$.

and $\mathbf{g}_{N,N}(\varepsilon)$ are those of the uncoupled N atom chain located between the center and the impurity. They are diagonal in the indices $(\alpha\sigma)$ and may be calculated analytically, with the results

$$\begin{aligned}
\{\mathbf{g}_{1,1}\}_{\alpha\sigma,\alpha\sigma} &= \{\mathbf{g}_{N,N}\}_{\alpha\sigma,\alpha\sigma} = \frac{\sin N\Phi_{\alpha\sigma}}{\pi_l \sin(N+1)\Phi_{\alpha\sigma}}, \\
\{\mathbf{g}_{1,N}\}_{\alpha\sigma,\alpha\sigma} &= \{\mathbf{g}_{N,1}\}_{\alpha\sigma,\alpha\sigma} = \frac{\sin \Phi_{\alpha\sigma}}{\pi_l \sin(N+1)\Phi_{\alpha\sigma}}
\end{aligned} \tag{5.15}$$

where $\Phi_{\alpha\sigma}$ is again defined through $\cos\Phi_{\alpha\sigma} = (\varepsilon - \varepsilon_{\alpha\sigma})/2\pi_l$. The resulting self energies remain diagonal in $(\alpha\sigma)$ and are in general oscillating functions of ε with an oscillation period proportional to the distance of the impurity from the center. By placing the impurity – a slightly reduced hopping $\pi_s = 0.8$ eV – $N = 751$ sites from the constriction, the results presented in Fig. 5.14(b,c) are obtained.

When an impurity is introduced in one of the chains the transmission changes drastically. We model it by using slightly reduced hoppings $\pi_s = 0.8$ eV between two atoms $N = 751$ sites away from the constriction in the right lead. The resulting transmission functions for $\theta = 0, \pi/2$ are shown in Figure 5.14(b). In addition to the expected oscillations in energy, there appears a modulation depending on θ that stems from the interference with the impurity.

When a finite voltage V is applied over the tip atoms, the nonlinear conductance $G(V) = dI/dV$ exhibits oscillations as a function of both voltage and the angle θ. The relative variations shown in Fig. 5.14(c) bear a striking resemblance to the experimental results of Ref. [54] [see example depicted in Fig.5.1(d)].

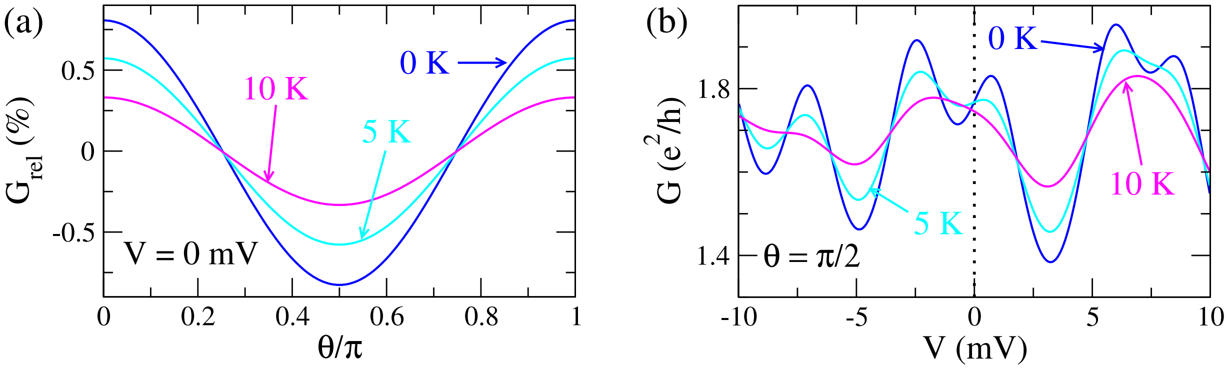

Figure 5.15: (a) Relative linear conductance vs. θ for indicated temperatures. (b) Voltage dependence of nonlinear conductance at $\theta = \pi/2$ and several temperatures. Results at 0 K correspond to the dashed lines in Fig. 5.14(c).

Finally, we show in Figs. 5.15(a,b) the temperature dependence of both the linear and non-linear conductance. The effect of temperature is to smooth the 0 K characteristics, again compatible with the experimental observations [176].

5.6 Conclusion

In conclusion we have shown that the anomalous magnitude and angular dependence of the AMR in ferromagnetic atomic-sized contacts can be explained naturally in terms of the reduced symmetry of the atomic junction geometries. We predict a strong anisotropy of the conductance channels, but have not found any signature of BAMR. We showed that the SOC induced orbital moment is an order of magnitude smaller than its spin counterpart. And finally we have presented a simple model which illustrates that the pronounced voltage and temperature dependence found in some experiments may originate from the presence of impurities close to the constriction.

Chapter 6

Summary

In this thesis we described the conduction properties of atomic-sized metallic contacts. It is divided into two parts:

In a first part – after an introduction to the theoretical framework in Chapter 2 – we described in Chapter 3 the conduction properties of nonmagnetic atomic-sized metal contacts within the NRL tight binding approach. First we reproduced well-established results of the conductance properties of one-atom contacts of metals with partially filled valence orbitals. We compared the results for Al with accurate *ab initio* calculations and find good overall agreement. Then we applied the NRL approach to the limiting case of the divalent metals Zn and Mg. In the case of small clusters these elements possess insulator properties due to filled s orbitals, whereas in the bulk limit they are metallic as a result of strong hybridization of the s and p orbitals. We found metallic transport properties for the intermediate case of atomic contacts for both materials. In atomic contacts of Zn a dominating conductance channel typically is accompanied by second and third less transmissive channels. These results were confirmed by simultaneously performed experiments of the group of Prof. Elke Scheer. Together with the mechanical stability of Zn atomic contacts and the fact that Zn is a superconductor, it may be an interesting electrode material for molecular electronics. For Mg we found insulating behaviour only in the case of the single-atom chain and metallic behaviour in all other atomic-sized contacts. In the single-atom contacts we always observed one close to fully open channel, which is confirmed by experimental conductance traces recorded at 4.2 K, which typically show a conductance plateau at $1G_0$ before breaking and yield a pronounced peak at $1G_0$ in the conductance histogram.

In a second part the NRL approach was extended to the investigation of atomic contacts of the $3d$ ferromagnets Fe, Co, and Ni. First, in Chapter 4, we analyzed the general transport properties of these systems and discussed in particular the contribution of the d orbitals to transport. In addition we could point to important predictions like the high degree of spin polarization of the current in the tunneling limit of atomic contacts of Ni. By combining the conductance calculation with a MD simulation of the stretching of a Ni contact (performed by Dr. Markus Dreher at the Universität Konstanz) we could analyze the mechanical properties and the conductance traces during the breaking of a Ni nanowire.

On this basis we could calculate a conductance histogram that can directly be compared with experimental results.

Finally in Chapter 5 we analyzed the Anisotropic Magnetoresistance (AMR) in ferromagnetic atomic contacts. In the case of macroscopic systems, the AMR is widely applied in sensor technology. For atomic-sized contacts a significant increase of the AMR amplitude was observed experimentally. We could confirm these observations theoretically. Furthermore we could predict a particularly strong anisotropy amplitude of the conductance channels. In a statistical analysis we could uniformly describe the evolution of the conductance anisotropy from bulky systems to the atomic contact limit. We could trace back the particular AMR properties of the atomic contacts to reduced symmetry in those contacts. At last we analyzed the interplay between the AMR in an atomic contact and a possible distant impurity in the leads. Our findings may serve to explain the abnormal conductance fluctuations observed in some experiments.

The present work may be as a basis for further investigation of ferromagnetic atomic contacts like the magnetoresistance or the electron-magnon interaction in those contacts.

Appendix A

Slater Koster two-center matrix elements

In the Table A.1 we give the full list of of the two-center Hamiltonian or overlap matrix elements of the s, p, and d orbitals as discussed in Sec. 2.1.3. They are expressed in terms of the 10 irreducible matrix elements ssσ, spσ, sdσ, ppσ, ppπ, pdσ, pdπ, ddσ, ddπ, and ddδ, which are functions of the distance between the two atoms under consideration.

Elements that do not appear explicitly in the list can be obtained by appropriate permutation of the indices:

In the particular case of a linear chain in $\vec{e}_z$ direction (see Secs. 3.1 and 5.2), the direction cosines in $\vec{e}_x$ and $\vec{e}_y$ direction vanish ($l = 0 = m$) and the form of the Hamiltonian as indicated in the Sections follows.

$\mathrm{K}_{is,js} =$	$\mathrm{ss}\sigma$
$\mathrm{K}_{is,jx} =$	$l\ \mathrm{sp}\sigma$
$\mathrm{K}_{ix,jx} =$	$l^2\ \mathrm{pp}\sigma + \left(1 - l^2\right)\ \mathrm{pp}\pi$
$\mathrm{K}_{ix,jy} =$	$lm\left(\mathrm{pp}\sigma - \mathrm{pp}\pi\right)$
$\mathrm{K}_{is,jxy} =$	$\sqrt{3}lm\ \mathrm{sd}\sigma$
$\mathrm{K}_{is,jx^2-y^2} =$	$\frac{1}{2}\sqrt{3}\left(l^2 - m^2\right)\ \mathrm{sd}\sigma$
$\mathrm{K}_{is,j3z^2-r^2} =$	$\left(n^2 - \frac{1}{2}\left(l^2 + m^2\right)\right)\ \mathrm{sd}\sigma$
$\mathrm{K}_{ix,jxy} =$	$\sqrt{3}l^2m\ \mathrm{pd}\sigma + m\left(1 - 2l^2\right)\ \mathrm{pd}\pi$
$\mathrm{K}_{ix,jyz} =$	$\sqrt{3}lmn\ \mathrm{pd}\sigma - 2lmn\ \mathrm{pd}\pi$
$\mathrm{K}_{ix,jzx} =$	$\sqrt{3}l^2n\ \mathrm{pd}\sigma + n\left(1 - 2l^2\right)\ \mathrm{pd}\pi$
$\mathrm{K}_{ix,jx^2-y^2} =$	$\frac{1}{2}\sqrt{3}l\left(l^2 - m^2\right)\ \mathrm{pd}\sigma + l\left(1 - l^2 + m^2\right)\ \mathrm{pd}\pi$
$\mathrm{K}_{iy,jx^2-y^2} =$	$\frac{1}{2}\sqrt{3}m\left(l^2 - m^2\right)\ \mathrm{pd}\sigma - l\left(1 + l^2 - m^2\right)\ \mathrm{pd}\pi$
$\mathrm{K}_{iz,jx^2-y^2} =$	$\frac{1}{2}\sqrt{3}n\left(l^2 - m^2\right)\ \mathrm{pd}\sigma - n\left(l^2 - m^2\right)\ \mathrm{pd}\pi$
$\mathrm{K}_{ix,j3z^2-r^2} =$	$l\left[n^2 - \frac{1}{2}\left(l^2 + m^2\right)\right]\ \mathrm{pd}\sigma - \sqrt{3}ln^2\ \mathrm{pd}\pi$
$\mathrm{K}_{iy,j3z^2-r^2} =$	$m\left[n^2 - \frac{1}{2}\left(l^2 + m^2\right)\right]\ \mathrm{pd}\sigma - \sqrt{3}mn^2\ \mathrm{pd}\pi$
$\mathrm{K}_{iz,j3z^2-r^2} =$	$n\left[n^2 - \frac{1}{2}\left(l^2 + m^2\right)\right]\ \mathrm{pd}\sigma + \sqrt{3}n\left(l^2 + m^2\right)\ \mathrm{pd}\pi$
$\mathrm{K}_{ixy,jxy} =$	$3l^2m^2\ \mathrm{dd}\sigma + \left(l^2 + m^2 - 4l^2m^2\right)\ \mathrm{dd}\pi + \left(n^2 + l^2m^2\right)\ \mathrm{dd}\delta$
$\mathrm{K}_{ixy,jyz} =$	$3lm^2n\ \mathrm{dd}\sigma + ln\left(1 - 4m^2\right)\ \mathrm{dd}\pi + lm\left(n^2 - 1\right)\ \mathrm{dd}\delta$
$\mathrm{K}_{ixy,jzx} =$	$3l^2mn\ \mathrm{dd}\sigma + mn\left(1 - 4l^2\right)\ \mathrm{dd}\pi + mn\left(l^2 - 1\right)\ \mathrm{dd}\delta$
$\mathrm{K}_{ixy,jx^2-y^2} =$	$\frac{3}{2}lm\left(l^2 - m^2\right)\ \mathrm{dd}\sigma + 2lm\left(m^2 - l^2\right)\ \mathrm{dd}\pi + \frac{1}{2}lm\left(l^2 - m^2\right)\ \mathrm{dd}\delta$
$\mathrm{K}_{iyz,jx^2-y^2} =$	$\frac{3}{2}mn\left(l^2 - m^2\right)\ \mathrm{dd}\sigma - mn\left[1 + 2\left(l^2 - m^2\right)\right]\ \mathrm{dd}\pi + mn\left[1 + \frac{1}{2}\left(l^2 - m^2\right)\right]\ \mathrm{dd}\delta$
$\mathrm{K}_{izx,jx^2-y^2} =$	$\frac{3}{2}nl\left(l^2 - m^2\right)\ \mathrm{dd}\sigma + nl\left[1 - 2\left(l^2 - m^2\right)\right]\ \mathrm{dd}\pi - nl\left[1 - \frac{1}{2}\left(l^2 - m^2\right)\right]\ \mathrm{dd}\delta$
$\mathrm{K}_{ixy,j3z^2-r^2} =$	$\sqrt{3}lm\left[n^2 - \frac{1}{2}\left(l^2 + m^2\right)\right]\ \mathrm{dd}\sigma - 2\sqrt{3}lmn^2\ \mathrm{dd}\pi + \frac{1}{2}\sqrt{3}lm\left(1 + n^2\right)\ \mathrm{dd}\delta$
$\mathrm{K}_{iyz,j3z^2-r^2} =$	$\sqrt{3}mn\left[n^2 - \frac{1}{2}\left(l^2 + m^2\right)\right]\ \mathrm{dd}\sigma + \sqrt{3}mn\left(l^2 + m^2 - n^2\right)\ \mathrm{dd}\pi - \frac{\sqrt{3}}{2}mn\left(l^2 + m^2\right)\ \mathrm{dd}\delta$
$\mathrm{K}_{izx,j3z^2-r^2} =$	$\sqrt{3}ln\left[n^2 - \frac{1}{2}\left(l^2 + m^2\right)\right]\ \mathrm{dd}\sigma + \sqrt{3}ln\left(l^2 + m^2 - n^2\right)\ \mathrm{dd}\pi - \frac{\sqrt{3}}{2}ln\left(l^2 + m^2\right)\ \mathrm{dd}\delta$
$\mathrm{K}_{ix^2-y^2,jx^2-y^2} =$	$\frac{3}{4}\left(l^2 - m^2\right)^2\ \mathrm{dd}\sigma + \left[l^2 + m^2 - \left(l^2 - m^2\right)^2\right]\ \mathrm{dd}\pi + \left[n^2 + \frac{1}{4}\left(l^2 - m^2\right)^2\right]\ \mathrm{dd}\delta$
$\mathrm{K}_{ix^2-y^2,j3z^2-r^2} =$	$\frac{\sqrt{3}}{2}\left(l^2 - m^2\right)\left[n^2 - \frac{1}{2}\left(l^2 + m^2\right)\right]\ \mathrm{dd}\sigma + \sqrt{3}n^2\left(m^2 - l^2\right)\ \mathrm{dd}\pi + \frac{\sqrt{3}}{4}\left(1 + n^2\right)\left(l^2 - m^2\right)\ \mathrm{dd}\delta$
$\mathrm{K}_{i3z^2-r^2,j3z^2-r^2} =$	$\left[n^2 - \frac{1}{2}\left(l^2 + m^2\right)\right]^2\ \mathrm{dd}\sigma + \sqrt{3}n^2\left(l^2 + m^2\right)\ \mathrm{dd}\pi + \frac{3}{4}\left(l^2 + m^2\right)^2\ \mathrm{dd}\delta$

Table A.1: Hamiltonian or overlap matrix elements between two s, p, and d orbitals located on atom i and j, respectively as discussed for the s, p orbitals in Sec. 2.1.3. The positions of atoms i and j being $\mathbf{r}_i = \left(r_{i,x}, r_{i,y}, r_{i,z}\right)$ and $\mathbf{r}_j = \left(r_{j,x}, r_{j,y}, r_{j,z}\right)$ the Hamilton (or overlap) matrix elements are obtained from the irreducible matrix elements with help of the direction cosines $l = \left(r_{j,x} - r_{i,x}\right)/r_{ij}$, $m = \left(r_{j,y} - r_{i,y}\right)/r_{ij}$, and $n = \left(r_{j,z} - r_{i,z}\right)/r_{ij}$, where $r_{ij} = \left|\mathbf{r}_j - \mathbf{r}_i\right|$ is the distance between the two atoms (see Ref. [82]).

Appendix B

Expectation values of observables in presence of spin-orbit coupling

In this chapter we will express equilibrium expectation values in terms of equilibrium Green's functions in the presence of spin-orbit coupling (SOC). First we will revisit the expression of the SOC Hamiltonian and write out explicitley its spin components, which allows for a simple perturbation expansion. Next we will write out the expectation values with full Green's functions. Then we will treat the SOC Hamiltonian as a perturbation and evaluate the same expectation values in the first orders of perturbation theory. Finally we will analyze the angular dependence of the total conductance in more detail.

Spin components of the spin-orbit Hamiltonian

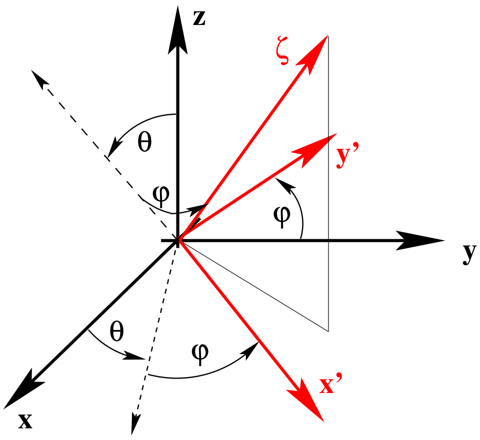

Figure B.1: Rotation of the coordination system $\{x, y, z\}$ fixed to the geometry to the coordination system $\{x', y', \zeta\}$ of the spin quantization axis in direction (θ, ϕ).

The SOC Hamiltonian couples the orbital momentum $\vec{l}$, fixed to the coordinate axis

$\{x, y, z\}$ of the geometry to the spin $\vec{s}$ pointing in direction $\vec{e}_\zeta$ of the spin quantization axis. The coordinate system $\{x', y', \zeta\}$ fixed to the spin quantization axis is obtained from $\{x, y, z\}$ by a rotation by θ around $y-$axis followed by a rotation by ϕ around z as indicated in Fig. B.1. We can explicitly write out the axis transformations:

$$(\vec{e}_{x'}|\vec{e}_{y'}|\vec{e}_\zeta) = \mathbf{R}_z(\phi)\mathbf{R}_y(\theta)\,(\vec{e}_x|\vec{e}_y|\vec{e}_z) \quad = \tag{B.1}$$

$$= \left(\begin{array}{lll} cos\phi cos\theta & -sin\phi & cos\phi sin\theta \\ sin\phi cos\theta & cos\phi & sin\phi sin\theta \\ -sin\theta & 0 & cos\theta \end{array}\right)(\vec{e}_x|\vec{e}_y|\vec{e}_z) \quad =: \quad \mathbf{R}\,(\vec{e}_x|\vec{e}_y|\vec{e}_z)\ . \tag{B.2}$$

Then the components of the vector of angular momentum matrices $\vec{\mathbf{l}} = \mathbf{l}_i\vec{e}_i = \mathbf{l}'_{i'}\vec{e}_{i'}$ in the two coordinate systems transform as:

$$\begin{array}{lcl} \mathbf{l}'_{x'} = \mathbf{l}_i R_{i1} & & \mathbf{l}_x = R_{1i}\mathbf{l}'_{i'} \\ \mathbf{l}'_{y'} = \mathbf{l}_i R_{i2} & | & \mathbf{l}_y = R_{2i}\mathbf{l}'_{i'} \\ \mathbf{l}'_\zeta = \mathbf{l}_i R_{i3} & & \mathbf{l}_z = R_{3i}\mathbf{l}'_{i'} \end{array} \quad . \tag{B.3}$$

With this, we can express the components of $\vec{\mathbf{l}}$ in the coordinate system of the spin quantization axis:

$$\mathbf{l}^\pm = \mathbf{l}'_{x'} \pm i\mathbf{l}'_{y'} = \mathbf{l}_i(R_{i1} \pm iR_{i2}) =: \{ \begin{array}{c} b_i^*\mathbf{l}_i \\ b_i\mathbf{l}_i \end{array} , b_i = R_{i1} - iR_{i2}, \tag{B.4}$$

$$\mathbf{l}'_\zeta = \mathbf{l}_i R_{i3} =: a_i\mathbf{l}_i, a_i = R_{i3} \tag{B.5}$$

Again with the definition of the Pauli matrices as in (5.3):

$$\boldsymbol{\tau}^{(1)} = \begin{pmatrix} 0 & 1 \\ 1 & 0 \end{pmatrix}, \quad \boldsymbol{\tau}^{(2)} = \begin{pmatrix} 0 & -i \\ i & 0 \end{pmatrix}, \quad \boldsymbol{\tau}^{(3)} = \begin{pmatrix} 1 & 0 \\ 0 & -1 \end{pmatrix} \quad . \tag{B.6}$$

and $\tau_\pm = \tau_1 \pm i\tau_2$, the SOC Hamiltonian can be written as:

$$\mathbf{H}^{(SO)} = \xi(\mathbf{l}'_\zeta\tau_3 + \mathbf{l}^+\tau_- + \mathbf{l}^-\tau_+) = \xi \left(\begin{array}{cc} a_i & b_i \\ b_i^* & -a_i \end{array}\right)\mathbf{l}_i, \tag{B.7}$$

where ξ is the spin-orbit coupling constant. Note that as for the vector of spin matrices $\vec{\mathbf{s}} = \frac{\hbar}{2}\vec{\tau}$, the factor $\frac{1}{2}$ might already be included in the spin-orbit coupling constant ξ.

Two important relations between the a_i and b_i follow directly from their definitions:

$$b_i b_j^* = -a_i a_j + \delta_{ij} + i\epsilon_{ijk}a_k, \tag{B.8}$$

$$a_i b_j - a_j b_i = -i\epsilon_{ijk}b_k. \tag{B.9}$$

Expectation values of equilibrium properties

For a single-electron operator $\hat{A}(t) = [\mathbf{A}]_{lk}\, \hat{c}_k^{\dagger}(t)\hat{c}_l(t)$ the expectation value $\left\langle \hat{A}(t) \right\rangle$ can be expressed with the help of Keldysh-Green's functions as: $[\mathbf{G}^{+-}]_{kl}\,(t,t^+) = i\left\langle \hat{c}_k^{\dagger}(t^+)\hat{c}_l(t) \right\rangle$ (with $t^+ = t+0^+$ infinitesimally after t). Here atom, orbital and spin indices were condensed in one index. This leads to $\left\langle \hat{A}(t) \right\rangle = \frac{1}{i}\,[\mathbf{A}]_{lk}\,[\mathbf{G}^{+-}]_{kl}\,(t,t^+)$. Fourier-transform at time $t=0$:

$$\left\langle \hat{A}(0) \right\rangle = [\mathbf{A}]_{lk} \int \frac{d\omega}{2\pi i}\, \left[\mathbf{G}^{+-}(\omega)\right]_{kl} = [\mathbf{A}]_{lk} \int \frac{d\omega}{2\pi i}\, \left[\mathbf{G}^{a}(\omega) - \mathbf{G}^{r}(\omega)\right]_{kl} f(\omega) \qquad \text{(B.10)}$$

Finally, at temperature $T=0$:

$$\left\langle \hat{A}(0) \right\rangle = [\mathbf{A}]_{lk} \int_{-\infty}^{\varepsilon_F} \frac{d\omega}{2\pi i}\, \left[(\mathbf{G}^{r})^{\dagger}(\omega) - \mathbf{G}^{r}(\omega)\right]_{kl}. \qquad \text{(B.11)}$$

Expectation values with full Green's function

Now we use the definition of the expectation values (B.11) to calculate them the full Green's function including SOC. Occupation n, total energy ε_{tot}, orbital angular moment $\vec{l}$, and spin moment $\vec{s}$ refer to atoms and therefore the trace is understood as summation over orbital- (and if necessary also spin-) indices of the atom under consideration. With the full retarded Green's function divided into its spin-components:

$$\mathbf{G}^{r}(\omega) = \begin{pmatrix} \mathbf{G}^{\uparrow\uparrow}(\omega) & \mathbf{G}^{\uparrow\downarrow}(\omega) \\ \mathbf{G}^{\downarrow\uparrow}(\omega) & \mathbf{G}^{\downarrow\downarrow}(\omega) \end{pmatrix}, \qquad \text{(B.12)}$$

the expressions for occupation n and total energy ε_{tot} of a site j read:

$$\langle n \rangle_j = -\frac{1}{\pi} \int_{-\infty}^{\varepsilon_F} d\omega\ \mathrm{Im}\left\{\mathrm{Tr}\left[\mathbf{G}^{\uparrow\uparrow}(\omega) + \mathbf{G}^{\downarrow\downarrow}(\omega)\right]\right\}_j \qquad \text{(B.13)}$$

$$\langle E_{tot} \rangle_j = -\frac{1}{\pi} \int_{-\infty}^{\varepsilon_F} \omega d\omega\ \mathrm{Im}\left\{Tr\left[\mathbf{G}^{\uparrow\uparrow}(\omega) + \mathbf{G}^{\downarrow\downarrow}(\omega)\right]\right\}_j, \qquad \text{(B.14)}$$

where the trace is understood to run over the remaining orbital indices.

The orbital momentum components in the coordinate system of the spin quantization axis are $\left\langle \vec{\mathbf{l}}' \right\rangle$, where we used $\mathbf{l}'_{i'} = c_{i'j}\mathbf{l}_j$ with the definition $c_{i'j} = \{\mathrm{Re}\,[b_j]\,,\ \mathrm{Im}\,[b_j]\,, a_j\}$ for the components of $\vec{\mathbf{l}}'$ on the axis $\{x', y', \zeta\}$. Then the expectation corresponding value read:

$$\langle \mathbf{l}'_{i'} \rangle = \frac{\hbar}{2\pi i} c_{i'j} \int_{-\infty}^{\varepsilon_F} d\omega\ \mathrm{Tr}\left\{\mathbf{l}_j\left[\left(\mathbf{G}^{\uparrow\uparrow}\right)^{\dagger} + \left(\mathbf{G}^{\downarrow\downarrow}\right)^{\dagger} - \mathbf{G}^{\uparrow\uparrow} - \mathbf{G}^{\downarrow\downarrow}\right]\right\}. \qquad \text{(B.15)}$$

The Pauli matrices τ_j from above fix the components of the spin $\langle \vec{\mathbf{s}} \rangle$ projected onto the coordinate axis of $\{x', y', \zeta\}$:

$$\langle \mathbf{s}_{i'} \rangle = \frac{\hbar}{4\pi i} \int_{-\infty}^{\varepsilon_F} d\omega\ \mathrm{Tr}\left\{\tau_i\left[(\mathbf{G}^{r})^{\dagger}(\omega) - \mathbf{G}^{r}(\omega)\right]\right\}. \qquad \text{(B.16)}$$

This reads for the components:

$$\begin{aligned}\langle \mathbf{s}_{x'} \rangle &= \frac{\hbar}{4\pi i}\int_{-\infty}^{\varepsilon_F} d\omega \ \mathrm{Tr}\left[(\mathbf{G}^{\uparrow\downarrow})^\dagger + (\mathbf{G}^{\downarrow\uparrow})^\dagger - \mathbf{G}^{\downarrow\uparrow} - \mathbf{G}^{\uparrow\downarrow}\right] \\ &= -\frac{\hbar}{2\pi}\int_{-\infty}^{\varepsilon_F} d\omega \ \mathrm{Im}\left\{\mathrm{Tr}\left[\mathbf{G}^{\downarrow\uparrow} + \mathbf{G}^{\uparrow\downarrow}\right]\right\} \qquad \text{(B.17)} \\ \langle \mathbf{s}_{y'} \rangle &= \frac{\hbar}{4\pi}\int_{-\infty}^{\varepsilon_F} d\omega \ \mathrm{Tr}\left[-(\mathbf{G}^{\uparrow\downarrow})^\dagger + (\mathbf{G}^{\downarrow\uparrow})^\dagger + \mathbf{G}^{\downarrow\uparrow} - \mathbf{G}^{\uparrow\downarrow}\right] \\ &= \frac{\hbar}{2\pi}\int_{-\infty}^{\varepsilon_F} d\omega \ \mathrm{Im}\left\{\mathrm{Tr}\left[\mathbf{G}^{\downarrow\uparrow} - \mathbf{G}^{\uparrow\downarrow}\right]\right\} \qquad \text{(B.18)} \\ \langle \mathbf{s}_{\zeta'} \rangle &= \frac{\hbar}{4\pi}\int_{-\infty}^{\varepsilon_F} d\omega \ \mathrm{Tr}\left[(\mathbf{G}^{\uparrow\uparrow})^\dagger - (\mathbf{G}^{\downarrow\downarrow})^\dagger - \mathbf{G}^{\uparrow\uparrow} + \mathbf{G}^{\downarrow\downarrow}\right] \\ &= -\frac{\hbar}{2\pi}\int_{-\infty}^{\varepsilon_F} d\omega \ \mathrm{Im}\left\{\mathrm{Tr}\left[\mathbf{G}^{\uparrow\uparrow} - \mathbf{G}^{\downarrow\downarrow}\right]\right\} \qquad \text{(B.19)}\end{aligned}$$

Finally the zero-bias conductance:

$$T(\varepsilon_F) = \frac{e^2}{h}\mathrm{Tr}\left[\mathbf{\Gamma}_L(\varepsilon_F)\left(\mathbf{G}^r\right)^\dagger(\varepsilon_F)\mathbf{\Gamma}_R(\varepsilon_F)\mathbf{G}^r(\varepsilon_F)\right] \qquad \text{(B.20)}$$

where now the Trace runs over the orbital and spin indices of the central atoms coupled to left lead. As the scattering matrices are positive definite, using the commutation properties of the trace, the conductance can be symmetrized as:

$$T(\varepsilon_F) = \frac{e^2}{h}\mathrm{Tr}\left[\mathbb{t}^\dagger(\varepsilon_F)\mathbb{t}(\varepsilon_F)\right], \qquad \text{(B.21)}$$

with $\mathbb{t}(E) = \left[\mathbf{\Gamma}_R(E)\right]^{1/2}\mathbf{G}^r(E)\left[\mathbf{\Gamma}_L(E)\right]^{1/2}$. In this form it is possible to decompose the total transmission τ into transmission-channels, whose transmissions τ_n are the eigenvalues of $\mathbb{t}^\dagger(E)\mathbb{t}(E)$.

Green's function from a perturbation series in the spin-orbit coupling

The full Green's function $\mathbf{G}(\omega) = \left[(\omega + i0^+)\mathbb{1} - \mathbf{H}_0 - \lambda\mathbf{H}_1\right]^{-1}$ corresponding to the Hamiltonian $\mathbf{H} = \mathbf{H}_0 + \lambda\mathbf{H}_1$ can be written in terms of the unperturbed Green's function $\mathbf{G}_0(\omega) = \left[(\omega + i0^+)\mathbb{1} - \mathbf{H}_0\right]^{-1}$ corresponding to $\mathbf{H}_0$ by means of a perturbation series in powers of λ with $\lambda\mathbf{H}_1$ as perturbation:

$$\mathbf{G} = \sum_{n=0}^{\infty}\lambda^n(\mathbf{G}_0\mathbf{H}_1)^n\mathbf{G}_0 = \mathbf{G}_0 + \lambda\mathbf{G}_0\mathbf{H}_1\mathbf{G}_0 + \lambda^2\mathbf{G}_0\mathbf{H}_1\mathbf{G}_0\mathbf{H}_1\mathbf{G}_0\cdots \qquad \text{(B.22)}$$

In particular, if we use the ferromagnetic Hamiltonian of (4.1) for the unperturbed part, $\mathbf{G}_0$ will be symmetric and diagonal in spin-space:

$$\mathbf{G}_0^t(\omega) = \mathbf{G}_0(\omega)\ ,\ \mathbf{G}_0(\omega) = \begin{pmatrix} \mathbf{G}^\uparrow(\omega) & 0 \\ 0 & \mathbf{G}^\downarrow(\omega) \end{pmatrix}\ . \qquad \text{(B.23)}$$

Using the SOC Hamiltonian of (B.7) as perturbation (and λ as dimensionless counting term set to unity at the end), we can write the total Green's function as:

$$\begin{aligned}\mathbf{G}(\omega) &= \sum_{n=0}^{\infty} \lambda^n (\mathbf{G}_0(\omega)\mathbf{H}^{(SO)})^n G_0(\omega) \qquad \text{(B.24)}\\ &= \begin{pmatrix} \mathbf{G}^{\uparrow}(\omega) & 0 \\ 0 & \mathbf{G}^{\downarrow}(\omega) \end{pmatrix} \sum_{n=0}^{\infty} \lambda^n \left[\Pi_{i=1}^{n} \begin{pmatrix} a_i & b_i \\ b_i^* & -a_i \end{pmatrix} \mathbf{l}_i \begin{pmatrix} \mathbf{G}^{\uparrow}(\omega) & 0 \\ 0 & \mathbf{G}^{\downarrow}(\omega) \end{pmatrix} \right] .\end{aligned}$$

For a given expectation value we can then for each order of λ separate the angular dependent part of the rest by tracing out the spin indices.

Expectation values with perturbation series

We are now in the position to plug in the perturbation series of the total Green's function in the expression of the expectation values. We apply the perturbation series to the total Green's function $\mathbf{G}^r$ and express the expectation values in powers of λ.

We will use the symmetry of the unperturbed Green's function G_0 (as in (B.23) $\mathbf{G}_0^t = \mathbf{G}_0$ and therefore $\mathbf{G}_0^{\dagger} = \mathbf{G}_0^*$) and the fact that they are diagonal in spin-space to trace out the corresponding entries in the expression of the expectation values. Furthermore in this real basis (that is the orbital functions, superpositions of complex spherical harmonics, are real), the orbital momenta matrices $\mathbf{l}_j$ are imaginary $\mathbf{l}_j = i \ \mathrm{Im}\left[\mathbf{l}_j\right]$ and therefore antisymmetric $\mathbf{l}_j^t = -\mathbf{l}_j$.

In the perturbation expressions we can then separate the angular dependence from the rest.

Occupation and total energy in perturbation series

Consider occupation n only. Expressions for total energy E_{tot} follow from n by replacing the integration infinitesimal $d\omega$ with $\omega d\omega$.

0th order in λ:

$$\langle n \rangle_0 = -\frac{1}{\pi} \int_{-\infty}^{\varepsilon_F} d\omega \ \mathrm{Im}\left\{ \mathrm{Tr}\left[\mathbf{G}^{\uparrow} + \mathbf{G}^{\downarrow} \right] \right\} = n^{(0)} \qquad \text{(B.25)}$$

1st order in λ:

$$\langle n \rangle_1 = \frac{\xi a_i}{2\pi i} \int_{-\infty}^{\varepsilon_F} d\omega \mathrm{Tr}\left[(\mathbf{G}^{\uparrow})^* \mathbf{l}_i (\mathbf{G}^{\uparrow})^* - \mathbf{G}^{\uparrow} \mathbf{l}_i \mathbf{G}^{\uparrow} - (\mathbf{G}^{\downarrow})^* \mathbf{l}_i (\mathbf{G}^{\downarrow})^* + \mathbf{G}^{\downarrow} \mathbf{l}_i \mathbf{G}^{\downarrow} \right] \qquad \text{(B.26)}$$

But as $(\mathbf{G}_0 \mathbf{l}_i \mathbf{G}_0)^t = -\mathbf{G}_0 \mathbf{l}_i \mathbf{G}_0$, the trace vanishes $\mathrm{Tr}[\mathbf{G}_0 \mathbf{l}_i \mathbf{G}_0] = 0$ and also $\langle n \rangle_1 = 0$.

2nd order in λ:

$$\langle n \rangle_2 = \frac{\xi^2}{2\pi i} \int_{-\infty}^{\varepsilon_F} d\omega \mathrm{Tr}\left[\mathbf{G}_0^* \mathbf{H}^{(SO)} \mathbf{G}_0^* \mathbf{H}^{(SO)} \mathbf{G}_0^* - \mathbf{G}_0 \mathbf{H}^{(SO)} \mathbf{G}_0 \mathbf{H}^{(SO)} \mathbf{G}_0 \right] \qquad \text{(B.27)}$$

Using the definition (B.7) of $\mathbf{H}^{(SO)}$ and (B.8):

$$\begin{aligned}
&\mathrm{Tr} \quad \left[\mathbf{G}_0\mathbf{H}^{(SO)}\mathbf{G}_0\mathbf{H}^{(SO)}\mathbf{G}_0\right] = && \text{(B.28)}\\
&\mathrm{Tr} \quad \left[a_ia_j\left(\mathbf{G}^{\uparrow}\mathbf{l}_i\mathbf{G}^{\uparrow}\mathbf{l}_j\mathbf{G}^{\uparrow}+\mathbf{G}^{\downarrow}\mathbf{l}_i\mathbf{G}^{\downarrow}\mathbf{l}_j\mathbf{G}^{\downarrow}\right)+b_ib_j^*\left(\mathbf{G}^{\uparrow}\mathbf{l}_i\mathbf{G}^{\downarrow}\mathbf{l}_j\mathbf{G}^{\uparrow}+\mathbf{G}^{\downarrow}\mathbf{l}_i\mathbf{G}^{\uparrow}\mathbf{l}_j\mathbf{G}^{\downarrow}\right)\right] = &&\\
&\mathrm{Tr} \quad \left\{a_ia_j\left[\mathbf{G}^{\uparrow}\mathbf{l}_i\left(\mathbf{G}^{\uparrow}-\mathbf{G}^{\downarrow}\right)\mathbf{l}_j\mathbf{G}^{\uparrow}-\mathbf{G}^{\downarrow}\mathbf{l}_i\left(\mathbf{G}^{\uparrow}-\mathbf{G}^{\downarrow}\right)\mathbf{l}_j\mathbf{G}^{\downarrow}\right)\right.&&\\
&+ \quad \left.(\delta_{ij}+i\epsilon_{ijk}a_k)\left(\mathbf{G}^{\uparrow}\mathbf{l}_i\mathbf{G}^{\downarrow}\mathbf{l}_j\mathbf{G}^{\uparrow}+\mathbf{G}^{\downarrow}\mathbf{l}_i\mathbf{G}^{\uparrow}\mathbf{l}_j\mathbf{G}^{\downarrow}\right)\right\}. &&
\end{aligned}$$

But as

$$[\epsilon_{ijk}(\mathbf{G}^{\uparrow}\mathbf{l}_i\mathbf{G}^{\downarrow}\mathbf{l}_j\mathbf{G}^{\uparrow})]^t = \epsilon_{ijk}(\mathbf{G}^{\uparrow}\mathbf{l}_j\mathbf{G}^{\downarrow}\mathbf{l}_i\mathbf{G}^{\uparrow}) = -\epsilon_{ijk}(\mathbf{G}^{\uparrow}\mathbf{l}_i\mathbf{G}^{\downarrow}\mathbf{l}_j\mathbf{G}^{\uparrow}) \tag{B.29}$$

the trace over the ϵ_{ijk} term vanishes. Then in (B.27) the remaining terms can be combined as:

$$\begin{aligned}
\langle n\rangle_2 &= -a_ia_j\frac{\xi^2}{\pi}\int_{-\infty}^{\varepsilon_F}d\omega\ \mathrm{Im}\left\{Tr\left[\mathbf{G}^{\uparrow}\mathbf{l}_i(\mathbf{G}^{\uparrow}-\mathbf{G}^{\downarrow})\mathbf{l}_j\mathbf{G}^{\uparrow}-\mathbf{G}^{\downarrow}\mathbf{l}_i(\mathbf{G}^{\uparrow}-\mathbf{G}^{\downarrow})\mathbf{l}_j\mathbf{G}^{\downarrow}\right]\right\}\\
&\quad -\delta_{ij}\frac{\xi^2}{\pi}\int_{-\infty}^{\varepsilon_F}d\omega\ \mathrm{Im}\left\{Tr\left[\mathbf{G}^{\uparrow}\mathbf{l}_i\mathbf{G}^{\downarrow}\mathbf{l}_j\mathbf{G}^{\uparrow}+\mathbf{G}^{\downarrow}\mathbf{l}_i\mathbf{G}^{\uparrow}\mathbf{l}_j\mathbf{G}^{\downarrow}\right]\right\} &&\text{(B.30)}\\
&= a_ia_j\ n_{ij}^{(2,1)}+\delta_{ij}n_{ij}^{(2,2)}
\end{aligned}$$

Up to second order in λ the occupation reads:

$$\langle n\rangle = n^{(0)}+a_ia_j\ n_{ij}^{(2,1)}+\delta_{ij}n_{ij}^{(2,2)}+O(\lambda^3). \tag{B.31}$$

This term is now the generalization of Bruno [181, 182]. A similar expression holds for ε_{tot}.

Orbital momentum in perturbation series

0th order in λ:

$$\langle\mathbf{l}'_{i'}\rangle_0 = \frac{\hbar}{2\pi i}c_{i'j}\int_{-\infty}^{\varepsilon_F}d\omega\ \mathrm{Tr}\left\{\mathbf{l}_j\left[(\mathbf{G}^{\uparrow})^*-\mathbf{G}^{\uparrow}+(\mathbf{G}^{\downarrow})^*-\mathbf{G}^{\downarrow}\right]\right\}, \tag{B.32}$$

but with $(\mathbf{l}_j\mathbf{G}_0)^t = -\mathbf{G}_0\mathbf{l}_j$ is $\mathrm{Tr}[\mathbf{l}_j\mathbf{G}_0] = 0$, therefore $\langle\mathbf{l}'_{i'}\rangle_0 = 0$.

1st order in λ:

$$\langle\mathbf{l}'_{i'}\rangle_1 = \frac{\hbar\xi}{2\pi i}c_{i'j}a_k\int_{-\infty}^{\varepsilon_F}d\omega\ \mathrm{Tr}\left\{\mathbf{l}_j\left[(\mathbf{G}^{\uparrow})^*\mathbf{l}_k(\mathbf{G}^{\uparrow})^*-\mathbf{G}^{\uparrow}\mathbf{l}_k\mathbf{G}^{\uparrow}-(\mathbf{G}^{\downarrow})^*\mathbf{l}_k(\mathbf{G}^{\downarrow})^*+\mathbf{G}^{\downarrow}\mathbf{l}_k\mathbf{G}^{\downarrow}\right]\right\}. \tag{B.33}$$

As $\mathbf{l}_j$ is imaginary, $\mathbf{l}_j(\mathbf{G}_0^*\mathbf{l}_k\mathbf{G}_0^*-\mathbf{G}_0\mathbf{l}_k\mathbf{G}_0) = -2i\ \ \mathrm{Im}[\mathbf{l}_j\mathbf{G}_0\mathbf{l}_k\mathbf{G}_0]$ so that:

$$\begin{aligned}
\langle\mathbf{l}'_{i'}\rangle_1 &= \frac{-\hbar\xi}{\pi}c_{i'j}a_k\int_{-\infty}^{\varepsilon_F}d\omega\ \mathrm{Im}\left\{\ \mathrm{Tr}\left[\mathbf{l}_j(\mathbf{G}^{\uparrow}\mathbf{l}_k\mathbf{G}^{\uparrow}-\mathbf{G}^{\downarrow}\mathbf{l}_k\mathbf{G}^{\downarrow})\right]\right\} &&\text{(B.34)}\\
&= c_{i'j}a_k\ l_{jk}^{(1)}. &&\text{(B.35)}
\end{aligned}$$

As pointed out by Bruno [181], the angular dependence of $\mathbf{l}_\zeta$ (with $c_{\zeta j} = a_j$) is the same as for ε_{tot}. However in an general geometry without translational symmetry (as for surfaces or monolayers), also $\mathbf{l}_{x'}$ and $\mathbf{l}_{y'}$ contribute and the angular dependence of $\vec{\mathbf{l}}$ is in general different from that of ε_{tot}.

Up to first order in λ, angular momentum reads:

$$\langle \mathbf{l}'_{i'} \rangle = c_{i'j} a_k \; l^{(1)}_{jk} + O(\lambda^2) \tag{B.36}$$

Spin momentum in perturbation series

0th order in λ:

$$\langle \mathbf{s}_k \rangle_0 = \frac{\hbar}{4\pi i} \int_{-\infty}^{\varepsilon_F} d\omega \mathrm{Tr}\left[\tau_k(\mathbf{G}_0^* - \mathbf{G}_0\right]. \tag{B.37}$$

The second factor in the trace is diagonal in spin space and so only $\mathbf{s}_\zeta$ is non-zero in 0th order: $\langle \mathbf{s}_{x'} \rangle_0 = 0 = \langle \mathbf{s}_{y'} \rangle_0$. The remaining:

$$\langle \mathbf{s}_\zeta \rangle_0 = -\frac{\hbar}{2\pi} \int_{-\infty}^{\varepsilon_F} d\omega \;\; \mathrm{Im}\left\{\mathrm{Tr}\left[(\mathbf{G}^\uparrow - \mathbf{G}^\downarrow\right]\right\} = s^{(0)}_\zeta. \tag{B.38}$$

1st order in λ:

$$\langle \mathbf{s}_k \rangle_1 = \frac{\hbar\xi}{4\pi i} \int_{-\infty}^{\varepsilon_F} d\omega \mathrm{Tr}\left[\tau_k(\mathbf{G}_0^* \mathbf{H}^{(SO)} \mathbf{G}_0^* - \mathbf{G}_0 \mathbf{H}^{(SO)} \mathbf{G}_0)\right]. \tag{B.39}$$

Again, using the definition (B.7) of $\mathbf{H}^{(SO)}$ and (B.8) it follows for the $\mathbf{s}_\zeta-$component:

$$\langle \mathbf{s}_\zeta \rangle_1 = \frac{\xi\hbar a_j}{4\pi i} \int_{-\infty}^{\varepsilon_F} d\omega \mathrm{Tr}\left[(\mathbf{G}^\uparrow)^* \mathbf{l}_j (\mathbf{G}^\uparrow)^* - \mathbf{G}^\uparrow \mathbf{l}_j \mathbf{G}^\uparrow - (\mathbf{G}^\downarrow)^* \mathbf{l}_j (\mathbf{G}^\downarrow)^* + \mathbf{G}^\downarrow \mathbf{l}_j \mathbf{G}^\downarrow\right] = 0, \tag{B.40}$$

as $(\mathbf{G}_0 \mathbf{l}_j \mathbf{G}_0)^t = -\mathbf{G}_0 \mathbf{l}_j \mathbf{G}_0$ and the trace vanishes. So only $\mathbf{s}'_x$ and $\mathbf{s}'_y$ contribute to first order in λ.

$$\begin{aligned}
\langle \mathbf{s}_{x'} \rangle_1 &= \frac{\xi\hbar}{4\pi i} \int_{-\infty}^{\varepsilon_F} d\omega \mathrm{Tr}\left[b_j^* \left((\mathbf{G}^\downarrow)^* \mathbf{l}_j (\mathbf{G}^\uparrow)^* - \mathbf{G}^\downarrow \mathbf{l}_j \mathbf{G}^\uparrow\right) + b_j \left((\mathbf{G}^\uparrow)^* \mathbf{l}_j (\mathbf{G}^\downarrow)^* - \mathbf{G}^\uparrow \mathbf{l}_j \mathbf{G}^\downarrow\right)\right] \\
&= \mathrm{Im}\{b_j\} \; \frac{-\xi\hbar}{\pi} \int_{-\infty}^{\varepsilon_F} d\omega \, \mathrm{Re}\{Tr\left[\mathbf{G}^\uparrow \mathbf{l}_j \mathbf{G}^\downarrow\right]\} = \mathrm{Im}\{b_j\} \; s^{(1)}_j,
\end{aligned} \tag{B.41}$$

where in the second step we used:

$$b_j \; \alpha \pm b_j^* \; \beta = \mathrm{Re}\{b_j\} \; (\alpha \pm \beta) + i \, \mathrm{Im}\{b_j\} \; (\alpha \mp \beta) \tag{B.42}$$

with

$$\alpha = ((\mathbf{G}^\uparrow)^* \mathbf{l}_j (\mathbf{G}^\downarrow)^* - \mathbf{G}^\uparrow \mathbf{l}_j \mathbf{G}^\downarrow), \quad \beta = ((\mathbf{G}^\downarrow)^* \mathbf{l}_j (\mathbf{G}^\uparrow)^* - \mathbf{G}^\downarrow \mathbf{l}_j \mathbf{G}^\uparrow). \tag{B.43}$$

Again, using $(\mathbf{G}^\uparrow \mathbf{l}_j \mathbf{G}^\downarrow)^t = -\mathbf{G}^\downarrow \mathbf{l}_j \mathbf{G}^\uparrow$, the trace over the sum $(\alpha \pm \beta)$ yields:

$$\mathrm{Tr}\left[\alpha \pm \beta\right] = \left\{ \begin{array}{ll} 0, & \text{'+'} \\ 2\mathrm{Tr}\left[(\mathbf{G}^\uparrow)^* \mathbf{l}_j (\mathbf{G}^\downarrow)^* - \mathbf{G}^\uparrow \mathbf{l}_j \mathbf{G}^\downarrow\right] = -4\Re\left\{\mathrm{Tr}\left[\mathbf{G}^\uparrow \mathbf{l}_j \mathbf{G}^\downarrow\right]\right\}, & \text{'}-\text{',} \end{array} \right. \tag{B.44}$$

where we used that $\mathbf{l}_j$ is imaginary. It follows the expression for $\mathbf{s}_{x'}$ in (B.41). With a similar argumentation we obtain for $\mathbf{s}_{y'}$:

$$\begin{aligned}\langle \mathbf{s}_{y'} \rangle_1 &= \frac{\xi\hbar}{4\pi}\int_{-\infty}^{\varepsilon_F} d\omega \mathrm{Tr}\,\{-b_j^*\,[(\mathbf{G}^{\downarrow})^*\mathbf{l}_j(\mathbf{G}^{\uparrow})^* - \mathbf{G}^{\downarrow}\mathbf{l}_j\mathbf{G}^{\uparrow}] + b_j\,[(\mathbf{G}^{\uparrow})^*\mathbf{l}_j(\mathbf{G}^{\downarrow})^* - \mathbf{G}^{\uparrow}\mathbf{l}_j\mathbf{G}^{\downarrow})] \\ &= \Re\{b_j\}\,\frac{-\xi\hbar}{\pi}\int_{-\infty}^{\varepsilon_F} d\omega\,\mathrm{Re}\left\{\mathrm{Tr}\left[\mathbf{G}^{\uparrow}\mathbf{l}_j\mathbf{G}^{\downarrow}\right]\right\} = \Re\{b_j\}\ s_j^{(1)}. \end{aligned} \tag{B.45}$$

<u>2nd order in λ:</u>

$$\begin{aligned}\langle \mathbf{s}_{x'} \rangle_2 &= \mathrm{Re}\{b_j\}a_k\frac{-\hbar\xi^2}{\pi}\int_{-\infty}^{\varepsilon_F} d\omega\ \mathrm{Im}\left\{\mathrm{Tr}\left[\mathbf{G}^{\downarrow}\mathbf{l}_j\mathbf{G}^{\uparrow}\mathbf{l}_k\mathbf{G}^{\uparrow} - \mathbf{G}^{\uparrow}\mathbf{l}_j\mathbf{G}^{\downarrow}\mathbf{l}_k\mathbf{G}^{\downarrow}\right]\right\} \\ &= \mathrm{Re}\{b_j\}a_k\ s_{jk}^{(2,1)} \end{aligned} \tag{B.46}$$

$$\begin{aligned}\langle \mathbf{s}_{y'} \rangle_2 &= \mathrm{Im}\{b_j\}a_k\frac{\hbar\xi^2}{\pi}\int_{-\infty}^{\varepsilon_F} d\omega\ \mathrm{Im}\left\{\mathrm{Tr}\left[\mathbf{G}^{\downarrow}\mathbf{l}_j\mathbf{G}^{\uparrow}\mathbf{l}_k\mathbf{G}^{\uparrow} + \mathbf{G}^{\uparrow}\mathbf{l}_j\mathbf{G}^{\downarrow}\mathbf{l}_k\mathbf{G}^{\downarrow}\right]\right\} \\ &= \mathrm{Im}\{b_j\}a_k\ s_{jk}^{(2,2)} \end{aligned} \tag{B.47}$$

$$\begin{aligned}\langle \mathbf{s}_{\zeta} \rangle_2 &= a_j a_k\frac{-\hbar\xi^2}{2\pi}\int_{-\infty}^{\varepsilon_F} d\omega\ \mathrm{Im}\left\{\mathrm{Tr}\left[\mathbf{G}^{\uparrow}\mathbf{l}_j\left(\mathbf{G}^{\uparrow}-\mathbf{G}^{\downarrow}\right)\mathbf{l}_k\mathbf{G}^{\uparrow} + \mathbf{G}^{\downarrow}\mathbf{l}_j\left(\mathbf{G}^{\uparrow}-\mathbf{G}^{\downarrow}\right)\mathbf{l}_k\mathbf{G}^{\downarrow}\right]\right\} \\ &+ \delta_{jk}\frac{-\hbar\xi^2}{2\pi}\int_{-\infty}^{\varepsilon_F} d\omega\ \mathrm{Im}\left\{\mathrm{Tr}\left[\mathbf{G}^{\uparrow}\mathbf{l}_j\mathbf{G}^{\downarrow}\mathbf{l}_k\mathbf{G}^{\uparrow} - \mathbf{G}^{\downarrow}\mathbf{l}_j\mathbf{G}^{\uparrow}\mathbf{l}_k\mathbf{G}^{\downarrow}\right]\right\} \\ &= a_j a_k\ s_{jk}^{(2,3)} + \delta_{jk}s_{jk}^{(2,4)} \end{aligned} \tag{B.48}$$

In total, up to second order in λ:

$$\langle \mathbf{s}_{x'} \rangle = \mathrm{Im}\{b_j\}\ s_j^{(1)} + \mathrm{Re}\{b_j\}a_k\ s_{jk}^{(2,1)} + O(\lambda^3) \tag{B.49}$$

$$\langle \mathbf{s}_{y'} \rangle = \mathrm{Re}\{b_j\}\ s_j^{(1)} + \mathrm{Im}\{b_j\}a_k\ s_{jk}^{(2,2)} + O(\lambda^3) \tag{B.50}$$

$$\langle \mathbf{s}_{\zeta} \rangle = s_{\zeta}^{(0)} + a_j a_k\ s_{jk}^{(2,3)} + \delta_{jk}s_{jk}^{(2,4)} + O(\lambda^3) \tag{B.51}$$

Transmission in perturbation series

Different to the quantities above, which like the occupation are properties integrated over the entire energy spectrum, the zero bias conductance just depends on the Fermi energy. Furthermore it is not a local property of a single atom site but depends on the entire interface that is transversed by the current. So the trace extends over all atoms (plus orbital-, spin-indices) coupled to the interface. Nevertheless the angular dependencies are similar to the quantities regarded above.

Let us remember the structure of the Hamiltonian of the central part coupled to the leads:

$$\mathbf{H}_0 = \begin{pmatrix} \mathbf{H}_L & \mathbf{H}_{LC} & 0 \\ \mathbf{H}_{LC}^{\dagger} & \mathbf{H}_C & \mathbf{H}_{CR} \\ 0 & \mathbf{H}_{CR}^{\dagger} & \mathbf{H}_R \end{pmatrix}. \tag{B.52}$$

The SOC Hamiltonian shall be limited to the central part only:

$$\mathbf{H}^{(SO)} = \begin{pmatrix} 0 & 0 & 0 \\ 0 & \mathbf{H}_C^{(SO)} & 0 \\ 0 & 0 & 0 \end{pmatrix} . \tag{B.53}$$

With this structure of the Hamiltonian the resulting expression for the central part's Green's function yields $\mathbf{G}_C(\omega) = \left[(\omega + i0^+) - \mathbf{H}_C - \mathbf{H}_C^{(SO)} - \mathbf{\Sigma}_L(\omega) - \mathbf{\Sigma}_R(\omega)\right]^{-1}$ with the selfenergies $\mathbf{\Sigma}_{L,R}(\omega)$ (diagonal in spin space and symmetric) due to the coupling to the leads. The scattering matrix is $\mathbf{\Gamma}_L = i\left(\mathbf{\Sigma}_L^\dagger - \mathbf{\Sigma}_L\right)$ and similar expression for the right. An important relation between Green's function and scattering matrix:

$$\mathbf{\Gamma}_L + \mathbf{\Gamma}_R = i\left(\mathbf{\Sigma}_L^\dagger + \mathbf{\Sigma}_R^\dagger - \mathbf{\Sigma}_L - \mathbf{\Sigma}_R\right) = i\left[(\mathbf{G}_C^\dagger)^{-1} - \mathbf{G}_C^{-1}\right] . \tag{B.54}$$

The central part's Green's function can be expressed in a perturbation series with the help of the unperturbed Green's function $\left[\mathbf{G}_C^{(0)}(\omega)\right]^{-1} = (\omega + i0^+)\mathbb{1} - \mathbf{H}_C - \mathbf{\Sigma}_L - \mathbf{\Sigma}_R$:

$$\mathbf{G}_C = \sum_{n=0}^{\infty} \lambda^n \left(\mathbf{G}_C^{(0)}\mathbf{H}_C^{(SO)}\right)^n \mathbf{G}_C^{(0)} \tag{B.55}$$

Finally, the transmission reads:

$$T(\omega) = \mathrm{Tr}\left[\mathbf{\Gamma}_L(\omega)\left[\mathbf{G}_C(\omega)\right]^\dagger \mathbf{\Gamma}_R(\omega)\mathbf{G}_C(\omega)\right] . \tag{B.56}$$

Expand the central part's Green's function in $\mathbf{H}^{(SO)}$ like in (B.55) leads to:

$$T(\omega) = \sum_{n=0}^{\infty} \lambda^n T^{(n)} , \tag{B.57}$$

where the $T^{(n)}$ for different orders n of λ if n even:

$$\begin{aligned} T^{(n)} &= \sum_{m=0}^{n/2-1} 2\,\mathrm{Re}\left\{\mathrm{Tr}\left[\mathbf{G}_C^{(0)}\left(\mathbf{H}^{(SO)}\mathbf{G}_C^{(0)}\right)^{n-m}\mathbf{\Gamma}_R\left(\mathbf{G}_C^{(0)}\right)^*\left[\mathbf{H}^{(SO)}\left(\mathbf{G}_C^{(0)}\right)^*\right]^m\mathbf{\Gamma}_L\right]\right\} \\ &+ \mathrm{Tr}\left[\mathbf{G}_C^{(0)}\left(\mathbf{H}^{(SO)}\mathbf{G}_C^{(0)}\right)^{n/2}\mathbf{\Gamma}_R\left(\mathbf{G}_C^{(0)}\right)^*\left[\mathbf{H}^{(SO)}\left(\mathbf{G}_C^{(0)}\right)^*\right]^{n/2}\Gamma_L\right] , \end{aligned} \tag{B.58}$$

and if n odd

$$T^{(n)} = \sum_{m=0}^{(n-1)/2} 2\,\mathrm{Re}\left\{\mathrm{Tr}\left[\mathbf{G}_C^{(0)}\left(\mathbf{H}^{(SO)}\mathbf{G}_C^{(0)}\right)^{m}\mathbf{\Gamma}_R\left(\mathbf{G}_C^{(0)}\right)^*\left[\mathbf{H}^{(SO)}\left(\mathbf{G}_C^{(0)}\right)^*\right]^{n-m}\mathbf{\Gamma}_L\right]\right\} \tag{B.59}$$

0th order, as $\mathbf{G}$ and $\mathbf{\Gamma}$ are diagonal in spin-space:

$$T^{(0)} = Tr\left[\mathbf{\Gamma}_L^{\uparrow}\left(\mathbf{G}^{\uparrow}\right)^*\mathbf{\Gamma}_R^{\uparrow}\mathbf{G}^{\uparrow}+\mathbf{\Gamma}_L^{\downarrow}\left(\mathbf{G}^{\downarrow}\right)^*\mathbf{\Gamma}_R^{\downarrow}\mathbf{G}^{\downarrow}\right] \tag{B.60}$$

1st order:

$$\begin{aligned} T^{(1)} &= 2\,\mathrm{Re}\left\{\mathrm{Tr}\left[\mathbf{H}^{(SO)}\mathbf{G}_C^{(0)}\mathbf{\Gamma}_R\left(\mathbf{G}_C^{(0)}\right)^*\mathbf{\Gamma}_L\mathbf{G}_C^{(0)}\right]\right\} = \\ & 2a_j\ \mathrm{Re}\left\{\mathrm{Tr}\left[\mathbf{l}_j\left[(\mathbf{G}\mathbf{\Gamma}_R\mathbf{G}^*\mathbf{\Gamma}_L\mathbf{G})^{\uparrow}-(\mathbf{G}\mathbf{\Gamma}_R\mathbf{G}^*\mathbf{\Gamma}_L\mathbf{G})^{\downarrow}\right]\right]\right\}. \end{aligned} \tag{B.61}$$

But as $\mathbf{l}_j$ is antisymmetric ($\mathbf{l}_j^t = -\mathbf{l}_j$), the trace of the symmetric part of $\mathbf{G}\mathbf{\Gamma}_R\mathbf{G}^*\mathbf{\Gamma}_L\mathbf{G}$ vanishes and it remains an expression of the kind:

$$\mathrm{Re}\left\{\mathrm{Tr}\left[\mathbf{l}_j\mathbf{G}\left[\mathbf{\Gamma}_R\mathbf{G}^*\mathbf{\Gamma}_L-(\mathbf{\Gamma}_R\mathbf{G}^*\mathbf{\Gamma}_L)^t\right]G_0\right]\right\} \tag{B.62}$$

adding in the trace terms proportional to $\pm\mathbf{l}_j\mathbf{G}\mathbf{\Gamma}_R\mathbf{G}^*\mathbf{\Gamma}_R\mathbf{G}$ and $\pm\mathbf{l}_j\mathbf{G}\mathbf{\Gamma}_L\mathbf{G}^*\mathbf{\Gamma}_L\mathbf{G}$ leads to:

$$\begin{aligned} \mathrm{Re}\,[\mathrm{Tr}\,\{\mathbf{l}_j\mathbf{G}\,[(\mathbf{\Gamma}_R+\mathbf{\Gamma}_L)\,\mathbf{G}^*\mathbf{\Gamma}_L+\mathbf{\Gamma}_R\mathbf{G}^*\,(\mathbf{\Gamma}_R+\mathbf{\Gamma}_L) \\ -(\mathbf{\Gamma}_R+\mathbf{\Gamma}_L)\,\mathbf{G}^*\mathbf{\Gamma}_R-\mathbf{\Gamma}_L\mathbf{G}^*\,(\mathbf{\Gamma}_R+\mathbf{\Gamma}_L)]\,\mathbf{G}\}]\ . \end{aligned} \tag{B.63}$$

Using the identity (B.54) this can be written as:

$$\mathrm{Re}\,\{\mathrm{Tr}\,[\mathbf{l}_j i\,\{(\mathbf{G}-\mathbf{G}^*)\,\mathbf{\Gamma}_L+\mathbf{\Gamma}_R\,(\mathbf{G}-\mathbf{G}^*)-(\mathbf{G}-\mathbf{G}^*)\,\mathbf{\Gamma}_R-\mathbf{\Gamma}_L\,(\mathbf{G}-\mathbf{G}^*)\}]\} \tag{B.64}$$

but the expression below the Trace is imaginary, its real part zero and therefore $T^{(1)} \equiv 0$. For a non-orthogonal basis with a finite overlap matrix $\mathbf{S}$, the central part Green's function reads $\mathbf{G}(\omega) = \left[(\omega+i\eta)\mathbf{S}-\mathbf{H}_0-\mathbf{H}^{(SO)}-\mathbf{\Sigma}_L-\mathbf{\Sigma}_R\right]^{-1}$, where $\eta \to 0^+$. In this case $T^{(1)} \to 0$ as $\eta \to 0$.

θ-dependence of the total conductance anisotropy

In the previous section we showed, that in the total transmission the first order term $T^{(1)}$ of the SOC perturbation vanishes. On the other hand, in the case of the minimal model in section 5.2.3 and the ideal contacts of section 5.3 we observed that only even harmonics of $\cos(2m\theta+\alpha_m)$ contributed to the total conductance anisotropy. Here we will evaluate this observation numerically.

First we observe that the real part of the SOC Hamiltonian (B.7)

$$\mathbf{H}_{sy}^{(SO)}(\phi) = i\xi\begin{pmatrix} 0 & \mathrm{Im}\,b_j \\ -\mathrm{Im}\,b_j & 0 \end{pmatrix}\mathbf{l}_j \tag{B.65}$$

only depends on $\cos\phi$, $\sin\phi$ and all the θ-dependence is in the imaginary part of the SOC Hamiltonian.[1] In the following we will treat the imaginary part of the SOC Hamiltonian as a perturbation.

---

[1] Indeed all entries of the imaginary part of the SOC Hamiltonian are proportional to $\cos\theta$ or $\sin\theta$.

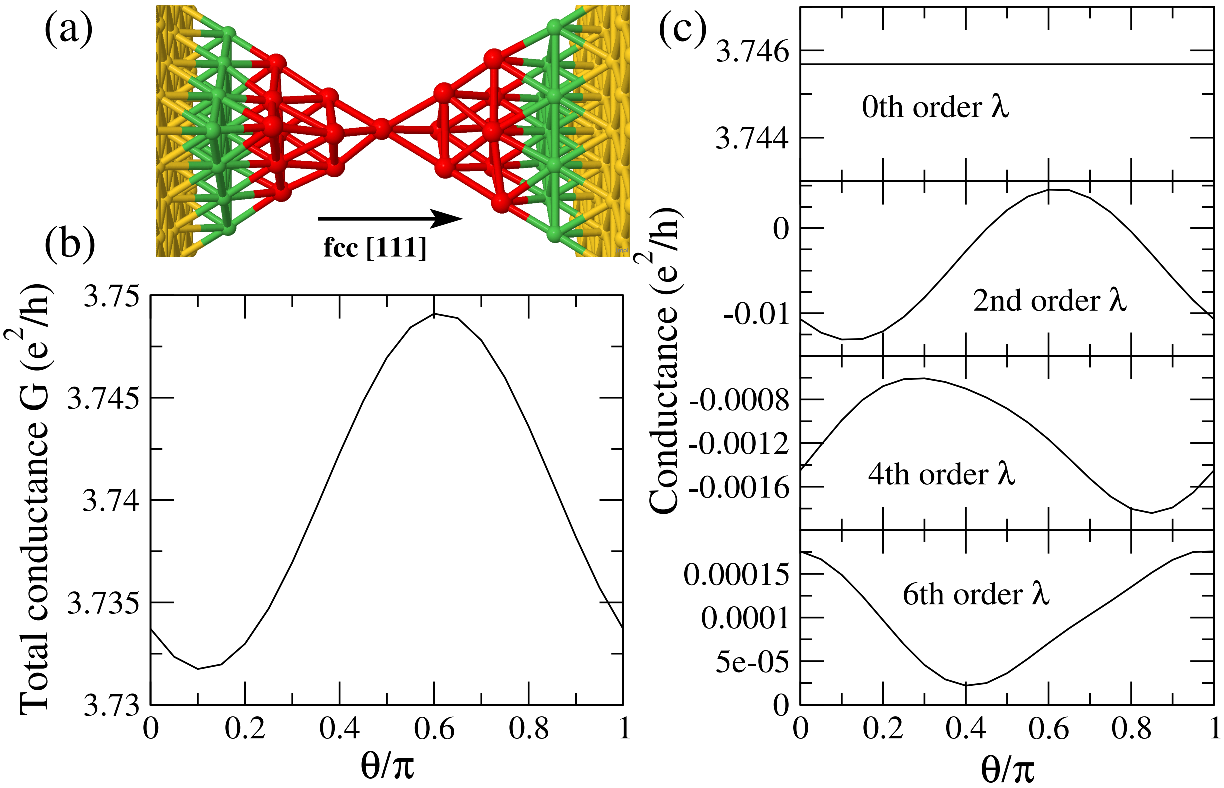

Figure B.2: (a) Disturbed contact geometry similar to Fig. 5.5(d) with the atoms marked in red randomly shifted from their lattice positions. (b) Anisotropy of the total linear conductance as a function of θ for one value of ϕ. (c) Lowest contributing orders of the perturbation series of the total conductance as discussed in the text.

Similar to (B.22) we write the unperturbed Green's function

$$\left[\mathbf{G}_C^{(1)}(\omega,\phi)\right]^{-1} = (\omega + i0^+)\mathbb{1} - \mathbf{H}_C - \mathbf{H}_{sy}^{(SO)}(\phi) - \mathbf{\Sigma}_L - \mathbf{\Sigma}_R \tag{B.66}$$

and the perturbation

$$\mathbf{H}_{asy}^{(SO)}(\theta,\phi) = \xi \begin{pmatrix} a_j & \mathrm{Re}\, b_j \\ \mathrm{Re}\, b_j & -a_j \end{pmatrix} \mathbf{l}_j \ . \tag{B.67}$$

Then the perturbation series for the total Green's function reads:

$$\mathbf{G}_C = \sum_{n=0}^{\infty} \lambda^n \left(\mathbf{G}_C^{(1)}\mathbf{H}_{asy}^{(SO)}\right)^n \mathbf{G}_C^{(1)} \tag{B.68}$$

Similar to (B.58) and (B.59) we can write the total conductance $G^{(n)}$ for even orders n of

λ :

$$\begin{aligned} G^{(n)} &= \sum_{m=0}^{n/2-1} 2\,\mathrm{Re}\left\{\mathrm{Tr}\left[\mathbf{G}_C^{(1)}\left(\mathbf{H}_{asy}^{(SO)}\mathbf{G}_C^{(1)}\right)^{n-m}\mathbf{\Gamma}_R\left(\mathbf{G}_C^{(1)}\right)^*\left[\mathbf{H}_{asy}^{(SO)}\left(\mathbf{G}_C^{(1)}\right)^*\right]^m\mathbf{\Gamma}_L\right]\right\} \\ &+ \mathrm{Tr}\left[\mathbf{G}_C^{(1)}\left(\mathbf{H}_{asy}^{(SO)}\mathbf{G}_C^{(1)}\right)^{n/2}\mathbf{\Gamma}_R\left(\mathbf{G}_C^{(1)}\right)^*\left[\mathbf{H}_{asy}^{(SO)}\left(\mathbf{G}_C^{(1)}\right)^*\right]^{n/2}\Gamma_L\right] \ , \end{aligned} \tag{B.69}$$

and for odd orders n

$$G^{(n)} = \sum_{m=0}^{(n-1)/2} 2\,\mathrm{Re}\left\{\mathrm{Tr}\left[\mathbf{G}_C^{(1)}\left(\mathbf{H}_{asy}^{(SO)}\mathbf{G}_C^{(1)}\right)^{m}\mathbf{\Gamma}_R\left(\mathbf{G}_C^{(1)}\right)^*\left[\mathbf{H}_{asy}^{(SO)}\left(\mathbf{G}_C^{(1)}\right)^*\right]^{n-m}\mathbf{\Gamma}_L\right]\right\} \ . \tag{B.70}$$

As all the terms in $\mathbf{H}_{asy}^{(SO)}$ are proportional to $\cos\theta$ or $\sin\theta$, each summand of the traces in (B.69) and (B.70) in order λ^n is proportional to

$$\begin{aligned} \cos^l\theta\sin^{2m-l}\theta &= \sum_{k=0}^{m}\tilde{a}_k\cos\left(2k\theta+\tilde{\alpha}_k\right) \ , \text{ if } n=2m \text{ is even,} \\ \cos^l\theta\sin^{2m+1-l}\theta &= \sum_{k=0}^{m}\tilde{b}_k\cos\left[\left(2k+1\right)\theta+\tilde{\beta}_k\right] \ , \text{ if } n=2m+1 \text{ is odd,} \end{aligned}$$

where $0 \leq l \leq n$. Then the traces corresponding to order λ^n contain either only even or only odd harmonics if n is even or odd.

In Fig. B.2(c) we show the resulting perturbation analysis of the total conductance of a disturbed contact geometry of Ni depicted in Fig. B.2(a) as a function of θ and for a fixed value of ϕ. We observe that only even orders of λ contribute, while odd orders of λ (not shown here) are zero within numerical precision. As a consequence we can conclude that to the total conductance anisotropy shown in Fig. B.2(b) only even harmonics $\cos(2m\theta+\alpha_m)$ contribute.

Bibliography

[1] N. Agraït, A. L. Yeyati, and J. M. van Ruitenbeek, *Quantum properties of atomic-sized conductors*, Physics Reports **377**, 81 – 279 (2003).

[2] J. C. Maxwell. *A treatise on electricity and magnetism*, volume 1 (Dover Publ., inc., New York, 1954).

[3] Y. V. Sharvin, *A possible method for studying Fermi surfaces*, Sov. Phys.-JETP **21**, 655–656 (1965). [Zh. Eksp. Teor. Fiz. 48, 984-985 (1965)].

[4] R. Landauer, *Spatial variation of currents and fields due to localized scatterers in metallic conduction*, IBM J. Res. Dev. **1**, 223–231 (1957).

[5] R. Landauer, *Electrical resistance of disordered one-dimensional lattices*, Philosophical Magazine **21**, 863–867 (1970).

[6] M. Büttiker, Y. Imry, R. Landauer, and S. Pinhas, *Generalized many-channel conductance formula with application to small rings*, Phys. Rev. B **31**, 6207–6215 (1985).

[7] M. Büttiker, *Four-Terminal Phase-Coherent Conductance*, Phys. Rev. Lett. **57**, 1761–1764 (1986).

[8] C. Caroli, R. Combescot, P. Nozières, and D. Saint-James, *Direct calculation of the tunneling current*, Journal of Physics C: Solid State Physics **4**, 916–929 (1971).

[9] J. Ferrer, A. Martín-Rodero, and F. Flores, *Contact resistance in the scanning tunneling microscope at very small distances*, Phys. Rev. B **38**, 10113–10115 (1988).

[10] G. Binnig, H. Rohrer, C. Gerber, and E. Weibel, *Surface Studies by Scanning Tunneling Microscopy*, Phys. Rev. Lett. **49**, 57–61 (1982).

[11] G. Binnig and H. Rohrer, *Scanning tunneling microscopy – from birth to adolescence*, Rev. Mod. Phys. **59**, 615–625 (1987).

[12] D. M. Eigler and E. K. Schweizer, *Positioning single atoms with a scanning tunnelling microscope*, Nature **344**, 524–526 (1990).

[13] M. F. Crommie, C. P. Lutz, and D. M. Eigler, *Confinement of Electrons to Quantum Corrals on a Metal Surface*, Science **262**, 218–220 (1993).

[14] J. K. Gimzewski and R. Möller, *Transition from the tunneling regime to point contact studied using scanning tunneling microscopy*, Phys. Rev. B **36**, 1284–1287 (1987).

[15] G. Rubio-Bollinger, S. R. Bahn, N. Agraït, K. W. Jacobsen, and S. Vieira, *Mechanical Properties and Formation Mechanisms of a Wire of Single Gold Atoms*, Phys. Rev. Lett. **87**, 026101 (2001).

[16] G. Rubio-Bollinger, N. Agraït, and S. Vieira, *Atomic-sized metallic contacts: Mechanical properties and electronic transport*, Physical Review Letters **76**, 2302–2305 (1996).

[17] N. Agraït, C. Untiedt, G. Rubio-Bollinger, and S. Vieira, *Onset of Energy Dissipation in Ballistic Atomic Wires*, Phys. Rev. Lett. **88**, 216803 (2002).

[18] C. J. Muller, J. M. van Ruitenbeek, and L. J. de Jongh, *Experimental observation of the transition from weak link to tunnel junction*, Physica C: Superconductivity **191**, 485 – 504 (1992).

[19] J. C. Cuevas, A. Martín-Rodero, and A. L. Yeyati, *Hamiltonian approach to the transport properties of superconducting quantum point contacts*, Phys. Rev. B **54**, 7366–7379 (1996).

[20] D. Averin and A. Bardas, *ac Josephson Effect in a Single Quantum Channel*, Phys. Rev. Lett. **75**, 1831–1834 (1995).

[21] E. Scheer, N. Agraït, J. C. Cuevas, A. L. Yeyati, B. Ludoph, A. Martín-Rodero, G. R.-B. Bollinger, J. M. van Ruitenbeek, and C. Urbina, *The signature of chemical valence in the electrical conduction through a single-atom contact*, Nature **394**, 154–157 (1998).

[22] A. I. Yanson. *Atomic chains and Electronic shells: quantum mechanisms for the formation of nanowires* (Ph. D thesis, University of Leiden, The Netherlands, 2001).

[23] M. R. Sørensen, M. Brandbyge, and K. W. Jacobsen, *Mechanical deformation of atomic-scale metallic contacts: Structure and mechanisms*, Phys. Rev. B **57**, 3283–3294 (1998).

[24] M. Brandbyge, M. R. Sørensen, and K. W. Jacobsen, *Conductance eigenchannels in nanocontacts*, Phys. Rev. B **56**, 14956–14959 (1997).

[25] J. C. Cuevas, A. L. Yeyati, and A. Martín-Rodero, *Microscopic Origin of Conducting Channels in Metallic Atomic-Size Contacts*, Phys. Rev. Lett. **80**, 1066–1069 (1998).

[26] J. C. Cuevas, A. Levy Yeyati, A. Martín-Rodero, G. Rubio-Bollinger, C. Untiedt, and N. Agraït, *Evolution of Conducting Channels in Metallic Atomic Contacts under Elastic Deformation*, Phys. Rev. Lett. **81**, 2990–2993 (1998).

[27] P. Damle, A. W. Ghosh, and S. Datta, *First-principles analysis of molecular conduction using quantum chemistry software*, Chemical Physics **281**, 171 – 187 (2002).

[28] A. Kohn, F. Weigend, and R. Ahlrichs, *Theoretical study on clusters of magnesium*, Physical Chemistry Chemical Physics **3**, 711–719 (2001).

[29] B. von Issendorff and O. Cheshnovsky, *Metal to Insulator Transitions in Clusters*, Annual Review of Physical Chemistry **56**, 549–580 (2005).

[30] I. Zutic, J. Fabian, and S. D. Sarma, *Spintronics: Fundamentals and applications*, Rev. Mod. Phys. **76**, 323–410 (2004).

[31] G. Binasch, P. Grünberg, F. Saurenbach, and W. Zinn, *Enhanced magnetoresistance in layered magnetic structures with antiferromagnetic interlayer exchange*, Phys. Rev. B **39**, 4828–4830 (1989).

[32] M. N. Baibich, J. M. Broto, A. Fert, F. N. Van Dau, F. Petroff, P. Etienne, G. Creuzet, A. Friederich, and J. Chazelas, *Giant Magnetoresistance of (001)Fe/(001)Cr Magnetic Superlattices*, Phys. Rev. Lett. **61**, 2472–2475 (1988).

[33] R. Skomski, *Nanomagnetics*, Journal of Physics: Condensed Matter **15**, R841–R896 (2003).

[34] N. García, M. Muñoz, and Y.-W. Zhao, *Magnetoresistance in excess of* 200% *in Ballistic Ni Nanocontacts at Room Temperature and 100 Oe*, Phys. Rev. Lett. **82**, 2923–2926 (1999).

[35] J. W. F. Egelhoff, L. Gan, H. Ettedgui, Y. Kadmon, C. J. Powell, P. J. Chen, A. J. Shapiro, R. D. McMichael, J. J. Mallett, T. P. Moffat, M. D. Stiles, and E. B. Svedberg. *Artifacts in ballistic magnetoresistance measurements (invited)* (AIP, 2004), volume 95, pp. 7554–7559.

[36] C. Sirvent, J. G. Rodrigo, S. Vieira, L. Jurczyszyn, N. Mingo, and F. Flores, *Conductance step for a single-atom contact in the scanning tunneling microscope: Noble and transition metals*, Phys. Rev. B **53**, 16086–16090 (1996).

[37] J. L. Costa-Krämer, *Conductance quantization at room temperature in magnetic and nonmagnetic metallic nanowires*, Phys. Rev. B **55**, R4875–R4878 (1997).

[38] H. Oshima and K. Miyano, *Spin-dependent conductance quantization in nickel point contacts*, Applied Physics Letters **73**, 2203–2205 (1998).

[39] F. Komori and K. Nakatsuji, *Quantized Conductance through Atomic-sized Iron Contacts at 4.2 K*, Journal of the Physical Society of Japan **68**, 3786–3789 (1999).

[40] T. Ono, Y. Ooka, H. Miyajima, and Y. Otani, *$2e^2/h$ to e^2/h switching of quantum conductance associated with a change in nanoscale ferromagnetic domain structure*, Applied Physics Letters **75**, 1622–1624 (1999).

[41] M. Viret, S. Berger, M. Gabureac, F. Ott, D. Olligs, I. Petej, J. F. Gregg, C. Fermon, G. Francinet, and G. L. Goff, *Magnetoresistance through a single nickel atom*, Phys. Rev. B **66**, 220401 (2002).

[42] F. Elhoussine, S. Mátéfi-Tempfli, A. Encinas, and L. Piraux, *Conductance quantization in magnetic nanowires electrodeposited in nanopores*, Applied Physics Letters **81**, 1681–1683 (2002).

[43] D. M. Gillingham, I. Linington, and J. A. C. Bland, *e^2/h quantization of the conduction in Cu nanowires*, Journal of Physics: Condensed Matter **14**, L567–L570 (2002).

[44] M. Shimizu, E. Saitoh, H. Miyajima, and Y. Otani, *Conductance quantization in ferromagnetic Ni nano-constriction*, Journal of Magnetism and Magnetic Materials **239**, 243 – 245 (2002).

[45] V. Rodrigues, J. Bettini, P. C. Silva, and D. Ugarte, *Evidence for Spontaneous Spin-Polarized Transport in Magnetic Nanowires*, Phys. Rev. Lett. **91**, 096801 (2003).

[46] D. M. Gillingham, C. Muller, and J. A. C. Bland, *Spin-dependent quantum transport effects in Cu nanowires*, Journal of Physics: Condensed Matter **15**, L291–L296 (2003).

[47] D. M. Gillingham, I. Linington, C. Müller, and J. A. C. Bland, *e^2/h quantization of the conduction in Cu nanowires*, Journal of Applied Physics **93**, 7388–7389 (2003).

[48] C. Untiedt, D. M. T. Dekker, D. Djukic, and J. M. van Ruitenbeek, *Absence of magnetically induced fractional quantization in atomic contacts*, Phys. Rev. B **69**, 081401(R) (2004).

[49] M. Gabureac, M. Viret, F. Ott, and C. Fermon, *Magnetoresistance in nanocontacts induced by magnetostrictive effects*, Phys. Rev. B **69**, 100401 (2004).

[50] C.-S. Yang, C. Zhang, J. Redepenning, and B. Doudin, *In situ magnetoresistance of Ni nanocontacts*, Applied Physics Letters **84**, 2865–2867 (2004).

[51] J. Costa-Kramer, M. Diaz, and P. Serena, *Magnetic field effects on total and partial conductance histograms in Cu and Ni nanowires*, Appl. Phys. A-Mater. Sci. Process. **81**, 1539–1543 (2005).

[52] K. I. Bolotin, F. Kuemmeth, A. N. Pasupathy, and D. C. Ralph, *From Ballistic Transport to Tunneling in Electromigrated Ferromagnetic Breakjunctions*, Nano Letters **6**, 123–127 (2006).

[53] Z. K. Keane, L. H. Yu, and D. Natelson, *Magnetoresistance of atomic-scale electromigrated nickel nanocontacts*, Applied Physics Letters **88**, 062514 (2006).

[54] K. I. Bolotin, F. Kuemmerth, and D. C. Ralph, *Anisotropic Magnetoresistance and Anisotropic Tunneling Magnetoresistance due to Quantum Interference in Ferromagnetic Metal Break Junctions*, Phys. Rev. Lett. **97**, 127202 (2006).

[55] M. Viret, M. Gabureac, F. Ott, C. Fermon, C. Barreteau, and R. Guirado-Lopez, *Giant Anisotropic Magneto-Resistance in ferromagnetic atomic contacts*, Eur. Phys. J. B **51**, 1–4 (2006).

[56] A. Martín-Rodero, A. L. Yeyati, and J. C. Cuevas, *Transport properties of normal and ferromagnetic atomic-size constrictions with superconducting electrodes*, Physica C: Superconductivity **352**, 67 – 72 (2001).

[57] A. Smogunov, A. D. Corso, and E. Tosatti, *Selective d-state conduction blocking in nickel nanocontacts*, Surface Science **507-510**, 609 – 614 (2002).

[58] A. Delin and E. Tosatti, *Magnetic phenomena in* 5*d transition metal nanowires*, Phys. Rev. B **68**, 144434 (2003).

[59] J. Velev and W. H. Butler, *Domain-wall resistance in metal nanocontacts*, Phys. Rev. B **69**, 094425 (2004).

[60] A. R. Rocha and S. Sanvito, *Asymmetric $I-V$ characteristics and magnetoresistance in magnetic point contacts*, Phys. Rev. B **70**, 094406 (2004).

[61] M. Wierzbowska, A. Delin, and E. Tosatti, *Effect of electron correlations in Pd, Ni, and Co monowires*, Phys. Rev. B **72**, 035439 (2005).

[62] A. Smogunov, A. D. Corso, and E. Tosatti, *Ballistic conductance and magnetism in short tip suspended Ni nanowires*, Phys. Rev. B **73**, 075418 (2006).

[63] J. C. Tung and G. Y. Guo, *Systematic ab initio study of the magnetic and electronic properties of all 3d transition metal linear and zigzag nanowires*, Phys. Rev. B **76**, 094413 (2007).

[64] A. Bagrets, N. Papanikolaou, and I. Mertig, *Magnetoresistance of atomic-sized contacts: An ab initio study*, Phys. Rev. B **70**, 064410 (2004).

[65] A. Bagrets, N. Papanikolaou, and I. Mertig, *Conduction eigenchannels of atomic-sized contacts: Ab initio KKR Green's function formalism*, Phys. Rev. B **75**, 235448 (2007).

[66] D. Jacob, J. Fernández-Rossier, and J. J. Palacios, *Magnetic and orbital blocking in Ni nanocontacts*, Phys. Rev. B **71**, 220403 (2005).

[67] H. Dalgleish and G. Kirczenow, *Theoretical study of spin-dependent electron transport in atomic Fe nanocontacts*, Phys. Rev. B **72**, 155429 (2005).

[68] D. Jacob and J. J. Palacios, *Orbital eigenchannel analysis for ab initio quantum transport calculations*, Phys. Rev. B **73**, 075429 (2006).

[69] J. D. Burton, R. F. Sabirianov, J. P. Velev, O. N. Mryasov, and E. Y. Tsymbal, *Effect of tip resonances on tunneling anisotropic magnetoresistance in ferromagnetic metal break-junctions: A first-principles study*, Phys. Rev. B **76**, 144430 (2007).

[70] D. Jacob, J. Fernández-Rossier, and J. J. Palacios, *Anisotropic magnetoresistance in nanocontacts*, Phys. Rev. B **77**, 165412 (2008).

[71] J. K. Viljas, J. C. Cuevas, F. Pauly, and M. Häfner, *Electron-vibration interaction in transport through atomic gold wires*, Phys. Rev. B **72**, 245415 (2005).

[72] F. Pauly, J. K. Viljas, U. Huniar, M. Häfner, S. Wohlthat, M. Bürkle, J. C. Cuevas, and G. Schön, *Cluster-based density-functional approach to quantum transport through molecular and atomic contacts*, New Journal of Physics **10**, 125019 (2008).

[73] M. Häfner, P. Konrad, F. Pauly, J. C. Cuevas, and E. Scheer, *Conduction channels of one-atom zinc contacts*, Phys. Rev. B **70**, 241404(R) (2004).

[74] E. Scheer, P. Konrad, C. Bacca, A. Mayer-Gindner, H. v. Löhneysen, M. Häfner, and J. C. Cuevas, *Correlation between transport properties and atomic configuration of atomic contacts of zinc by low-temperature measurements*, Phys. Rev. B **74**, 205430 (2006).

[75] R. H. M. Smit, A. Mares, M. Häfner, P. Pou, J. C. Cuevas, and J. M. van Ruitenbeek, *Metallic properties of magnesium point contacts*, Submitted to New Journal of Physics (2009).

[76] M. Häfner, J. K. Viljas, D. Frustaglia, F. Pauly, M. Dreher, P. Nielaba, and J. C. Cuevas, *Theoretical study of the conductance of ferromagnetic atomic-sized contacts*, Phys. Rev. B **77**, 104409 (2008).

[77] F. Pauly, M. Dreher, J. K. Viljas, M. Häfner, J. C. Cuevas, and P. Nielaba, *Theoretical analysis of the conductance histograms and structural properties of Ag, Pt, and Ni nanocontacts*, Phys. Rev. B **74**, 235106 (2006).

[78] M. Häfner, J. K. Viljas, and J. C. Cuevas, *Theory of anisotropic magnetoresistance in atomic-sized ferromagnetic metal contacts*, Phys. Rev. B **79**, 140410(R) (2009).

[79] N. W. Ashcroft and D. N. Mermin. *Solid State Physics* (Harcourt College Publ, New York, 2000).

[80] W. A. Harrison. *Electronic Structure and the Properties of Solids* (Dover Publications, New York, 1989).

[81] J. C. Cuevas and E. Scheer. *Molecular Electronics* (in preparation).

[82] J. C. Slater and G. F. Koster, *Simplified LCAO Method for the Periodic Potential Problem*, Phys. Rev. **94**, 1498–1524 (1954).

[83] E. W. Schpolski. *Atomphysik Bd. II* (VEB Deutscher Verlag der Wissenschaften, Berlin, 1958).

[84] D. A. Papaconstantopoulos. *Handbook of the band structure of elemental solids* (Plenum Press, New York, 1986).

[85] M. D. Stiles, *Generalized Slater-Koster method for fitting band structures*, Phys. Rev. B **55**, 4168–4173 (1997).

[86] O. K. Andersen and O. Jepsen, *Advances in the theory of one-electron energy states*, Physica B+C **91**, 317 – 328 (1977).

[87] O. K. Andersen, W. Klose, and H. Nohl, *Electronic structure of Chevrel-phase high-critical-field superconductors*, Phys. Rev. B **17**, 1209–1237 (1978).

[88] R. E. Cohen, M. J. Mehl, and D. A. Papaconstantopoulos, *Tight-binding total-energy method for transition and noble metals*, Phys. Rev. B **50**, 14694–14697 (1994).

[89] M. J. Mehl and D. A. Papaconstantopoulos, *Applications of a tight-binding total-energy method for transition and noble metals: Elastic constants, vacancies, and surfaces of monatomic metals*, Phys. Rev. B **54**, 4519–4530 (1996).

[90] M. J. Mehl and D. A. Papaconstantopoulos. *Topics in Computational Materials Science ed. by C.Y. Fong ch 5* (World Scientific, Singapore, 1998).

[91] D. A. Papaconstantopoulos and M. J. Mehl, *The Slater&Koster tight-binding method: a computationally efficient and accurate approach*, Journal of Physics: Condensed Matter **15**, R413–R440 (2003).

[92] C. E. Lekka, M. J. Mehl, N. Bernstein, and D. A. Papaconstantopoulos, *Tight-binding simulations of Nb surfaces and surface defects*, Phys. Rev. B **68**, 035422 (2003).

[93] F. Pauly. *Phase-coherent electron transport through metallic atomic-sized contacts and organic molecules* (Ph. D thesis, Universtät Karlsruhe, Germany, 2007).

[94] P. Hohenberg and W. Kohn, *Inhomogeneous Electron Gas*, Phys. Rev. **136**, B864–B871 (1964).

[95] L. H. Thomas, *The calculation of atomic fields*, Mathematical Proceedings of the Cambridge Philosophical Society **23**, 542–548 (1927).

[96] E. Fermi, *Un Metodo Statistico per la Determinazione di alcune Priorieta dell'Atome*, Rendiconti Lincei **6**, 602âĂŞ607 (1927).

[97] W. Kohn and L. J. Sham, *Self-Consistent Equations Including Exchange and Correlation Effects*, Phys. Rev. **140**, A1133–A1138 (1965).

[98] E. N. Economou. *Green's Functions in Quantum Physics* (Springer, Berlin, 2006).

[99] A. Szabo and N. S. Ostlund. *Modern quantum chemistry: introduction to advanced electronic structure theory* (Dover Publications, New York, 1996).

[100] M. Brandbyge, N. Kobayashi, and M. Tsukada, *Conduction channels at finite bias in single-atom gold contacts*, Phys. Rev. B **60**, 17064–17070 (1999).

[101] D. C. Langreth. *Linear and Non-Linear Response Theory with Applications.* In *Linear and Nonlinear Electron Transport in Solids*, *NATO-ASI Series B*, volume 17, edited by J. Devrees and E. van Doren (Plenum, New York, 1976), *NATO-ASI Series B*, volume 17.

[102] P. W. Anderson, *Localized Magnetic States in Metals*, Phys. Rev. **124**, 41–53 (1961).

[103] D. M. Newns, *Self-Consistent Model of Hydrogen Chemisorption*, Phys. Rev. **178**, 1123–1135 (1969).

[104] F. Guinea, C. Tejedor, F. Flores, and E. Louis, *Effective two-dimensional Hamiltonian at surfaces*, Phys. Rev. B **28**, 4397–4402 (1983).

[105] J. C. Cuevas. *Electronic transport in normal and superconducting nanostructures* (Ph. D thesis, Universidad Autónoma de Madrid, Spain, 1999).

[106] S. H. Yang, M. J. Mehl, and D. A. Papaconstantopoulos, *Application of a tight-binding total-energy method for Al, Ga, and In*, Phys. Rev. B **57**, R2013–R2016 (1998).

[107] N. C. Bacalis, D. A. Papaconstantopoulos, M. J. Mehl, and M. Lach-hab, Physica B **296** (2001).

[108] M. J. Mehl, D. A. Papaconstantopoulos, I. I. Mazin, N. C. Bacalis, and W. E. Pickett. *Applications of the NRL tight-binding method to magnetic systems* (AIP, 2001), volume 89, pp. 6880–6882.

[109] H. J. Gotsis, D. A. Papaconstantopoulos, and M. J. Mehl, *Tight-binding calculations of the band structure and total energies of the various phases of magnesium*, Phys. Rev. B **65**, 134101 (2002).

[110] M. I. Haftel, N. Bernstein, M. J. Mehl, and D. A. Papaconstantopoulos, *Interlayer surface relaxations and energies of fcc metal surfaces by a tight-binding method*, Phys. Rev. B **70**, 125419 (2004).

[111] D. Papaconstantopoulos, M. Mehl, and B. Akdim. *Applications of a new tight-binding total energy method*. In *NOVEL MATERIALS DESIGN AND PROPERTIES*, edited by B. Rao and S. Behera (NOVA SCIENCE PUBLISHERS, INC, 1998), pp. 393–403. International Conference on Novel Materials, PURI, INDIA, MAR 03-07, 1997.

[112] M. Dreher, F. Pauly, J. Heurich, J. C. Cuevas, E. Scheer, and P. Nielaba, *Structure and conductance histogram of atomic-sized Au contacts*, Phys. Rev. B **72**, 075435 (2005).

[113] S. Wohlthat. *Phasenkohärenter Transport durch Aluminium-Punktkontakte in der Gegenwart von Gasmolekülen* (Diploma thesis, Universtät Karlsruhe, Germany, 2006).

[114] D. R. Lide. *CRC Handbook of Chemistry and Physics, 79th Edition* (CRC Press, Boca Raton, FL, 1998).

[115] E. Scheer, P. Joyez, D. Esteve, C. Urbina, and M. H. Devoret, *Conduction Channel Transmissions of Atomic-Size Aluminum Contacts*, Phys. Rev. Lett. **78**, 3535–3538 (1997).

[116] J. M. van Ruitenbeek, A. Alvarez, I. Piñeyro, C. Grahmann, P. Joyez, M. H. Devoret, D. Esteve, and C. Urbina, *Adjustable nanofabricated atomic size contacts*, Review of Scientific Instruments **67**, 108–111 (1996).

[117] C. R. Cleavelin and B. J. Marshall, *Ultrasonic-attenuation determination of the anisotropic energy gap in superconducting zinc*, Phys. Rev. B **10**, 1902–1911 (1974).

[118] A. Mayer-Gindner, H. v. Löhneysen, and E. Scheer. *Electrical transport properties of stable single-atom contacts of zinc* (2004).

[119] U. Schulz, P. Wilbrandt, and R. Tidecks, *Growth and crystallographic orientations of zinc and zinc-silver whiskers*, Journal of Crystal Growth **85**, 472 – 476 (1987).

[120] P. Jelínek, R. Pérez, J. Ortega, and F. Flores, *First-principles simulations of the stretching and final breaking of Al nanowires: Mechanical properties and electrical conductance*, Phys. Rev. B **68**, 085403 (2003).

[121] A. I. Yanson and J. M. van Ruitenbeek, *Do Histograms Constitute a Proof for Conductance Quantization?*, Phys. Rev. Lett. **79**, 2157 (1997).

[122] H. E. van den Brom and J. M. van Ruitenbeek, *Quantum Suppression of Shot Noise in Atom-Size Metallic Contacts*, Phys. Rev. Lett. **82**, 1526–1529 (1999).

[123] R. Cron, M. F. Goffman, D. Esteve, and C. Urbina, *Multiple-Charge-Quanta Shot Noise in Superconducting Atomic Contacts*, Phys. Rev. Lett. **86**, 4104–4107 (2001).

[124] B. Ludoph, M. H. Devoret, D. Esteve, C. Urbina, and J. M. van Ruitenbeek, *Evidence for Saturation of Channel Transmission from Conductance Fluctuations in Atomic-Size Point Contacts*, Phys. Rev. Lett. **82**, 1530–1533 (1999).

[125] B. Ludoph and J. M. v. Ruitenbeek, *Thermopower of atomic-size metallic contacts*, Phys. Rev. B **59**, 12290–12293 (1999).

[126] M. F. Goffman, R. Cron, A. Levy Yeyati, P. Joyez, M. H. Devoret, D. Esteve, and C. Urbina, *Supercurrent in Atomic Point Contacts and Andreev States*, Phys. Rev. Lett. **85**, 170–173 (2000).

[127] H. Ohnishi, Y. Kondo, and K. Takayanagi, *Quantized conductance through individual rows of suspended gold atoms*, Nature **395**, 780–783 (Oct 1998).

[128] V. Rodrigues, T. Fuhrer, and D. Ugarte, *Signature of Atomic Structure in the Quantum Conductance of Gold Nanowires*, Phys. Rev. Lett. **85**, 4124–4127 (2000).

[129] T. Böhler, J. Grebing, A. Mayer-Gindner, H. v. Löhneysen, and E. Scheer, *Mechanically controllable break-junctions for use as electrodes for molecular electronics*, Nanotechnology **15**, S465–S471 (2004).

[130] B. Ludoph, N. van der Post, E. N. Bratus', E. V. Bezuglyi, V. S. Shumeiko, G. Wendin, and J. M. van Ruitenbeek, *Multiple Andreev reflection in single-atom niobium junctions*, Phys. Rev. B **61**, 8561–8569 (2000).

[131] P. Konrad, C. Bacca, E. Scheer, P. Brenner, A. Mayer-Gindner, and H. v. Löhneysen, *Stable single-atom contacts of zinc whiskers*, Applied Physics Letters **86**, 213115 (2005).

[132] O. C. Thomas, W. Zheng, S. Xu, and K. H. Bowen, *Onset of Metallic Behavior in Magnesium Clusters*, Phys. Rev. Lett. **89**, 213403 (2002).

[133] T. P. Martin, *Shells Of Atoms*, Physics Reports **273**, 199–241 (1996).

[134] T. P. Martin, T. Bergmann, H. Göhlich, and T. Lange, *Evidence for icosahedral shell structure in large magnesium clusters*, Chemical Physics Letters **176**, 343–347 (1991).

[135] T. Diederich, T. Döppner, J. Braune, J. Tiggesbäumker, and K. H. Meiwes-Broer, *Electron Delocalization in Magnesium Clusters Grown in Supercold Helium Droplets*, Physical Review Letters **86**, 4807–4810 (2001).

[136] A. I. Yanson, I. K. Yanson, and J. M. van Ruitenbeek, *Crossover from Electronic to Atomic Shell Structure in Alkali Metal Nanowires*, Physical Review Letters **87**, 216805 (2001).

[137] A. I. Mares and J. M. van Ruitenbeek, *Observation of shell effects in nanowires for the noble metals Cu, Ag, and Au*, Phys. Rev. B **72**, 205402 (2005).

[138] A. I. Mares, D. F. Urban, J. Bürki, H. Grabert, C. A. Stafford, and J. M. van Ruitenbeek, *Electronic and atomic shell structure in aluminium nanowires*, Nanotechnology **18**, 265403 (2007).

[139] A. I. Yanson, I. K. Yanson, and J. M. van Ruitenbeek, *Observation of shell structure in sodium nanowires*, Nature **400**, 144–146 (1999).

[140] B. Sakintuna, F. Lamari-Darkrim, and M. Hirscher, *Metal hydride materials for solid hydrogen storage: A review*, International Journal of Hydrogen Energy **32**, 1121–1140 (2007).

[141] J. M. Krans, J. M. van Ruitenbeek, V. V. Fisun, I. K. Yanson, and L. J. de Jongh, *The signature of conductance quantization in metallic point contacts*, Nature **375**, 767–769 (1995).

[142] J. A. Torres, J. I. Pascual, and J. J. Sáenz, *Theory of conduction through narrow constrictions in a 3-dimensional electron-gas*, Phys. Rev. B **49**, 16581–16584 (1994).

[143] C. Höppler and W. Zwerger. *Comment on "Jellium Model of Metallic Nanocohesion"* (1998). Comment on C. A. Stafford, D. Baeriswyl, and J. BÃijrki, Phys. Rev. Lett. 79, 2863 (1997).

[144] E. Ogando, N. Zabala, and M. J. Puska, *Analysis of the shell- and supershell structures of metallic nanowires with jellium models*, Nanotechnology **13**, 363–368 (2002).

[145] D. F. Urban, J. Bürki, C. A. Stafford, and H. Grabert, *Stability and symmetry breaking in metal nanowires: The nanoscale free-electron model*, Phys. Rev. B **74**, 245414 (2006).

[146] A. Lyalin, I. A. Solov'yov, A. V. Solov'yov, and W. Greiner, *Evolution of the electronic and ionic structure of Mg clusters with increase in cluster size*, Phys. Rev. A **67**, 063203 (2003).

[147] A. I. Mares, A. F. Otte, L. G. Soukiassian, R. H. M. Smit, and J. M. van Ruitenbeek, *Observation of electronic and atomic shell effects in gold nanowires*, Phys. Rev. B **70**, 073401 (2004).

[148] M. C. Payne, M. P. Teter, D. C. Allan, T. A. Arias, and J. D. Joannopoulos, *Iterative minimization techniques for ab initio total-energy calculations: molecular dynamics and conjugate gradients*, Rev. Mod. Phys. **64**, 1045–1097 (1992).

[149] D. Vanderbilt, *Soft self-consistent pseudopotentials in a generalized eigenvalue formalism*, Phys. Rev. B **41**, 7892–7895 (1990).

[150] J. P. Perdew, K. Burke, and M. Ernzerhof, *Generalized Gradient Approximation Made Simple*, Phys. Rev. Lett. **77**, 3865–3868 (1996).

[151] H. J. Monkhorst and J. D. Pack, *Special points for Brillouin-zone integrations*, Phys. Rev. B **13**, 5188–5192 (1976).

[152] K. Hansen, E. Lægsgaard, I. Stensgaard, and F. Besenbacher, *Quantized conductance in relays*, Phys. Rev. B **56**, 2208–2220 (1997).

[153] F. Ott, S. Barberan, J. G. Lunney, J. M. D. Coey, P. Berthet, A. M. de Leon-Guevara, and A. Revcolevschi, *Quantized conductance in a contact between metallic oxide crystals*, Phys. Rev. B **58**, 4656–4659 (1998).

[154] B. Ludoph and J. M. v. Ruitenbeek, *Conductance fluctuations as a tool for investigating the quantum modes in atomic-size metallic contacts*, Phys. Rev. B **61**, 2273–2285 (2000).

[155] P. S. Krstić, X.-G. Zhang, and W. H. Butler, *Generalized conductance formula for the multiband tight-binding model*, Phys. Rev. B **66**, 205319 (2002).

[156] P. A. Khomyakov, G. Brocks, V. Karpan, M. Zwierzycki, and P. J. Kelly, *Conductance calculations for quantum wires and interfaces: Mode matching and Green's functions*, Phys. Rev. B **72**, 035450 (2005).

[157] J. Fernández-Rossier, D. Jacob, C. Untiedt, and J. J. Palacios, *Transport in magnetically ordered Pt nanocontacts*, Phys. Rev. B **72**, 224418 (2005).

[158] K. Xia, M. Zwierzycki, M. Talanana, P. J. Kelly, and G. E. W. Bauer, *First-principles scattering matrices for spin transport*, Phys. Rev. B **73**, 064420 (2006).

[159] A. R. Rocha, T. Archer, and S. Sanvito, *Search for magnetoresistance in excess of 1000% in Ni point contacts: Density functional calculations*, Phys. Rev. B **76**, 094406 (2007).

[160] D. J. Bakker, Y. Noat, A. I. Yanson, and J. M. van Ruitenbeek, *Effect of disorder on the conductance of a Cu atomic point contact*, Phys. Rev. B **65**, 235416 (2002).

[161] G. Autes, C. Barreteau, D. Spanjaard, and M.-C. Desjonqueres, *Magnetism of iron: from the bulk to the monatomic wire*, Journal of Physics: Condensed Matter **18**, 6785–6813 (2006).

[162] R. Soulen, J. Byers, M. Osofsky, B. Nadgorny, T. Ambrose, S. Cheng, P. Broussard, C. Tanaka, J. Nowak, J. Moodera, A. Barry, and J. Coey, *Measuring the spin polarization of a metal with a superconducting point contact*, Science **282**, 85–88 (1998).

[163] A. Messiah. *Quantum Mechanics, Vol. I*, volume 1 (Wiley & Sons, New York, 1958).

[164] K. W. Jacobsen, P. Stoltze, and J. K. Nørskov, *A semi-empirical effective medium theory for metals and alloys*, Surface Science **366**, 394–402 (1996).

[165] P. Stoltze. *Simulation methods in atomic-scale materials physics* (Polyteknisk Forlag, Lyngby, 1997).

[166] D. Frenkel and B. Smit. *Understanding Molecular Simulation* (Academic Press, 2nd edition, San Diego, 1996).

[167] A. Nakamura, M. Brandbyge, L. B. Hansen, and K. W. Jacobsen, *Density Functional Simulation of a Breaking Nanowire*, Phys. Rev. Lett. **82**, 1538–1541 (1999).

[168] S. R. Bahn and K. W. Jacobsen, *Chain Formation of Metal Atoms*, Phys. Rev. Lett. **87**, 266101 (2001).

[169] A. M. Bratkovsky, A. P. Sutton, and T. N. Todorov, *Conditions for conductance quantization in realistic models of atomic-scale metallic contacts*, Phys. Rev. B **52**, 5036–5051 (1995).

[170] P. García-Mochales, S. Peláez, P. Serena, E. Medina, and A. Hasmy, *Breaking processes in nickel nanocontacts: a statistical description*, Appl. Phys. A-Mater. Sci. Process. **81**, 1545–1549 (2005).

[171] T. McGuire and R. Potter, *Anisotropic magnetoresistance in ferromagnetic 3d alloys*, IEEE Transactions on Magnetics **11**, 1018–1038 (1975).

[172] S. Adam, M. Kindermann, S. Rahav, and P. W. Brouwer, *Mesoscopic anisotropic magnetoconductance fluctuations in ferromagnets*, Phys. Rev. B **73**, 212408 (2006).

[173] A. Sokolov, E. Y. Tsymbal, J. Redepenning, and B. Doudin, *Quantized magnetoresistance in atomic-size contacts*, Nature Nanotechnology **2**, 171–175 (2007).

[174] J. Velev, R. F. Sabirianov, S. S. Jaswal, and E. Y. Tsymbal, *Ballistic Anisotropic Magnetoresistance*, Phys. Rev. Lett. **94**, 127203 (2005).

[175] S.-F. Shi and D. C. Ralph, *Atomic motion in ferromagnetic break junctions*, Nature Nanotechnology **2**, 522 (2007).

[176] S. F. Shi, K. I. Bolotin, F. Kuemmeth, and D. C. Ralph, *Temperature dependence of anisotropic magnetoresistance and atomic rearrangements in ferromagnetic metal break junctions*, Phys. Rev. B **76**, 184438 (2007).

[177] H. Takayama, K. P. Bohnen, and P. Fulde, *Magnetic surface anisotropy of transition metals*, Phys. Rev. B **14**, 2287–2295 (1976).

[178] V. M. García-Suárez, D. Z. Manrique, C. J. Lambert, and J. Ferrer, *Anisotropic magnetoresistance in atomic chains of iridium and platinum from first principles*, Phys. Rev. B **79**, 060408 (2009).

[179] R. A. Guirado-López, J. Dorantes-Dávila, and G. M. Pastor, *Orbital Magnetism in Transition-Metal Clusters: From Hund's Rules to Bulk Quenching*, Phys. Rev. Lett. **90**, 226402 (2003).

[180] M.-C. Desjonquères, C. Barreteau, G. Autès, and D. Spanjaard, *Orbital contribution to the magnetic properties of iron as a function of dimensionality*, Phys. Rev. B **76**, 024412 (2007).

[181] P. Bruno, *Tight-binding approach to the orbital magnetic moment and magnetocrystalline anisotropy of transition-metal monolayers*, Phys. Rev. B **39**, 865(R) (1989).

[182] P. Bruno. *Anisotropie Magnétique et Hystérésis du Cobalt à l'Échelle du Plan Atomique: Théorie et Expérience* (Ph. D thesis, Université Paris Sud - Paris XI, France, 1989).

[183] G. Autès, C. Barreteau, D. Spanjaard, and M.-C. Desjonquères, *Electronic transport in iron atomic contacts: From the infinite wire to realistic geometries*, Phys. Rev. B **77**, 155437 (2008).

[184] B. T. Thole, P. Carra, F. Sette, and G. van der Laan, *X-ray circular dichroism as a probe of orbital magnetization* .

[185] C. Untiedt, G. Rubio-Bollinger, S. Vieira, and N. Agraït, *Quantum interference in atomic-sized point contacts*, Phys. Rev. B **62**, 9962–9965 (2000).

Abbreviations

AMR	Anisotropic Magnetoresistance
BAMR	Ballistic Anisotropic Magnetoresistance
BCS	Bardeen Cooper Schrieffer model of superconductivity
bcc	Body Centered Cubic crystal structure
CN	Charge Neutrality
DOS	Density of States
ε_F	Fermi energy
EOM	Equation of Motion
fcc	Face Centered Cubic crystal structure
hcp	Hexagonal Closed Package crystal structure
HOMO	Highest Occupied Molecular Orbital
I-V	Current-voltage
LCAO	Linear Combination of Atomic Orbitals
LDOS	Local Density of States
LUMO	Lowest Unoccupied Molecular Orbital
MAR	Multiple Andreev reflections
MCBJ	Mechanically Controllable Break Junction
MD	Molecular Dynamics
MIT	Metal to Insulator Transition
NEGF	Nonequilibrium Green's Function
NN	Nearest Neighbour
NRL	Naval Research Laboratory
SK	Slater-Koster
SOC	Spin-orbit coupling
STM	Scanning Tunneling Microscope
TB	Tight-Binding
UHV	Ultra High Vacuum

Research project, Diploma theses:

1. *Modeling of a protoplanetary disk*, M. Häfner, Stage du deuxième année de l'ENSPG (2nd year internship) with Prof. Dr. Jordi Isern, IEEC Barcelona, Spain (2001).
2. *Etude de l'effet de peau dans le borocarbure $LuNi_2B_2C$*, M. Häfner, Projet de fin d'études de l'ENSPG (Diploma thesis) with Prof. Dr. Jean-Pascal Brison, CRTBT Grenoble, France (2002).
3. *Elektronischer Transport in metallischen Atomkontakten*, M. Häfner, Diplomarbeit (Diploma thesis) with Prof. Dr. Gerd Schön and Prof. Dr. Juan Carlos Cuevas, TFP Universität Karlsruhe (2004).

Regular articles:

4. *Conductance Channels of One-Atom Zinc Contacts*, M. Häfner, P. Konrad, F. Pauly, J.C. Cuevas, and E. Scheer, Phys. Rev. B **70**, 241404(R) (2004).
5. *Electron-vibration interaction in transport through atomic gold wires*, J.K. Viljas, J.C. Cuevas, F. Pauly, and M. Häfner, Phys. Rev. B. **72**, 245415 (2005).
6. *Correlation between transport properties and atomic configuration of atomic contacts of zinc by low-temperature measurements*, E. Scheer, P. Konrad, C. Bacca, A. Mayer-Gindner, H. v. Löhneysen, M. Häfner, and J.C. Cuevas, Phys. Rev. B. **74**, 205430 (2006).
7. *Theoretical analysis of the conductance histograms and structural properties of Ag, Pt, and Ni nanocontacts*, F. Pauly, M. Dreher, J.K. Viljas, M. Häfner, J.C. Cuevas, and P. Nielaba, Phys. Rev. B. **74**, 235106 (2006).
8. *Theoretical study of the conductance of ferromagnetic atomic-sized contacts*, M. Häfner, J.K. Viljas, D. Frustaglia, F. Pauly, M. Dreher, P. Nielaba, and J.C. Cuevas, Phys. Rev. B. **77**, 104409 (2008).
9. *Cluster-based density-functional approach to quantum transport through molecular and atomic contacts*, F. Pauly, J.K. Viljas, U. Huniar, M. Häfner, S. Wohlthat, M. Bürkle, J.C. Cuevas, and G. Schön, New J. Phys. **10**, 125019 (2008).
10. *Theory of anisotropic magnetoresistance in atomic-sized ferromagnetic metal contacts*, M. Häfner, J.K. Viljas, and J.C. Cuevas, Phys. Rev. B **79**, 140410(R) (2009).

Preprint:

11. *Metallic properties of magnesium point contacts*, R.H.M. Smit, A.I. Mares, M. Häfner, P. Pou, J.C. Cuevas, and J.M. van Ruitenbeek, submitted to New J. Phys. (2009).